

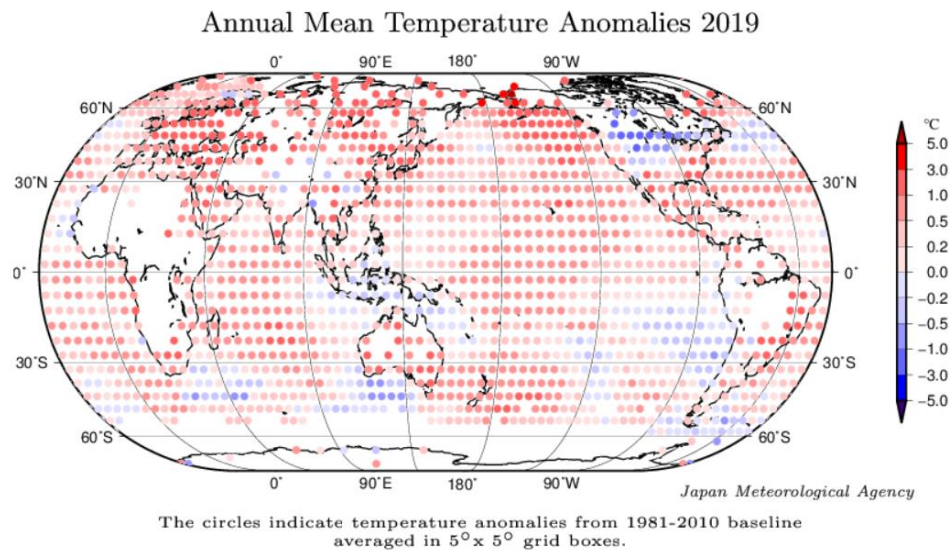
Reviewer comments are in black and author responses are in blue.

The authors have addressed two of my major comments almost to satisfaction (1 and 4), and for two others I'm willing to agree to disagree (5 and 6). However, the answers to major comment 3, and to lesser extent 2, remain unsatisfactory.

Major comment 1)

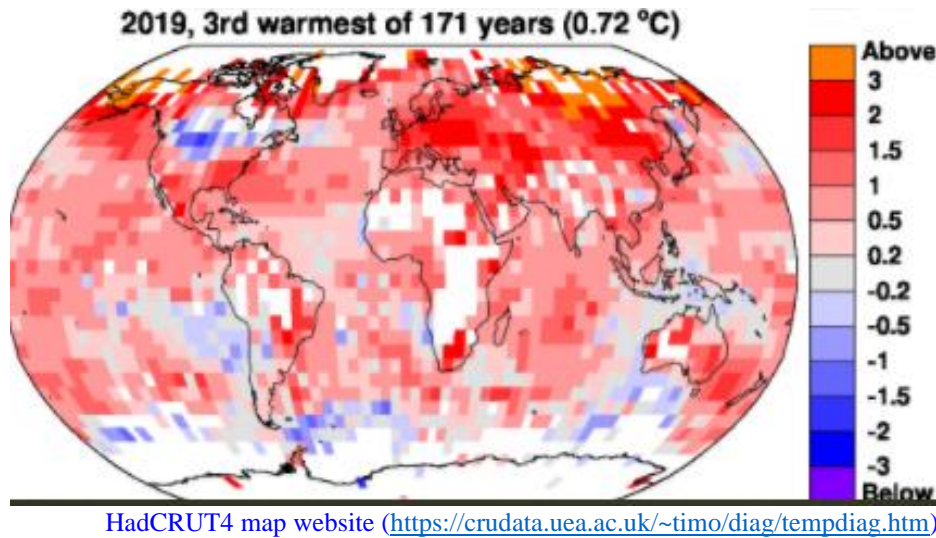
I see no reason to include JMA in the analysis. It has an even lower spatial coverage than HadCRUT4 and is therefore not a global temperature. Its uncritical inclusion may therefore lead to a biased understanding of the topic. Furthermore, the images are really crammed. Similarly, Cowtan can be dropped, now that HadCRUT5 is out, improving Figures 6 and 7.

It is important for us to continue to show results for both JMA and Cowtan and Way (CW14) datasets. These two maps show the spatial coverage of the JMA and HadCRUT4 data sets in 2019. They have similar spatial coverage. Hence, the notion that the JMA data set does not reflect global mean surface temperature could be applied as well to the HadCRUT4 data set, which has long been used in studies similar to our analysis.



JMA map website (https://ds.data.jma.go.jp/tcc/tcc/products/gwp/temp/map/temp_map.html)

We strongly prefer to retain both the JMA and CW14 data sets to represent the current state of knowledge based on the seven GMST data sets that are available. Including CW14 is important because our analysis displayed in Figs. 6 and 7 is now the first to show that the transformation of HadCRUT4 into a more complete global coverage data set by CW14 results in very similar values of AAWR and ECS obtained from HadCRUT5. This is an important result that will be of interest to the community. It would not be fair to Kevin Cowtan and Robert Way, creators of this data set, to relegate the result found using their time series of GMST to the supplement.



Major comment 3)

In Figure 14, the authors show that their model gives a good fit for a wide variety of assumptions on λ . They show that an 50% higher ECS is very well in line with observations, and that even a doubling is still consistent with their criterion of $X^2 < 2$. Despite this, the authors say choosing a point estimate is reasonable, by visual inspection of the graph (14e-h) that I find questionable and is not in line with the $X^2 < 2$ criterion used in the rest of the manuscript.

Thank you for this comment. We have heavily revised our discussion of effective climate sensitivity in Sect. 3.3.6, the Abstract, and the Conclusions to reflect values found using time varying climate feedback. The specific, detailed changes are given in the response to comments that appear below.

With the insistence of using the assumption that λ is constant, the authors do not compute ECS and do not give a 'comprehensive analysis of uncertainties in AAWR, ECS, and projections of ΔT in our EM-GC framework,' as they claim in the conclusion. Instead, the authors compute what is sometimes called effective climate sensitivity (<https://iopscience.iop.org/article/10.1088/1748-9326/ab738f>), and their analysis of future temperatures should be described as a lower bound consistently throughout the entire manuscript. By comparing effective ECS with ECS computed with the Gregory method, they compare apples with pears. In discussing other papers, the authors also do not make this important distinction.

We have examined several other studies to determine the type of climate sensitivity we are estimating within the EM-GC framework and for the CMIP6 GCMs via the Gregory et al. (2004) method. As indicated by the paper you provided (Tokarska et al., 2020) that is now cited, we are indeed estimating effective climate sensitivity with the EM-GC. We have updated our abstract, Sect. 2.4, Sect. 3.2, and the conclusions to make it clear to the reader we are estimating effective climate sensitivity rather than equilibrium climate sensitivity. In our abstract on line 13, we define ECS as effective climate sensitivity. For

Sect. 2.4, we have renamed the section header **Effective climate sensitivity**. We also added a new sentence starting on line 564 that reads: **In our model framework, we infer the climate sensitivity based on an estimate of climate feedback from the historical record, resulting in the effective climate sensitivity (ECS) (Tokarska et al., 2020a).** In Sect. 3.2, we redefine ECS as **Effective climate sensitivity**.

Close inspection of Gregory et al. (2004), Zelinka et al. (2020) and Sherwood et al. (2020) indicate that the method devised by Gregory et al. (2004) also computes *effective climate sensitivity* from the GCMs rather than true equilibrium climate sensitivity, because the Gregory et al. (2004) method assumes the feedbacks inferred from the first 150 years following the abrupt $4\times\text{CO}_2$ simulation persist until equilibrium. We have added the following text starting on line 576: **We refer to the quantity in Eq. (10) as effective climate sensitivity, rather than equilibrium climate sensitivity, because for most of our analysis we assume a constant value of climate feedback inferred from prior observations.** and on line 581: **The Gregory et al. (2004) method also estimates effective climate sensitivity from the CMIP6 GCMs (Gregory et al., 2004; Sherwood et al., 2020; Zelinka et al., 2020) because it assumes the feedbacks inferred from the first 150 years of the abrupt $4\times\text{CO}_2$ CMIP6 GCM simulations persist until equilibrium**

The estimates of effective climate sensitivity based on Eq. (10) and the Gregory et al. (2004) method are not comparing the exact same type of effective climate sensitivity because the Gregory et al. (2004) method involves a large perturbation to RF that has not occurred in the historical climate record. We have added the following text starting on line 593 to make this point clear to the reader: **The estimates of climate sensitivity from Eq. (10) and those found using the Gregory et al. (2004) method are termed “effective” because they assume climate feedback inferred from either the historical climate record or the abrupt $4\times\text{CO}_2$ experiment persists until equilibrium. However, these estimates of ECS differ in that the perturbation to the RF of climate over the historical record is considerably smaller than the RF of climate that underlies the $4\times\text{CO}_2$ experiment of the Gregory et al. (2004) method. We quantify the impact of time variable climate feedback on climate sensitivity in Sect. 3.3.6.**

We have also added information to the Fig. 8 caption designating whether the estimate of climate sensitivity provided by other studies are effective climate sensitivity or equilibrium climate sensitivity. We use the definitions given by Gregory et al. (2004), Tokarska et al. (2020), and Zelinka et al. (2020) that effective climate sensitivity estimates assume values of climate feedback inferred from either the historical record or the first 150 years of the Gregory method will persist until equilibrium. Some of the studies have designated their estimates of climate sensitivity as effective, while others have demonstrated why theirs are true estimates of equilibrium climate sensitivity. A few studies have not specified if their estimates of climate sensitivity are truly at equilibrium, so we used information from the manuscripts to make a designation. We added the following text to the Fig. 8 caption designating which studies provide estimates of

effective or equilibrium climate sensitivity: **The studies estimating effective climate sensitivity are AO13, NL+PG18, RS18, FN20, SS20 KT20a, KT20b, and MZ20. The studies estimating equilibrium climate sensitivity are KA17, AD18, PC18, MR20, and CP+PH17. See the supplement for...more information about which studies are estimating effective and equilibrium climate sensitivity.**

We added new text starting on line 250 of the supplement to explain to the reader how we designate the studies providing effective or equilibrium climate sensitivity: **The Fig. 8 caption in Sect. 3.2 also refers to the supplement for information about which studies are estimating effective climate sensitivity or equilibrium climate sensitivity. We designate each study based on information found in their manuscripts if their analysis uses the Gregory et al. (2004) method or infers climate feedback from the historical climate record will persist until equilibrium. The use of either of these two factors results in our designation of effective climate sensitivity (Gregory et al., 2004; Sherwood et al., 2020; Tokarska et al., 2020a; Zelinka et al., 2020). Based on our examination of IPCC 2013, it seems their estimate is a combination of effective climate sensitivity and equilibrium climate sensitivity.**

I had very much hoped the researchers would extend their model so that they compute true ECS instead. A simultaneous evaluation of time variation in lambda and aerosol uncertainty would lead to interesting results, considering the authors are able to account for internal variability.

* The authors state in the abstract that RF of aerosols is the main uncertainty but show in their results that the time-component of lambda is equally uncertain (I quote: Increasing λ^{-1} by 50% results in a similar value of ΔT_{2100} as when utilizing a higher value of AER RF2011 (i.e., AER RF2011 less than -0.9 W m^{-2}) in the EM-GC framework).

Thanks for these excellent comments that has led to an important improvement to our paper.

First, the uncertainty in aerosol radiative forcing (AER RF) is the main uncertainty for values of AAWR. The value of climate feedback, if it has varied over the historical climate record, would change by only a small amount from 1975-2014, the time period of the analysis for AAWR. The impact of uncertainty on AAWR of time variant lambda would be very small, so the dominant uncertainty for AAWR remains AER RF.

For effective climate sensitivity (ECS), the uncertainty in AER RF is still the dominant form of uncertainty. However, the variation in λ^{-1} over time does introduce an additional, important uncertainty in our estimates of ECS that we now consider. New Figure 14 shows the change in ΔT for SSP2-4.5 using a simulation of the EM-GC that is trained to the HadCRUT5 GMST record, uses a value of $\text{AER RF}_{2011} = -0.9 \text{ W m}^{-2}$, and the average of the five data sets for the OHC record. The best estimate of ECS given in Sect. 3.2 of our manuscript is 2.33°C . If we allow λ^{-1} to vary over time in a manner that mimics the behavior of GCMs, the best estimate of ECS, which we denote as $\text{ECS}_{\lambda(t)}$, is

3.08°C (range 2.23 to 5.53°C). We have added new text to the Abstract, Sect. 3.3.6, and the Conclusions pointing out these numerical values of $ECS_{\lambda(t)}$. We also added information to the supplement for estimates of $ECS_{\lambda(t)}$ if we allow λ^{-1} to increase over time so values of χ^2_{RECENT} are less than or equal to two. Our estimate of $ECS_{\lambda(t)}$ rises to 3.52°C (range of 2.71 to 5.53°C)

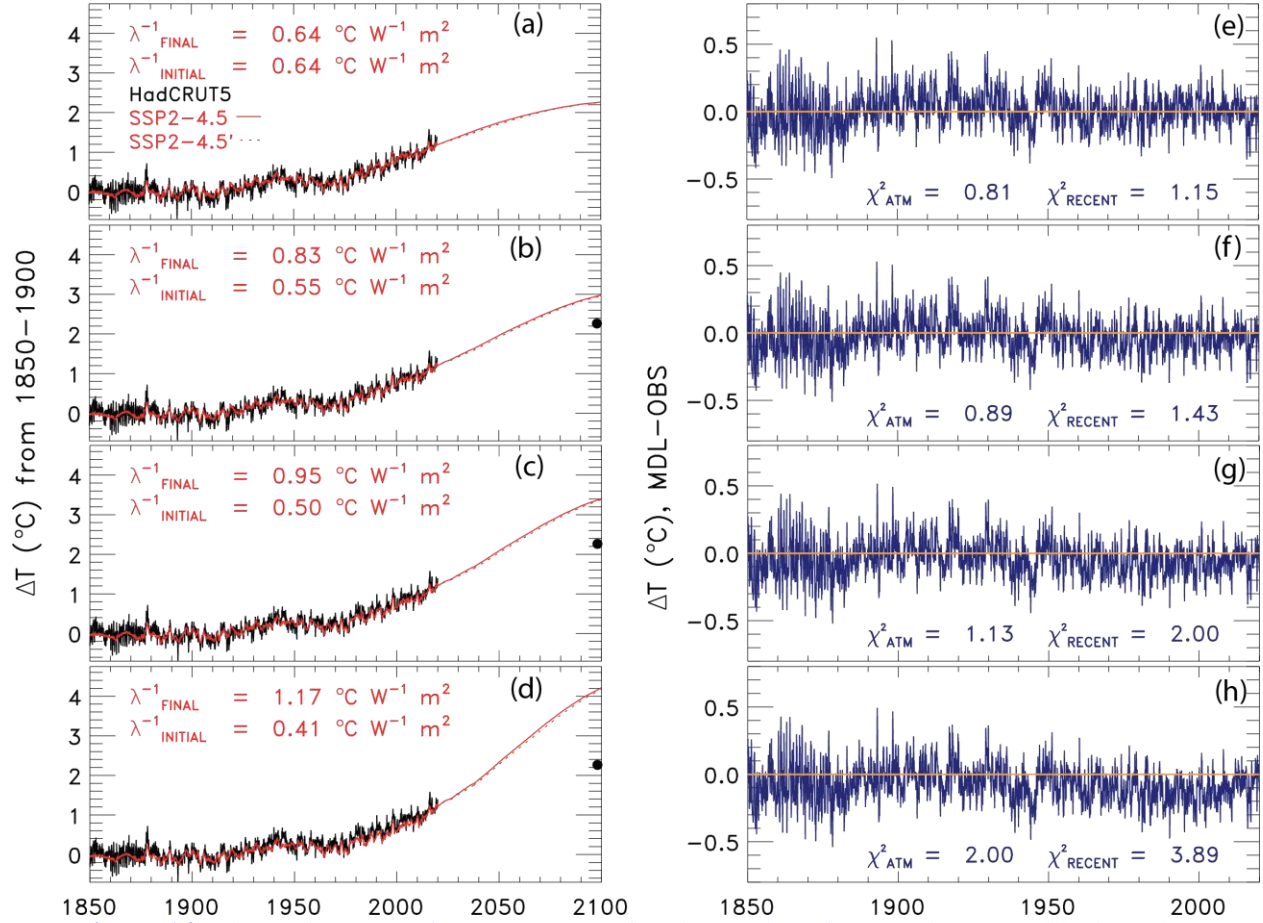
We added New Fig. 14 to the main manuscript and New Figs. S24 and S25 to the supplement to address this comment and support our estimates of $ECS_{\lambda(t)}$. We also added text starting on line 1125 illustrating how our estimates of ECS will change if we allow λ^{-1} to rise over time. We have also added the new estimate of $ECS_{\lambda(t)}$ to the abstract and the conclusions. We added the following text to the end of Sect. 3.3.6 starting on line 1143 to indicate that the change in λ^{-1} is an additional uncertainty for ECS: **If λ^{-1} is allowed to increase by 50%, our best estimate of ECS would rise from 2.33 to 3.08°C, which is a 32% increase. Time variant λ^{-1} introduces additional uncertainty into our estimates of ECS; however, the largest uncertainty is still due to the imprecise knowledge of the RF due to tropospheric aerosols.**

To further address this reviewer’s comment, we have extended our analysis to include a model simulation where only the RF due to CO₂ changes into the future. We denote this scenario as SSP2-4.5'. All other GHGs and the RF due to tropospheric aerosols are held constant at their December 2019 values into the future. We used SSP2-4.5 because CO₂ doubles from preindustrial concentrations in this scenario, approximating the definition of equilibrium climate sensitivity. The results from SSP2-4.5' are shown as the dotted lines in Fig. 14, S23, S24, and S25.

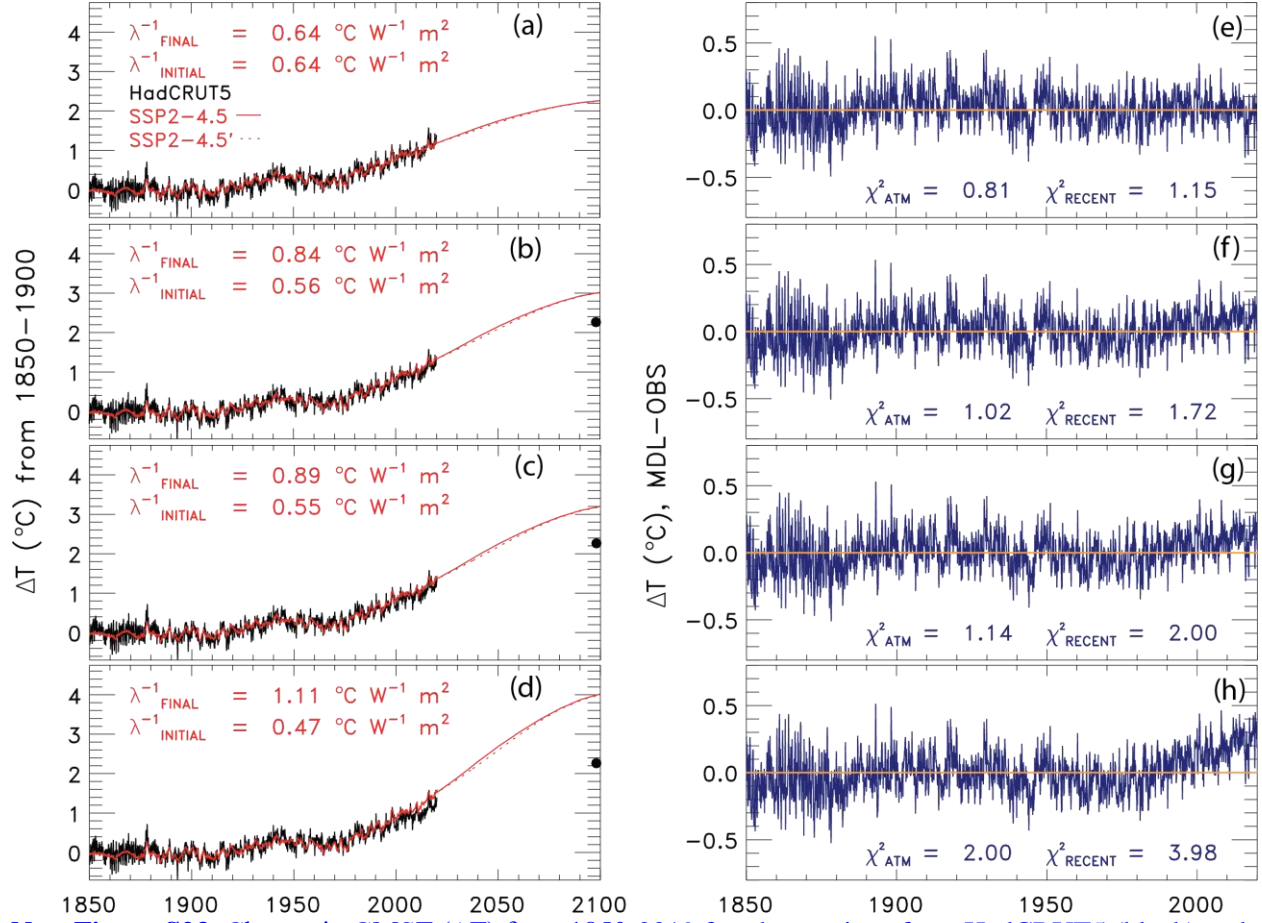
We have added the following text starting on line 1077 of our main manuscript describing our SSP2-4.5' simulation: **In Figs. 14 and S23 we also analyze a RF scenario termed SSP2-4.5' that serves as a doubled CO₂ scenario (dotted lines). For SSP2-4.5', the RFs due to all GHGs other than CO₂ as well as tropospheric aerosols from the start of 2020 onwards are held constant at end of 2019 values. The only component of RF allowed to vary after the start of 2020 is CO₂. The RF of climate due to all GHGs and tropospheric aerosols for SSP2-4.5' is identical to that in SSP2-4.5 from the start of the simulation until the end of 2019. Since the mixing ratio of CO₂ at the end of century is 566 ppm, the warming found at the end of century for SSP2-4.5' serves as the transient response of ΔT to rising CO₂ in our model framework. The fact that projections of ΔT found allowing only for future increases in CO₂ (dotted lines) agree so closely with those found assuming changes in RF due to all GHGs and tropospheric aerosols (solid lines) means that under the AER $RF_{2011} = -0.9 \text{ W m}^{-2}$ scaling assumption, the future change in RF due to all agents other than CO₂ nearly cancel. Projections found using the original SSP2-4.5 scenario may serve as a useful surrogate for a double CO₂ simulation. Figures S24 and S25 are the same as Fig. 14, except for the use of AER RF_{2011} values of -0.4 and -1.5 W m^{-2} , respectively. There are slight departures between the SSP2-4.5 and SSP2-4.5' projections of ΔT for these alternate aerosol scaling assumptions.**

Nonetheless, these projections are quite similar because the future decline in RF due to the assumption of declining CH₄ within SSP2-4.5 nearly balances the future increase in RF due to N₂O and all of the minor GHGs.

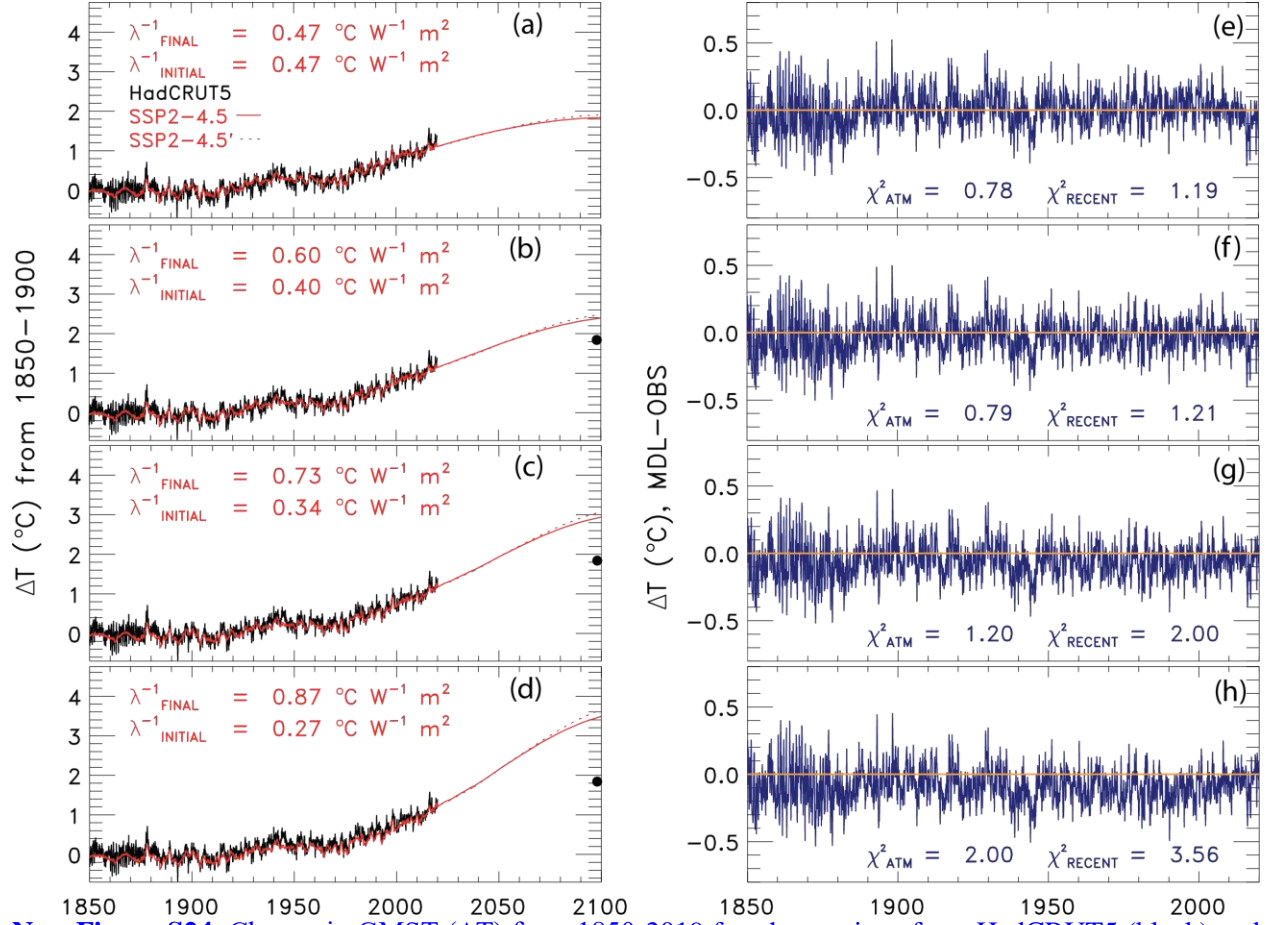
We have also added the following text starting on line 281 of the supplement to further describe our SSP2-4.5' simulation: Section 3.3.6 also states “In Figs. 14 and S23 we also analyze a RF scenario termed SSP2-4.5' that serves as a doubled CO₂ scenario (dotted lines)”. In the SSP2-4.5' simulation, only CO₂ is allowed to change after the end of 2019. All other GHGs and aerosols are kept constant at their December 2019 values. This simulation allows us to examine the effect of time variant λ^{-1} on changes in ΔT due only to the future rise in CO₂. In the SSP2-4.5 scenario, CH₄, tropospheric O₃, and ODSs decrease after 2019 leading to a future decline in RF, whereas N₂O and tropospheric aerosols result in a future increase in RF. When all of these RF are kept constant in the SSP2-4.5' scenario for the AER RF₂₀₁₁ = -0.9 W m^{-2} scaling assumption, the terms result in a near balance out to 2100. For the weaker aerosol cooling scenario (AER RF₂₀₁₁ = -0.4 W m^{-2}), the value of RF due to tropospheric aerosols is not large enough to completely offset the other GHGs that are held constant. Consequently, the SSP2-4.5' simulation (dotted line) results in slightly larger total RF and associated warming than the SSP2-4.5 scenario (solid line) shown in Fig. S24. For the stronger aerosol cooling scenario (AER RF₂₀₁₁ = -1.5 W m^{-2}), the value of RF due to tropospheric aerosols is larger than the RF due to the other GHGs that are held constant, resulting in the SSP2-4.5' having a slightly lower total RF and associated warming than the SSP2-4.5 scenario (Fig. S25).



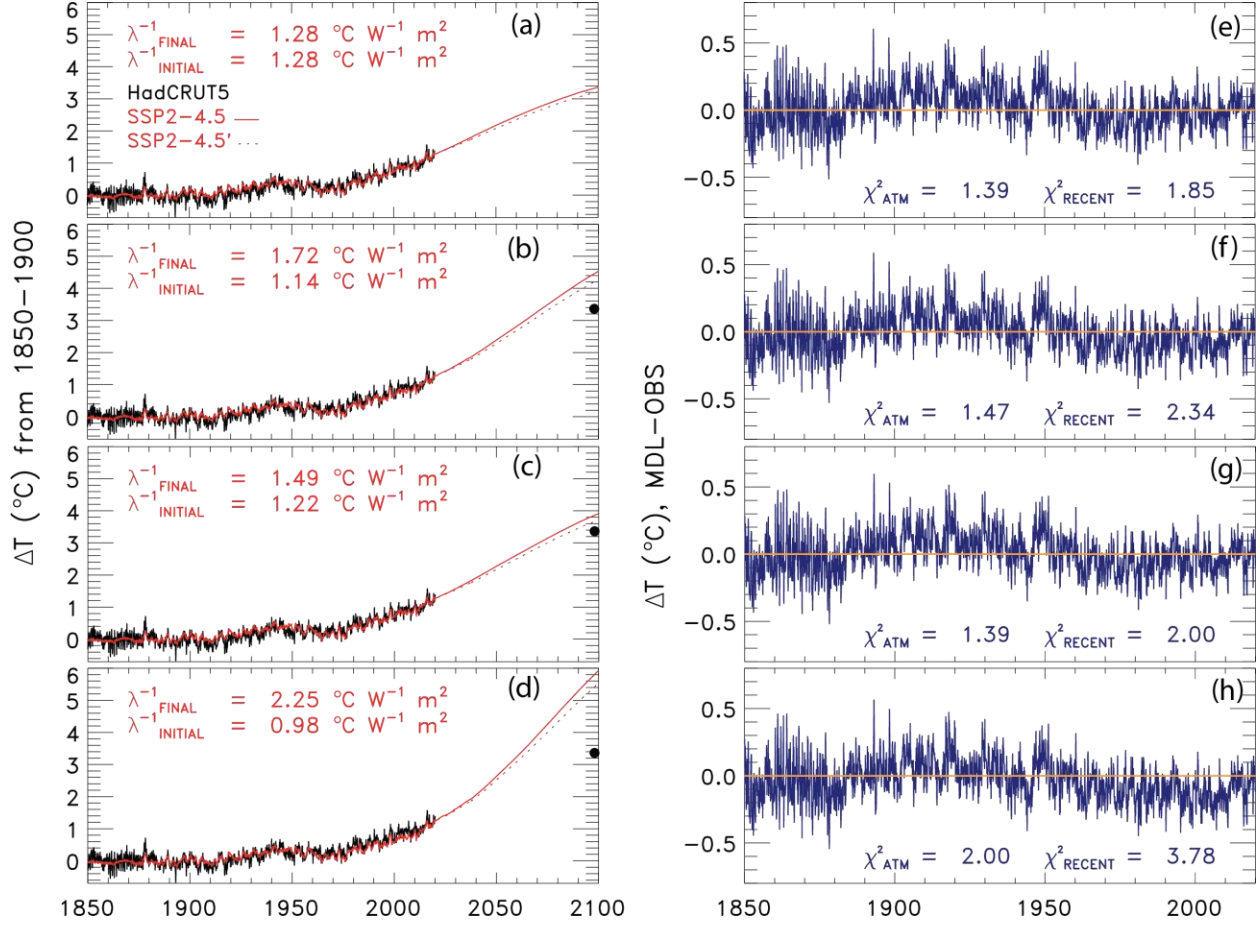
New Figure 14. Change in GMST from 1850-2019 for observations from HadCRUT5 (black) and 1850-2100 for modeled (red) using SSP2-4.5 and a value of AER $RF_{2011} = -0.9 \text{ W m}^{-2}$ and the residual between modeled and observations incorporating a 32.5-year delay between λ^{-1} and a change in RF. The solid line denotes a simulation for the original SSP2-4.5 scenario and the dashed line indicates the SSP2-4.5' simulation (see text). (a) Rise in GMST assuming a constant value of λ^{-1} . (b) Rise in GMST allowing λ^{-1} to increase by 50%. (c) Rise in GMST allowing λ^{-1} to vary while the value of χ^2_{RECENT} is kept below 2. (d) Rise in GMST allowing λ^{-1} to vary while the value of χ^2_{ATM} is kept below 2. (e) Residual between modeled and observed rise in GMST from 1850-2019 for constant λ^{-1} . (f) Same as (e) but for increasing λ^{-1} by 50%. (g) Same as (f) but for varying λ^{-1} while the value of χ^2_{RECENT} is kept below 2. (h) same as (g) but for varying λ^{-1} while the value of χ^2_{ATM} is kept below 2.



New Figure S23. Change in GMST (ΔT) from 1850-2019 for observations from HadCRUT5 (black) and 1850-2100 for modeled (red) using SSP2-4.5 and a value of AER $RF_{2011} = -0.9 \text{ W m}^{-2}$ and the residual between modeled and observations using an instantaneous time variant λ^{-1} . The solid line denotes a simulation for the original SSP2-4.5 scenario and the dashed line indicates the SSP2-4.5' simulation (see Sect. 3.3.6). (a) ΔT assuming a constant value of λ^{-1} . (b) ΔT allowing λ^{-1} to increase by 50%. (c) ΔT allowing λ^{-1} to vary while the value of χ^2_{RECENT} is kept below 2. (d) ΔT allowing λ^{-1} to vary while the value of χ^2_{ATM} is kept below 2. (e) Residual between modeled and observed ΔT from 1850-2019 for constant λ^{-1} . (f) Same as (e) but for increasing λ^{-1} by 50%. (g) Same as (f) but for varying λ^{-1} while the value of χ^2_{RECENT} is kept below 2. (h) same as (g) but for varying λ^{-1} while the value of χ^2_{ATM} is kept below 2.



New Figure S24. Change in GMST (ΔT) from 1850-2019 for observations from HadCRUT5 (black) and 1850-2100 for modeled (red) using SSP2-4.5 and a value of AER $\text{RF}_{2011} = -0.4 \text{ W m}^{-2}$ and the residual between modeled and observations incorporating a 32.5-year delay between λ^{-1} and a change in RF. The solid line denotes a simulation for the original SSP2-4.5 scenario and the dashed line indicates the SSP2-4.5' simulation (see Sect. 3.3.6). (a) ΔT assuming a constant value of λ^{-1} . (b) ΔT allowing λ^{-1} to increase by 50%. (c) ΔT allowing λ^{-1} to vary while the value of χ^2_{RECENT} is kept below 2. (d) ΔT allowing λ^{-1} to vary while the value of χ^2_{ATM} is kept below 2. (e) Residual between modeled and observed ΔT from 1850-2019 for constant λ^{-1} . (f) Same as (e) but for increasing λ^{-1} by 50%. (g) Same as (f) but for varying λ^{-1} while the value of χ^2_{RECENT} is kept below 2. (h) same as (g) but for varying λ^{-1} while the value of χ^2_{ATM} is kept below 2.



New Figure S25. Change in GMST (ΔT) from 1850-2019 for observations from HadCRUT5 (black) and 1850-2100 for modeled (red) using SSP2-4.5 and a value of AER $RF_{2011} = -1.5 \text{ W m}^{-2}$ and the residual between modeled and observations incorporating a 32.5-year delay between λ^{-1} and a change in RF. The solid line denotes a simulation for the original SSP2-4.5 scenario and the dashed line indicates the SSP2-4.5' simulation (see Sect. 3.3.6). (a) ΔT assuming a constant value of λ^{-1} . (b) ΔT allowing λ^{-1} to increase by 50%. (c) ΔT allowing λ^{-1} to vary while the value of χ^2_{RECENT} is kept below 2. (d) ΔT allowing λ^{-1} to vary while the value of χ^2_{ATM} is kept below 2. (e) Residual between modeled and observed ΔT from 1850-2019 for constant λ^{-1} . (f) Same as (e) but for increasing λ^{-1} by 50%. (g) Same as (f) but for varying λ^{-1} while the value of χ^2_{RECENT} is kept below 2. (h) same as (g) but for varying λ^{-1} while the value of χ^2_{ATM} is kept below 2.

* The manuscript misrepresents the findings by Rugenstein. They did not study CMIP6 models (but mostly CMIP5, and some CMIP3), and they found that all models had an increasing feedback parameter over time, not just some

Thank you for pointing out this oversight. We have updated the text such that it is now clear the Rugenstein et al. (2020) study examined output from CMIP5 GCMs (rather than CMIP6), and we have changed “some” to “many”.

* Similarly, Marvel et al show that estimates from historical simulations strongly underestimate true ECS in virtually all CMIP5 models. This is misrepresented by saying 'some' models. The

mean bias is 0.8 degrees. This difference would bring the manuscript in line with conventional estimates of ECS of around 3 degrees.

We have changed “some” to “many”.

* In the authors want to include a reference for CMIP6, <https://journals.ametsoc.org/view/journals/clim/33/18/jcliD191011.xml> may work, shows that 26 out of 29 models show an increasing $1/\lambda$, also not 'some'.

Thank you for pointing out this study by Dong et al. (2020), which we now cite. Dong et al. (2020) show that the median increase in λ in the CMIP6 GCMs is $+0.4 \text{ W m}^{-2}\text{K}^{-1}$. The median estimate of λ from the CMIP6 GCMs is $-1.2 \text{ W m}^{-2}\text{K}^{-1}$. This $+0.4 \text{ W m}^{-2}\text{K}^{-1}$ increase in λ corresponds to a 50% increase in λ^{-1} , which is similar to the findings by Marvel et al., 2018.

We have added a citation to Dong et al., 2020 on lines 1054, 1118 and 1120, and 1139. We have also added the following sentence on line 1115: **An analysis by Dong et al. (2020) estimates a median increase in λ of $+0.4 \text{ W m}^{-2} \text{ K}^{-1}$, which corresponds to a 50% increase in λ^{-1} (Fig. 1c, d of Dong et al. (2020)).**

* The manuscript misrepresents Goodwin et al (2018). That paper indicates that there are time lags up to a hundred years, and they model a time-scale lag of 20 to 45 years for the Cloud – spatial SST adjustment feedback. The manuscript claims they have a maximum time delay of 20 years.

Thanks again for pointing out this oversight, which has also been addressed.

We now use a 32.5-year delay (midpoint between 20 and 45 years) to represent the time delay between the response of climate feedback to a change in RF for Figs. 14, S24, and S25. The text in Sect. 3.3.6 has been changed to read: **We use a lag of 32.5 years to represent the mean value of the slowest response of the climate system to a RF perturbation reported by Goodwin (2018), which is associated with clouds and spatial adjustments of SST (32.5 years is the average of 20 and 45 years, the minimum and maximum values of the slowest response given in his Table 1).**

The 32.5-year delay is the longest value of a time delay noted in Table 1 of Goodwin (2018), due to the response of feedbacks involving clouds and the spatial adjustment of SST to a RF perturbation.

Goodwin (2018) does also estimate a value of ECS for a 100-year response timescale for climate sensitivity, although the specific mechanism (presumably the cryosphere) is not named. Their estimate of ECS for the 100-year response is 2.9°C (range of 2.3 to 3.6°C). Our best estimate of $\text{ECS}_{\lambda(t)}$ found using a 32.5-year delay is 3.08°C (2.23 - 5.53°C), which is quite similar to the value of ECS reported by Goodwin. We have added the following text starting on line 1132 of the main manuscript to highlight this similarity:

Our best estimate of $ECS_{\lambda(t)}$ of 3.08°C (range of 2.23 to 5.53°C) for a 32.5-year delay is similar to the value of ECS reported by Goodwin (2018) for a 100-year response time (2.9°C; range of 2.3 to 3.6°C).

We have explored the possibility of using time delays longer than 32.5 years to analyze the GMST record using our EM-GC, but quite simply:

- a) The modern temperature record does not extend far enough in time for this constraint to be applied in a meaningful manner.
- b) Since our projections extend only to 2100, a time delay of longer than the time it will take for the calendar to reach 2100 does not seem appropriate.
- c) Our results for $ECS_{\lambda(t)}$ found using the 32.5-year delay are, as noted above and now mentioned in the paper, quite similar to the value given by Goodwin (2018) upon his consideration of a 100-year response.

Major comment 2)

I had wanted the authors to compare model effective ECS with model Gregory ECS. This would show whether empirically estimated effective ECS can be compared with model Gregory ECS. The authors have instead done a sensitivity analysis of what happens if less data is used. I don't think that exercise is insightful, and certainly does not answer my question.

We have updated the manuscript to indicate we are comparing effective climate sensitivity from the EM-GC to effective climate sensitivity from the Gregory et al. (2004) method. We have also added more information to Sect. 3.3.6 on how our estimates of ECS will change based on a rise in λ^{-1} over time. We will retain the analysis of the various training periods because this analysis was specifically requested by the other reviewer.

Comparison of CMIP6 Historical Climate Simulations and Future Projected Warming to an Empirical Model of Global Climate

Laura A. McBride¹, Austin P. Hope², Timothy P. Canty², Brian F. Bennett², Walter R. Tribett², Ross J. Salawitch^{1,2,3}

5 ¹Department of Chemistry and Biochemistry, University of Maryland College Park, College Park, 20740, USA

²Department of Atmospheric and Oceanic Science, University of Maryland College Park, College Park, 20740, USA

³Earth System Science Interdisciplinary Center, University of Maryland College Park, College Park, 20740, USA

Correspondence to: Laura McBride (mcbridel@umd.edu)

Abstract.

10 The sixth phase of the Coupled Model Intercomparison Project (CMIP6) is the latest modeling effort for general circulation models to simulate and project various aspects of climate change. Many of the general circulation models (GCMs) participating in CMIP6 provide archived output that can be used to calculate equilibrium-effective climate sensitivity (ECS) and forecast future temperature change based on emissions scenarios from several Shared Socioeconomic Pathways (SSPs). Here we use our multiple linear
15 regression energy balance model, the Empirical Model of Global Climate (EM-GC), to simulate and project changes in global mean surface temperature (GMST), calculate ECS, and compare to results from the CMIP6 multi-model ensemble. An important aspect of our study is comprehensive analysis of uncertainties due to radiative forcing of climate from tropospheric aerosols (AER RF) in the EM-GC framework. We quantify the attributable anthropogenic warming rate (AAWR) from the climate record
20 using the EM-GC and use AAWR as a metric to determine how well CMIP6 GCMs replicate human-driven global warming over the last forty years. The CMIP6 multi-model ensemble indicates a median value of AAWR over 1975-2014 of $0.221^{\circ}\text{C} \text{ decade}^{-1}$ ~~/decade~~ (range of 0.151 to $0.299^{\circ}\text{C} \text{ decade}^{-1}$ ~~/decade~~; all ranges given here are for 5th and 95th confidence intervals), which is notably faster warming than our median estimate for AAWR of $0.157^{\circ}\text{C} \text{ decade}^{-1}$ ~~/decade~~ (range of 0.120 to $0.195^{\circ}\text{C} \text{ decade}^{-1}$ ~~/decade~~)
25 decade⁻¹/decade) inferred from analysis of the Hadley Center Climatic Research Unit Version 5 data record for GMST. Estimates of ECS found using the EM-GC assuming climate feedback does not vary over time (best estimate 2.33°C ; range of 1.40 to 3.57°C) are generally consistent with the range of ECS

of 1.5 to 4.5°C given by IPCC’s Fifth Assessment Report. The CMIP6 multi-model ensemble exhibits considerably larger values of ECS (median 3.74°C; range of 2.19 to 5.65°C). Our best estimate of ECS increases to 3.08°C (range of 2.23 to 5.53°C) if we allow climate feedback to vary over time. The dominant factor in the uncertainty for our empirical determinations of AAWR and ECS is imprecise knowledge of AER RF for the contemporary atmosphere, though the uncertainty due to time dependent climate feedback is also important for estimates of ECS. We calculate the likelihood of achieving the Paris Agreement target (1.5°C) and upper limit (2.0°C) of global warming relative to pre-industrial for seven of the SSPs using both the EM-GC and the CMIP6 multi-model ensemble. In our model framework, SSP1-2.6 has a 53% probability of limiting warming at or below the Paris target by the end of century and SSP4-3.4 has a 64% probability of achieving the Paris upper limit. These estimates are based on the assumptions that climate feedback has been and will remain constant over time since the prior temperature record can be fit so well assuming constant climate feedback. In addition, we quantify the sensitivity of future warming to the curbing of the current rapid growth of atmospheric methane and show major near-term limits on the future growth of methane are especially important for achievement of the 1.5°C goal of future warming. We also quantify warming scenarios assuming climate feedback will rise over time, a feature common among many CMIP6 GCMs; under this assumption, it becomes more difficult to achieve any specific warming target. Finally, we assess warming projections in terms of future anthropogenic emissions of atmospheric carbon. In our model framework, humans can emit only another 150 ± 79 Gt C after 2019 to have a 66% likelihood of limiting warming to 1.5°C, and another 400 ± 104 Gt C to have the same probability of limiting warming to 2.0°C. Given the estimated emission of 11.7 Gt C per year for 2019 due to combustion of fossil fuels and deforestation, our EM-GC simulations suggest the 1.5°C warming target of the Paris Agreement will not be achieved unless carbon and methane emissions are severely curtailed in the next 10 years.

1 Introduction

The goals of the Paris Agreement, negotiated in December of 2015, are to keep global warming below 2.0°C relative to the start of the Industrial Era and pursue efforts to limit global warming to 1.5°C. General

circulation models (GCMs) project future temperature change using various evolutions of greenhouse
55 gases and determine the likelihood of achieving the goals of the agreement. Many GCMs are participating
in the sixth phase of the Coupled Model Intercomparison Project (CMIP6) to quantify how the models
represent different aspects of climate change (Eyring et al., 2016). Accurate projections of future
temperature are critical for achieving the goals of the Paris Agreement. Chapter 11 of IPCC's Fifth
Assessment Report shows that some of the previous generations of these models participating in phase 5
60 of the Coupled Model Intercomparison Project (CMIP5) (Taylor et al., 2012) tended to overestimate the
increase in global mean surface temperature (GMST) for the 21st century (Kirtman et al., 2013). In this
analysis we use a multiple linear regression energy balance model to quantify the change in GMST from
1850-2019, project future changes in GMST, compare to the CMIP6 multi-model ensemble, and
determine the likelihood of achieving the goals of the Paris Agreement.

65 Several prior studies have used a multiple linear regression approach to model the GMST anomaly
in order to quantify the impact of anthropogenic and natural factors on climate (Foster and Rahmstorf,
2011; Lean and Rind, 2008, 2009; Zhou and Tung, 2013). Typically, total solar irradiance, volcanoes,
and El Niño southern oscillation (ENSO) are the natural components represented in the multiple linear
regression. Greenhouse gases and aerosols are the anthropogenic factors. We use multiple linear
70 regression, in connection with a dynamic ocean module that accounts for the export of heat from the
atmosphere to the ocean, to represent the natural and anthropogenic components of the climate system.
In addition to the typical natural factors listed above, we include the Atlantic meridional overturning
circulation (AMOC), Pacific decadal oscillation (PDO), and Indian Ocean dipole (IOD) to provide a
robust representation of the natural climate system (Canty et al., 2013; Hope et al., 2017). Our
75 anthropogenic components also include the effect of land-use change (i.e., deforestation) on Earth's
albedo and the export of heat from the atmosphere to the ocean as the atmosphere warms.

Our analysis builds on the work of Canty et al. (2013) and Hope et al. (2017) and includes several
key updates. One is the extension back in time of our analysis to 1850. The Hadley Center Climatic
Research Unit (Morice et al., 2012, 2021), Berkley Earth Group (Rohde and Hausfather, 2020), and
80 Cowtan and Way (2014) provide GMST records starting in 1850, which now allows for simulations of
GMST that cover 170 years. The second update is the use of the Shared Socioeconomic Pathways (SSPs)

(O'Neill et al., 2017) as our climate scenarios for greenhouse gas and aerosol abundances. The third is the adoption of an upper ocean to our model, formulated in a manner that matches the equations of Bony et al. (2006) and Schwartz (2012). A description of the model, the various input parameters used, and the updates listed above is given in Sect. 2. Section 3 shows results of CMIP6 and EM-GC comparisons to the historical climate record, estimations of equilibrium-effective climate sensitivity (ECS), as well as comparisons of our model and CMIP6 projections of future GMST change. Discussion of these results is provided in Sect. 4, along with concluding remarks.

90 **2 Data and Methodology**

2.1 Empirical model of global climate

In this analysis we use the empirical model of global climate (EM-GC), which provides a multiple linear regression, energy balance simulation of GMST. As detailed in the following paragraphs, the EM-GC solves for ocean heat uptake efficiency (κ) and six regression coefficients to minimize the cost function in Eq. (1).

$$Cost\ Function = \sum_{i=1}^{N_{MONTHS}} \frac{1}{\sigma_{OBSi}^2} (\Delta T_{OBSi} - \Delta T_{MDLi})^2 \quad (1)$$

In this equation, ΔT_{OBS} represents a time series of observed monthly GMST anomalies, ΔT_{MDL} is the modeled monthly change in GMST, σ_{OBS} is the 1-sigma uncertainty associated with each temperature observation, i is the index for each month, and N_{MONTHS} is the total number of months used in the analysis. For this analysis, we trained the model from 1850-2019. The observed GMST anomalies are blended near surface air and sea surface temperature differences relative to the GMST anomaly over 1850-1900, which is assumed to represent pre-industrial conditions.

We consider several anthropogenic and natural factors as components of ΔT_{MDL} . The radiative forcing (RF) due to greenhouse gases (GHGs), anthropogenic aerosols (AER), land-use change (LUC), and the export of heat from the atmosphere to the world's oceans are the anthropogenic components of ΔT_{MDL} . The influence on GMST from total solar irradiance (TSI), El Niño southern oscillation (ENSO), the Atlantic meridional overturning circulation (AMOC), volcanic eruptions that reach the stratosphere and enhance stratospheric aerosol optical depth (SAOD), the Pacific decadal oscillation, (PDO) and the

Indian Ocean dipole (IOD) are the natural components of ΔT_{MDL} . Equation (2) shows how we calculate
 110 ΔT_{MDL} , the modeled monthly change in GMST.

$$\Delta T_{MDLi} = \frac{1 + \gamma}{\lambda_p} \{GHG \Delta RF_i + AER \Delta RF_i + LUC \Delta RF_i - Q_{OCEAN i}\} + C_0 + C_1 \times SAOD_{i-6} + C_2 \times TSI_{i-1} + C_3 \times ENSO_{i-2} + C_4 \times AMOC_i + C_5 \times PDO_i + C_6 \times IOD_i \quad (2)$$

In Eq. (2), $GHG \Delta RF_i$, $AER \Delta RF_i$, and $LUC \Delta RF_i$ represent monthly time series of the increase in the stratospheric adjusted values of the RF of climate (Solomon, 2007) since 1750. The parameter λ_p
 115 represents the response of a blackbody to a perturbation in the absence of climate feedback (3.2 W m^{-2} , (Bony et al., 2006)). The SAOD, TSI, and ENSO are lagged by 6, 1, and 2 months respectively. The lag of 6 months for SAOD is representative of the time needed for the surface temperature to respond to a change in the aerosol loading due to a volcanic eruption (Douglass and Knox, 2005). This lag is the same as used by Lean and Rind (2008) and Foster and Rahmstorf (2011). The 1 month delay for TSI yields the
 120 maximum value of C_2 , the solar irradiance regression coefficient. Lean and Rind (2008) and Foster and Rahmstorf (2011) also use a 1 month lag for TSI in their analyses. The 2 month delay for the response of GMST to ENSO is the lag needed to obtain the largest value of the correlation coefficient of the Multivariate ENSO Index version 2 (MEI.v2) (Wolter and Timlin, 1993; Zhang et al., 2019) versus the value of T_{ENSO} calculated by Thompson et al. (2009). In Thompson et al. (2009), T_{ENSO} is the simulated
 125 response of GMST to variability induced by ENSO, taking into consideration the effective heat capacity of the atmospheric-ocean mixed layer. Lean and Rind (2008) used a 4-month lag for ENSO.

The term $AMOC_i$ represents the influence of the change in the strength of the thermohaline circulation on GMST (Knight et al., 2005; Medhaug and Furevik, 2011; Stouffer et al., 2006; Zhang and Delworth, 2007). We use the Atlantic multidecadal variability, based on the area weighted monthly mean
 130 sea surface temperature (SST) in the Atlantic Ocean between the equator and 60°N (Schlesinger and Ramankutty, 1994), as a proxy for the strength of AMOC. A strong AMOC is characterized by northward flow of energy that would otherwise be radiated to space, which occurs in both the ocean and atmosphere and leads to particularly warm summers in Europe (Kavvada et al., 2013) as well as a number of other well documented influences in other climatic regions (Nigam et al., 2011). The total anthropogenic RF is

135 used to detrend the AMOC signal. This method provides a more realistic approach to infer the changes in the strength of AMOC and its effect on GMST than other detrending options (Canty et al., 2013).

The dimensionless parameter γ represents the sensitivity of the global climate to feedbacks that occur due to a change in the RF of GHGs, AER, and LUC. We relate γ to the climate feedback parameter, λ_Σ , as shown in Eq. (3).

$$140 \quad 1 + \gamma = \frac{1}{1 - \left(\frac{\lambda_\Sigma}{\lambda_P}\right)}$$

where $\lambda_\Sigma = \Sigma$ all climate feedbacks (3)

i.e., $\lambda_\Sigma = \lambda_{\text{Water Vapor}} + \lambda_{\text{Lapse Rate}} + \lambda_{\text{Clouds}} + \lambda_{\text{Surface Albedo}}$

The relation between λ_Σ and γ in Eq. (3) is commonly used in the climate modeling community (Sect. 8.6 of Solomon (2007)). Our value of λ_Σ is related to the IPCC's Fifth Assessment Report ((Stocker et al., 145 2013), hereafter IPCC 2013) definition of λ via $\lambda_\Sigma = \lambda_P - \lambda$.

Our model explicitly accounts for the export of heat from the atmosphere to the world's oceans (i.e., ocean heat export or OHE). The quantity Q_{OCEAN} in Eq. (2) represents OHE. In our previous analyses (Canty et al., 2013; Hope et al., 2017), Q_{OCEAN} was subtracted outside of the climate feedback multiplicative term $(1+\gamma)/\lambda_P$. We have rewritten Eq. (2) to be comparable to the formulation for this term 150 used by Bony et al. (2006) and Schwartz (2012). Due to this update, our model fits the historical climate record with higher values of climate feedback, especially for strong aerosol cooling (see Fig. S1 and supplement for more information). We calculate Q_{OCEAN} by simulating the long-term trend in observed ocean heat content (OHC) as shown in Eq. (4) and Eq. (5).

$$Q_{\text{OCEAN}i} = \kappa (\Delta T_{\text{ATM}, \text{HUMAN}i} - \Delta T_{\text{OCEAN}, \text{HUMAN}i}) \quad (4)$$

$$155 \quad \kappa = \frac{\text{OHE} \times \Delta t}{\int_{t_{\text{START}}}^{t_{\text{END}}} \left(\left[\frac{1+\gamma}{\lambda_P} \{ \text{GHG RF}_{i-72} + \text{AER RF}_{i-72} + \text{LUC RF}_{i-72} \} \right] - [f_0 \sum_0^{i-72} Q_{\text{OCEAN}}] \right) dt} \quad (5)$$

The κ term is the ocean heat uptake efficiency ($\text{W m}^{-2} \text{ } ^\circ\text{C}^{-1}$) and is based on the definition used in Raper et al. (2002), where κ is the ratio between the atmosphere and ocean temperature difference that best fits observed OHC data (Sect. 2.2.8 describes the OHC data records used in our analysis). The value of κ is determined based on the best fit (described below) between Q_{OCEAN} and the observed OHC record. The 160 term $\Delta T_{\text{OCEAN}, \text{HUMAN}}$ represents the temperature response of the well-mixed, top 100 m of the ocean due

to the total anthropogenically driven rise in OHC. This formulation of $\Delta T_{\text{OCEAN,HUMAN}}$ allows the model ocean to warm in response to an atmospheric warming. We use a 6 year lag (72 months) for Q_{OCEAN} to account for the time needed for the energy leaving the atmosphere to heat the upper ocean and penetrate to depth, based on Schwartz (2012). Our analysis of modeled GMST is insensitive to whether this 6 year lag or the 10 year lag from Lean and Rind (2009) is used. The t_{START} and t_{END} limits on the integral in Eq. (5) are the start and end years associated with each OHC record. The start and end years vary between the 5 OHC records (see supplement for the different start and end years). The constant f_0 term in Eq. (5) is a combination of the heat capacity of ocean water, the fraction of total ocean volume in the surface layer, and the fraction of total Q_{OCEAN} that warms the surface layer, and is equal to $8.76 \times 10^{-5} \text{ } ^\circ\text{C m}^2 \text{ W}^{-1}$. We represent the global ocean as being 1 km deep for 10% of the ocean area (representing the continental shelves) and 4 km deep for the remaining area, which approximates the average depth of the actual world's oceans to within 3%; 3.7 km compared to 3.682-3.814 km from Charette and Smith (2010). Based on our analysis of decadal ocean warming as a function of depth extracted from CMIP5 GCMs, we have determined that 13.7% of the rise in total OHC occurs in the well mixed, upper 100 m of the ocean, the term represented by $\Delta T_{\text{OCEAN,HUMAN}}$ in equation (4). The bottom panel of Fig. 1 compares our modeled OHC to the observed OHC record based on the average of five data sets; the value of κ resulting in the best simulation of observed OHC is shown.

We use the reduced chi-squared (χ^2) metric to define the goodness of fit between the modeled and measured GMST anomaly for the atmosphere and also between simulated and observed OHC. Equation (6) and Eq. (7) show the calculations for χ^2 for the atmosphere, and Eq. (8) shows the calculation for χ^2 for the ocean. Minimization of the difference between the measured and modeled GMST anomaly results in the EM-GC being able to replicate the observed rise in temperature over the past 170 years quite well, as shown in Fig. 1. We have added two additional new features to the model to assure accurate representation of the rise in OHC as well as the rise in GMST since 1940. The first new feature, Eq. (7), was added to ensure all simulations matched the past 80 years of observations well. Without the χ^2_{RECENT} constraint, some solutions with a value of χ^2_{ATM} less than or equal to 2 have visually poor simulations of the rise in GMST over the past 4 to 5 decades. The second new feature, Eq. (8), was added because in the original model formulation some selections of the radiative forcing due to tropospheric aerosols (AER

ΔRF_i in Eq. (2)) converged in a way that produced simulations of OHC that seemed physically improper based on visual inspection of observed and modeled OHC. As a result of these two issues, all calculations shown here are subject to three goodness-of-fit constraints, described by Eq. (6) to (8):

$$\chi_{ATM}^2 = \frac{1}{N_{YEARS} - N_{FITTING\ PARAMETERS} - 1} * \sum_{j=1}^{N_{YEARS}} \frac{1}{\langle \sigma_{OBSj} \rangle^2} (\langle \Delta T_{OBSj} \rangle - \langle \Delta T_{MDLj} \rangle)^2 \quad (6)$$

$$\chi_{RECENT}^2 = \frac{1}{N_{YEARS,REC} - N_{FITTING\ PARAMETERS} - 1} * \sum_{j=1}^{N_{YEARS,REC}} \frac{1}{\langle \sigma_{OBSj} \rangle^2} (\langle \Delta T_{OBSj} \rangle - \langle \Delta T_{MDLj} \rangle)^2 \quad (7)$$

$$\chi_{OCEAN}^2 = \frac{1}{N_{YEARS} - N_{FITTING\ PARAMETERS} - 1} * \sum_{j=1}^{N_{YEARS,OHC}} \frac{1}{\langle \sigma_{OBSj} \rangle^2} (\langle OHC_{OBSj} \rangle - \langle OHC_{MDLj} \rangle)^2 \quad (8)$$

Here, $\langle \Delta T_{OBS} \rangle$, $\langle \Delta T_{MDL} \rangle$, and $\langle \sigma_{OBS} \rangle$ in Eq. (6) and Eq. (7) represent the annually averaged observed, modeled, and uncertainty in the GMST anomaly, respectively. The variable $N_{FITTING\ PARAMETERS}$ is equal to 9 for typical simulations, the sum of 7 (the number of regression coefficients) plus 2 (model output parameters γ and κ). In Eq. (8), $\langle OHC_{OBS} \rangle$ and $\langle OHC_{MDL} \rangle$ represent the annual averaged observed and modeled OHC. The σ_{OBS} term in Eq. (8) is the uncertainty in the OHC record (see Sect. 2.2.8 for more information). The equation for all three formulations of χ^2 is based on annual averages, rather than monthly time series. We calculate χ^2 with annual values because the autocorrelation functions of ΔT_{OBS} and ΔT_{MDL} display similar shapes using annual averages, and do not match utilizing monthly averages (see supplement of Canty et al. (2013) for further explanation). The Hadley Center Climate Research Unit (HadCRUT) version 4 uncertainties for GMST are used for the σ_{OBS} in Eq. (6) to (8) for all of the GMST records analyzed here (see Sect. 2.2.1 and the supplement for more information). For Eq. (6) to (8), we define an acceptable fit to the climate record as $\chi^2 \leq 2$. The number of years (N_{YEARS}) varies across the three equations. Equation (6) uses the total number of years in the GMST record, which for HadCRUT5 is 170 years. The number of years in Eq. (8), $N_{YEARS,OHC}$, depends on the OHC data set used, as each data set spans a different range. The average of five OHC data sets, which we use as our primary OHC series, extends from 1955-2017, a total of 63 years. The value of χ_{OCEAN}^2 found using Eq. (8) is displayed on the bottom panel of Fig. 1. All model simulations shown throughout this paper have $\chi_{OCEAN}^2 \leq 2$, representing a good fit to the observed rise in OHC over the time of the data record.

The calculation of χ_{RECENT}^2 shown in Eq. (7) is used to constrain the model to match the observed changes in GMST over the time frame 1940-2019, a total of 80 years ($N_{YEARS,REC}$ equals 80). This time

215 frame was chosen to include a full cycle of AMOC, as the strength of the thermohaline circulation tends to vary on a period of 60-80 years (Chen and Tung, 2018; Kushnir, 1994; Schlesinger and Ramankutty, 1994). As noted above, the χ^2_{RECENT} constraint was added to our model framework because without this constraint the model is able to provide numerically good but poor visual fits to the GMST anomaly under certain conditions (i.e., the red line in the top panel of Fig. 1 starts to strongly deviate from the black line beginning in about 2000 under certain conditions). All model simulations shown below have $\chi^2_{\text{RECENT}} \leq 2$ representing a good fit to the observed rise in GMST over the past 80 years, which results in modeled GMST that replicates observed GMST for the entire time series.

Figure 1 shows the observed (HadCRUT5) and modeled GMST anomaly from 1850-2019, and the various anthropogenic and natural components that constitute modeled GMST. Figure 1a shows the value of climate feedback, $1.62 \text{ W m}^{-2} \text{ }^{\circ}\text{C}^{-1}$, that is needed to achieve a best fit to the climate record for this simulation, resulting in values of $\chi^2_{\text{ATM}} = 0.80$ and $\chi^2_{\text{OCEAN}} = 0.31$. Figure 1b is the total contribution of human activity to variations in GMST, which includes GHGs, AER, LUC, and the export of heat from the atmosphere to the ocean. For the simulation shown, the aerosol radiative forcing is -0.9 W m^{-2} , the best estimate given by IPCC 2013 (Myhre et al., 2013). This panel also notes the best estimate of the time rate of change of GMST attributed to humans from 1975-2014, or the attributable anthropogenic warming rate (AAWR (see Sect. 2.3)). Figure 1c illustrates the contribution to the GMST anomaly from TSI and SAOD over the 170-year period. The influences of ENSO and AMOC are indicated in Figs. 1d and 1e, respectively. Furthermore, the contribution of AMOC to the rise in GMST over 1975-2014 (the same time period used to define AAWR) is also specified on Fig. 1e (dotted black line). Figure 1f indicates the small effect of IOD and PDO on GMST in our model framework. The last panel, Fig. 1g, shows the time series of observed OHC based on the average of five data sets for the upper 700 m of the ocean (black points and blue error bars; see Sect. 2.2.8) and the modeled value of OHC (red line). For this simulation, a value of κ equal to $1.17 \text{ W m}^{-2} \text{ }^{\circ}\text{C}^{-1}$ fits the OHC data best. This value of κ falls within the range of empirical estimates for this parameter given by Raper et al. (2002). The sum of the contributions of human activity, TSI, SAOD, ENSO, AMOC, PDO and IOD to the GMST anomaly shown in Fig. 1b to 1f plus the value of C_0 equals the modeled GMST anomaly, shown by the red line in Fig. 1a.

Altering the training period of our model has a slight effect on our results (see Fig. S2, S3, and the supplement for information on various training periods). We project relatively similar results for end of century warming for training periods that start in 1850 and end in either 2009 or 1999, compared to
245 results shown throughout the paper for a training period of 1850 to 2019, indicating the stability of our approach. As detailed in the supplement, we do find some differences from the results shown in the paper upon use of a training period of 1850 to 1989 due to the reduction in the number of years considered from the available OHC records.

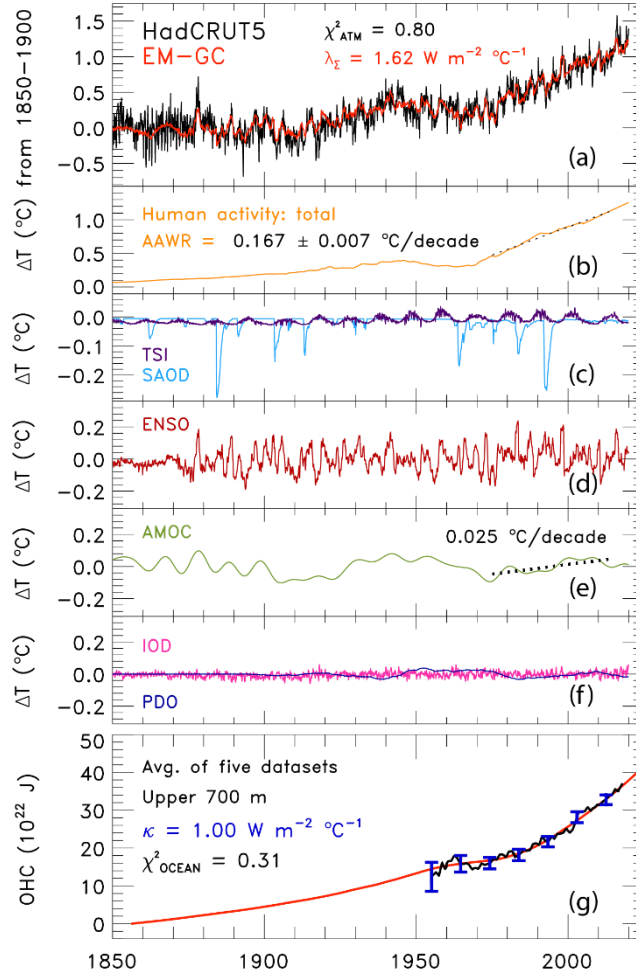


Figure 1. Measured and modeled GMST anomaly (ΔT) relative to a pre-industrial (1850-1900) baseline. (a) Observed (black) HadCRUT5 and modeled (red) ΔT from 1850-2019. This panel also displays the values of λ_{Σ} and χ^2_{ATM} (see text) for this best-fit simulation. (b) Contributions from total human activity. This panel also denotes the best estimate value of the attributable anthropogenic warming rate from 1975-2014 (black dashed) as well as the 2σ uncertainty in the slope for a model run that uses the best estimate of AER RF₂₀₁₁ of -0.9 W m^{-2} . (c) TSI (purple) and SAOD (light blue). (d) Influences from ENSO on ΔT . (e) Contributions from AMOC to ΔT and to observed warming from 1975-2014. (f) Influences from PDO (blue) and IOD (pink) on ΔT . (g) Measured (black) and modeled (red) ocean heat content (OHC) as a function of time for the average of five data sets (see text), the value of χ^2_{OCEAN} for this run, as well as the ocean heat uptake efficiency, κ , needed to provide the best-fit to the OHC record. The error bars (blue) denote the uncertainty in OHC used in this analysis (see Sect. 2.2.8).

250 2.2 Model Inputs

2.2.1 Temperature data

We use seven global mean surface temperature anomaly records. These records include the Hadley Centre Climatic Research Unit version 4 (HadCRUT4, (Morice et al., 2012)) and version 5 (HadCRUT5 (Morice et al., 2021)) from 1850-2019, National Centers for Environmental Information NOAA GlobalTemp v5 (NOAAGT, (Smith et al., 2008; Zhang et al., 2019)) from 1880-2019, NASA Goddard Institute of Space Studies Surface Temperature Analysis v4 (GISTEMP, (Hansen et al., 2010)) from 1880-2019, Berkeley Earth Group (BEG, (Rohde and Hausfather, 2020)) from 1850-2019, Cowtan and Way (2014) (CW14) from 1850-2019, and the Japanese Meteorological Agency (JMA (Ishihara, 2006)) from 1891-2019. We use the uncertainty time series from HadCRUT4 for all GMST records because the HadCRUT4 uncertainty provides a realistic description of the variation in GMST among the seven records (see the supplement, Figs. S4 and S5, and Table S1 for more information). Our analysis primarily uses the HadCRUT5 GMST data set, but in some sections, results are shown for the other data sets. All temperature anomalies are with respect to a pre-industrial baseline (1850-1900). To alter each data record so that the temperature anomaly is relative to the same pre-industrial baseline, we adjust all data sets relative to the HadCRUT5 baseline of 1961-1990. We then adjust each data set by the same amount to the HadCRUT5 pre-industrial baseline as described in the supplement.

2.2.2 Shared Socioeconomic Pathways

For this analysis, we use the estimates of the future abundances of greenhouse gases and aerosols provided by the SSPs. There are twenty-six scenarios, five baseline pathways and twenty-one mitigation scenarios. The baseline pathways follow specific narratives for factors such as population, education, economic growth, and technological developments of sources of renewable energy (Calvin et al., 2017; Fricko et al., 2017; Fujimori et al., 2017; Kriegler et al., 2017; van Vuuren et al., 2017) to represent several possible futures spanning different challenges for adaptation and mitigation to climate change as illustrated in Fig. 1 of O'Neill et al. (2014). The twenty-one mitigation scenarios follow one of the baseline pathways but include specific climate policy to reach a designated radiative forcing at the end of the century.

As part of CMIP6, the ScenarioMIP experiment (O'Neill et al., 2016) includes eight SSPs (SSP1-1.9, SSP1-2.6, SSP4-3.4, SSP2-4.5, SSP4-6.0, SSP3-7.0, SSP5-8.5, and SSP5-3.4-OS) that GCMs use to project future GMST. The first number is the reference pathway that the scenario follows (i.e., SSP1 follows the first SSP narrative) and the numbers after the dash are the target radiative forcing at the end of the century (i.e., SSP1-2.6 reaches around 2.6 W m^{-2} in 2100). The ScenarioMIP experiment designates Tier 1 and Tier 2 scenarios. The Tier 1 scenarios are SSP1-2.6, SSP2-4.5, SSP3-7.0, and SSP5-8.5, and the Tier 2 scenarios are SSP1-1.9, SSP4-3.4, SSP4-6.0, and SSP5-3.4-OS (an overshoot pathway that follows SSP5-8.5 until around 2040, where carbon dioxide emissions drastically decrease and become negative in 2065). Our analysis includes seven of the eight ScenarioMIP SSPs: all but the overshoot pathway. We highlight four in the main paper: two Tier 1 (SSP1-2.6 and SSP2-4.5) and two Tier 2 (SSP1-1.9 and SSP4-3.4) scenarios. Analysis of the other three SSPs is included in the supplement. Figure 2 shows the atmospheric abundance of the three major anthropogenic GHGs (carbon dioxide, methane, and nitrous oxide) for each of the seven SSPs we consider as well as observations of the global mean atmospheric abundance for these gases to the end of 2019 (Dlugokencky, 2020; Dlugokencky and Tans, 2020).

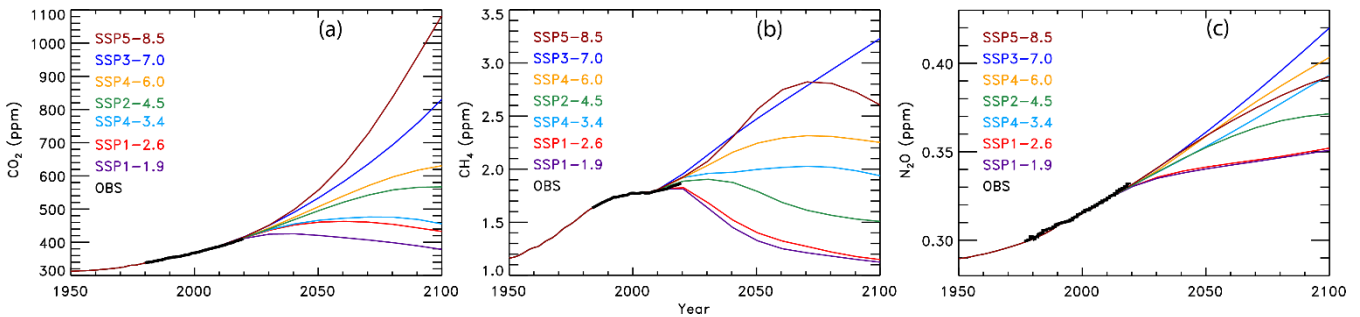


Figure 2. Observed and projected greenhouse gas mixing ratios. (a) Carbon dioxide abundances from observations (black) and seven of the ScenarioMIP SSPs (colors, as indicated). (b) Methane abundances from observations and ScenarioMIP SSPs. (c) Nitrous oxide abundances from observations and ScenarioMIP SSPs.

2.2.3 Greenhouse gases

The historical values of GHG mixing ratios were provided by Meinshausen et al. (2017) from 1850-2014. We used the equations from Myhre (1998) to calculate the change in RF due to carbon dioxide (CO_2), methane (CH_4), nitrous oxide (N_2O), ozone depleting substances (ODS), hydrofluorocarbons,

perfluorocarbons, and sulfur hexafluoride relative to RF in year 1850. We also used the updated pre-industrial values of CH₄ and N₂O from IPCC 2013 and the radiative efficiencies from WMO (2018). The radiative forcing of CH₄ also includes the 15% enhancement from the increase in stratospheric water vapor due to rising atmospheric CH₄ (Myhre et al., 2007). Values of GHG mixing ratios, other than ODSs, from 2015-2100 are from the SSP Database (Calvin et al., 2017; Fricko et al., 2017; Fujimori et al., 2017; Kriegler et al., 2017; Rogelj et al., 2018; van Vuuren et al., 2017) and are provided on a decadal basis. These mixing ratios were interpolated onto a monthly time scale. We used the estimates of future ODS abundances provided in Table 6-4 of the 2018 Ozone Assessment Report (Carpenter et al., 2018), because the SSP database did not provide these estimates. We also include tropospheric ozone (O₃^{TROP}) as a GHG, because tropospheric ozone rivals N₂O as the third most important anthropogenic GHG (Fig 8.15 of Myhre et al. (2013)). The RF due to O₃^{TROP} from the RCPs provided by the Potsdam Institute for Climate Impact Research (Meinshausen et al., 2011) is used, because the SSP database does not provide estimates. Values of RF due to O₃^{TROP} from RCP2.6, RCP4.5, RCP6.0, and RCP8.5 are substituted in for SSP1-2.6, SSP2-4.5, SSP4-6.0, and SSP5-8.5, respectively. We created new time series for the RF due to O₃^{TROP} for SSP4-3.4 and SSP3-7.0 using linear combinations of RF time series from RCP2.6 and RCP8.5, with weights based on the end of century total RF value due to all GHGs of the respective time series. Finally, the RF time series for O₃^{TROP} from RCP2.6 was also used for SSP1-1.9. Figure S6 shows the ozone RF time series used in this analysis and the supplement provides more information about the creation of the time series for the RF due to O₃^{TROP}.

2.2.4 Aerosol radiative forcing

The value of the change in total aerosol radiative forcing (direct and indirect) in 2011 relative to pre-industrial (AER RF₂₀₁₁) is highly uncertain. Chapter 8 of the IPCC 2013 report gives a best estimate of AER RF₂₀₁₁ as -0.9 W m⁻², a likely range between -0.4 and -1.5 W m⁻², and a 5th to 95th percent confidence interval between -0.1 and -1.9 W m⁻² (Myhre et al., 2013). This substantial range in AER RF₂₀₁₁ results in a large spread in future projections of global GMST. Figure 3 shows the effect of varying the value of AER RF₂₀₁₁ on projections of GMST in our EM-GC framework, for the same SSP4-3.4 GHG scenario. The middle panel on Figs. 3a, 3b, and 3c shows the contribution to GMST of GHGs, LUC,

325 AER, as well as net human activities. As the value of AER RF₂₀₁₁ decreases and aerosols cool more strongly, the value of climate feedback (model parameter λ_{Σ}) rises, and the net contribution of human impact on GMST by the end of the century increases. Depending on which value of AER RF₂₀₁₁ is used, the rise in GMST by year 2100 for the SSP4-3.4 pathway could range from 1.5°C (Fig. 3a) to 2.8°C (Fig. 3c) relative to pre-industrial. Strong aerosol cooling offsets a substantial fraction of GHG-induced
 330 warming, and a large value of climate feedback ($\lambda_{\Sigma} = 2.41 \text{ W m}^{-2} \text{ }^{\circ}\text{C}^{-1}$) is needed to fit the historical climate record (Fig. 3c). In this case, future warming is large, well above the goals of the Paris Agreement by the end of the century. Conversely, weak aerosol cooling offsets only a small fraction of GHG-induced warming, resulting in a small value of climate feedback ($\lambda_{\Sigma} = 1.08 \text{ W m}^{-2} \text{ }^{\circ}\text{C}^{-1}$) needed to fit the observed GMST record (Fig. 3a). The use of any of the values of AER RF₂₀₁₁ in Fig. 3 can result in a very good fit
 335 to the climate record (i.e., $\chi^2_{\text{ATM}} \leq 2$, $\chi^2_{\text{RECENT}} \leq 2$, and $\chi^2_{\text{OCEAN}} \leq 2$).

We use the total aerosol RF time series provided by the SSP database for each SSP scenario. The database provides AER RF from 2005-2100, with values for all SSPs nearly identical until about 2010 (Riahi et al., 2017; Rogelj et al., 2018). In the EM-GC, we calculate temperature projections over the entire observational period, beginning in 1850. We create AER RF time series that begin in 1850 and
 340 span the range of uncertainty given by Chapter 8 of IPCC 2013. We use historical estimates of AER RF from 1850-2014 for the four RCPs provided by the Potsdam Institute for Climate Research (Meinshausen et al., 2011). The AER RF value in 2014 from the appropriate historical estimate (i.e., RCP 4.5 is used for SSP2-4.5) is scaled by a constant factor, such that the historical RCP value at the end of 2014 matches the SSP time series at the start of 2015. This scaling yields a continuous time series for the RF of climate
 345 due to tropospheric aerosols. This scaled time series has AER RF₂₀₁₁ nearly equal to -1.0 W m^{-2} , which we take as the SSP-based best estimate of the change in total aerosol radiative forcing in 2011 relative to pre-industrial. Next, the single continuous time series is scaled, again by a constant multiplicative factor, to match the IPCC 2013 best estimate and range of uncertainty for AER RF₂₀₁₁ (Myhre et al., 2013). This procedure results in five additional time series of AER RF. Six time series of AER RF are created for
 350 each SSP, having values of AER RF₂₀₁₁ equal to -0.1 , -0.4 , -0.9 , -1.0 , -1.5 , and -1.9 W m^{-2} . Figure S7 shows these six AER RF time series for SSP1-2.6 and SSP4-3.4. In the EM-GC framework, we further

scale these six time series to create a total of 400 AER RF time series to fully analyze the range of AER RF₂₀₁₁ given by Myhre et al. (2013).

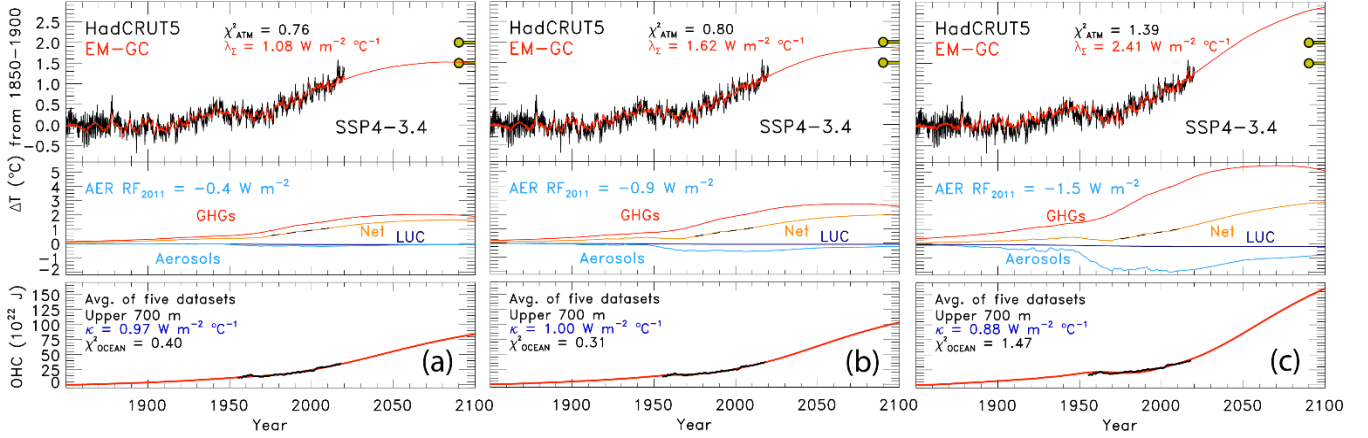


Figure 3. Measured (HadCRUT5) and EM-GC simulated GMST anomaly (ΔT) relative to a pre-industrial (1850-1900) baseline, as well as projected ΔT to end of century for SSP4-3.4. Top panel of each plot displays observed (black) and simulated (red) ΔT , as well as the values of λ_T and χ^2_{ATM} for each model run. The Paris Agreement target (1.5°C) and upper limit (2.0°C) are shown (gold circles). The second panel shows the contribution of GHGs, aerosols, and land-use change to ΔT , as well as the net human component. The bottom panel compares observed (black) and modeled (red) values of OHC for simulations constrained by the average of five data sets (see text) and also provides the numerical values of κ needed to obtain best-fits to the OHC record as well as best-fit values of χ^2_{OCEAN} . The only difference between (a), (b), and (c) is the time series for RF due to tropospheric aerosols used to constrain the EM-GC; values of AER RF₂₀₁₁ for each time series are (a) -0.4 W m^{-2} , (b) -0.9 W m^{-2} , (c) -1.5 W m^{-2} .

355 2.2.5 Total solar irradiance and stratospheric aerosol optical depth

We use the TSI time series provided for the CMIP6 models from 1850-2014 (Matthes et al., 2017) and append values from the Solar Radiation and Climate Experiment (SORCE) (Dudok de Wit et al., 2017) for 2015 to the end of 2019. The values of TSI_i used in Eq. (2) are differences of monthly mean values minus the long-term average (i.e., TSI anomalies). Consistent with prior studies (e.g., Lean and Rind
360 (2008) and Foster and Rahmstorf (2011)) variations in solar irradiance due to the 11-year solar cycle have a small but noticeable effect on the EM-GC simulation of the GMST anomaly (Fig. 1c). For projections of future warming, we set the term TSI_i in Eq. (2) equal to zero from the start of 2020 until 2100.

The time series for SAOD is a combination of values computed from extinction coefficients for the CMIP6 GCMs (Arfeuille et al., 2014) from 1850-1978 and the Global Space-based Stratospheric
365 Aerosol Climatology (GloSSAC v2.0) (Thomason et al., 2018) from 1979-2018. Extinction coefficients

at 550 nm were integrated from the tropopause to 39.5 km and averaged over the globe using a cosine of latitude weighting. The CMIP6 and GloSSAC extinction coefficients span 80°S to 80°N. To extend the SAOD time series to the end of 2019, we use the level 3, gridded SAOD product from the Cloud-Aerosol Lidar and Infrared Pathfinder Satellite Observations (CALIPSO) (Vaughan et al., 2004). Time series of globally averaged SAOD from CALIPSO have a very similar shape to the GloSSAC time series over the period of overlap (2006-2018) with a slight offset because GloSSAC uses estimates of CALIPSO data for SAOD. To append the SAOD after 2018, we took the average difference between the two time series for the overlapping months and then adjusted the CALIPSO time series by this offset. This slight adjustment to the CALIPSO record has no bearing on our results, since the effect of volcanic activity on GMST has been small over the past 2 decades (Fig. 1c). We set the term $SAOD_i$ in Eq. (2) equal to the value in December 2019 from the start of 2020 until 2100.

2.2.6 El Niño southern oscillation, Pacific decadal oscillation, and Indian Ocean dipole

We use the MEI.v2 (Wolter and Timlin, 1993; Zhang et al., 2019) to characterize the influence of ENSO on GMST. In order to obtain a time series that spans the entire training period of our model, 1850-2019, we append three time series to create an MEI.v2 index over the full extent of our model training period. The MEI.v2 provides two month averages of empirical orthogonal functions of five different climatic variables from 1979 to present (Zhang et al., 2019). To have the ENSO index extend back to 1850, we compute differences in SST anomalies over the tropical Pacific basin as defined by the MEI.v2 from 1850-1870 using HadSST3 (Kennedy et al., 2011). Our internal computation of this surrogate for the MEI index is then appended to the MEI.ext of Wolter and Timlin (2011), which extends from 1871-1978, and the MEI.v2 index of (Zhang et al., 2019) (1979-2019). This full time series provides a representation of ENSO that covers from 1850 to present. Consistent with prior regression-based approaches (Foster and Rahmstorf, 2011; Lean and Rind, 2008), we find a significant portion of the monthly and at times annual variation in GMST is well explained by ENSO (Fig. 1d). As for the other natural terms, we assume $ENSO_i$ in Eq. (2) is zero for 2020-2100.

The Pacific decadal oscillation is the leading principal component of North Pacific monthly SST variability poleward of 20°N (Barnett et al., 1999). The PDO index maintained by the University of

Washington provides monthly values from 1900-2018. The PDO varies on a multidecadal time scale and
 395 affects climate in the North Pacific and North America, and has secondary effects in the tropics (Barnett
 et al., 1999). In our model framework, the expression of PDO on GMST is dependent on the model
 specification of the AER RF time series, as shown in Fig. S8. At low values of AER RF₂₀₁₁, such as -0.1
 W m^{-2} , the effect of PDO on GMST is negligible and the contribution from AMOC dominates. At high
 values of AER RF₂₀₁₁ (-1.5 W m^{-2}), the effect of PDO on GMST is equal to the contribution from AMOC.
 400 At high values of AER RF₂₀₁₁, we obtain results similar to findings from England et al. (2014) and
 Trenberth and Fasullo (2013) that shows the PDO exhibits an appreciable influence on GMST, especially
 for the 2000-2010 time period.

The Indian Ocean dipole is based on the difference in the anomalous sea surface temperatures
 (SST) between the western equatorial Indian Ocean (50° - 70° E and 10° S- 10° N) and the south eastern
 405 equatorial Indian Ocean (90° E- 110° E & 10° S- 0° N) as defined in Saji et al. (1999). We use $1^{\circ} \times 1^{\circ}$ SSTs
 from the Centennial in situ Observation-Based Estimate (COBE) (Ishii et al., 2005) to create an IOD
 index from 1850-2019. As noted above and shown on Fig. 1f, the regression coefficients for PDO and
 IOD are quite small. We find little influence of either PDO or IOD in the HadCRUT5 time series of
 GMST, but these terms are retained for completeness. We assume PDO_i and IOD_i in Eq. (2) are zero after
 410 the start of 2019 and 2020, respectively.

2.2.7 Atlantic meridional overturning circulation

We use the Atlantic multidecadal variability (AMV) index as the area weighted, monthly mean SST from
 HadSST4 (Kennedy et al., 2019), between the equator and 60° N in the Atlantic Ocean (Schlesinger and
 415 Ramankutty, 1994) to characterize the influence of the AMOC on GMST. The AMV index is detrended
 using the RF anomaly due to anthropogenic activity over the historical time frame of the analysis, as
 discussed in Sect. 3.2.3 of Canty et al. (2013), because this detrending option removes the influence of
 long-term global warming on the AMV index. The detrended AMV index serves as a proxy for variations
 in the strength of the AMOC (Knight et al., 2005; Medhaug and Furevik, 2011; Zhang and Delworth,
 420 2007), which has particularly noticeable effects on climate in the Northern Hemisphere (Jackson et al.,
 2015; Kavvada et al., 2013; Nigam et al., 2011). For this analysis, the index has been Fourier filtered to

remove frequencies above 9 yr^{-1} to retain only the low frequency, high amplitude component of the thermohaline circulation (Canty et al., 2013). As noted above and shown in Fig. 1, a considerable portion of the long-term variability in GMST is attributed to variations in the strength of AMOC, including about
 425 $0.025^{\circ}\text{C} \text{ decade}^{-1}$ over the 1975-2014 time period. There is considerable debate about the validity of the use of a proxy such as the AMV index as a surrogate for the climatic effects of AMOC that is centered mainly around how much of the variability of the index is either internal or externally forced (Haustein et al., 2019; Knight et al., 2005; Medhaug and Furevik, 2011; Stouffer et al., 2006). We stress, as explained in Sect. 2.3, none of our major scientific conclusions are altered if we neglect AMV as a
 430 regression variable.

2.2.8 Ocean heat content records

Ocean heat content data records from five recent and independent papers are used in this study. We utilize OHC data from Balmaseda et al. (2013), Carton et al. (2018), Cheng et al. (2017), Ishii et al. (2017), and
 435 Levitus et al. (2012), as well as the average of the records to model the export of heat (OHE) from the atmosphere to the ocean. Figure S9 shows these five OHC records as well as the multi-measurement average. While most of these data sets have a common origin, they differ in how extensive temporal and spatial gaps in the coverage of ocean temperatures have been handled, ranging from data assimilation (Carton et al., 2018) to an iterative radius of influence mapping method (Cheng et al., 2017). The five
 440 data sets are all set to zero in 1986, which is the midpoint of the multi-measurement time series, by applying an offset for visual comparison. Since OHE, in units of W m^{-2} , is based on the slope of each OHC data set, this offset has no impact on the computation of OHE from OHC that is central to our study. For the computation of OHE from OHC, we use a value of the surface area of the world's oceans equal to $3.3 \times 10^{14} \text{ m}^2$ (Domingues et al., 2008). The OHC records we analyze are for the upper 700 m of the
 445 ocean. To calculate the OHE for the whole ocean, we multiply the OHE by $1/0.7$ to account for the fact that the upper 700 m of the ocean holds 70% of the heat (Sect. 5.2.2.1 (Solomon, 2007)). When we subtract the amount of heat going into the ocean in Eq. 2 (Q_{OCEAN}), we also must account for the difference in surface area between the global atmosphere and the world's oceans. Since the Q_{OCEAN} term is computed for the surface area of the ocean, but the forcing is applied to the whole atmosphere, we multiply the

450 Q_{OCEAN} term by the ratio of the surface area of the ocean to the surface area of the atmosphere, which is 0.67.

As noted above, the calculation of χ^2_{OCEAN} shown in Eq. (8) is used to constrain our model representation of the rise in OHC. Only model runs that provide a good fit to the observed OHC record are shown below. For these five OHC data sets, uncertainty estimates are not always provided. 455 Furthermore, some studies that do provide uncertainties give estimates that seem unreasonably small (see Fig. S10 and the supplement). Because of the discrepancy in uncertainties between OHC records, we create a new uncertainty time series using both the 1σ standard deviation of the average of the five OHC records and the uncertainties from the Cheng et al. (2017) (hereafter Cheng 2017) OHC record. We create this new uncertainty from 1955-2019 by a monthly time step and use either the 1σ standard deviation of 460 the average of the five OHC records or the uncertainties from the Cheng 2017 OHC record, whichever is larger, for that month. We use the Cheng 2017 OHC uncertainties because these estimates are the largest of the five data sets. Additionally, the standard deviation from the mean of the five OHC records is very low in the 1980s, which is an artifact of our normalization treatment, not inherent to any of the records. This combined uncertainty estimate is substituted in for each individual data set and the average, resulting 465 in our use of the same time varying uncertainty in OHC for all data sets. Figure S10 and the supplement provide more detail on the creation of this time dependent uncertainty estimate for OHC.

The choice of OHC record has only a small effect on future projections of GMST using the EM-GC. Figure 4 illustrates the effect of varying OHC record on future temperature. The bottom panels show the observed and modeled OHC, the value of κ needed to best fit the OHC data record, and the resulting 470 value of χ^2_{OCEAN} . Of the two OHC records shown, Balmaseda et al. (2013) (Fig. 4a) yields the lowest value of κ and Ishii et al. (2017) (Fig. 4b) results in the highest estimate of κ . For the same value of AER RF_{2011} (i.e., -0.9 W m^{-2}) and GHG scenario (SSP4-3.4), we find a difference of 0.25°C in the modeled rise in GMST in year 2100 for these two simulations (red lines on top panels). For most of the remaining analysis, we use the multi-measurement average of the five OHC data records. In Sects. 3.1 and 3.2 we 475 quantify the effect of OHC data record on both attributable anthropogenic warming rate and equilibrium effective climate sensitivity.

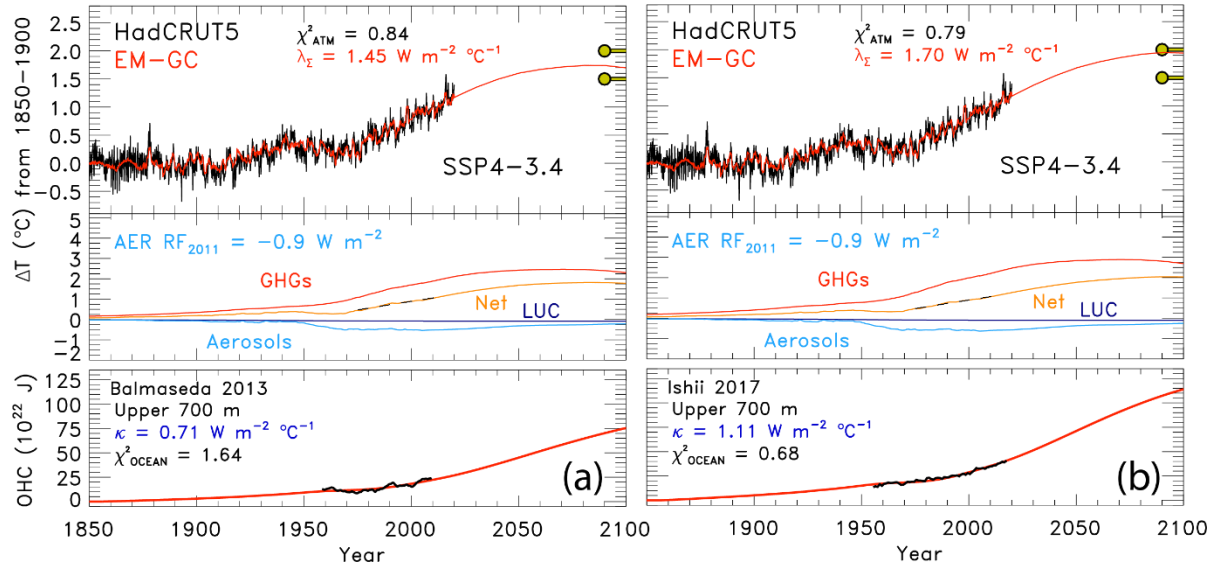


Figure 4. Measured (HadCRUT5) and EM-GC simulated GMST change (ΔT) from 1850-2019, as well as projected ΔT to year 2100 for SSP4-3.4. Top panel of each plot shows observed (black) and simulated (red) ΔT , the λ_{Σ} and χ^2_{ATM} values, and the Paris Agreement target and upper limit. The second panel displays the contribution of GHGs, aerosols, and land-use change on ΔT . The bottom panel compares the observed (black) and modeled (red) OHC for two different OHC records and displays the value of κ needed to provide best-fits to the OHC record, as well as best-fit values of χ^2_{OCEAN} . Both use an aerosol RF in 2011 of -0.9 W m^{-2} . (a) OHC record from Balmaseda et al. (2013). (b) OHC record from Ishii et al. (2017).

2.3 Attributable anthropogenic warming rate

480 The attributable anthropogenic warming rate, or AAWR, is the time rate of change of GMST due to humans from 1975-2014. We use AAWR as a metric in the EM-GC framework to quantify the human influence on global warming over the past few decades, and most importantly to also assess how well the CMIP6 GCMs can replicate this quantity. This analysis is motivated by the study of Foster and Rahmstorf (2011), who examined the human influence on the time rate of change of GMST from 1979-2010 using

485 a residual method. We extend the end year of our analysis to 2014 because this is the last year of the CMIP6 Historical simulation. We pushed the start year back to 1975 so that our analysis covers a forty-year period, over which the effect of human activity on GMST rose nearly linear with respect to time (Fig. 1b and Fig. S10c).

We calculate AAWR utilizing the EM-GC by computing a linear fit to the $\Delta T_{HUMAN,ATM}$ term:

$$\Delta T_{ATM,HUMANi} = \frac{1+\gamma}{\lambda_p} \{GHG \Delta RF_i + AER \Delta RF_i + LUC \Delta RF_i - Q_{OCEAN}\} \quad (9)$$

for a regression that spans 1850-2019. The $\Delta T_{HUMAN,ATM}$ term represents the net impact of the change in GMST due to RF of climate by anthropogenic GHGs, tropospheric aerosols, as well as the variation in surface reflectivity due to land-use change (deforestation), taking into account that for each model time step, a portion of the human-induced climate forcing is exported to the world's oceans. For each simulation, the slope of the linear least squares fit to the 480 monthly values of $\Delta T_{HUMAN,ATM}$ is used to determine AAWR. For the time period 1975-2014, a value for AAWR of 0.144 ± 0.005 °C ~~decade~~^{-1/decade} is found using a value of AER RF₂₀₁₁ equal to -0.9 W m⁻², where the uncertainty corresponds to the 2σ standard error of a linear least squares fit. The computation of AAWR found by fitting monthly values of $\Delta T_{HUMAN,ATM}$ is insensitive to modest changes in start and end year for the AAWR calculation (see Table S1). The value of λ_Σ , and therefore AAWR, is also insensitive whether or not the AMOC, PDO, or IOD terms are included in the regression framework (Canty et al., 2013; Hope et al., 2017). We are able to fit the climate record better (i.e., smaller values of χ^2 in Eqs. (6), (7), and (8)) by including the AMOC term. However, computed values of AAWR are insensitive to whether AMOC is used in the regression because whatever contributions the variation in the strength of the thermohaline circulation may have had on GMST are not considered in Eq. (9) (see Fig. S11 for further explanation).

The determination of AAWR from historical CMIP6 near surface air temperature output involves conducting a regression of deseasonalized, globally averaged, monthly ΔT ($\Delta T^{DES,GLB}$) from each GCM (Hope et al., 2017), termed the REG method. The archived CMIP6 Historical runs are constrained by observed variations in SAOD and influenced by other factors such as internal model generated ENSOs. The $\Delta T^{DES,GLB}$ time series for all of the runs from each CMIP6 GCM are averaged together to obtain one time series of $\Delta T^{DES,GLB}$ for each GCM. This average $\Delta T^{DES,GLB}$ time series is used to compute AAWR. The regression approach is used to compute the influence of SAOD on GMST from CMIP6 GCMs. The time needed for GMST to respond to a change in the aerosol loading in the stratosphere due to a volcanic eruption in each GCM can exhibit a significant difference compared to the empirically determined response time of 6 months discussed in Sect. 2.1. A lag was determined for each GCM by calculating the value of the monthly delay between volcanic eruptions and the surface temperature response that resulted

in the largest regression coefficient for SAOD. We regress the $\Delta T^{\text{DES, GLB}}$ against SAOD and the anthropogenic effect on temperature, which is approximated as a linear function from 1975-2014. The value of AAWR is the slope of the anthropogenic effect on temperature. Figure S12 illustrates the REG method used to determine AAWR from the CMIP6 GCMs. Table S3 depicts the slight effect on values of AAWR for the CMIP6 GCMs of changing the start or end year for the regression. At the time of analysis, there are 50 CMIP6 GCMs with the necessary archived output to calculate AAWR, with the values of AAWR found using REG shown in Table S3. Figure S13 and the supplement compare values of AAWR found using the REG method applied to EM-GC output with values of AAWR found using Eq. (9), as support for the validity of using the REG method to determine AAWR from CMIP6 output.

We also use a second method to extract the value of AAWR from the CMIP6 multi-model ensemble. This method, termed LIN, involves a linear regression of global, annual average values of GMST from the CMIP6 multi-model ensemble (Hope et al., 2017). For LIN, we exclude the years of obvious volcanic influence on the rise in GMST from the CMIP6 multi-model ensemble Historical simulations: i.e., data for 1982 and 1983 (following the eruption of El Chichón) and 1991 and 1992 (following the eruption of Mount Pinatubo) are excluded. Archived global, annual average values of GMST covering 1975-2014, excluding these four years, are fit using linear regression, with the AAWR set equal to the slope of the fit. Values of AAWR for 1975-2014 found using LIN are also shown in Table S4 for each GCM. Analysis of AAWR for these 50 GCMs of LIN versus REG (see Fig. S14) results in a correlation coefficient (r^2) of 0.995 and a mean ratio of 1.009 ± 0.015 , with LIN-based AAWR exceeding REG-based AAWR by about 1%. The close agreement of AAWR found using both methods provides strong evidence for the accurate determination of AAWR from the CMIP6 GCMs. We use the REG method in this analysis because it provides a more rigorous technique to remove the influence of SAOD on GMST from the CMIP6 multi-model ensemble compared to the LIN method.

The CMIP6 multi-model ensemble provides simulations of near surface air temperature (TAS), which we use to calculate AAWR. The EM-GC uses blended near surface air temperature to determine values of AAWR. Cowtan et al. (2015) provide a method to create blended near surface air temperature output from the GCMs. The CMIP6 multi-model ensemble contains archived fields of TAS and the temperature at the interface of the atmosphere and the upper boundary of the ocean (TOS) (Griffies et al.,

2016), whereas only a subset of GCM groups provide the archived land fraction needed to calculate blended near surface air temperature using the Cowtan et al. (2015) method. Cowtan et al. (2015) compare the modeled and measured trend in global temperature over 1975-2014 and found a 4.0% difference in the trend upon the use of blended temperature from CMIP5 GCMs, rather than global modeled TAS. Their analysis focused on a comparison of modeled and measured temperature, not just the anthropogenic component. We have used the method of Cowtan et al. (2015) to create blended CMIP6 temperature output, for the CMIP6 GCMs that provide TAS, TOS, and the land fraction. Upon our use of blended CMIP6 temperature output for these GCMs, and calculation of AAWR for 1975-2014, we find that AAWR based on blended CMIP6 temperature is 3.5% lower than AAWR found when using only TAS. Tokarska et al. (2020b) estimate an effect of $0.013^{\circ}\text{C} \text{ decade}^{-1}$ in the trend of CMIP6 temperature output upon the use of blended CMIP6 temperature instead of TAS, while Cowtan et al. (2015) report a difference of $0.030^{\circ}\text{C} \text{ decade}^{-1}$ between the trend in observations and modeled output. Since the difference between values of AAWR found using blended CMIP6 temperature output and TAS is so small and does not affect any of our conclusions, we use TAS output from the CMIP6 multi-model archive because this choice allows many more GCMs to be examined.

560

2.4 ~~Equilibrium~~ Effective climate sensitivity

The equilibrium climate sensitivity (~~ECS~~), ~~which~~ represents the warming that would occur after climate has equilibrated with atmospheric CO_2 at the $2\times$ pre-industrial level (Kiehl, 2007; Otto et al., 2013; Schwartz, 2012). In our model framework, we infer the climate sensitivity based on an estimate of climate feedback from the historical record, resulting in the effective climate sensitivity (ECS) (Tokarska et al., 2020a). Effective climate sensitivity is defined by IPCC 2013 as “an estimate of the global mean surface temperature response to doubled carbon dioxide concentration evaluated from model output or observations for evolving non-equilibrium conditions”. ~~is also used to compare results of our EM-GC to CMIP6 multi-model output.~~ To calculate ECS from the EM-GC, we use ~~the following equation:~~

570

$$ECS = \frac{1+\gamma}{\lambda_p} \times 5.35 \text{ W m}^{-2} \times \ln(2) \quad (10)$$

~~That~~ which represents the rise in GMST for a doubling of CO_2 , assuming no other perturbations as well as equilibrium in other components of the climate system (i.e., $Q_{\text{OCEAN}} = 0$) (Mascioli et al., 2013). The

expression for the radiative forcing of CO₂ is from Myhre (1998). The quantity γ in Eq. (10), which represents the sensitivity of the GMST to feedbacks within the climate system, is the only variable component of ECS. We only use values of γ that result in good fits ($\chi^2 \leq 2$ for Eq. (6) to (8)) between modeled and observed GMST and modeled and observed OHC. We refer to the quantity in Eq. (10) as effective climate sensitivity, rather than equilibrium climate sensitivity, because for most of our analysis we assume a constant value of climate feedback inferred from prior observations.

For the estimate of ECS-climate sensitivity from the CMIP6 multi-model ensemble, we use the method described by Gregory et al. (2004) (See the supplement and Fig. S15 for more information). The Gregory et al. (2004) method also estimates effective climate sensitivity from the CMIP6 GCMs (Gregory et al., 2004; Sherwood et al., 2020; Zelinka et al., 2020) because it assumes the feedbacks inferred from the first 150 years of the abrupt 4×CO₂ CMIP6 GCM simulations persist until equilibrium. At the time of this analysis, 28 models released the necessary output to the CMIP6 archive (see Table S5 for the list of models and individual values of ECS). Several ~~There have been some~~ recent analyses ~~that~~ suggest the Gregory method ~~may~~ underestimates the true value of equilibrium climate sensitivity from the CMIP6 multi-model output ~~ECS~~ (Rugenstein et al., 2020; Sherwood et al., 2020; Zelinka et al., 2020). However, effective climate sensitivity is strongly correlated with the amount of warming simulated by GCMs for high carbon emission scenarios and is more relevant for warming over the time scale of interest (rest of this century) due to the long time needed to achieve equilibrium (Sherwood et al., 2020). ~~However, w~~ We use the Gregory method to calculate ECS from the CMIP6 GCMs because this procedure is preferred by Eyring et al. (2016) for the use ~~by~~ within the CMIP6 community.

The estimates of climate sensitivity from Eq. (10) and those found using the Gregory et al. (2004) method are termed “effective” because they assume climate feedback inferred from either the historical climate record or the abrupt 4×CO₂ experiment persists until equilibrium. However, these estimates of ECS differ in that the perturbation to the RF of climate over the historical record is considerably smaller than the RF of climate that underlies the 4×CO₂ experiment of the Gregory et al. (2004) method. We quantify the impact of time variable climate feedback on climate sensitivity in Sect. 3.3.6.

2.5 Aerosol weighting method

Probabilistic forecasts of the future rise in GMST for various SSPs are an important part of our analysis. Probabilities of AAWR and ECS are computed by considering the uncertainty in AER RF₂₀₁₁. We also provide probabilistic estimates of AAWR and ECS. All of these quantities are computed by incorporating the uncertainty in the radiative forcing of climate due to tropospheric aerosols within results of our EM-
605 GC simulations. We use an asymmetric Gaussian to assign weights to the value of GMST, AAWR or ECS found for various time series of radiative forcing by aerosols associated with particular values of AER RF₂₀₁₁. Figure 5a shows the asymmetric Gaussian function we use to maximize the values of AAWR or ECS at the best estimate of AER RF₂₀₁₁ of -0.9 W m^{-2} , accomplished by giving these values the highest weighting. The IPCC 2013 “likely” range limits of AER RF₂₀₁₁ of -0.4 and -1.5 W m^{-2} (Myhre et al.,
610 2013) are assigned to the 1σ values of the Gaussian, and the AAWR or ECS estimates occurring at the “likely” range AER RF₂₀₁₁ limits are given the same weighting. The -0.1 and -1.9 W m^{-2} limits of the AER RF₂₀₁₁ range are assigned as the 2σ values of the asymmetric Gaussian, based on the IPCC 2013 description of these two values as being 5 and 95% uncertainty limits (Myhre et al., 2013). The Gaussian we use is asymmetric due to the fact that the distribution of the likely range and 5th and 95th percentiles
615 of the values of AER RF₂₀₁₁ are not distributed symmetrically from the best estimate of -0.9 W m^{-2} . For example, the likely ranges of AER RF₂₀₁₁ are given as -0.4 W m^{-2} and -1.5 W m^{-2} ; the -0.4 W m^{-2} value is 0.5 W m^{-2} from the best estimate whereas -1.5 W m^{-2} is 0.6 W m^{-2} from the best estimate. We fit a Gaussian to the likely range and 5th and 95th percentiles that has slightly different shape on either side of the best estimate, as shown in Fig. 5a.

620 Figure 5b shows the value of AAWR in $^{\circ}\text{C} \text{ decade}^{-1} / \text{decade}$ as a function of the climate feedback parameter, λ_{Σ} , and AER RF₂₀₁₁. We are able to find more good fits to the observed GMST for small values of AER RF₂₀₁₁ than at larger values of AER RF₂₀₁₁. Therefore, we bin values of AAWR (Fig. 5b), ECS (Fig. 5c), or future GMST (described in Sect. 3.3) by AER RF₂₀₁₁ and find the probability distribution for values of AAWR, ECS, or future GMST within each bin. The resulting probability distributions are
625 assigned the weights associated with each value of AER RF₂₀₁₁ in the bins to arrive at the probabilistic estimates of AAWR or ECS shown in Sect. 3. If we did not use this procedure and instead simply averaged all of the values for AAWR and ECS shown in Fig. 5, undue emphasis would be given to model results that occur at small AER RF₂₀₁₁ (see Fig. S16 for unweighted ECS values). This aerosol weighting method

allows the expert assessment of the likely range of RF due to tropospheric aerosols given in Chapter 8 of
 630 IPCC 2013 (Myhre et al., 2013) to be quantitatively incorporated into our computations of AAWR, ECS,
 and GMST.

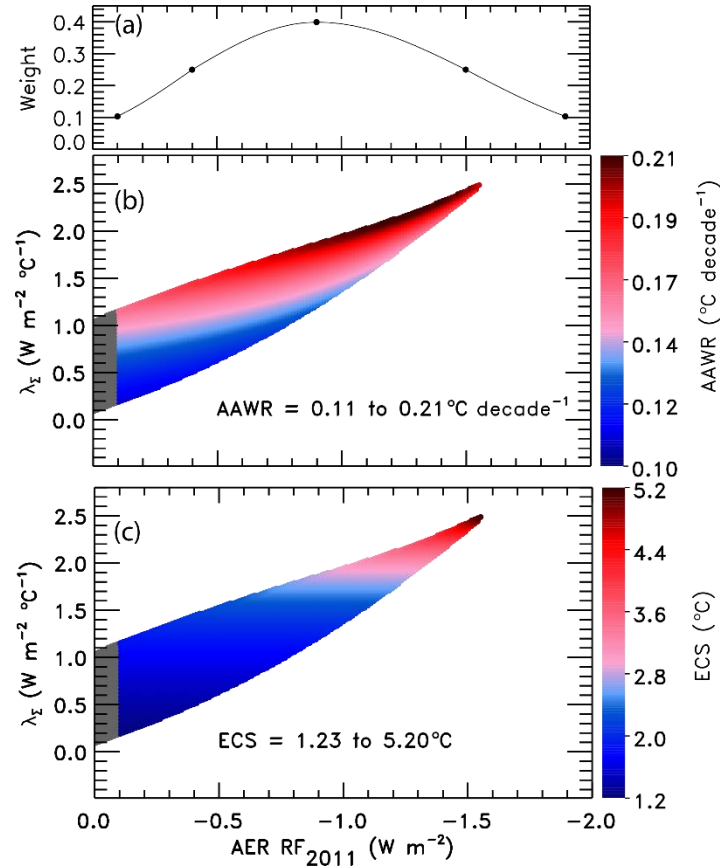


Figure 5. Aerosol weighting method. (a) The weights assigned to an asymmetric Gaussian distribution of AER RF₂₀₁₁ based on values provided by chapter 8 of IPCC 2013. The five black circles indicate the assigned weights for the AER RF₂₀₁₁ best estimate of -0.9 W m^{-2} , likely range of -0.4 and -1.5 W m^{-2} , and the 5th and 95th confidence intervals of -0.1 and -1.9 W m^{-2} . (b) Values of AAWR in $^{\circ}\text{C decade}^{-1}/\text{decade}$ as a function of climate feedback parameter, λ_{Σ} , and the value of AER RF₂₀₁₁ associated with various time series for the RF of climate due to tropospheric aerosols. The colors denote the values of AAWR calculated from 1975-2014 using the EM-GC trained with the HadCRUT5 ΔT record. (c) ECS in $^{\circ}\text{C}$ as a function of λ_{Σ} and the value of AER RF₂₀₁₁. The colors denote values of ECS found using the EM-GC. For panels (b) and (c), model results are shown only for combinations of λ_{Σ} and RF due to tropospheric aerosols for which good fits to the climate record could be achieved.

3 Results

3.1 AAWR, comparison to CMIP6 multi-model ensemble

635 An important measure of any climate model is the ability to accurately simulate the human influence on the global mean surface temperature (GMST) anomaly. We use the attributable anthropogenic warming rate (AAWR) found by our highly constrained Empirical Model of Global Climate (EM-GC) to quantify how well the CMIP6 multi-model ensemble (see Table S7 for a list of CMIP6 GCMs analyzed in this study) is able to simulate the human influence on global warming over the past several decades.

640 Figure 6 compares values of AAWR from 1975-2014 computed using our EM-GC with AAWR found utilizing archived output from the CMIP6 multi-model ensemble. Seven GMST data sets and five OHC records can be used to estimate AAWR with the EM-GC. For each choice, AAWR exhibits sensitivity to the variation of the time series of radiative forcing due to tropospheric aerosols. Each box and whisker plot found using our EM-GC shows, for a particular choice of GMST and OHC data record, the 25th, 50th, and 75th percentiles of AAWR (box), and 5th and 95th percentiles (whiskers) found using the aerosol weighting method described in Sect. 2.5. The star symbol indicates the minimum and maximum values of AAWR for each value of GMST data set and OHC record. The choice of OHC record and GMST data set has a slight effect on AAWR, as shown by the colored EM-GC symbols in Fig. 6. The

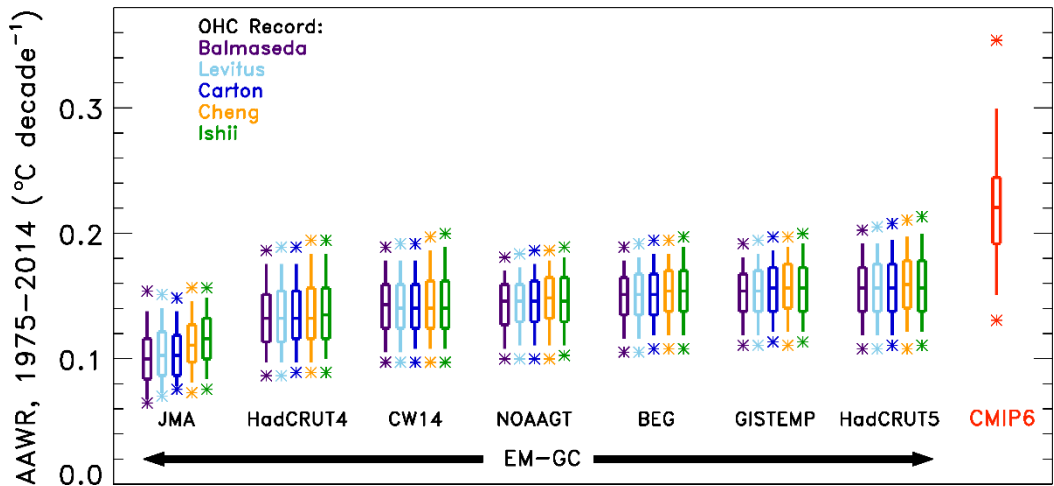


Figure 6. AAWR from the EM-GC and CMIP6 multi-model ensemble for 1975-2014. Seven temperature data sets and five ocean heat content records are used to compare values of AAWR computed from the EM-GC. The box represents the 25th, 50th, and 75th percentiles, the whiskers denote the 5th and 95th percentiles, and the stars show the minimum and maximum values of AAWR from the EM-GC based on the aerosol weighting method described in Sect. 2.5. The red box labeled “CMIP6” shows the 25th, 50th, and 75th percentiles, the whiskers represent the 5th and 95th percentiles, and the stars denote the minimum and maximum values of AAWR from the 50 member CMIP6 multi-model ensemble.

averages of the five 25th, 50th, and 75th percentiles of AAWR found using the HadCRUT5 data set for GMST are 0.138, 0.157, and 0.176°C ~~decade⁻¹~~/decade, respectively. The 5th and 95th percentile values of AAWR from HadCRUT5 are 0.120 and 0.195°C ~~decade⁻¹~~/decade.

The box and whisker symbol labeled CMIP6 in Fig. 6 shows the 5th, 25th, 50th, 75th, and 95th percentiles of AAWR calculated from 50 GCMs, also from 1975-2014, as described in Sect. 2.3. The stars denote the minimum and maximum values of AAWR from the GCMs. Two CMIP6 models exhibit values of AAWR similar to the median values we infer from the HadCRUT4, CW14, NOAAGT, BEG, GISTEMP, and HadCRUT5 data records using the EM-GC. In particular INM-CM5-0 (Volodin and Gritsun, 2018) yields 0.147°C ~~decade⁻¹~~/decade and MIROC6 (Tatebe et al., 2019) results in 0.157°C ~~decade⁻¹~~/decade (Table S4 provides values of AAWR for all individual CMIP6 GCMs). The median value of AAWR from the CMIP6 multi-model ensemble is 0.221°C ~~decade⁻¹~~/decade, about 40% larger than the 50th percentile value of AAWR found using the HadCRUT5 data set for GMST. The 5th, 25th, 75th, and 95th percentiles of AAWR from the CMIP6 multi-model ensemble are 0.151, 0.192, 0.245, and 0.299°C ~~decade⁻¹~~/decade, respectively. Some CMIP6 GCMs exhibit values of AAWR that are 0.14°C ~~decade⁻¹~~/decade larger than our largest empirical estimates for 1975-2014; the maximum value of AAWR from the GCMs is 0.354 °C ~~decade⁻¹~~/decade. The maximum value of AAWR based off the historical climate record using the EM-GC is 0.213°C ~~decade⁻¹~~/decade (HadCRUT5 data set using the Ishii et al. (2017) OHC record and a time series for RF due to tropospheric aerosols consistent with AER RF₂₀₁₁ equal to -1.5 W m⁻²). All of the EM-GC based values of AAWR in Fig. 6 are below the 50th percentile of AAWR from the CMIP6 multi-model ensemble of 0.221°C ~~decade⁻¹~~/decade, supporting the notion that CMIP6 GCMs tend to exhibit a faster rate of anthropogenic warming over the past four decades than the actual atmosphere.

Our determination that the rate of global warming from the CMIP6 multi-model ensemble over the time period 1975-2014 significantly exceeds the rise in GMST attributed to human activity is aligned with a similar finding highlighted in Figure 11.25b of chapter 11 of the IPCC 2013 report that CMIP5 models tend to warm too quickly compared to the actual climate system over the time period 1975-2014 (Kirtman et al., 2013). The values of AAWR from the CMIP6 multi-model ensemble from our analysis

present a similar finding as Tokarska et al. (2020^b) and CONSTRAIN (2020), that some of the CMIP6 models over estimate recent warming trends. Tokarska et al. (2020^b) examine the trend in the human component of GMST from 1981-2014. We arrive at a similar conclusion as these studies that CMIP6 GCMs overestimate the rate of global warming for the 1982-2014 time period of AAWR as shown in Table S2 and S3. Our results, the finding by the IPCC 2013 report, Tokarska et al. (2020^b), and CONSTRAIN (2020) appear to be quite different than the conclusion of Hausfather et al. (2020) that past climate models have matched recent temperature observations quite well. The Hausfather et al. (2020) study does not examine CMIP5 GCMs, let alone CMIP6 GCMs, and the last two rows of their Table 1 indicate that the skill of climate models forecasting the change in GMST over time decreased considerably between the Third Assessment Report (TAR) and the Fourth Assessment Report (AR4). The change in temperature over time for the TAR and AR4 only span 17 and 10 years, respectively (Hausfather et al., 2020). In Fig. 6, we examine the ability of the GCMs to simulate the rise in GMST attributed to humans over a 40 year time period, which provides a better measure of how well the models simulate the observations than the shorter time period. The temperature change over time for the TAR and AR4 examined by Hausfather et al. (2020) ends in 2017, which was right after a very strong ENSO, so their analysis may be influenced by the 2015 to 2016 ENSO event. In contrast, our analysis of AAWR is not influenced by natural variability such as ENSO because we examine the human component of global warming after explicitly accounting for and removing the influence of ENSO on GMST. Consequently, our determination of AAWR from observations (Table S2) and GCMs (Table S3) depends only to a small extent on the specification of start year (for values ranging from 1970 to 1984) and end year (2004 to 2018). Our analysis shows that upon quantification of the human driver to global warming within both the data record and climate models, the CMIP6 GCMs warm faster than observed GMST over the past four decades, regardless of precise specification of start and end year.

3.2 ECS

~~Equilibrium~~-climate sensitivity (~~ECS~~) is a metric often used to compare the sensitivity of warming among GCMs, as well as with warming inferred from the historical climate record. Figure 7 shows values of effective climate sensitivity (ECS) inferred from the climate record using our EM-GC, seven GMST

data sets, and five OHC records. As for AAWR, the largest variation in ECS is driven by uncertainty in
705 AER RF₂₀₁₁. The colored circles represent the ECS values found using the IPCC 2013 best estimate of
AER RF₂₀₁₁ of -0.9 W m^{-2} (Myhre et al., 2013). The ECS values found utilizing the EM-GC are displayed
using a box and whisker symbol. The middle line represents the median values of ECS, and the box is
bounded by the 25th and 75th percentiles. The whiskers connect to the 5th and 95th percentiles, and the stars
denote the minimum and maximum values. We use the aerosol weighting method described in Sect. 2.5
710 to calculate the percentiles for ECS; values of ECS found without aerosol weighting are shown in Fig.
S16. Varying the choice of GMST data record has a slight effect on the value of ECS, whereas the choice
of OHC record has a larger effect, as indicated by the various heights of the box and whiskers and the
maximum values of ECS. In the EM-GC framework, the ocean heat export term (Q_{OCEAN}) represents
disequilibrium in the climate system. We compute values of Q_{OCEAN} from various records of OHC. If the
715 current value of Q_{OCEAN} is as large as suggested by the Cheng 2017 and Ishii et al. (2017) OHC records,
then Earth's climate will exhibit a larger rise in GMST to reach equilibrium than if the value of Q_{OCEAN}
inferred from the OHC record of Balmaseda et al. (2013) is correct. The averages of the 25th, 50th, and
75th percentiles of ECS found using the HadCRUT5 data set for GMST are 1.74, 2.12, and 2.67°C,
respectively. The average best estimate of ECS using the HadCRUT5 data set and an AER RF₂₀₁₁ value
720 of -0.9 W m^{-2} is 2.33°C.

The box and whisker symbol labeled CMIP6 in Fig. 7 shows the 25th, 50th, 75th, and 5th and 95th
percentiles of ECS calculated from output of 28 CMIP6 models, as described in Sect. 2.4. Minimum and
maximum values are represented by the stars. The values of ECS from the CMIP6 multi-model ensemble
are larger than the majority of values inferred from the climate record using the EM-GC. The height of
725 the box for the CMIP6 multi-model ensemble estimate of ECS is larger than the height of the boxes for
ECS inferred from the climate record using the EM-GC, indicating that the GCMs exhibit a wide range
of ECS values. The 25th and 75th percentiles of ECS from the CMIP6 multi-model ensemble are 2.84°C
and 4.93°C, respectively. The 5th percentile of ECS from the CMIP6 multi-model ensemble is 2.19°C,
and the 95th percentile is 5.65°C (see Table S4 for ECS values for specific models). In contrast, the average
730 5th and 95th percentiles from the EM-GC are 1.40°C and 3.57°C, respectively. The median value of ECS
from the CMIP6 multi-model ensemble is 3.74°C, 1.6 times the best estimate of 2.33°C found using the

HadCRUT5 temperature record. All estimates of ECS described above are found assuming constant climate feedback over time. If climate feedback changes over time, then our estimates of ECS will increase as discussed in Sect. 3.3.6.

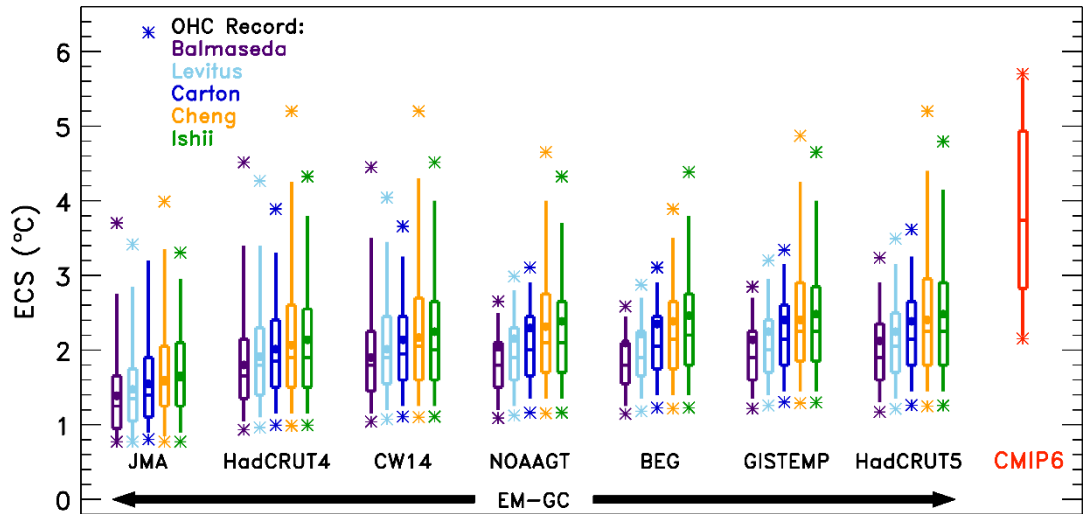


Figure 7. ECS from the EM-GC and the CMIP6 multi-model ensemble. Seven GMST data sets and five ocean heat content records are used to compare values of ECS computed from the EM-GC. The box represents the 25th, 50th, and 75th percentiles, the whiskers denote the 5th and 95th percentiles, and the stars indicate the minimum and maximum values of ECS using the EM-GC based on the weighting method described in Sect. 2.5. The circles denote the value of ECS associated with the best estimate of AER RF₂₀₁₁ of −0.9 W m^{−2}. The red box labeled “CMIP6” represents the 25th, 50th, and 75th percentiles, the whiskers denote the 5th and 95th percentiles, and the stars indicate the minimum and maximum values of ECS from the 28 member CMIP6 multi-model ensemble.

735 Figure 8 summarizes values of ECS found utilizing the analysis of the century and a half long climate record using our EM-GC, our examination of a 28 member CMIP6 GCM ensemble, and 13 other recent studies. The studies are divided into three categories: those that estimated ECS based on observations (Historical Analysis), others that used GCM output but constrained the output in some way (Constrained GCM Output), and studies that examined raw GCM output (GCM Output). We obtain a best
740 estimate for ECS of 2.33°C using the HadCRUT5 data record and a value of AER RF₂₀₁₁ = −0.9 W m^{−2} with a range of ECS of 1.40-3.57°C (5th and 95th percent confidence interval). The use of HadCRUT5 rather than HadCRUT4 imparts a significant rise to our best estimate of ECS, which is 1.99°C (range of 1.12-3.63°C) upon use of HadCRUT4. ThisBoth of these estimates of ECS largely falls within the range provided by IPCC 2013 of 1.5°C to 4.5°C for ECS and is supported by three other derivations of ECS

745 from the empirical climate record: 2.0°C (range of 1.2-3.9°C) given by Otto et al. (2013), 1.87°C (range of 1.1-4.05°C) given by Lewis and Grünwald (2018), and 2.0°C (range of 1.2-3.1°C) given by Skeie et al. (2018) (all range values are for the 5th and 95th percent confidence interval). All of these studies proceeded the release of HadCRUT5. Our estimate of ECS covers a similar range of values given by Cox et al. (2018), Dessler et al. (2018), and Nijssse et al. (2020), as illustrated in Fig. 8. Our determination of ECS

750 from the CMIP6 GCMs resembles that from Proistosescu and Huybers (2017) and Zelinka et al. (2020) as indicated in the GCM Output category of Fig. 8.

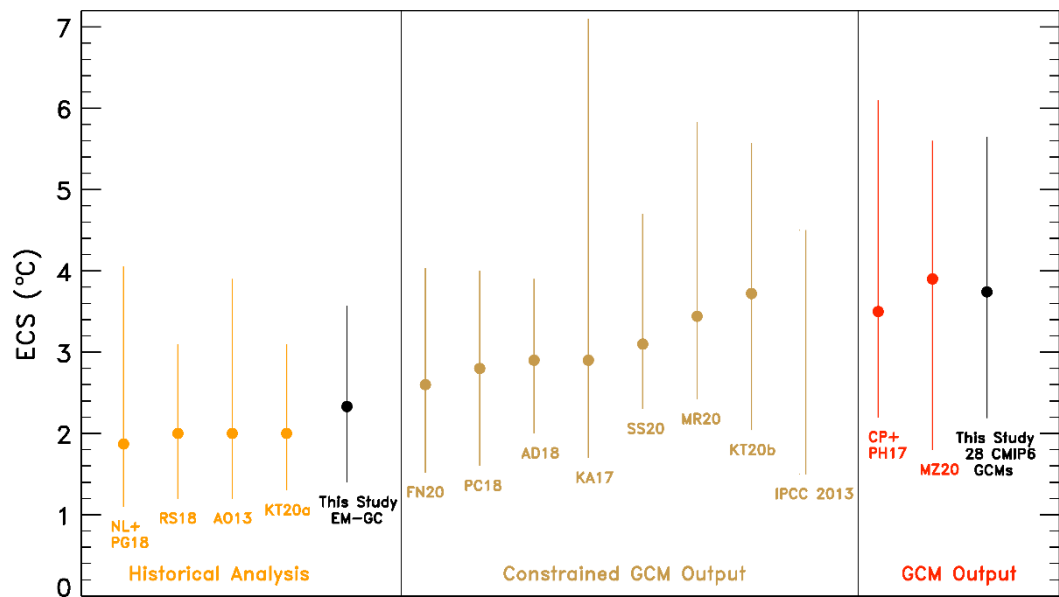


Figure 8. Values of ECS from the EM-GC (black) trained using the HadCRUT5 GMST record, our analysis of the CMIP6 multi-model ensemble (black), and 13 other studies grouped by type of analysis. The studies are listed by lead author (first initial of their first name and first initial of their last name) and the year of publication, unless there are only two authors, in which case initials of both authors are listed. Historical analysis includes Lewis and Grünwald (2018) NL+PG18, Otto et al. (2013) AO13, ~~and~~ Skeie et al. (2018) RS18, and Tokarska et al. (2020a) KT20a. Constrained GCM output includes Armour (2017) KA17, Cox et al. (2018) PC18, Dessler et al. (2018) AD18, Nijssse et al. (2020) FN20, Rugenstein et al. (2020) MR20, Sherwood et al. (2020) SS20, Stocker et al. (2013) IPCC 2013, and Tokarska et al. (2020**b**) KT20**b**. GCM output includes Proistosescu and Huybers (2017) CP+PH17 and Zelinka et al. (2020) MZ20. The studies estimating effective climate sensitivity are AO13, NL+PG18, RS18, FN20, SS20 KT20a, KT20b, and MZ20. The studies estimating equilibrium climate sensitivity are KA17, AD18, PC18, MR20, and CP+PH17. See the supplement for the confidence intervals shown for each study and more information about which studies are estimating effective or equilibrium climate sensitivity.

Recent studies have shown that the CMIP6 multi-model ensemble exhibits higher values of ECS than the CMIP5 models because of larger, positive cloud feedbacks within the latest models (Gettelman

et al., 2019; Meehl et al., 2020; Sherwood et al., 2020; Zelinka et al., 2020). The IPCC 2013 report gives
755 a likely range of 1.5°C to 4.5°C for ECS-climate sensitivity (Stocker et al., 2013), and some of the CMIP6
GCMs analyzed in this study have values of ECS more than 1°C above this range. However, some in the
climate community seem to currently doubt whether the very large values of ECS are representative of
the real world (CONSTRAIN, 2020; Forster et al., 2020; Lewis and Curry, 2018; Tokarska et al., 2020b).
Gettelman et al. (2019) found that the newest version of the Community Earth System Model (CESM2)
760 has a higher value of ECS than CESM1 (5.3°C versus 4.0°C) and urge the climate community to work
together to determine the plausibility of such high values of ECS. Zhu et al. (2020) found that the high
values of ECS in CESM2 and other GCMs is not supported by the paleoclimate record and are biased too
warm. An analysis by Nijse et al. (2020) coupled the CMIP6 multi-model ensemble to a two-box energy
balance model and the climate record and obtained a median value of ECS of 2.6°C and range of 1.52-
765 4.03°C (5th and 95th percentiles). Similarly, Sherwood et al. (2020) conclude cooling during the Last
Glacial Maximum provides strong evidence against ECS being greater than 4.5°C and conclude ECS lies
within the range of 2.3 to 4.7°C at the 5th to 95th percent confidence intervals.

We obtain a wide range of ECS values from our EM-GC simulations of the climate record due to
consideration of the uncertainty in the radiative forcing of climate from tropospheric aerosols (Figs. 5c
770 and 7). However, under one circumstance, we find values of ECS using the EM-GC that are similar to the
maximum value of ECS from the CMIP6 multi-model ensemble. Our large estimate of ECS occurs if we
assume that anthropogenic aerosols have exhibited strong cooling and offset a large amount of greenhouse
gas warming, such that the observed GMST record can only be well simulated under the condition of
large climate feedback (i.e., values of λ_{Σ} in Eq. (3) greater than or equal to 2.45 W m⁻² °C⁻¹). If aerosols
775 have truly strongly cooled the climate, offsetting the vast majority of the rise in RF due to greenhouse
gases as suggested by Shen et al. (2020), the actual value of ECS may lie close to 5°C or larger. Under
the scenario that aerosols have not cooled this strongly (Bond et al., 2013)), then it is feasible that ECS
lies well below 5°C. The highest values of ECS found using our analysis (red portion of Fig 5c) are
assigned low weights due to the assessment by Myhre et al. (2013) that the large AER RF₂₀₁₁ associated
780 with these ECS values is unlikely.

Four empirical determinations of ECS (our study plus Lewis and Grünwald (2018), Otto et al. (2013), and Skeie et al. (2018)) and the CMIP5 or CMIP6-constrained estimates of Cox et al. (2018), Dessler et al. (2018), and Nijssen et al. (2020) are in slight contrast with the 2.3-4.7°C range for ECS (5th and 95th confidence interval) published recently by Sherwood et al. (2020) (Fig 8). As noted above, Sherwood et al. (2020) use paleoclimate data to rule out the high range of ECS. They rely on a determination that the feedback due to clouds is moderately to strongly positive to rule out the low range of ECS found by our analysis and the studies noted above. We caution that knowledge of the cloud feedback from observations is generally limited to databases such as the International Satellite Cloud Climatology Project (ISCCP) (Schiffer and Rossow, 1983) and Pathfinder Atmospheres Extended (PATMOS-x) (Foster and Heidinger, 2013). While these databases are monumental in terms of complexity and scope, they cover only a fairly short (i.e., about 36 years) part of the century and a half climate record (Klein et al., 2017; Sherwood et al., 2020). Most assessments of total cloud feedback rely on some combination of observations such as ISCCP, PATMOS-x, or other satellite records together with the results of regression analysis, GCM projections, and large eddy simulations that are able to resolve some of the convective processes involved in cloud formation (Klein et al., 2017; Sherwood et al., 2020). The most important component of the global cloud feedback is tropical low clouds, which Sherwood et al. (2020) consider to exert a positive feedback on climate based largely on the results of Klein et al. (2017). The determination by Klein et al. (2017) of a likely positive feedback for tropical low altitude clouds is based on the mean and standard deviation of the central value of this feedback determined by five studies, even though four of these studies exhibit uncertainties that encompass zero feedback and the fifth nearly reaches zero (their Fig. 3). This fact, combined with the recent study by Weaver et al. (2020) who report no long term statistically significant trend in global cloud reflectivity at 340 nm averaged between 45° S and 45° N based on analysis of data collected by a variety of NOAA and NASA satellite instruments, causes us to suggest the true value of ECS may lie below the 2.3°C lower limit given by Sherwood et al. (2020).

In our model framework, the largest uncertainty in ECS is driven by imprecise knowledge of the radiative forcing of climate by tropospheric aerosols. As shown in Fig. 5c, a wide range of ECS values can be inferred from the century and a half long climate record. We stress that each value of ECS shown

in Fig. 5c is based on a simulation for which χ^2_{ATM} , χ^2_{RECENT} , and χ^2_{OCEAN} are all less than or equal to 2.
810 Better knowledge of AER RF for the contemporary atmosphere would lead to a reduction in the uncertainty of ECS. Numerous studies of the climate record, including our century and a half simulations, infer the possibility of lower values of ECS than was given by a recent analysis of studies that involve examination of data from compendiums such as ISCCP and PATMOS-x (Sherwood et al., 2020). However, the analysis by Sherwood et al. (2020) did not examine consistency of the inferred value of
815 ECS with the ability of models to accurately simulate the GMST anomaly between 1850 and present or over the past 40 years.

We conclude this section by commenting on the relationship between ECS and AAWR in our model framework. Eight of the CMIP6 GCMs (GFDL-ESM4, GISS-E2-1-G, INM-CM5-0, INM-CM4-8, MIROC6, MIROC-ES2L, NorESM2-LM, and NorESM2-MM) exhibit values of ECS and AAWR
820 consistent with the minimum and maximum estimates based on our EM-GC constrained by the HadCRUT5 GMST record (Table S5 and Fig. S17). An analysis of the relationship between AAWR and ECS from the CMIP6 GCMs illustrates that 78% of the variance in ECS among the 28 CMIP6 GCMs that provide both quantities is explained by AAWR (see Fig. S17). This result indicates CMIP6 GCMs that accurately simulate the rise in observed ΔT over the past few decades exhibit values of ECS that are
825 in line with our empirically based estimate.

3.3 Future projections

3.3.1 CMIP6

The CMIP6 multi-model archive provides future projections of the GMST anomaly relative to pre-
830 industrial (ΔT) using the ScenarioMIP Shared Socioeconomic Pathways (SSPs). Figure 9 shows the CMIP6 multi-model ensemble projections of ΔT for the four SSPs (SSP1-1.9, SSP1-2.6, SSP4-3.4, and SSP2-4.5) highlighted in our analysis. Each SSP scenario has varying amounts of gridded, monthly mean TAS projections submitted to the CMIP6 archive by GCMs. The global, monthly ΔT time series for all of the runs for each CMIP6 GCM were averaged together to obtain one time series of ΔT . The varying
835 amount of GCM output available for each SSP scenario is due to the fact that: a) SSP1-2.6 and SSP2-4.5 are Tier 1 scenarios (O'Neill et al., 2016) and are designated as priority over the other SSPs (as described

in Sect. 2.2.2), and b) not all GCMs have provided results to the CMIP6 archive at the time of the analysis. More CMIP6 multi-model output will likely become available as modeling groups who have not submitted output to the CMIP6 archive finalize their results. However, we do not expect additional GCM simulations will affect our conclusions unless the GCM output is significantly different than that currently available.

The red trapezoid in Fig. 9 labeled as the IPCC 2013 likely range is the same trapezoid as that displayed on Figure 11.25b from chapter 11 of the IPCC 2013 report (Kirtman et al., 2013). The recent observations of ΔT from HadCRUT5 lie towards the top of the likely range of warming designated by this trapezoid. Many of the projections of the rise in ΔT from the CMIP6 multi-model ensemble lie above the IPCC 2013 likely range of warming. The Paris Agreement target of 1.5°C and upper limit of 2.0°C are shown as yellow circles, included to allow for comparison of the future projections of ΔT from the CMIP6 multi-model ensemble with the goals of the agreement. The thick blue line on each plot is the CMIP6 multi-model mean of ΔT , and the dashed blue lines are the minimum and maximum ΔT projections from the CMIP6 multi-model ensemble. For SSP1-1.9, the multi-model mean projection of ΔT in 2100 from the CMIP6 GCMs lies just above the Paris Agreement target at 1.6°C, whereas for SSP1-2.6 the CMIP6 multi-model mean reaches the Paris Agreement upper limit of 2.0°C at the end of this century. For both SSP4-3.4 and SSP2-4.5, the end of century CMIP6 multi-model mean lies above the Paris Agreement upper limit at 3.0°C and 3.1°C, respectively.

Figure 9 illustrates there are two groups of CMIP6 multi-model projections of ΔT , with a few GCMs having future values of ΔT that are considerably higher than others. This divergence for GCM projections of ΔT is especially evident in Fig. 9a, c, and d. The two CMIP6 GCMs that have the highest values of ΔT across the four SSPs are CanESM5 (Swart et al., 2019) and UKESM1 (Sellar et al., 2020). The CanESM5 and UKESM1 GCMs have the highest values of AAWR ($0.354^{\circ}\text{C decade}^{-1}/\text{decade}$ and $0.299^{\circ}\text{C decade}^{-1}/\text{decade}$, respectively), large values of ECS (5.70°C and 5.40°C , respectively), and exceed observed ΔT reported by HadCRUT5 for the past few decades.

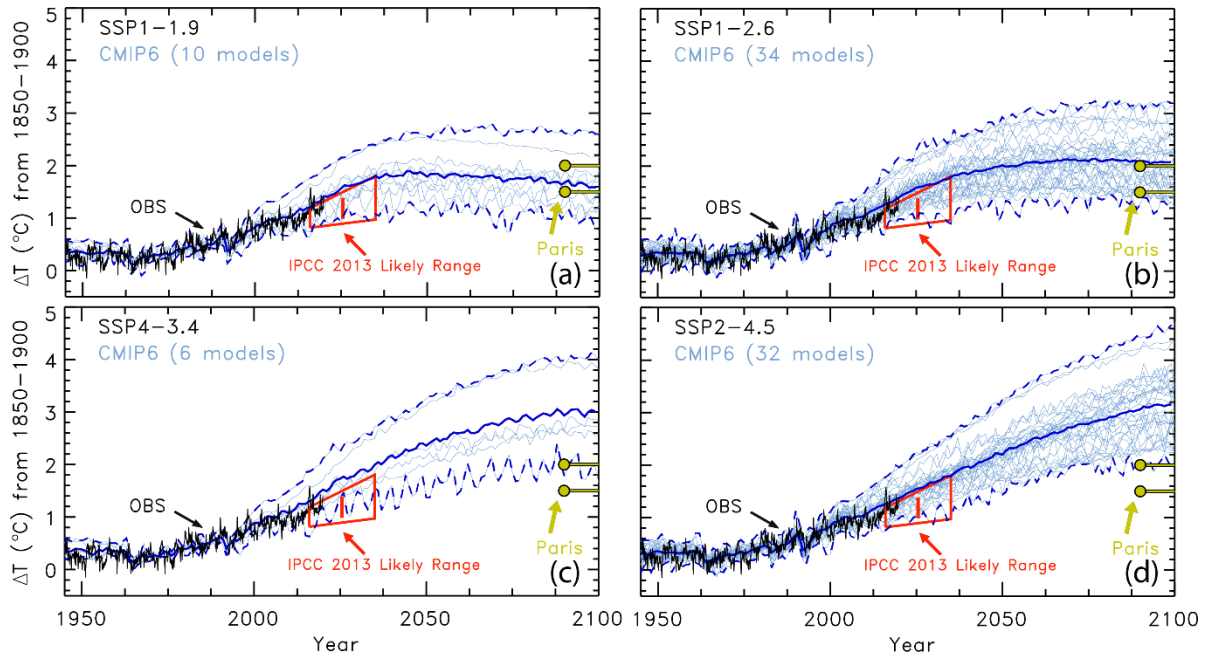


Figure 9. Historical simulations and future projections of GMST from the CMIP6 multi-model ensemble for several SSP scenarios. (a) GCM simulations from the Historical experiment, and future model projections from SSP1-1.9. Observations (black) are from HadCRUT5 to the end of 2019. The IPCC 2013 likely range of warming (red) is from Figure 11.25b from chapter 11 of the IPCC 2013 report. The CMIP6 multi-model mean (thick, blue) and minimum and maximum (dashed, blue) lines are shown. Global, monthly ΔT was created by averaging the TAS output over the globe with a cosine latitude weighting. The Paris Agreement target of 1.5°C and upper limit (yellow) of 2.0°C are included to demonstrate how the GCM projections compare. (b) Future GMST projections from SSP1-2.6. (c) Future GMST projections from SSP4-3.4. (d) Future GMST projections from SSP2-4.5.

3.3.2 EM-GC

The EM-GC is also used to project future changes in ΔT using the SSPs. Figure 10 shows the GMST anomaly in 2100 from pre-industrial (ΔT_{2100}) as a function of the climate feedback parameter and AER RF_{2011} , for the four SSPs highlighted throughout. Only model runs from the EM-GC that achieved a good fit to the climate record ($\chi^2_{ATM} \leq 2$, $\chi^2_{RECENT} \leq 2$, $\chi^2_{OCEAN} \leq 2$) are shown. The EM-GC runs that satisfy these three χ^2 constraints but fall outside of the IPCC 2013 range for AER RF_{2011} (Myhre et al., 2013) are shaded grey (left hand side of each panel). We do not consider the EM-GC projections that lie outside of the IPCC 2013 range for AER RF_{2011} in our projections of ΔT , yet these results are shown to illustrate that the EM-GC can fit the climate record with estimates of the RF due to tropospheric aerosols that lie below (i.e., less cooling) of the 5th confidence interval of -0.1 W m^{-2} for AER RF_{2011} given by IPCC 2013. We cannot establish any good fits of the HadCRUT5 GMST record for AER RF_{2011} with a cooling

stronger than about -1.55 W m^{-2} . The range of ΔT_{2100} we compute using the EM-GC for SSP1-1.9, SSP1-
875 2.6, SSP4-3.4, and SSP2-4.5 are $0.75\text{-}2.06^{\circ}\text{C}$, $0.96\text{-}2.58^{\circ}\text{C}$, $1.18\text{-}3.01^{\circ}\text{C}$, and $1.45\text{-}3.47^{\circ}\text{C}$, respectively.
Results for SSP4-6.0, SSP3-7.0, and SSP5-8.5 are shown in Fig. S18: ΔT_{2100} ranges are $1.70\text{-}4.02^{\circ}\text{C}$,
 $2.26\text{-}4.93^{\circ}\text{C}$, and $2.62\text{-}6.02^{\circ}\text{C}$ for these three scenarios.

The large range of ΔT_{2100} found for any given SSP scenario is caused by the fact that the climate
record can be fit nearly equally well by a considerably large combination of the climate feedback
880 parameter (our λ_{Σ}) and scenarios for radiative forcing due to tropospheric aerosols. The more aerosols
have cooled, offsetting the relatively well-known warming due to GHGs, the larger λ_{Σ} must be to fit the
climate record. Since the RF of aerosols is set to diminish in the future due largely to public health
concerns (Lelieveld et al., 2015; Shindell et al., 2016; Smith and Bond, 2014), the part of our model
ensemble requiring relatively large values of λ_{Σ} to achieve a good fit to the climate record will result in
885 higher values of ΔT_{2100} than other members of our model ensemble with small values of λ_{Σ} . Most GCMs
sample only a small portion of the possible combinations of λ_{Σ} and AER RF_{2011} shown in Figs. 10 and
S18.

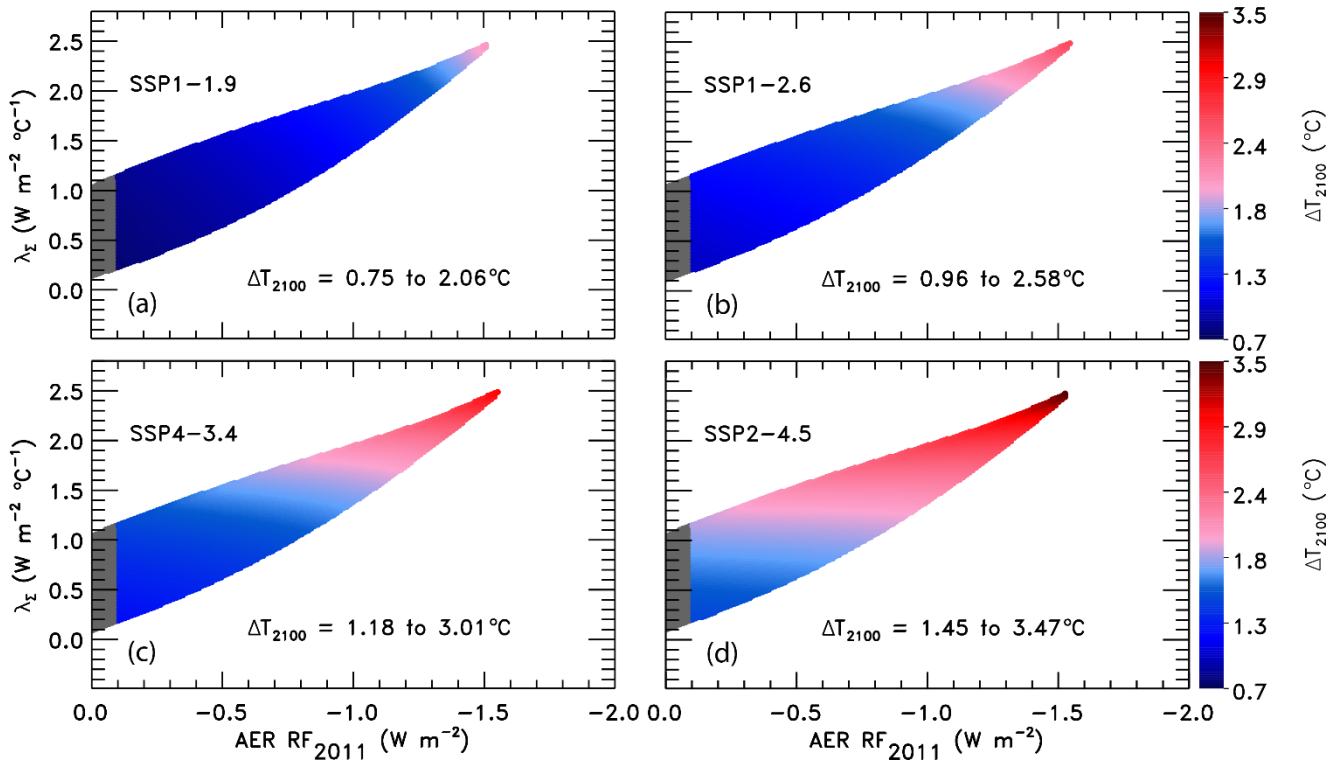


Figure 10. ΔT_{2100} as a function of climate feedback parameter and tropospheric aerosol radiative forcing in 2011 using the EM-GC trained with the HadCRUT5 ΔT record. (a) Future GMST change for SSP1-1.9. The region outside of the AER RF_{2011} range provided by IPCC 2013 is shaded (grey). Colors denote the GMST change in year 2100 relative to pre-industrial. The color bar is the same across all four panels for comparison. (b) GMST anomaly for SSP1-2.6. (c) Future temperature change for SSP4-3.4. (d) GMST anomaly for SSP2-4.5.

3.3.3 Comparing CMIP6 and EM-GC

Time series of future projections of ΔT from the EM-GC can be illustrated as probabilistic forecasts. Figure 11 shows the change in future ΔT for SSP1-1.9, SSP1-2.6, SSP4-3.4, and SSP2-4.5 colored by the probability of reaching at least that rise in ΔT by the end of the century. The EM-GC probabilities are computed from ensemble members for model runs constrained by the HadCRUT5 data records for GMST and the average of 5 OHC data records (Fig. S9) based on the aerosol weighting method, described in Sect. 2.5. The trapezoid from chapter 11 of IPCC 2013 (Kirtman et al., 2013) is shown on Fig. 11 in black to highlight that the EM-GC projections of the future rise in ΔT lie within the IPCC 2013 likely range of warming. The Paris Agreement target and upper limit are included to compare the EM-GC projections of future ΔT to the Paris Agreement goals. The white shaded region is the EM-

GC's median estimate of future ΔT for each SSP scenario. The median estimate for ΔT_{2100} for simulations using SSP1-1.9 and SSP1-2.6 falls below the Paris Agreement target at 1.1°C and 1.4°C, respectively. The median estimate of ΔT_{2100} from the EM-GC for SSP4-3.4 is between the Paris Agreement target and upper limit at 1.8°C. For SSP2-4.5 the median estimate of ΔT_{2100} is 2.1°C, which is just above the Paris Agreement upper limit. The CMIP6 minimum, multi-model mean, and maximum projections of ΔT , based on the ensembles in Fig. 9, are also shown in Fig. 11. The CMIP6 minimum projection of the rise in ΔT falls near the EM-GC median estimate of ΔT for each SSP scenario. The CMIP6 multi-model mean value of the future change in ΔT falls below the EM-GC maximum value of ΔT , while the CMIP6 maximum value is far above the maximum projections of the future rise in ΔT using the EM-GC. Results for SSP4-6.0, SSP3-7.0, and SSP5-8.5 are provided in Fig. S19.

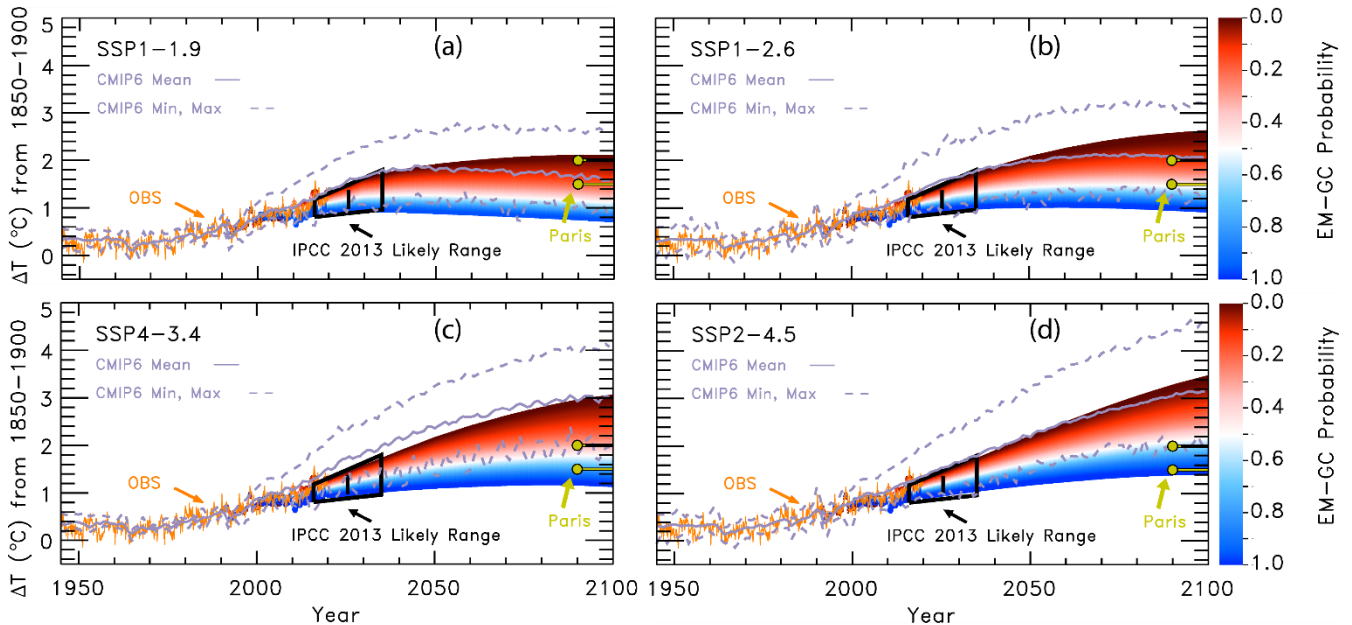


Figure 11. Probabilistic forecasts of the future rise in ΔT from the EM-GC trained using the HadCRUT5 ΔT record for several SSPs. (a) Future projections of ΔT for SSP1-1.9. Observations (orange) are from HadCRUT5. The IPCC 2013 likely range of warming (black) is from Figure 11.25b of chapter 11 of IPCC 2013. The Paris Agreement target and upper limit (yellow) are shown for comparison to EM-GC projections. The CMIP6 minimum, multi-model mean, and maximum values of ΔT are shown to compare to EM-GC projections. Colors denote the probability of reaching at least that temperature by the end of the century. (b) Future projections of ΔT for SSP1-2.6. (c) Future projections of ΔT for SSP4-3.4. (d) Future projections of ΔT for SSP2-4.5.

Figure 12 compares probability distribution functions (PDFs) for the projection of ΔT_{2100} utilizing the EM-GC with the HadCRUT5 GMST record and average of the five OHC data sets and the CMIP6

multi-model ensemble. For the CMIP6 multi-model results, we compute the probabilities of achieving the Paris Agreement target of 1.5°C and upper limit of 2.0°C (at the end of the century) by calculating how many of the GCMs participating in each scenario have projections of ΔT_{2100} below the target or upper limit. The probabilities for the projections of ΔT_{2100} using the EM-GC are computed using the aerosol weighting method, described in Sect. 2.5. The height of each histogram represents the probability that a particular range of ΔT_{2100} , defined by the width of each line segment, will occur. The left-hand y-axis displays the probability of ΔT_{2100} using the EM-GC, while the right-hand y-axis represents the probability of ΔT_{2100} using the CMIP6 multi-model simulations. The values on the CMIP6 multi-model ensemble y-axis are double the values on the EM-GC y-axis, for visual comparison. The solid black line denotes the Paris Agreement target and the dotted black line signifies the upper limit on each panel. The PDFs for SSP4-6.0, SSP3-7.0, and SSP5-8.5 are shown in Fig. S20.

Numerical values of probabilities for staying at or below the Paris Agreement target for SSP1-2.6 or upper limit for SSP4-3.4 are given for the seven GMST records using the EM-GC and CMIP6 multi-model ensemble in Table 1. Projections of ΔT_{2100} based on the EM-GC provide more optimism for achieving the Paris Agreement goals than the CMIP6 multi-model ensemble, regardless of which GMST data record is used. For simulations constrained using the HadCRUT5 record, the SSP1-2.6 scenario provides a 53% (Table 1) likelihood of ΔT_{2100} staying at or below 1.5°C and SSP4-3.4 results in a 64% likelihood of limiting warming to 2.0°C by end of century. The probability of achieving the Paris Agreement target or upper limit increases upon using HadCRUT4 rather than HadCRUT5 in the EM-GC framework. The probability of achieving the 1.5°C target for SSP1-2.6 and 2.0°C upper limit for SSP4-3.4 using the HadCRUT4 GMST record are 64% and 74%, respectively (Table 1). This decline in attainment of the goals of the Paris Agreement upon use of HadCRUT5 reflects more rapid warming of this data record compared to HadCRUT4 (Fig. S4e versus S4c). The rapid warming in HadCRUT5 is driven by more accurate buoy records for SST and a statistical gap filling procedure to attain global coverage (Morice et al., 2021). The impact on the likelihood of achieving the Paris Agreement goals of for the other SSP scenarios upon using the HadCRUT4 or HadCRUT5 data records is detailed in Table S6.

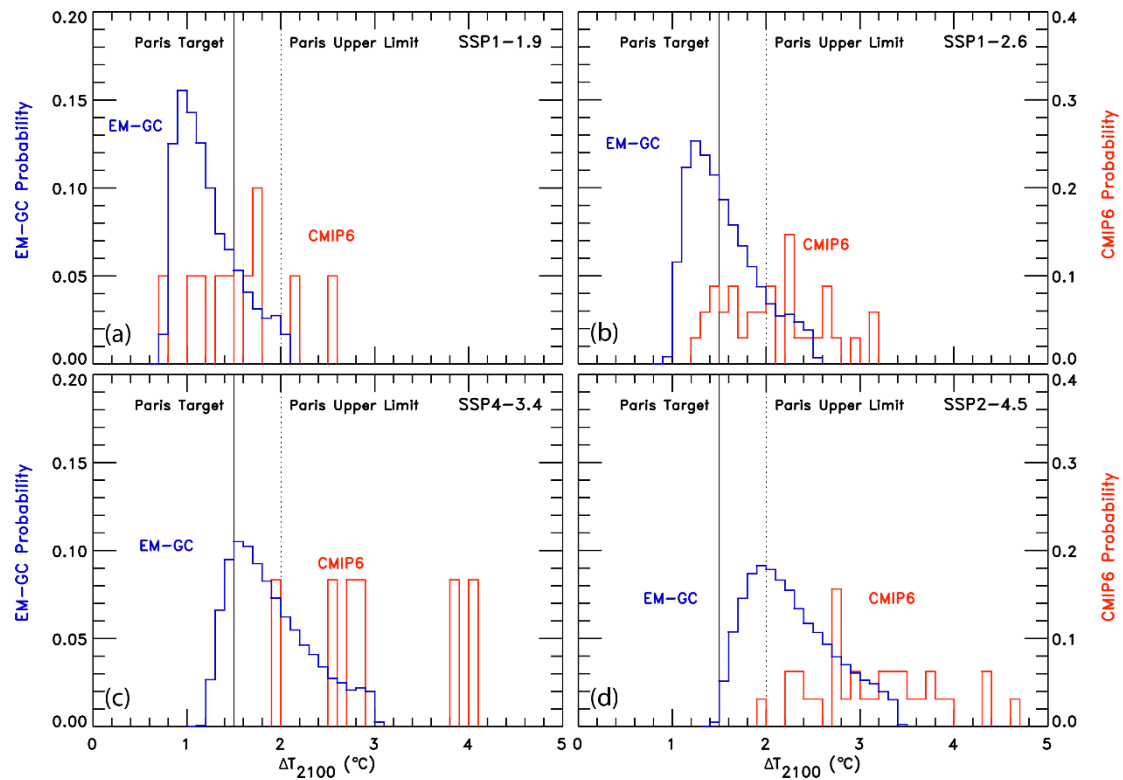


Figure 12. Probability density functions (PDF) for ΔT_{2100} found using the EM-GC trained with the HadCRUT5 temperature record (dark blue) and CMIP6 multi-model results (red). (a) PDF for EM-GC results and CMIP6 multi-model results for SSP1-1.9. The left-hand y-axis is for EM-GC probabilities and the righthand y-axis is for the CMIP6 multi-model ensemble probabilities. (b) PDF for SSP1-2.6. (c) PDF for SSP4-3.4. (d) PDF for SSP2-4.5.

An analysis by Tokarska et al. (2020b) supports our finding of a higher likelihood of attaining the goals of the Paris Agreement than suggested by the CMIP6 multi-model ensemble. Tokarska et al. (2020b) filter the CMIP6 multi-model output on the level of agreement with observations to show that the SSP1-2.6 scenario has a likely range of warming at 1.33-1.99°C above preindustrial by end of century. Previous studies suggested that a 2.6 W m^{-2} scenario was in line with the 2.0°C goal (Kriegler et al., 2014, 2015; O'Neill et al., 2016; Riahi et al., 2015). Our analysis suggests the 2.6 W m^{-2} scenario provides between a 86-98% probability of limiting warming to 2.0°C and a 53-78% probability of achieving the more stringent 1.5°C target, depending on the GMST record (Table 1). If GHGs were to follow SSP4-3.4, we find a 19-58% probability of limiting warming to 1.5°C and a 64-87% probability of limiting warming to

2.0°C. Significant climate mitigation efforts will be required to keep the growth of CO₂, CH₄, and N₂O below the trajectories shown for SSP1-2.6 and SSP4-3.4 (Fig. 2).

Table 1. Probability of achieving the Paris Agreement target (SSP1-2.6) or upper limit (SSP4-3.4) for seven GMST records using the EM-GC and the CMIP6 multi-model ensemble. The probabilities using the EM-GC are computed using the aerosol weighting method. The probabilities using the CMIP6 models are computed by calculating how many of the models for that scenario are below the temperature limits compared to the total number of models.

	Probability of Staying at or Below 1.5°C		Probability of Staying at or Below 2.0°C	
	SSP1-2.6	SSP4-3.4	SSP1-2.6	SSP4-3.4
CMIP6	18%	0%	47%	17%
HadCRUT5	53%	19%	86%	64%
GISTEMP	55%	20%	88%	69%
CW14	60%	29%	89%	71%
NOAAGT	61%	27%	90%	74%
BEG	62%	26%	98%	76%
HadCRUT4	64%	35%	90%	74%
JMA	78%	58%	95%	87%

3.3.4 Carbon budgets

The transient climate response to cumulative emissions (TCRE) relates the rise in ΔT to the cumulative amount of carbon released into the atmosphere by human activities. We illustrate TCRE from the EM-GC as probabilistic forecasts, as shown in Fig. S21, to analyze future projections of ΔT. We use the probabilistic forecasts in Fig. S21 to determine the carbon budgets in Table 2. Table 2 contains estimated carbon budgets in the form of the total CO₂ emissions (Gt C) since 1870 that result in a 95%, 66%, and 50% probability of the future rise in ΔT staying below the Paris Agreement target of 1.5°C and upper limit of 2.0°C and the future CO₂ emissions since 2019. The largest variation in our carbon budget estimates is driven by the uncertainty in AER RF, which is incorporated into the probability of achieving the Paris Agreement target and upper limit (see Fig. S21 and the supplement). We include a 10% uncertainty, determined from examination of CMIP5 coupled atmospheric / carbon cycle models from Friedlingstein et al. (2014) and Murphy et al. (2014) (see the supplement for more information), within each probability of attaining the Paris goals to represent how atmospheric CO₂ will respond to the prescribed carbon emissions.

To obtain a 66% likelihood of limiting the rise in future ΔT below 1.5°C, only 790 ± 79 Gt C can be released. For a 66% likelihood of the rise in ΔT staying below the 2.0 °C upper limit, $1,040 \pm 104$ Gt C can be emitted. To place these numbers in their proper perspective, about 640 Gt C have been released from 1870 through the end of 2019 due to land-use change, fossil fuel emissions, gas flaring, and cement production according to the Global Carbon Budget project (Friedlingstein et al., 2019). In our model framework, after 2019 society can therefore only emit 150 ± 79 Gt C to have a 66% chance of limiting warming to 1.5°C. This future emissions estimate rises to 400 ± 104 Gt C to have a 66% chance of limiting warming to 2.0°C.

Table 2. Total cumulative and future carbon emissions that will lead to crossing the Paris temperature thresholds based on the EM-GC trained using the HadCRUT5 ΔT record. Estimates of $\Sigma CO_2^{EMISSIONS}$ that would cause global warming to stay below indicated thresholds for 95%, 66%, and 50% probabilities and are rounded to the nearest 10 Gt C. The values in the top half of the table are the estimates of total cumulative carbon emissions that will lead to crossing the Paris Agreement thresholds with the 10% uncertainty for how atmospheric CO2 responds to prescribed carbon emissions (see text) included. The values in the bottom half of the table are the estimates of future cumulative carbon emissions after 2019 that will lead to crossing the Paris Agreement thresholds, with the same 10% uncertainty. The range of years given represents when the Paris Agreement thresholds will be passed based on the rate of emissions from SSP5-8.5 or continuing the 2019 rate of emissions of 11.7 Gt C yr⁻¹ (Friedlingstein et al., 2019).

Total $\Sigma CO_2^{EMISSIONS}$ since 1870 from the EM-GC			
	95%	66%	50%
1.5°C	730 ± 73 Gt C	790 ± 79 Gt C	830 ± 83 Gt C
2.0°C	920 ± 92 Gt C	1040 ± 104 Gt C	1110 ± 111 Gt C
Future $\Sigma CO_2^{EMISSIONS}$ (assuming 640 Gt C released between 1870-2019)			
	95%	66%	50%
1.5°C	90 ± 73 Gt C	150 ± 79 Gt C	190 ± 83 Gt C
	(2021 ^a -2031 ^a)	(2025-2035)	(2027-2038)
	(2021 ^b -2033 ^b)	(2026-2039)	(2029-2043)
2.0°C	280 ± 92 Gt C	400 ± 104 Gt C	470 ± 111 Gt C
	(2033 ^a -2043 ^a)	(2039-2049)	(2047-2052)
	(2036 ^b -2051 ^b)	(2045-2063)	(2050-2069)

^a Year the 1.5°C target or 2.0°C upper limit will be exceeded assuming the rate of emission inferred from SSP5-8.5 and the 1σ uncertainty. Applies to the 66% and 50% probabilities.

^b Year the 1.5°C target or 2.0°C upper limit will be exceeded assuming the 2019 rate of emission of 11.7 Gt C yr⁻¹ and the 1σ uncertainty Applies to the 66% and 50% probabilities.

An analysis by van Vuuren et al. (2020) assesses remaining carbon budgets based on cumulative emissions after 2010. Their analysis indicates only 228 Gt C can be released after 2010 to have a 66% probability of achieving the Paris Agreement target of limiting the rise in ΔT below 1.5°C in 2100. They
990 base this estimate on an analysis of climate sensitivity and carbon cycle components, including an adjustment to TCRE for the tendency of CMIP5 GCMs to warm too quickly that had been suggested by Millar et al. (2017). We find a 66% probability of limiting warming to 1.5°C upon the release of 250 ± 79 Gt C between 2010 and 2100. Our results are similar to the findings in van Vuuren et al. (2020). Between 2010 and 2019, about 100 Gt C has been released to the atmosphere (Friedlingstein et al., 2019), so the
995 remaining budget after 2019 for limiting warming to 1.5°C is about 128 Gt C according to van Vuuren et al. (2020). The remaining budget from our analysis is 150 ± 79 Gt C. Our analysis and that by van Vuuren et al. (2020) suggest at the pace of emissions in 2019 of 11.7 Gt C yr⁻¹ (Friedlingstein et al., 2019), society will cross this threshold in the next 10 years.

1000 3.3.5 Blended methane

Atmospheric abundances of methane will likely continue to increase as society expands natural gas production and agriculture, making it important to analyze the impact of various methane scenarios on the rise of GMST. It is unlikely future atmospheric methane abundances will progress as indicated by SSP1-2.6 (see Fig. 2), a low radiative forcing scenario. Current observations shown in Fig. 2 illustrate
1005 that the methane mixing ratio is following SSP2-4.5 and has missed the initial decline needed to follow the SSP1-2.6 pathway. To analyze the effect varying future methane abundance pathways will have on GMST, we have generated linear interpolations of the SSP1-2.6 and SSP3-7.0 methane abundances and created four alternate scenarios (see Fig. S22), which we call blended methane scenarios. We can substitute one of the blended methane scenarios into the EM-GC instead of using the projection of
1010 methane specified by the SSP database to quantify the sensitivity of future warming to various evolutions of methane on the rise in GMST.

Figure 13 shows the probability of staying at or below the Paris Agreement target (gold colors) or upper limit (purple colors) for SSP1-2.6 (solid) and SSP4-3.4 (dotted) as a function of the methane mixing

ratio in 2100. The lowest atmospheric methane mixing ratio value in 2100 of 1.15 ppm is from the SSP1-2.6 methane pathway, the highest mixing ratio in 2100 of 3.20 ppm is from the SSP3-7.0 methane pathway. The four in between are the blended methane scenarios. As the atmospheric methane abundance increases, the likelihood of achieving the goals in the Paris Agreement decreases. For SSP1-2.6, the probability of limiting the rise in GMST below the 1.5°C target begins at 53% for HadCRUT5 using the SSP1-2.6 designated methane pathway and decreases as the blended scenarios are considered. The probability of achieving the Paris Agreement target declines to 30% if methane reaches 2.4 ppm in 2100 and to 16% if methane increases to 3.2 ppm in 2100. Even though SSP1-2.6 can have a 53% probability of limiting warming to 1.5°C, achieving this goal can likely only be attained by strict limits on both emissions of carbon dioxide and methane.

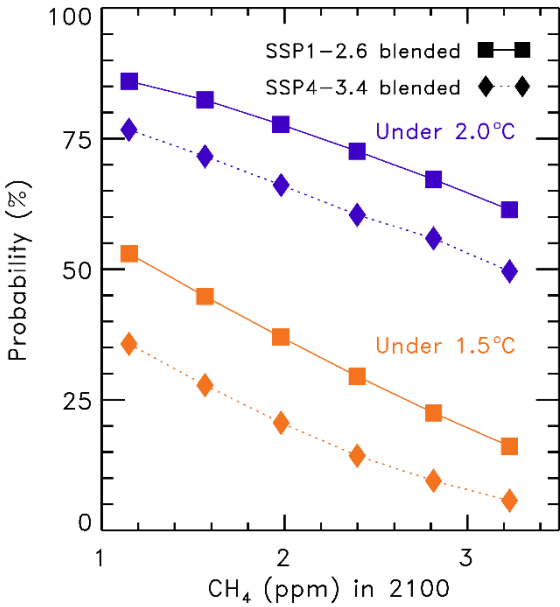


Figure 13. Probability of staying at or below the Paris Agreement target and upper limit for SSP1-2.6 and SSP4-3.4 as a function of varying methane scenarios using the EM-GC trained with the HadCRUT5 ΔT record. The atmospheric methane scenarios are calculated using linear combinations of methane abundances from SSP1-2.6 and SSP3-7.0 to span the range of future methane abundances.

In Sect. 3.3.3, we showed that if all GHGs follow the SSP4-3.4 scenario there would be a 64% probability of limiting warming to 2.0°C. If the methane pathway instead follows SSP1-2.6, which has an end of century mixing ratio of only 1.15 ppm, then the probability of achieving the Paris Agreement goal

rises to 77%. If the methane pathway follows SSP3-7.0 and the end of century mixing ratio increases to 3.2 ppm, then the probability of achieving the Paris Agreement goal declines to 50%.

Reducing the future anthropogenic emissions of methane might be more challenging than
1030 controlling future emissions of carbon dioxide, because methane has such a wide variety of sources related to energy, agriculture, and ruminants (Kirschke et al., 2013). Given the current widespread use of methane as a source of energy in the United States and parts of Europe (Saunio et al., 2020), combined with the continued growth in the global number of ruminants (Wolf et al., 2017), it seems unrealistic for atmospheric methane to follow the peak and sharp decline starting in 2025 of the SSP1-2.6 pathway (Fig.
1035 3b). Our analysis suggests failure to limit methane to the SSP1-2.6 trajectory will have a larger impact on the achievement of the 1.5°C Paris goal compared to the 2.0°C upper limit. Figure 13 is designed to provide some perspective on the importance of limiting the growth of methane in the atmosphere.

3.3.6 Climate feedback

1040 In our analysis above, we have assumed the value of λ_{Σ} (and thus λ , see Eq (3) and corresponding text in Sect. 2.1) is constant over time. Time-constant λ_{Σ} is the simplest assumption one can make. The climate record can be fit very well based on this conjecture, as shown in Fig. 1a. However, many GCMs suggest that climate feedback may vary over time (Dong et al., 2020; Marvel et al., 2018; Rugenstein et al., 2020). An analysis by Goodwin (2018) finds there is a delay in the response of climate feedback to a change in
1045 radiative forcing, on the order of a few days to several decades. In our EM-GC framework, we are able to conduct calculations allowing the value of λ_{Σ} to vary over time with a delay between the change in radiative forcing and the response of λ_{Σ} (~~see Fig. S23 and the supplement for results without the time delay~~), and to project future temperature with such an assumption. Up until this point, our simulations have used time-invariant λ_{Σ} to be consistent with how our model results had been presented in prior
1050 publications (Canty et al., 2013; Hope et al., 2017) as well as several other empirically-based approaches (Chylek et al., 2014; Lean and Rind, 2008, 2009; Zhou and Tung, 2013). Recall from Sect. 2.1 that $\lambda_{\Sigma} = \lambda_P - \lambda$. To assess the effect of time varying climate feedback on our projections of global warming, we examine the sensitivity in terms of λ^{-1} , because this quantity scales proportionally with ΔT and our use of

the inverse λ allows for direct comparison to the results of [Dong et al \(2020\)](#), [Marvel et al. \(2018\)](#), and [Rugenstein et al. \(2020\)](#).

Figure 14 shows the change in observed and modeled GMST [for an EM-GC simulation training to the HadCRUT5 GMST record and using an AER RF time series with a value of \$\text{AER RF}_{2011} = -0.9 \text{ W m}^{-2}\$](#) under four assumptions ~~regarding for~~ λ^{-1} , [all for SSP2-4.5 \(solid lines\)](#). First, the value of λ^{-1} is constant over time (Figs. 14a, e). Second, the value of λ^{-1} ~~varies rises~~ by 50% between 1850-2100 (Figs. 14b, f; further discussion of Fig. 14b and f will occur at the end of ~~the this~~ section). The third assumption ~~involves allows~~ λ^{-1} ~~to vary~~ over time while χ^2_{RECENT} is always less than or equal to two (Figs 14c, g). Fourth, λ^{-1} varies over time while χ^2_{ATM} is always less than or equal to two (Figs. 14d, h). ~~In all cases for time varying feedback, we also assume the value of λ^{-1} has the same shape as the SSP4-3.4 RF time series along with a lag of 20 years~~ [We also assume and that](#) the new time series for λ^{-1} maintains an average value over the observational record identical to the constant value ~~for λ^{-1} of $0.63\text{--}64 \text{ }^{\circ}\text{C W}^{-1} \text{ m}^{-2}$~~ [of \$0.63\text{--}64 \text{ }^{\circ}\text{C W}^{-1} \text{ m}^{-2}\$](#) . ~~We use a lag~~ [We chose a lag of 20–32.5 years to represent the longest mean value of the slowest delay in response of the climate system to a RF perturbation reported by Goodwin \(2018\), which is associated with clouds and spatial adjustments of SST \(32.5 years is the average of 20 and 45 years, the minimum and maximum values of the slowest response given in his Table 1\). Figure S23 is identical to Fig. 14, except for the use of no delay between the RF perturbations and the response of climate feedback. The use of the response delays shorter than 32.5 years will result in projections between those shown in Fig. S23 and Fig. 14.](#) ~~climate feedback to a change in RF suggested by Goodwin (2018). If we use the shorter delays represented in Goodwin (2018), then our results would be between those from the instantaneous response of climate feedback to a change in RF (Fig. S23) and the 20 year delay. Finally, in the simulations described below, the value of λ^{-1} is assumed to continue to rise into the future at the same proportionality to $\Delta T_{\text{ATM,HUMAN}}$ as the prior increase.~~

[In Figs. 14 and S23 we also analyze a RF scenario termed SSP2-4.5' that serves as a doubled \$\text{CO}_2\$ scenario \(dotted lines\). For SSP2-4.5', the RFs due to all GHGs other than \$\text{CO}_2\$ as well as tropospheric aerosols from the start of 2020 onwards are held constant at end of 2019 values. The only component of RF allowed to vary after the start of 2020 is \$\text{CO}_2\$. The RF of climate due to all GHGs and tropospheric aerosols for SSP2-4.5' is identical to that in SSP2-4.5 from the start of the simulation until the end of](#)

2019. Since the mixing ratio of CO₂ at the end of century is 566 ppm, the warming found at the end of century for SSP2-4.5' serves as the transient response of ΔT to rising CO₂ in our model framework. The fact that projections of ΔT found allowing only for future increases in CO₂ (dotted lines) agree so closely with those found assuming changes in RF due to all GHGs and tropospheric aerosols (solid lines) means that under the AER RF₂₀₁₁ = -0.9 W m⁻² scaling assumption, the future change in RF due to all agents other than CO₂ nearly cancel. Projections found using the original SSP2-4.5 scenario may serve as a useful surrogate for a double CO₂ simulation. Figures S24 and S25 are the same as Fig. 14, except for the use of AER RF₂₀₁₁ values of -0.4 and -1.5 W m⁻², respectively. There are slight departures between the SSP2-4.5 and SSP2-4.5' projections of ΔT for these alternate aerosol scaling assumptions. Nonetheless, these projections are quite similar because the future decline in RF due to the assumption of declining CH₄ within SSP2-4.5 nearly balances the future increase in RF due to N₂O and all of the minor GHGs.

We fit the climate record over the past 170 years (χ^2_{ATM}) and past 80 years (χ^2_{RECENT}) extremely well for constant λ^{-1} (Fig. 14a, e). If we allow the value of λ^{-1} to scale with anthropogenic forcing by as much as possible such that the maximum value of χ^2_{RECENT} is always less than or equal to two, we obtain the result shown in Figs. 14c, f. This ~~scaling of λ^{-1} simulation~~ results in an increase in λ^{-1} by nearly a factor of two in 2100 and a value of ΔT₂₁₀₀ of 2.83.4°C, about 1.0°C higher than when a constant value of λ^{-1} is used ~~and an increase in λ^{-1} by nearly a factor of two in 2100. The modeled change in GMST starts to deviate from the observations around year 2010. This deviation is seen in the residual between modeled and observed GMST in Fig. 14g.~~ If we allow the value of λ^{-1} to scale with anthropogenic forcing as much as possible ~~such~~ that the maximum value of χ^2_{ATM} is less than or equal to two, we arrive at the result shown in Figs. 14d, h. This ~~variation in λ^{-1} simulation~~ yields a rise in λ^{-1} over two and a half centuries by a factor of 2.9 and a value of ΔT₂₁₀₀ of 3.54.2°C that is nearly double the estimate of ΔT₂₁₀₀ for the time invariant λ^{-1} (Fig 14a) ~~and a rise in λ^{-1} over two and a half centuries by a factor of 3.5.~~ The modeled change in ΔTGMST starts to deviate from observations around year 20051960 and persistently disagrees with the data out to present time (Fig. 14h). ~~The deviation is seen in the residual between modeled and observed GMST in Fig. 14h. This simulation results in a χ^2_{RECENT} value in Fig. 14h is of 3.8589, which does not satisfy our reduced chi-squared constraints indicates poor agreement with observations.~~

Several other studies have investigated the degree-amount of change in λ^{-1} . Marvel et al. (2018) suggest that the increase in the median value of ECS from the CMIP5 GCMs between the historical and abrupt 4xCO₂ simulations may be driven by an increase in ~~rise due to time varying~~ λ^{-1} ~~increasing from 1850-2100 by of~~ 28 to 72%. Rugenstein et al. (2020) estimates a median increase of 17% for values of ECS from ~~CMIP6-CMIP5~~ GCMs when examining millennial length simulations compared to the 150-year Gregory et al. (2004) method, which is consistent with about an 11% rise in λ^{-1} (Fig. 2b of Rugenstein et al. (2020)). An analysis by Dong et al. (2020) estimates a median increase in λ of +0.4 W m⁻² K⁻¹, which corresponds to a 50% increase in λ^{-1} (Fig. 1c, d of Dong et al. (2020)). Consequently, A doubling (Fig. 14c) or almost tripling of λ^{-1} (Fig. 14d) over two and a half centuries is ~~faster-larger~~ than the increase indicated by Marvel et al. (2018) and Dong et al. (2020) and the millennia order timescale in Sect. 12.5.3 of IPCC 2013 and Rugenstein et al. (2020). An increase in λ^{-1} of 50% or lower ~~in λ^{-1}~~ (Fig. 14b) is in line with the estimate of the change in ECS due to time-variant λ^{-1} indicated by Dong et al. (2020), Marvel et al. (2018), and Rugenstein et al. (2020). ~~The use of a 20-year delay in the response of the feedback to a change in RF results in good fits to the HadCRUT5 GMST record (Fig. 14b). However, we are not able to achieve as low values of χ^2_{RECENT} and χ^2_{ATM} to this record for time variant feedback if we assume an instantaneous response (Fig. 14 a-d versus Fig. S23 a-d).~~

Allowing λ^{-1} to increase over time introduces important, additional uncertainty to our estimate of ECS. We denote values of ECS found using time-variant λ^{-1} as $\text{ECS}_{\lambda(t)}$. Our best estimate of $\text{ECS}_{\lambda(t)}$ is 3.08°C (range of 2.23 to 5.53°C), which is derived from model results shown in Fig. 14b (AER RF₂₀₁₁ = -0.9 W m⁻²), Fig. S24b (AER RF₂₀₁₁ = -0.4 W m⁻²), and Fig. S25c (AER RF₂₀₁₁ = -1.5 W m⁻²). For this new estimate of $\text{ECS}_{\lambda(t)}$, we allow λ^{-1} to increase by 50% or rise as much as possible and still achieve a value of χ^2_{RECENT} less than or equal to two. Simulations with strong aerosol cooling (AER RF₂₀₁₁ = -1.5 W m⁻²) cannot have λ^{-1} rise by 50% and maintain a good fit to the climate record over the past 80 years (Fig. S25b, f). Our best estimate of $\text{ECS}_{\lambda(t)}$ of 3.08°C (range of 2.23 to 5.53°C) for a 32.5-year delay is similar to the value of ECS reported by Goodwin (2018) for a 100-year response time (2.9°C; range of 2.3 to 3.6°C).

The assumption of constant feedback within the EM-GC framework used in the rest of the manuscript is reasonable because there is no strong evidence from the climate record for a noticeable increase in λ^{-1} on the multidecadal time scale associated with the simulations in Fig. 14. Assuming climate feedback is constant over time results in the best fits to the climate record for both of our χ^2 constraints.

140 If the true value of λ^{-1} actually rises over time as suggested by ~~some of~~ the CMIP6 (Dong et al., 2020) and CMIP5 GCMs (Marvel et al., 2018; Rugenstein et al., 2020), our projections of global warming would be a few tenths of a degree warmer than our current best estimates assuming constant λ^{-1} , as shown in Fig. 14b. If λ^{-1} is allowed to increase by 50%, our best estimate of ECS would rise from 2.33 to 3.08°C, which is a 32% increase. Time variant λ^{-1} introduces additional uncertainty into our estimates of ECS;

145 however, the largest uncertainty is still due to the imprecise knowledge of the RF due to tropospheric aerosols. Increasing λ^{-1} by 50% results in a similar value of ΔT_{2100} as when utilizing a higher value of AER RF_{2011} (i.e. AER RF_{2011} less than -0.9 W m^{-2}) in the EM-GC framework.

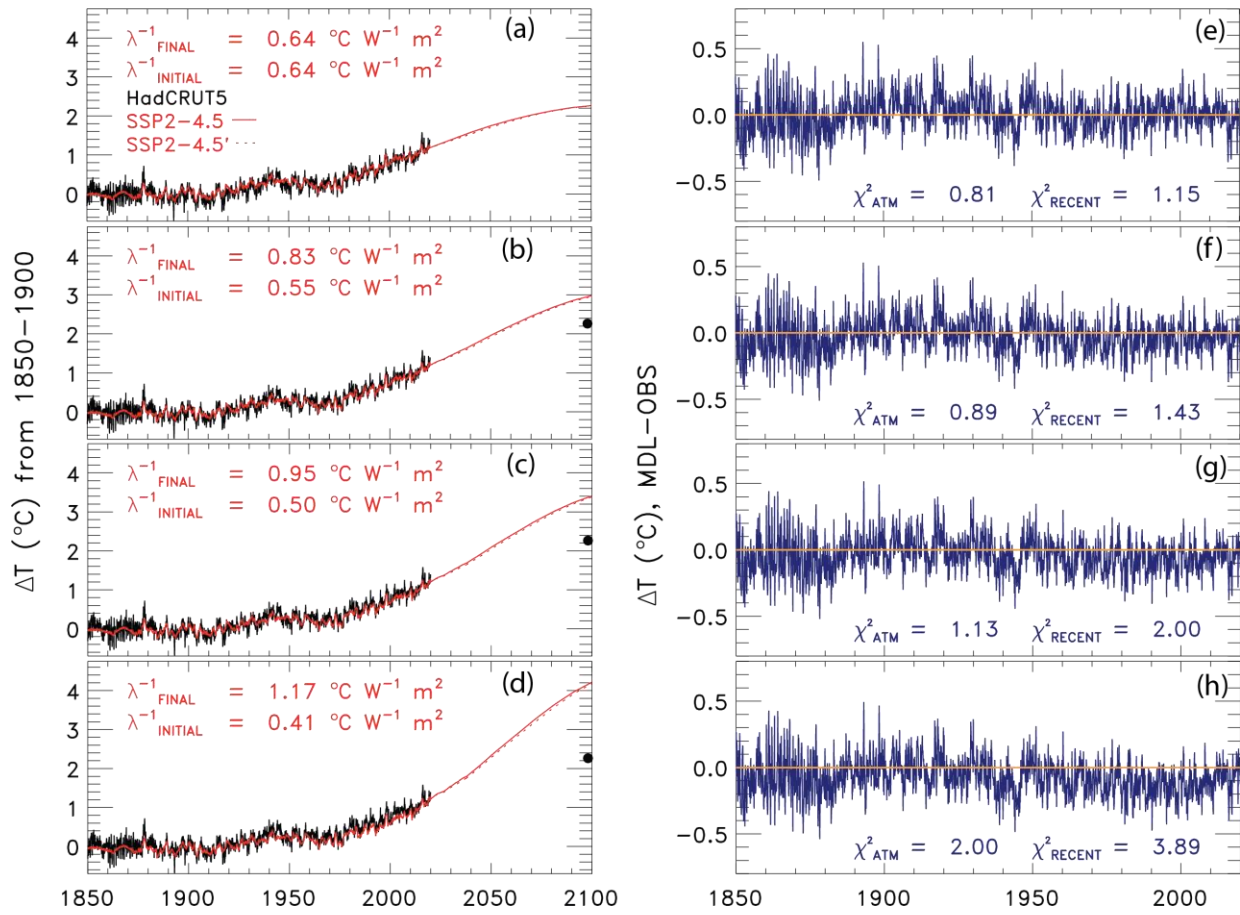


Figure 14. Change in GMST from 1850-2019 for observations from HadCRUT5 (black) and 1850-2100 for modeled (red) using SSP4-3.42-4.5 and a value of AER RF₂₀₁₁ = -0.9 W m⁻² and the residual between modeled and observations incorporating a 2032.5-year delay between λ⁻¹ and a change in RF. The solid line denotes a simulation for the original SSP2-4.5 scenario and the dashed line indicates the SSP2-4.5' simulation (see text). (a) Rise in GMST assuming a constant value of λ⁻¹. (b) Rise in GMST allowing λ⁻¹ to increase by 50%. (c) Rise in GMST allowing λ⁻¹ to vary while the value of χ²_{RECENT} is kept below 2. (d) Rise in GMST allowing λ⁻¹ to vary while the value of χ²_{ATM} is kept below 2. (e) Residual between modeled and observed rise in GMST from 1850-2019 for constant λ⁻¹. (f) Same as (e) but for increasing λ⁻¹ by 50%. (g) Same as (f) but for varying λ⁻¹ while the value of χ²_{RECENT} is kept below 2. (h) same as (g) but for varying λ⁻¹ while the value of χ²_{ATM} is kept below 2.

4 Conclusions

In this paper we use a multiple linear regression energy balance model (EM-GC), to analyze and project changes in the future rise in global mean surface temperature (GMST), calculate the attributable anthropogenic warming rate (AAWR, the component of the rise in GMST caused by human activities) over the past four decades, and compute the equilibrium-effective climate sensitivity (ECS, the rise in

GMST that would occur ~~after climate has equilibrated~~ with atmospheric CO₂ at the 2×pre-industrial level
155 ~~assuming constant climate feedback~~). Projections of the rise in GMST (ΔT) are conducted for seven of
the Shared Socioeconomic Pathway (SSP) projections of GHGs (O'Neill et al., 2017). We compare
computations of AAWR, ECS, and projections of ΔT to values for each quantity computed from archived
output provided by GCMs as part of CMIP6 (Eyring et al., 2016). A critical component of our study is
comprehensive analysis of uncertainties in AAWR, ECS, and projections of ΔT in our EM-GC
1160 framework, due to the rather large uncertainty in radiative forcing of climate from tropospheric aerosols
(AER RF).

The median value of AAWR from 1975-2014 computed using our EM-GC constrained by the
century and a half long record for GMST provided by HadCRUT5 is 0.157°C ~~decade⁻¹/decade~~ and the
5th, and 95th percentiles are 0.120 and 0.195°C ~~decade⁻¹/decade~~, respectively. The median value of AAWR
165 from the CMIP6 multi-model ensemble is 0.221°C ~~decade⁻¹/decade~~ and the 5th, and 95th percentiles are
0.151 and 0.299°C ~~decade⁻¹/decade~~, respectively. We show that the component of GMST attributed to
human activity within the CMIP6 multi-model ensemble warms considerably faster than observations
over the past four decades, a result that is consistent with recent analyses of output from the CMIP6 multi-
model ensemble (CONSTRAIN, 2020; Tokarska et al., 2020b) as well as output from CMIP5 GCMs
1170 assessed in AR5 (i.e, Fig. 11.25b of Kirtman et al. (2013)). This finding differs from the conclusion of
Hausfather et al. (2020), who showed fairly good agreement between projections of global warming from
GCMs and observed ΔT . As detailed in Sect. 3.1, this paper examined GCMs that proceeded CMIP5 and
examined ΔT for a time period that ends in 2017, a time when global temperature was influenced by a
strong ENSO event that ended in 2016. The majority of the uncertainty in our EM-GC based estimate of
1175 AAWR is due to imprecise knowledge of the true value of AER RF.

In our model framework, the best estimate of ECS is 2.33°C and the 5th and 95th percentiles are
1.40 and 3.57°C, respectively. The median value of ECS from the CMIP6 multi-model ensemble is
3.74°C, which is around 1.6 times the best estimate value of ECS inferred from the observed climate
record. The 5th and 95th percentiles of ECS from the CMIP6 multi-model ensemble are 2.19 and 5.65°C,
1180 respectively. We obtain a wide range of ECS values using the EM-GC because of the uncertainty in AER

RF. With an AER RF_{2011} equal to -1.6 W m^{-2} , the EM-GC calculates a value of ECS similar to the maximum value of ECS from the CMIP6 multi-model mean. We cannot rule out the very high value of ECS, but we assign a low probability based on the IPCC 2013 low likelihood for the needed value of AER RF_{2011} . Our empirically based determination of ECS is in good overall agreement with the recent
1185 empirical determinations of Lewis and Grünwald (2018) (1.87°C , range of $1.1\text{--}4.05^{\circ}\text{C}$) and Skeie et al. (2018) (2.0°C , range of $1.2\text{--}3.1^{\circ}\text{C}$) and the slightly older empirically determination reported by Otto et al. (2013) (2.0°C , range of $1.2\text{--}3.9^{\circ}\text{C}$) (all range values are for the 5th and 95th percent confidence interval). A recent review of climate feedback and climate sensitivity published by Sherwood et al. (2020) reported ECS lies within the range of 2.3 to 4.7°C at the 5th to 95th percent confidence intervals; their lower bound
1190 for ECS is quite a bit higher than the lower bound found in our analysis, as well as by Cox et al. (2018), Dessler et al. (2018), Lewis and Grünwald (2018), Nijssse et al. (2020), Otto et al. (2013), Skeie et al. (2018), and Tokarska et al. (2020b). Our best estimate of ECS increases to 3.08°C (range of 2.23 to 5.53°C) if we allow climate feedback to rise over time, with the largest uncertainty in ECS still driven by the imprecise knowledge of the RF due to tropospheric aerosols.

1195 We also examined the probability of limiting the future rise in GMST below the Paris Agreement target of 1.5°C and upper limit of 2.0°C . Our probabilistic forecasts of projections of ΔT include a comprehensive treatment of the uncertainty in AER RF, a capability outside the scope of the GCM intercomparisons conducted for CMIP6. Our analysis indicates that if GHGs were to follow the SSP1-2.6 pathway, there would be a 53% likelihood that the rise in ΔT would remain below the Paris Agreement
1200 target of 1.5°C (relative to pre-industrial) by the end of century based on HadCRUT5. We find that the SSP4-3.4 scenario provides a 64% likelihood of limiting global warming to below the Paris Agreement upper limit of 2.0°C by end of century. These probabilities have declined upon our use of HadCRUT5 compared to the GMST record of HadCRUT4 to 64% and 74% for the SSP1-2.6 and SSP4-3.4 scenarios, respectively. In contrast, the CMIP6 multi-model mean only suggests a 18% probability of achieving the
1205 Paris Agreement target for SSP1-2.6 and a 17% probability of attaining the Paris Agreement goal for SSP4-3.4. The lower probabilities suggested by the CMIP6 multi-model ensemble is not surprising, given the tendency of most CMIP6 GCMs to warm faster observations over the past four decades. Our

projections of ΔT using a physically based model tied to observations of ocean heat content, quantification of natural as well as anthropogenic drivers of variations in GMST, and consideration of uncertainty in AER RF are shown to be remarkably similar to the expert assessment of the future rise in GMST that was sketched out in Fig. 11.25b of AR5 (Kirtman et al., 2013), and the empirically-based filtering of CMIP6 model output recently published by Tokarska et al. (2020b). Finally and most importantly, our estimates are based on the assumption that climate feedback has been and will continue to remain constant over time, since the prior temperature record can be fit so well under this assumption. As described in Section 3.3.6, if climate feedback rises over time, larger warming will be realized than that found under this assumption of temporally invariant feedback.

We also quantify the sensitivity of the probability of achieving the Paris Agreement target (1.5°C) or upper limit (2.0°C) to future atmospheric abundances of methane. The end of century mixing ratio of methane in the SSP1-2.6 scenario is 1.15 ppm, considerably less than the contemporary abundance of 1.88 ppm. The likelihood of attaining the 1.5°C target for SSP1-2.6 decreases as future methane emissions increase, declines to 30% if methane reaches 2.4 ppm in 2100 and to 16% if methane increases to 3.2 ppm at end of century. Our analysis described in Sect. 3.3.5 demonstrates that major near-term limits on the future growth of methane are especially important for achievement of the 1.5°C limit to future warming that constitutes the goal of the Paris Agreement.

Finally, we have also quantified in the EM-GC framework the remaining budgets of carbon (i.e., CO_2) emissions that can occur while attaining either the goal or upper limit of the Paris Agreement. We find that after 2019, society can only emit another 150 ± 79 Gt C to have a 66% likelihood of limiting warming to 1.5°C . This future emissions estimate rises to 400 ± 104 Gt C to have a 66% probability of limiting warming to 2.0°C . Given the anthropogenic emissions of carbon due to combustion of fossil fuels, cement production, gas flaring, and land-use change were about 11.7 Gt C per year in 2019 (Friedlingstein et al., 2019), our study indicates that the target (1.5°C warming) of the Paris Agreement will not be achieved unless carbon emissions are severely curtailed in the next 10 years.

We conclude by noting that the CMIP6 multi-model ensemble provides many useful parameters such as sea level rise, sea ice decline, and precipitation changes, that provide a great societal understanding of the impact of climate change. We do not mean to undermine the importance of the

CMIP6 GCMs by this analysis. Rather, we hope that studies such as this, along with other recent evaluations of CMIP6 multi-model output such as Nijssse et al. (2020) and Tokarska et al. (2020b) will provide improved use of the CMIP6 multi-model ensemble for policy decisions. Our EM-GC was built to specifically simulate and project changes in GMST; we do not examine numerous other components of the climate system that affect society. We emphasize that our projections show that unless society can implement steep reductions in the emissions of carbon (CO₂) and methane (CH₄) in the next 10 years, 1.5°C global warming goal of the Paris Agreement will not be achieved.

5 Acronyms

- 1245 AAWR – Attributable anthropogenic warming rate
- AR4 – Fourth Assessment Report
- AER – Anthropogenic aerosols
- AER RF₂₀₁₁ – Radiative forcing due to anthropogenic aerosols in 2011
- AMOC – Atlantic meridional overturning circulation
- 1250 AMV – Atlantic multidecadal variability
- BEG – Berkley Earth Group
- CALIPSO – Cloud-Aerosol Lidar and Infrared Pathfinder Satellite Observations
- CMIP5 – Coupled Model Intercomparison Project Phase 5
- CMIP6 – Coupled Model Intercomparison Project Phase 6
- 1255 COBE - Centennial in situ Observation-Based Estimate
- CW14 – Cowtan and Way (2014) temperature record
- ECS – ~~Equilibrium~~-Effective climate sensitivity
- ECS_{λ(t)} – Effective climate sensitivity, time dependent feedback
- EM-GC – Empirical Model of Global Climate
- 1260 ENSO – El Niño Southern Oscillation
- GCM – General Circulation Model
- GHG – Greenhouse gas
- GISTEMP – Goddard Institute for Space Studies Surface Temperature Analysis v4

GloSSAC – Global Space-based Stratospheric Aerosol Climatology

1265 GMST – Global mean surface temperature

HadCRUT – Hadley Center Climatic Research Unit

IPCC – Intergovernmental Panel on Climate Change

ISCCP – International Satellite Cloud Climatology Project

IOD – Indian Ocean dipole

1270 LIN – Linear method

LUC – Land-use change

MEI – Multivariate ENSO index

NOAAGT – National Center for Environmental Information NOAA GlobalTemp v5

ODS – Ozone depleting substances

1275 OHC – Ocean heat content

OHE – Ocean heat export

PATMOS-X - Pathfinder Atmospheres Extended

PDO – Pacific decadal oscillation

RCP – Representative concentration pathway

1280 REG – Regression method

RF – Radiative forcing

SAOD – Stratospheric aerosol optical depth

SORCE – Solar Radiation and Climate Experiment

SSP – Shared Socioeconomic Pathway

1285 SST – Sea surface temperature

TAR – Third Assessment Report

TAS – Near surface air temperature

TCRE – Transient climate response to cumulative emissions

TOS – Temperature at the interface of the atmosphere and the upper boundary of the ocean

1290 TSI – Total solar irradiance

6 Data availability

All data used as inputs into the EM-GC are available from resources on the web. We have provided the links to the resources below. The data are also available along with the EM-GC output ~~data~~ used in this analysis at <https://doi.org/10.5281/zenodo.4300780> (McBride et al., 2021) on Zenodo.org.

IOD: The COBE SST data is provided by the NOAA ESRL physical sciences division from their web site <https://www.esrl.noaa.gov/psd/>.

Tropospheric ozone RF: <http://www.pik-potsdam.de/~mmalte/rcps/> .

MEI.v2 and MEI.ext: <https://psl.noaa.gov/enso/mei/data/meiv2.data> and <https://psl.noaa.gov/enso/mei.ext/table.ext.html>

PDO: <http://research.jisao.washington.edu/pdo/PDO.latest.txt>

SAOD: <https://eosweb.larc.nasa.gov/project/glossac/glossac>

TSI: <http://lasp.colorado.edu/home/sorce/data/tsi-data/>

OHC Records:

Balmaseda: <http://www.cgd.ucar.edu/cas/catalog/ocean/OHC700m.tar.gz>

Carton: https://www.atmos.umd.edu/~ocean/index_files/soda3_readme.htm

Cheng: <http://159.226.119.60/cheng/>

Ishii: <http://159.226.119.60/cheng/>

Levitus: https://www.nodc.noaa.gov/OC5/3M_HEAT_CONTENT/

SSP Database: All information for the SSPs obtained from the SSP database is at <https://tntcat.iiasa.ac.at/SspDb/dsd?Action=htmlpage&page=about> .

CMIP6 Input Data:

https://docs.google.com/document/d/1pU9IiJvPJwRvIgVaSDdJ4O0Jeorv_2ekEttd34K9cA/edit#heading=h.jdoykiw7tpen

CMIP6 Model Output Archive: <https://esgf-node.llnl.gov/search/cmip6/>

7 Author Contribution

LAM, APH, and TPC developed the model code used in this analysis, LAM, APH, and BFB
1330 collected data, RJS supervised, administrated, and developed the project, LAM wrote the original draft,
and RJS, APH, BFB, TPC, and WRT participated in the review and editing of the manuscript.

8 Competing Interests

The authors declare that they have no conflict of interest.

1335

9 Acknowledgements

We would like to acknowledge the World Climate Research Programme for coordinating and
promoting CMIP6 through its Working Group on Coupled Modelling. We thank the climate modeling
groups participating in CMIP6 for producing and making their model results available, the Earth System
1340 Grid Federation (ESGF) for archiving the data and providing access, and the several funding agencies
who support ESGF and CMIP6. This project could not occur without the results from CMIP6. We
appreciate very much financial support from the NASA Climate Indicators and Data Products for Future
National Climate Assessments (INCA) program (award NNX16AG34G). This study was partially
supported by NOAA grants NA14NES4320003 and NA19NES4320002 (Cooperative Institute for
1345 Satellite Earth System Studies - CISESS) at the University of Maryland/ESSIC. We thank University of
Maryland Undergraduate Lauren Borgia for participating in extensive, in-depth discussions of recent
papers on cloud feedback and climate sensitivity. Finally, we thank both reviewers for very careful reads
of the original paper that led to substantial improvements in the manuscript, as well as Martin Stolpe for
contacting us privately, while the paper was in discussion, regarding an erroneous description of the effect
1350 of creating blended near surface air temperature that had appeared in the submitted paper.

10 References

- Arfeuille, F., Weisenstein, D., MacK, H., Rozanov, E., Peter, T. and Brönnimann, S.: Volcanic forcing for climate modeling:
A new microphysics-based data set covering years 1600-present, *Clim. Past*, 10(1), 359–375, doi:10.5194/cp-10-359-
2014, 2014.
- 1355 Armour, K. C.: Energy budget constraints on climate sensitivity in light of inconstant climate feedbacks, *Nat. Clim. Chang.*,
7(5), 331–335, doi:10.1038/nclimate3278, 2017.
- Balmaseda, M. A., Trenberth, K. E. and Källén, E.: Distinctive climate signals in reanalysis of global ocean heat content,

Geophys. Res. Lett., 40(9), 1754–1759, doi:10.1002/grl.50382, 2013.

- 1360 Barnett, T. P., Pierce, D. W., Latif, M., Dommenges, D. and Saravan, R.: Interdecadal interactions between the tropics and midlatitudes in the Pacific basin, *Geophys. Res. Lett.*, 26(5), 615–618, 1999.
- Bond, T. C., Doherty, S. J., Fahey, D. W., Forster, P. M., Berntsen, T., Deangelo, B. J., Flanner, M. G., Ghan, S., Kärcher, B., Koch, D., Kinne, S., Kondo, Y., Quinn, P. K., Sarofim, M. C., Schultz, M. G., Schulz, M., Venkataraman, C., Zhang, H., Zhang, S., Bellouin, N., Guttikunda, S. K., Hopke, P. K., Jacobson, M. Z., Kaiser, J. W., Klimont, Z., Lohmann, U., Schwarz, J. P., Shindell, D., Storelvmo, T., Warren, S. G. and Zender, C. S.: Bounding the role of black carbon in the climate system: A scientific assessment, *J. Geophys. Res. Atmos.*, 118(11), 5380–5552, doi:10.1002/jgrd.50171, 2013.
- 1365 Bony, S., Colman, R., Kattsov, V. M., Allan, R. P., Bretherton, C. S., Dufresne, J. L., Hall, A., Hallegatte, S., Holland, M. M., Ingram, W., Randall, D. A., Soden, B. J., Tselioudis, G. and Webb, M. J.: How well do we understand and evaluate climate change feedback processes?, *J. Clim.*, 19(15), 3445–3482, doi:10.1175/JCLI3819.1, 2006.
- 1370 Calvin, K., Bond-Lamberty, B., Clarke, L., Edmonds, J., Eom, J., Hartin, C., Kim, S., Kyle, P., Link, R., Moss, R., McJeon, H., Patel, P., Smith, S., Waldhoff, S. and Wise, M.: The SSP4: A world of deepening inequality, *Glob. Environ. Chang.*, 42, 284–296, doi:10.1016/j.gloenvcha.2016.06.010, 2017.
- Canty, T., Mascioli, N. R., Smarte, M. D. and Salawitch, R. J.: An empirical model of global climate – Part 1: A critical evaluation of volcanic cooling, *Atmos. Chem. Phys.*, 13(8), 3997–4031, doi:10.5194/acp-13-3997-2013, 2013.
- 1375 Carpenter, L. J., Daniel, J. S. (Lead A., Fleming, E. L., Hanaoka, T., Ravishankara, A. R., Ross, M. N., Tilmes, S., Wallington, T. J. and Wuebbles, D. J.: Scenarios and information for policymakers., 2018.
- Carton, J. A., Chepurin, G. A. and Chen, L.: SODA3: A New Ocean Climate Reanalysis, *J. Clim.*, 31(17), 6967–6983, doi:10.1175/jcli-d-18-0149.1, 2018.
- Charette, M. A. and Smith, W. H. F.: The Volume of Earth ’ s Ocean, *Oceanography*, 23(2), 112–114, 2010.
- 1380 Chen, X. and Tung, K. K.: Global surface warming enhanced by weak Atlantic overturning circulation, *Nature*, 559(7714), 387–391, doi:10.1038/s41586-018-0320-y, 2018.
- Cheng, L., Trenberth, K. E., Fasullo, J., Boyer, T., Abraham, J. and Zhu, J.: Improved estimates of ocean heat content from 1960 to 2015, *Sci. Adv.*, 3(3), 1–11, doi:10.1126/sciadv.1601545, 2017.
- Church, J. A., White, N. J., Konikow, L. F., Domingues, C. M., Graham Cogley, J., Rignot, E., Gregory, J. M., Van Den Broeke, M. R., Monaghan, A. J. and Velicogna, I.: Revisiting the Earth’s sea-level and energy budgets from 1961 to 1385 2008, *Geophys. Res. Lett.*, 40(15), 4066, doi:10.1002/grl.50752, 2013.
- Chylek, P., Klett, J. D., Lesins, G., Dubey, M. K. and Hengartner, N.: The Atlantic Multidecadal Oscillation as a dominant factor of oceanic influence on climate, *Geophys. Res. Lett.*, 1689–1697, doi:10.1002/2014GL059274. Received, 2014.
- CONSTRAIN: ZERO IN ON: A new generation of climate models, COVID-19 and the Paris Agreement, CONSTRAIN Proj. Annu. Rep. 2020, doi:10.5281/zenodo.428461, 2020.
- 1390 Cowtan, K. and Way, R. G.: Coverage bias in the HadCRUT4 temperature series and its impact on recent temperature trends, *Q. J. R. Meteorol. Soc.*, 140(683), 1935–1944, doi:10.1002/qj.2297, 2014.
- Cowtan, K., Hausfather, Z., Hawkins, E., Jacobs, P., Mann, M. E., Miller, S. K., Steinman, B. A., Stolpe, M. B. and Way, R. G.: Robust comparison of climate models with observations using blended land air and ocean sea surface temperatures, *Geophys. Res. Lett.*, 42(15), 6526–6534, doi:10.1002/2015GL064888, 2015.
- 1395 Cox, P. M., Huntingford, C. and Williamson, M. S.: Emergent constraint on equilibrium climate sensitivity from global temperature variability, *Nature*, 553(7688), 319–322, doi:10.1038/nature25450, 2018.
- Dessler, A. E., Mauritsen, T. and Stevens, B.: The influence of internal variability on Earth’s energy balance framework and implications for estimating climate sensitivity, *Atmos. Chem. Phys.*, 18(7), 5147–5155, doi:10.5194/acp-18-5147-2018, 2018.
- 1400 Dlugokencky, E.: Trends in Atmospheric Methane, [online] Available from: www.esrl.noaa.gov/gmd/ccgg/trends_ch4/, 2020.
- Dlugokencky, E. and Tans, P.: Trends in Atmospheric Carbon Dioxide, [online] Available from: www.esrl.noaa.gov/gmd/ccgg/trends/, 2020.
- Domingues, C. M., Church, J. A., White, N. J., Gleckler, P. J., Wijffels, S. E., Barker, P. M. and Dunn, J. R.: Improved estimates of upper-ocean warming and multi-decadal sea-level rise, *Nature*, 453(7198), 1090–1093, doi:10.1038/nature07080, 2008.
- 1405 Dong, Y., Armour, K. C., Zelinka, M. D., Proistosescu, C., Battisti, D. S., Zhou, C. and Andrews, T.: Intermodel spread in the pattern effect and its contribution to climate sensitivity in CMIP5 and CMIP6 models, *J. Clim.*, 33(18), 7755–7775,

doi:10.1175/JCLI-D-19-1011.1, 2020.

- 1410 Douglass, D. H. and Knox, R. S.: Climate forcing by the volcanic eruption of Mount Pinatubo, *Geophys. Res. Lett.*, 32(5), 1–5, doi:10.1029/2004GL022119, 2005.
- Dudok de Wit, T., Kopp, G., Fröhlich, C. and Schöll, M.: Methodology to create a new total solar irradiance record: Making a composite out of multiple data records, *Geophys. Res. Lett.*, 44(3), 1196–1203, doi:10.1002/2016GL071866, 2017.
- England, M. H., McGregor, S., Spence, P., Meehl, G. A., Timmermann, A., Cai, W., Gupta, A. Sen, Mcphaden, M. J., Purich, A. and Santos, A.: Recent intensification of wind-driven circulation in the Pacific and the ongoing warming hiatus, *Nat. Clim. Chang.*, 4(3), 222–227, doi:10.1038/nclimate2106, 2014.
- 1415 Eyring, V., Bony, S., Meehl, G. A., Senior, C. A., Stevens, B., Stouffer, R. J. and Taylor, K. E.: Overview of the Coupled Model Intercomparison Project Phase 6 (CMIP6) experimental design and organization, *Geosci. Model Dev.*, 9(5), 1937–1958, doi:10.5194/gmd-9-1937-2016, 2016.
- Forster, P. M., Maycock, A. C., McKenna, C. M. and Smith, C. J.: Latest climate models confirm need for urgent mitigation, *Nat. Clim. Chang.*, 10(1), 7–10, doi:10.1038/s41558-019-0660-0, 2020.
- 1420 Foster, G. and Rahmstorf, S.: Global temperature evolution 1979–2010, *Environ. Res. Lett.*, 6(4), 044022, doi:10.1088/1748-9326/6/4/044022, 2011.
- Foster, M. J. and Heidinger, A.: PATMOS-x: Results from a diurnally corrected 30-yr satellite cloud climatology, *J. Clim.*, 26(2), 414–425, doi:10.1175/JCLI-D-11-00666.1, 2013.
- 1425 Fricko, O., Havlik, P., Rogelj, J., Klimont, Z., Gusti, M., Johnson, N., Kolp, P., Strubegger, M., Valin, H., Amann, M., Ermolieva, T., Forsell, N., Herrero, M., Heyes, C., Kindermann, G., Krey, V., McCollum, D. L., Obersteiner, M., Pachauri, S., Rao, S., Schmid, E., Schoepp, W. and Riahi, K.: The marker quantification of the Shared Socioeconomic Pathway 2: A middle-of-the-road scenario for the 21st century, *Glob. Environ. Chang.*, 42, 251–267, doi:10.1016/j.gloenvcha.2016.06.004, 2017.
- 1430 Friedlingstein, P., Meinshausen, M., Arora, V. K., Jones, C. D., Anav, A., Liddicoat, S. K. and Knutti, R.: Uncertainties in CMIP5 climate projections due to carbon cycle feedbacks, *J. Clim.*, 27(2), 511–526, doi:10.1175/JCLI-D-12-00579.1, 2014.
- Friedlingstein, P., Jones, M. W., Sullivan, M. O., Andrew, R. M., Hauck, J., Peters, G. P., Peters, W., Pongratz, J., Sitch, S., Quéré, C. Le, Bakker, D. C. E., Canadell, J. G., Ciais, P., Jackson, R. B., Anthoni, P., Barbero, L., Bastos, A., Bastrikov, V., Becker, M., Bopp, L., Buitenhuis, E., Chandra, N., Chevallier, F., Chini, L. P., Currie, K., Feely, R. A., Gehlen, M., Gilfillan, D., Gkritzalis, T., Goll, D. S., Gruber, N., Gutekunst, S., Harris, I., Haverd, V., Houghton, R. A., Hurtt, G., Ilyina, T., Jain, A. K., Joetzjer, E., Kaplan, J. O., Kato, E., Goldewijk, K. K., Korsbakken, J. I., Landschützer, P., Lauvset, S. K., Lefevre, N., Lenton, A., Lienert, S., Lombardozzi, D., Marland, G., McGuire, P. C., Melton, J. R., Metzl, N., Munro, D. R., Nabel, J. E. M. S., Nakaoka, S., Neill, C., Omar, A. M., Ono, T., Peregón, A., Pierrot, D., Poulter, B., Rehder, G., Resplandy, L., Robertson, E., Rodenbeck, C., Seferian, R., Schwinger, J., Smith, N., Tans, P. P., Tian, H., Tilbrook, B., Tubiello, F. N., Van Der Werf, G. R., Wiltshire, A. J. and Zaehle, S.: Global Carbon Budget 2019, *Earth Syst. Sci. Data*, (11), 1783–1838, 2019.
- 1440 Fujimori, S., Hasegawa, T., Masui, T., Takahashi, K., Herran, D. S., Dai, H., Hijioka, Y. and Kainuma, M.: SSP3: AIM implementation of Shared Socioeconomic Pathways, *Glob. Environ. Chang.*, 42, 268–283, doi:10.1016/j.gloenvcha.2016.06.009, 2017.
- 1445 Gettelman, A., Hannay, C., Bacmeister, J. T., Neale, R. B., Pendergrass, A. G., Danabasoglu, G., Lamarque, J. F., Fasullo, J. T., Bailey, D. A., Lawrence, D. M. and Mills, M. J.: High Climate Sensitivity in the Community Earth System Model Version 2 (CESM2), *Geophys. Res. Lett.*, 46(14), 8329–8337, doi:10.1029/2019GL083978, 2019.
- Goodwin, P.: On the Time Evolution of Climate Sensitivity and Future Warming, *Earth’s Futur.*, 6(9), 1336–1348, doi:10.1029/2018EF000889, 2018.
- 1450 Gregory, J. M., Ingram, W. J., Palmer, M. A., Jones, G. S., Stott, P. A., Thorpe, R. B., Lowe, J. A., Johns, T. C. and Williams, K. D.: A new method for diagnosing radiative forcing and climate sensitivity, *Geophys. Res. Lett.*, 31(3), 2–5, doi:10.1029/2003GL018747, 2004.
- 1455 Griffies, S. M., Danabasoglu, G., Durack, P. J., Adcroft, A. J., Balaji, V., Böning, C. W., Chassignet, E. P., Curchitser, E., Deshayes, J., Drange, H., Fox-Kemper, B., Gleckler, P. J., Gregory, J. M., Haak, H., Hallberg, R. W., Heimbach, P., Hewitt, H. T., Holland, D. M., Ilyina, T., Jungclaus, J. H., Komuro, Y., Krasting, J. P., Large, W. G., Marsland, S. J., Masina, S., McDougall, T. J., George Nurser, A. J., Orr, J. C., Pirani, A., Qiao, F., Stouffer, R. J., Taylor, K. E., Treguier,

- A. M., Tsujino, H., Uotila, P., Valdivieso, M., Wang, Q., Winton, M. and Yeager, S. G.: OMIP contribution to CMIP6: Experimental and diagnostic protocol for the physical component of the Ocean Model Intercomparison Project, *Geosci. Model Dev.*, 9(9), 3231–3296, doi:10.5194/gmd-9-3231-2016, 2016.
- 1460 Hansen, J., Ruedy, R., Sato, M. and Lo, K.: Global surface temperature change, *Rev. Geophys.*, 48(4), RG4004, doi:10.1029/2010RG000345.1.INTRODUCTION, 2010.
- Hausfather, Z., Drake, H. F., Abbott, T. and Schmidt, G. A.: Evaluating the Performance of Past Climate Model Projections, *Geophys. Res. Lett.*, 47(1), 0–3, doi:10.1029/2019GL085378, 2020.
- 1465 Haustein, K., Otto, F. E. L., Venema, V., Jacobs, P., Cowtan, K., Hausfather, Z., Way, R. G., White, B., Subramanian, A. and Schurer, A. P.: A limited role for unforced internal variability in twentieth-century warming, *J. Clim.*, 32(16), 4893–4917, doi:10.1175/JCLI-D-18-0555.1, 2019.
- Hope, A. P., Canty, T. P., Salawitch, R. J., Tribett, W. R. and Bennett, B. F.: Forecasting Global Warming, in *Paris Climate Agreement: Beacon of Hope*, pp. 51–114, Springer Climate., 2017.
- 1470 Ishihara, K.: Calculation of global surface temperature anomalies with COBE-SST, *Weather Serv. Bull.*, 73, S19–S25, 2006.
- Ishii, M., Shouji, A., Sugimoto, S. and Matsumoto, T.: Objective analyses of sea-surface temperature and marine meteorological variables for the 20th century using ICOADS and the Kobe Collection, *Int. J. Climatol.*, 25(7), 865–879, doi:10.1002/joc.1169, 2005.
- 1475 Ishii, M., Fukuda, Y., Hirahara, S., Yasui, S., Suzuki, T. and Sato, K.: Accuracy of Global Upper Ocean Heat Content Estimation Expected from Present Observational Data Sets, *Sci. Online Lett. Atmos.*, 13(0), 163–167, doi:10.2151/sola.2017-030, 2017.
- Jackson, L. C., Kahana, R., Graham, T., Ringer, M. A., Woollings, T., Mecking, J. V. and Wood, R. A.: Global and European climate impacts of a slowdown of the AMOC in a high resolution GCM, *Clim. Dyn.*, 45(11–12), 3299–3316, doi:10.1007/s00382-015-2540-2, 2015.
- 1480 Kavvada, A., Ruiz-Barradas, A. and Nigam, S.: AMO’s structure and climate footprint in observations and IPCC AR5 climate simulations, *Clim. Dyn.*, 41(5–6), 1345–1364, doi:10.1007/s00382-013-1712-1, 2013.
- Kennedy, J. J., Rayner, N. A., Smith, R. O., Parker, D. E. and Saunby, M.: Reassessing biases and other uncertainties in sea surface temperature observations measured in situ since 1850: 2. Biases and homogenization, *J. Geophys. Res.*, 116(D14), 1–22, doi:10.1029/2010jd015220, 2011.
- 1485 Kennedy, J. J., Rayner, N. A., Atkinson, C. P. and Killick, R. E.: An Ensemble Data Set of Sea Surface Temperature Change From 1850: The Met Office Hadley Centre HadSST.4.0.0.0 Data Set, *J. Geophys. Res. Atmos.*, 124(14), 7719–7763, doi:10.1029/2018JD029867, 2019.
- Kiehl, J. T.: Twentieth century climate model response and climate sensitivity, *Geophys. Res. Lett.*, 34(22), 1–4, doi:10.1029/2007GL031383, 2007.
- 1490 Kirschke, S., Bousquet, P., Ciais, P., Saunoy, M., Canadell, J. G., Dlugokencky, E. J., Bergamaschi, P., Bergmann, D., Blake, D. R., Bruhwiler, L., Cameron-Smith, P., Castaldi, S., Chevallier, F., Feng, L., Fraser, A., Heimann, M., Hodson, E. L., Houweling, S., Josse, B., Fraser, P. J., Krummel, P. B., Lamarque, J. F., Langenfelds, R. L., Le Quéré, C., Naik, V., O’doherly, S., Palmer, P. I., Pison, I., Plummer, D., Poulter, B., Prinn, R. G., Rigby, M., Ringeval, B., Santini, M., Schmidt, M., Shindell, D. T., Simpson, I. J., Spahni, R., Steele, L. P., Strode, S. A., Sudo, K., Szopa, S., Van Der Werf, G. R., Voulgarakis, A., Van Weele, M., Weiss, R. F., Williams, J. E. and Zeng, G.: Three decades of global methane sources and sinks, *Nat. Geosci.*, 6(10), 813–823, doi:10.1038/ngeo1955, 2013.
- 1495 Kirtman, B., Power, S. B., Adedoyin, A. J., Boer, G. J., Bojariu, R., Camilloni, I., Doblas-Reyes, F., Fiore, A. M., Kimoto, M., Meehl, G., Prather, M., Sarr, A., Schär, C., Sutton, R., van Oldenborgh, G. J., Vecchi, G. and Wang, H. J.: Near-term climate change: Projections and predictability, *Clim. Chang. 2013 Phys. Sci. Basis Work. Gr. I Contrib. to Fifth Assess. Rep. Intergov. Panel Clim. Chang.*, 9781107057, 953–1028, doi:10.1017/CBO9781107415324.023, 2013.
- 1500 Klein, S. A., Hall, A., Norris, J. R. and Pincus, R.: Low-Cloud Feedbacks from Cloud-Controlling Factors: A Review, *Surv. Geophys.*, 38(6), 1307–1329, doi:10.1007/s10712-017-9433-3, 2017.
- Knight, J. R., Allan, R. J., Folland, C. K., Vellinga, M. and Mann, M. E.: A signature of persistent natural thermohaline circulation cycles in observed climate, *Geophys. Res. Lett.*, 32(20), 1–4, doi:10.1029/2005GL024233, 2005.
- 1505 Kriegler, E., Weyant, J. P., Blanford, G. J., Krey, V., Clarke, L., Edmonds, J., Fawcett, A., Luderer, G., Riahi, K., Richels, R., Rose, S. K., Tavoni, M. and van Vuuren, D. P.: The role of technology for achieving climate policy objectives: Overview of the EMF 27 study on global technology and climate policy strategies, *Clim. Change*, 123(3–4), 353–367,

doi:10.1007/s10584-013-0953-7, 2014.

- 1510 Kriegler, E., Riahi, K., Bauer, N., Schwanitz, V. J., Petermann, N., Bosetti, V., Marcucci, A., Otto, S., Paroussos, L., Rao, S., Arroyo Currás, T., Ashina, S., Bollen, J., Eom, J., Hamdi-Cherif, M., Longden, T., Kitous, A., Méjean, A., Sano, F., Schaeffer, M., Wada, K., Capros, P., P. van Vuuren, D. and Edenhofer, O.: Making or breaking climate targets: The AMPERE study on staged accession scenarios for climate policy, *Technol. Forecast. Soc. Change*, doi:10.1016/j.techfore.2013.09.021, 2015.
- 1515 Kriegler, E., Bauer, N., Popp, A., Humpenöder, F., Leimbach, M., Streffler, J., Baumstark, L., Bodirsky, B. L., Hilaire, J., Klein, D., Mouratiadou, I., Weindl, I., Bertram, C., Dietrich, J. P., Luderer, G., Pehl, M., Pietzcker, R., Piontek, F., Lotze-Campen, H., Biewald, A., Bonsch, M., Giannousakis, A., Kreidenweis, U., Müller, C., Rolinski, S., Schultes, A., Schwanitz, J., Stevanovic, M., Calvin, K., Emmerling, J., Fujimori, S. and Edenhofer, O.: Fossil-fueled development (SSP5): An energy and resource intensive scenario for the 21st century, *Glob. Environ. Chang.*, 42, 297–315, doi:10.1016/j.gloenvcha.2016.05.015, 2017.
- 1520 Kushnir, Y.: Interdecadal Variations in North Atlantic Sea Surface Temperature and Associated Atmospheric Conditions, *J. Clim.*, 7(1), 141–157, doi:10.1175/1520-0442(1994)007<0141:IVINAS>2.0.CO;2, 1994.
- Lean, J. L. and Rind, D. H.: How natural and anthropogenic influences alter global and regional surface temperatures: 1889 to 2006, *Geophys. Res. Lett.*, 35(18), 1–6, doi:10.1029/2008GL034864, 2008.
- Lean, J. L. and Rind, D. H.: How will Earth’s surface temperature change in future decades?, *Geophys. Res. Lett.*, 36(15), 1–5, doi:10.1029/2009GL038932, 2009.
- 1525 Lelieveld, J., Evans, J. S., Fnais, M., Giannadaki, D. and Pozzer, A.: The contribution of outdoor air pollution sources to premature mortality on a global scale, *Nature*, 525(7569), 367–371, doi:10.1038/nature15371, 2015.
- Levitus, S., Antonov, J. I., Boyer, T. P., Baranova, O. K., Garcia, H. E., Locarnini, R. A., Mishonov, A. V., Reagan, J. R., Seidov, D., Yarosh, E. S. and Zweng, M. M.: World ocean heat content and thermosteric sea level change (0–2000m), 1955–2010, *Geophys. Res. Lett.*, 39(10), 1–5, doi:10.1029/2012GL051106, 2012.
- 1530 Lewis, N. and Curry, J.: The impact of recent forcing and ocean heat uptake data on estimates of climate sensitivity, *J. Clim.*, 31(15), 6051–6071, doi:10.1175/JCLI-D-17-0667.1, 2018.
- Lewis, N. and Grünwald, P.: Objectively combining AR5 instrumental period and paleoclimate climate sensitivity evidence, *Clim. Dyn.*, 50(5), 2199–2216, doi:10.1007/s00382-017-3744-4, 2018.
- 1535 Marvel, K., Pincus, R., Schmidt, G. A. and Miller, R. L.: Internal Variability and Disequilibrium Confound Estimates of Climate Sensitivity From Observations, *Geophys. Res. Lett.*, 45(3), 1595–1601, doi:10.1002/2017GL076468, 2018.
- Mascioli, N. R., Canty, T. and Salawitch, R. J.: An empirical model of global climate – Part 2: Implications for future temperature, *Atmos. Chem. Phys.*, 2013.
- 1540 Matthes, K., Funke, B., Andersson, M. E., Barnard, L., Beer, J., Charbonneau, P., Clilverd, M. A., Dudok de Wit, T., Haberreiter, M., Hendry, A., Jackman, C. H., Kretzschmar, M., Kruschke, T., Kunze, M., Langematz, U., Marsh, D. R., Maycock, A. C., Misios, S., Rodger, C. J., Scaife, A. A., Seppala, A., Shangguan, M., Sinnhuber, M., Tourpali, K., Usoskin, I., van de Kamp, M., Verronen, P. T. and Versick, S.: Solar forcing for CMIP6 (v3.2), *Geosci. Model Dev.*, 10, 2247–2302, 2017.
- McBride, L. A., Hope, A. P., Canty, T. P., Bennett, B. F., Tribett, W. R. and Salawitch, R. J.: Input and Output Files EMGC, doi:10.5281/zenodo.4300780, 2021.
- 1545 Medhaug, I. and Furevik, T.: North Atlantic 20th century multidecadal variability in coupled climate models: Sea surface temperature and ocean overturning circulation, *Ocean Sci.*, 7(3), 389–404, doi:10.5194/os-7-389-2011, 2011.
- Meehl, G. A., Senior, C. A., Eyring, V., Flato, G., Lamarque, J. F., Stouffer, R. J., Taylor, K. E. and Schlund, M.: Context for interpreting equilibrium climate sensitivity and transient climate response from the CMIP6 Earth system models, *Sci. Adv.*, 6(26), 1–11, doi:10.1126/sciadv.aba1981, 2020.
- 1550 Meinshausen, M., Smith, S. J., Calvin, K., Daniel, J. S., Kainuma, M. L. T., Lamarque, J., Matsumoto, K., Montzka, S. A., Raper, S. C. B., Riahi, K., Thomson, A., Velders, G. J. M. and van Vuuren, D. P. P.: The RCP greenhouse gas concentrations and their extensions from 1765 to 2300, *Clim. Change*, 109(1), 213–241, doi:10.1007/s10584-011-0156-z, 2011.
- 1555 Meinshausen, M., Vogel, E., Nauels, A., Lorbacher, K., Meinshausen, N., Etheridge, D. M., Fraser, P. J., Montzka, S. A., Rayner, P. J., Trudinger, C. M., Krummel, P. B., Beyerle, U., Canadell, J. G., Daniel, J. S., Enting, I. G., Law, R. M., Lunder, C. R., O’Doherty, S., Prinn, R. G., Reimann, S., Rubino, M., Velders, G. J. M., Vollmer, M. K., Wang, R. H. J.

- and Weiss, R.: Historical greenhouse gas concentrations for climate modelling (CMIP6), *Geosci. Model Dev.*, 10(5), 2057–2116, doi:10.5194/gmd-10-2057-2017, 2017.
- 1560 Millar, R. J., Fuglestedt, J. S., Friedlingstein, P., Rogelj, J., Grubb, M. J., Matthews, H. D., Skeie, R. B., Forster, P. M., Frame, D. J. and Allen, M. R.: Emission budgets and pathways consistent with limiting warming to 1.5°C, *Nat. Geosci.*, 11(6), 454–455, doi:10.1038/s41561-018-0153-1, 2017.
- Morice, C. P., Kennedy, J. J., Rayner, N. A. and Jones, P. D.: Quantifying uncertainties in global and regional temperature change using an ensemble of observational estimates: The HadCRUT4 data set, *J. Geophys. Res. Atmos.*, 117(8), 1–22, doi:10.1029/2011JD017187, 2012.
- 1565 Morice, C. P., Kennedy, J. J., Rayner, N. A., Winn, J. P., Hogan, E., Killick, R. E., Dunn, R. J. H., Osborn, T. J., Jones, P. D. and Simpson, I. R.: An updated assessment of near-surface temperature change from 1850: the HadCRUT5 dataset, *J. Geophys. Res. Atmos.*, doi:10.1029/2019jd032361, 2021.
- Murphy, J. M., Booth, B. B. B., Boulton, C. A., Clark, R. T., Harris, G. R., Lowe, J. A. and Sexton, D. M. H.: Transient climate changes in a perturbed parameter ensemble of emissions-driven earth system model simulations, *Clim. Dyn.*, 43(9–10), 2855–2885, doi:10.1007/s00382-014-2097-5, 2014.
- 1570 Myhre, G., Highwood, E. J., Shine, K. P. and Stordal, F.: New estimates of radiative forcing due to well mixed greenhouse gases, *Geophys. Res. Lett.*, 25(14), 2715–2718, 1998.
- Myhre, G., Nilsen, J. S., Gulstad, L., Shine, K. P., Røgnrud, B. and Isaksen, I. S. A.: Radiative forcing due to stratospheric water vapour from CH₄ oxidation, *Geophys. Res. Lett.*, 34(1), 3–7, doi:10.1029/2006GL027472, 2007.
- 1575 Myhre, G., Shindell, D., Bréon, F.-M., Collins, W., Fuglestedt, J., Huang, J., Koch, D., Lamarque, J.-F., Lee, D., Mendoza, B., Nakajima, T., Robock, A., Stephens, G., Takemura, T. and Zhang, H.: Anthropogenic and Natural Radiative Forcing, *Clim. Chang. 2013 Phys. Sci. Basis. Contrib. Work. Gr. I to Fifth Assess. Rep. Intergov. Panel Clim. Chang.*, 659–740, doi:10.1017/CBO9781107415324.018, 2013.
- 1580 Nigam, S., Guan, B. and Ruiz-Barradas, A.: Key role of the Atlantic Multidecadal Oscillation in 20th century drought and wet periods over the Great Plains, *Geophys. Res. Lett.*, 38(16), 1–6, doi:10.1029/2011GL048650, 2011.
- Nijssen, F. J. M. M., Cox, P. M. and Williamson, M. S.: Emergent constraints on transient climate response (TCR) and equilibrium climate sensitivity (ECS) from historical warming in CMIP5 and CMIP6 models, *Earth Syst. Dyn.*, 11, 737–750, 2020.
- 1585 O’Neill, B. C., Kriegler, E., Riahi, K., Ebi, K. L., Hallegatte, S., Carter, T. R., Mathur, R. and van Vuuren, D. P.: A new scenario framework for climate change research: The concept of shared socioeconomic pathways, *Clim. Change*, 122(3), 387–400, doi:10.1007/s10584-013-0905-2, 2014.
- O’Neill, B. C., Tebaldi, C., Van Vuuren, D. P., Eyring, V., Friedlingstein, P., Hurtt, G., Knutti, R., Kriegler, E., Lamarque, J. F., Lowe, J., Meehl, G. A., Moss, R., Riahi, K. and Sanderson, B. M.: The Scenario Model Intercomparison Project (ScenarioMIP) for CMIP6, *Geosci. Model Dev.*, 9(9), 3461–3482, doi:10.5194/gmd-9-3461-2016, 2016.
- 1590 O’Neill, B. C., Kriegler, E., Ebi, K. L., Kemp-Benedict, E., Riahi, K., Rothman, D. S., van Ruijven, B. J., van Vuuren, D. P., Birkmann, J., Kok, K., Levy, M. and Solecki, W.: The roads ahead: Narratives for shared socioeconomic pathways describing world futures in the 21st century, *Glob. Environ. Chang.*, 42, 169–180, doi:10.1016/j.gloenvcha.2015.01.004, 2017.
- 1595 Otto, A., Otto, F. E. L., Boucher, O., Church, J., Hegerl, G., Forster, P. M., Gillett, N. P., Gregory, J., Johnson, G. C., Knutti, R., Lewis, N., Lohmann, U., Marotzke, J., Myhre, G., Shindell, D., Stevens, B. and Allen, M. R.: Energy budget constraints on climate response, *Nat. Geosci.*, 6(6), 415–416, doi:10.1038/ngeo1836, 2013.
- Proistosescu, C. and Huybers, P. J.: Slow climate mode reconciles historical and model-based estimates of climate sensitivity, *Sci. Adv.*, 3(7), 1–7, doi:10.1126/sciadv.1602821, 2017.
- 1600 Raper, S. C. B., Gregory, J. M. and Stouffer, R. J.: The role of climate sensitivity and ocean heat uptake on AOGCM transient temperature response, *J. Clim.*, 15(1), 124–130, doi:10.1175/1520-0442(2002)015<0124:TROCSA>2.0.CO;2, 2002.
- Riahi, K., Kriegler, E., Johnson, N., Bertram, C., den Elzen, M., Eom, J., Schaeffer, M., Edmonds, J., Isaac, M., Krey, V., Longden, T., Luderer, G., Méjean, A., McCollum, D. L., Mima, S., Turton, H., van Vuuren, D. P., Wada, K., Bosetti, V., Capros, P., Crippi, P., Hamdi-Cherif, M., Kainuma, M. and Edenhofer, O.: Locked into Copenhagen pledges - Implications of short-term emission targets for the cost and feasibility of long-term climate goals, *Technol. Forecast. Soc. Change*, 90(PA), 8–23, doi:10.1016/j.techfore.2013.09.016, 2015.
- 1605 Riahi, K., van Vuuren, D. P., Kriegler, E., Edmonds, J., O’Neill, B. C., Fujimori, S., Bauer, N., Calvin, K., Dellink, R., Fricko,

- O., Lutz, W., Popp, A., Cuaresma, J. C., KC, S., Leimbach, M., Jiang, L., Kram, T., Rao, S., Emmerling, J., Ebi, K., Hasegawa, T., Havlik, P., Humpenöder, F., Da Silva, L. A., Smith, S., Stehfest, E., Bosetti, V., Eom, J., Gernaat, D., Masui, T., Rogelj, J., Strefler, J., Drouet, L., Krey, V., Luderer, G., Harmsen, M., Takahashi, K., Baumstark, L., Doelman, J. C., Kainuma, M., Klimont, Z., Marangoni, G., Lotze-Campen, H., Obersteiner, M., Tabeau, A. and Tavoni, M.: The Shared Socioeconomic Pathways and their energy, land use, and greenhouse gas emissions implications: An overview, *Glob. Environ. Chang.*, 42, 153–168, doi:10.1016/j.gloenvcha.2016.05.009, 2017.
- Rogelj, J., Popp, A., Calvin, K. V., Luderer, G., Emmerling, J., Gernaat, D., Fujimori, S., Strefler, J., Hasegawa, T., Marangoni, G., Krey, V., Kriegler, E., Riahi, K., Van Vuuren, D. P., Doelman, J., Drouet, L., Edmonds, J., Fricko, O., Harmsen, M., Havlik, P., Humpenöder, F., Stehfest, E. and Tavoni, M.: Scenarios towards limiting global mean temperature increase below 1.5 °C, *Nat. Clim. Chang.*, 8(4), 325–332, doi:10.1038/s41558-018-0091-3, 2018.
- Rohde, R., Muller, R., Jacobsen, R., Muller, E. and Wickham, C.: A New Estimate of the Average Earth Surface Land Temperature Spanning 1753 to 2011, *Geoinformatics Geostatistics An Overv.*, 01(01), 1–7, doi:10.4172/2327-4581.1000101, 2013.
- Rohde, R. A. and Hausfather, Z.: The Berkeley Earth Land/Ocean Temperature Record, *Earth Syst. Sci. Data*, 12(4), 3469–3479, doi:10.5194/essd-12-3469-2020, 2020.
- Rugenstein, M., Bloch-Johnson, J., Gregory, J., Andrews, T., Mauritsen, T., Li, C., Frölicher, T. L., Paynter, D., Danabasoglu, G., Yang, S., Dufresne, J. L., Cao, L., Schmidt, G. A., Abe-Ouchi, A., Geoffroy, O. and Knutti, R.: Equilibrium Climate Sensitivity Estimated by Equilibrating Climate Models, *Geophys. Res. Lett.*, 47(4), 1–12, doi:10.1029/2019GL083898, 2020.
- Saji, N. H., Goswami, B. N., Vinayachandran, P. N. and Yamagata, T.: A dipole mode in the tropical Indian ocean, *Nature*, 401(6751), 360–363, doi:10.1038/43854, 1999.
- Saunio, M., Stavert, A., Poulter, B., Bousquet, P., Canadell, J., Jackson, R., Raymond, P., Dlugokencky, E., Houweling, S., Patra, P., Ciais, P., Arora, V., Bastviken, D., Bergamaschi, P., Blake, D., Brailsford, G., Bruhwiler, L., Carlson, K., Carrol, M., Castaldi, S., Chandra, N., Crevoisier, C., Crill, P., Covey, K., Curry, C., Etiope, G., Frankenberg, C., Gedney, N., Hegglin, M., Höglund-Isaksson, L., Hugelius, G., Ishizawa, M., Ito, A., Janssens-Maenhout, G., Jensen, K., Joos, F., Kleinen, T., Krummel, P., Langenfelds, R., Laruelle, G., Liu, L., Machida, T., Maksyutov, S., McDonald, K., McNorton, J., Miller, P., Melton, J., Morino, I., Müller, J., Murguía-Flores, F., Naik, V., Niwa, Y., Noce, S., O’Doherty, S., Parker, R., Peng, C., Peng, S., Peters, G., Prigent, C., Prinn, R., Ramonet, M., Regnier, P., Riley, W., Rosentreter, J., Segers, A., Simpson, I., Shi, H., Smith, S., Steele, L. P., Thornton, B., Tian, H., Tohjima, Y., Tubiello, F., Tsuruta, A., Viovy, N., Voulgarakis, A., Weber, T., van Weele, M., van der Werf, G., Weiss, R., Worthy, D., Wunch, D., Yin, Y., Yoshida, Y., Zhang, W., Zhang, Z., Zhao, Y., Zheng, B., Zhu, Q., Zhu, Q. and Zhuang, Q.: The Global Methane Budget 2000–2017, *Earth Syst. Sci. Data*, 12(3), 1561–1623, doi:10.5194/essd-12-1561-2020, 2020.
- Schiffer, R. A. and Rossow, W. B.: The International Satellite Cloud Climatology Project (ISCCP): The first project of the World Climate Research Programme, *Bull. Am. Meteorol. Soc.*, (76), 779–784, 1983.
- Schlesinger, M. E. and Ramankutty, N.: An oscillation in the global climate system of period 65–70 years, *Nature*, 367, 723–726, 1994.
- Schwartz, S. E.: Determination of Earth’s Transient and Equilibrium Climate Sensitivities from Observations Over the Twentieth Century: Strong Dependence on Assumed Forcing, *Surv. Geophys.*, 33(3–4), 745–777, doi:10.1007/s10712-012-9180-4, 2012.
- Sellar, A. A., Walton, J., Jones, C. G., Wood, R., Abraham, N. L., Andrejczuk, M., Andrews, M. B., Andrews, T., Archibald, A. T., de Mora, L., Dyson, H., Elkington, M., Ellis, R., Florek, P., Good, P., Gohar, L., Haddad, S., Hardiman, S. C., Hogan, E., Iwi, A., Jones, C. D., Johnson, B., Kelley, D. I., Kettleborough, J., Knight, J. R., Köhler, M. O., Kuhlbrodt, T., Liddicoat, S., Linova-Pavlova, I., Mizieliński, M. S., Morgenstern, O., Mulcahy, J., Neining, E., O’Connor, F. M., Petrie, R., Ridley, J., Rioual, J. C., Roberts, M., Robertson, E., Rumbold, S., Seddon, J., Shepherd, H., Shim, S., Stephens, A., Teixeira, J. C., Tang, Y., Williams, J., Wiltshire, A. and Griffiths, P. T.: Implementation of U.K. Earth System Models for CMIP6, *J. Adv. Model. Earth Syst.*, 12(4), 1–27, doi:10.1029/2019MS001946, 2020.
- Shen, Z., Ming, Y. and Held, I. M.: Using the fast impact of anthropogenic aerosols on regional land temperature to constrain aerosol forcing, *Sci. Adv.*, (August), 1–8, 2020.
- Sherwood, A. S., Webb, M. J., Annan, J. D., Armour, K. C., Forster, P. M., Hargreaves, J. C., Hegerl, G., Klein, S. A., Marvel, K. D., Rohling, E. J., Watanabe, M., Andrews, T., Braconnot, P., Bretherton, C. S., Foster, G. L., Hausfather, Z., von

- der Heydt, A. S., Knutti, R., Mauritsen, T., Norris, J. R., Proistosescu, C., Rugenstein, M., Schmidt, G. A. and Tokarska, K. B., Zelinka, M. D.: An assessment of Earth ' s climate sensitivity using multiple lines of evidence, *Rev. Geophys.*, 1–166, 2020.
- 1660 Shindell, D. T., Lee, Y. and Faluvegi, G.: Climate and health impacts of US emissions reductions consistent with 2 °c, *Nat. Clim. Chang.*, 6(5), 503–507, doi:10.1038/nclimate2935, 2016.
- Skeie, R., Berntsen, T., Aldrin, M., Holden, M. and Myhre, G.: Climate sensitivity estimates - Sensitivity to radiative forcing time series and observational data, *Earth Syst. Dyn.*, 9(2), 879–894, doi:10.5194/esd-9-879-2018, 2018.
- 1665 Smith, S. J. and Bond, T. C.: Two hundred fifty years of aerosols and climate: The end of the age of aerosols, *Atmos. Chem. Phys.*, 14(2), 537–549, doi:10.5194/acp-14-537-2014, 2014.
- Smith, T. M., Reynolds, R. W., Peterson, T. C. and Lawrimore, J.: Improvements to NOAA's historical merged land-ocean surface temperature analysis (1880-2006), *J. Clim.*, 21(10), 2283–2296, doi:10.1175/2007JCLI2100.1, 2008.
- 1670 Solomon, S.: Climate change 2007-the physical science basis: Working group I contribution to the fourth assessment report of the IPCC, Cambridge University Press., 2007.
- Stocker, T., Qin, D., Plattner, G., Tignor, M., Allen, S., Boschung, J., Nauels, A., Xia, Y., Bex, V. and Midgely, P.: IPCC, 2013: climate change 2013: The physical science basis. Contribution of working group I to the fifth assessment report of the intergovernmental panel on climate change., Cambridge, UK and New York, NY USA., 2013.
- 1675 Stouffer, R. J., Yin, J., Gregory, J. M., Dixon, K. W., Spelman, M. J., Hurlin, W., Weaver, A. J., Eby, M., Flato, G. M., Hasumi, H., Hu, A., Jungclaus, J. H., Kamenkovich, I. V., Levermann, A., Montoya, M., Murakami, S., Nawrath, S., Oka, A., Peltier, W. R., Robitaille, D. Y., Sokolov, A., Vettoretti, G. and Weber, S. L.: Investigating the cause of the response of the thermohaline circulation to past and future climate changes, *J. Clim.*, 19(8), 1365–1387, doi:10.1175/JCLI3689.1, 2006.
- Swart, N. C., Cole, J. N. S., Kharin, V. V., Lazare, M., Scinocca, J. F., Gillett, N. P., Anstey, J., Arora, V., Christian, J. R., Hanna, S., Jiao, Y., Lee, W. G., Majaess, F., Saenko, O. A., Seiler, C., Seinen, C., Shao, A., Sigmond, M., Solheim, L., Von Salzen, K., Yang, D. and Winter, B.: The Canadian Earth System Model version 5 (CanESM5.0.3), *Geosci. Model Dev.*, 12(11), 4823–4873, doi:10.5194/gmd-12-4823-2019, 2019.
- 1680 Tatebe, H., Ogura, T., Nitta, T., Komuro, Y., Ogochi, K., Takemura, T., Sudo, K., Sekiguchi, M., Abe, M., Saito, F., Chikira, M., Watanabe, S., Mori, M., Hirota, N., Kawatani, Y., Mochizuki, T., Yoshimura, K., Takata, K., O'Ishi, R., Yamazaki, D., Suzuki, T., Kurogi, M., Kataoka, T., Watanabe, M. and Kimoto, M.: Description and basic evaluation of simulated mean state, internal variability, and climate sensitivity in MIROC6, *Geosci. Model Dev.*, 12(7), 2727–2765, doi:10.5194/gmd-12-2727-2019, 2019.
- 1685 Taylor, K. E., Stouffer, R. J. and Meehl, G. A.: An overview of CMIP5 and the experiment design, *Bull. Am. Meteorol. Soc.*, 93(4), 485–498, doi:10.1175/BAMS-D-11-00094.1, 2012.
- 1690 Thomason, L. W., Ernest, N., Millán, L., Rieger, L., Bourassa, A., Vernier, J. P., Manney, G., Luo, B., Arfeuille, F. and Peter, T.: A global space-based stratospheric aerosol climatology: 1979-2016, *Earth Syst. Sci. Data*, 10(1), 469–492, doi:10.5194/essd-10-469-2018, 2018.
- Thompson, D. W. J., Wallace, J. M., Jones, P. D. and Kennedy, J. J.: Identifying signatures of natural climate variability in time series of global-mean surface temperature: Methodology and insights, *J. Clim.*, 22(22), 6120–6141, doi:10.1175/2009JCLI3089.1, 2009.
- 1695 Tokarska, K. B., Hegerl, G. C., Schurer, A. P., Forster, P. M. and Marvel, K.: Observational constraints on the effective climate sensitivity from the historical period, *Environ. Res. Lett.*, 15(3), doi:10.1088/1748-9326/ab738f, 2020a.
- Tokarska, K. B., Stolpe, M. B., Sippel, S., Fischer, E. M., Smith, C. J., Lehner, F. and Knutti, R.: Past warming trend constrains future warming in CMIP6 models, *Sci. Adv.*, 6(12), 1–13, doi:10.1126/sciadv.aaz9549, 2020b.
- 1700 Trenberth, K. E. and Fasullo, J. T.: An apparent hiatus in global warming?, *Earth's Futur.*, 1, 19–32, doi:10.1002/2013EF000165, Received, 2013.
- Vaughan, M. A., Young, S. A., Winker, D. M., Powell, K. A., Omar, A. H., Liu, Z., Hu, Y. and Hostetler, C. A.: Fully automated analysis of space-based lidar data: an overview of the CALIPSO retrieval algorithms and data products, in *Proc.SPIE*, vol. 5575., 2004.
- 1705 Volodin, E. and Gritsun, A.: Simulation of observed climate changes in 1850-2014 with climate model INM-CM5, *Earth Syst. Dyn.*, 9(4), 1235–1242, doi:10.5194/esd-9-1235-2018, 2018.
- van Vuuren, D. P., Stehfest, E., Gernaat, D. E. H. J., Doelman, J. C., van den Berg, M., Harmsen, M., de Boer, H. S., Bouwman,

- 1710 L. F., Daioglou, V., Edelenbosch, O. Y., Girod, B., Kram, T., Lassaletta, L., Lucas, P. L., van Meijl, H., Müller, C., van
Ruijven, B. J., van der Sluis, S. and Tabeau, A.: Energy, land-use and greenhouse gas emissions trajectories under a
green growth paradigm, *Glob. Environ. Chang.*, 42, 237–250, doi:10.1016/j.gloenvcha.2016.05.008, 2017.
- van Vuuren, D. P., van der Wijst, K.-I., Marsman, S., van den Berg, M., Hof, A. F. and Jones, C. D.: The costs of achieving
climate targets and the sources of uncertainty, *Nat. Clim. Chang.*, 10(April), doi:10.1038/s41558-020-0732-1, 2020.
- Weaver, C. J., Wu, D. L., Bhartia, P. K., Labow, G. J. and Haffner, D. P.: A long-term cloud albedo data record since 1980
from UV satellite sensors, *Remote Sens.*, 12(12), 1–18, doi:10.3390/rs12121982, 2020.
- 1715 WMO: World Meteorological Organization, Scientific assessment of ozone depletion: 2018, *Glob. Ozone Res. Monit. Proj.*
#58, 2018.
- Wolf, J., Asrar, G. R. and West, T. O.: Revised methane emissions factors and spatially distributed annual carbon fluxes for
global livestock, *Carbon Balance Manag.*, 12(1), doi:10.1186/s13021-017-0084-y, 2017.
- Wolter, K. and Timlin, M. S.: Monitoring ENSO in COADS with a seasonally adjusted principal component index, *Proc 17th*
1720 *Clim. Diagnostics Work.*, 52–57 [online] Available from:
[http://www.esrl.noaa.gov/psd/enso/mei/WT1.pdf%5Cnpapers2://publication/uuid/123434A4-48AA-4F4B-A3F7-
506504693A80](http://www.esrl.noaa.gov/psd/enso/mei/WT1.pdf%5Cnpapers2://publication/uuid/123434A4-48AA-4F4B-A3F7-506504693A80), 1993.
- Wolter, K. and Timlin, M. S.: El Niño/Southern Oscillation behaviour since 1871 as diagnosed in an extended multivariate
ENSO index (MEI.ext), *Int. J. Climatol.*, 31(7), 1074–1087, doi:10.1002/joc.2336, 2011.
- 1725 Zelinka, M. D., Myers, T. A., McCoy, D. T., Po-Chedley, S., Caldwell, P. M., Ceppi, P., Klein, S. A. and Taylor, K. E.: Causes
of Higher Climate Sensitivity in CMIP6 Models, *Geophys. Res. Lett.*, 47(1), doi:10.1029/2019GL085782, 2020.
- Zhang, H.-M., Lawrimore, J., Huang, B., Menne, M. J., Yin, X., Sanchez-Lugo, A., Gleason, B. E., Vose, R., Arndt, D.,
Rennie, J. J. and Williams, C. N.: Updated Temperature Data Give a Sharper View of Climate Trends, *Eos (Washington*
DC), 100, doi:10.1029/2019EO128229, 2019.
- 1730 Zhang, R. and Delworth, T. L.: Impact of the Atlantic Multidecadal Oscillation on North Pacific climate variability, *Geophys.*
Res. Lett., 34(23), 2–7, doi:10.1029/2007GL031601, 2007.
- Zhou, J. and Tung, K. K.: Deducing multidecadal anthropogenic global warming trends using multiple regression analysis, *J.*
Atmos. Sci., 70(1), 3–8, doi:10.1175/JAS-D-12-0208.1, 2013.
- 1735 Zhu, J., Poulsen, C. J. and Otto-Bliesner, B. L.: High climate sensitivity in CMIP6 model not supported by paleoclimate, *Nat.*
Clim. Chang., 10(5), 378–379, doi:10.1038/s41558-020-0764-6, 2020.

Supplement

Section 2.1 states “The effect of this update results in our model being able to fit the historical climate record with higher values of climate feedback, especially for strong aerosol cooling (see Fig. S1 and supplement for more information)”. Figure S1 illustrates the impact of updating Eq. (2) in our model to be comparable to the formulation in Bony et al. (2006) and Schwartz (2012). This figure displays the change in GMST anomaly in 2100 relative to pre-industrial (ΔT_{2100}) as a function of λ_{Σ} and AER RF₂₀₁₁ for the two formulations of Eq. (2). Figure S1a uses the previous version of the EM-GC, where Q_{OCEAN} was subtracted outside of the climate feedback multiplicative term, and Fig. 1b uses the new version of the EM-GC where Q_{OCEAN} is subtracted within the climate feedback multiplicative term.

In the EM-GC framework, we calculate our value of Q_{OCEAN} by finding the κ needed to multiply the temperature difference between the atmosphere and the ocean to fit the observed OHC record. The model iterates over the ocean module, specifically the value of $\Delta T_{\text{OCEAN,HUMAN}}$ in Eq. (4), until the EM-GC converges on an estimate of κ for a single OHC record and value of AER RF₂₀₁₁. Figure S1 illustrates that the effect of changing Eq. (2) in the EM-GC impacts our estimates of the rise in ΔT_{2100} at high values of AER RF₂₀₁₁. Strong aerosol cooling results in the ocean taking up more heat from the atmosphere than in the previous version of the EM-GC. The larger value of Q_{OCEAN} results in a higher value of climate feedback needed to fit the historical climate record, because both AER RF₂₀₁₁ and Q_{OCEAN} are acting to cool the climate system. The higher values of climate feedback increase our maximum value of ΔT_{2100} . This change brings some of the projections of ΔT_{2100} from the EM-GC closer to values of ΔT_{2100} from the CMIP6 multi-model ensemble.

Section 2.1 states “Altering the training period of our model has a slight effect on our results (see Fig. S2, S3, and the supplement for information on various training periods).” Figure S2 shows the end of century projected warming as a function of λ_{Σ} and AER RF₂₀₁₁, for four different training periods: 1850-1989 (Fig. S2a), 1850-1999 (Fig. S2b), 1850-2009 (Fig. S2c) and 1850-2019 (Fig. S2d), which is the normal training period used in our analysis. Values of ΔT_{2100} are shown only for combinations of λ_{Σ} and AER RF₂₀₁₁ that lead to good fits ($\chi^2 \leq 2$) to the climate record. We project relatively similar results for end of century warming for the training periods that end in 2019 and 2009. Our results using the training period from 1850-1999 are similar to observations and other reduced complexity models (Nicholls et al., 2020). The training period that ends in 1989 (Fig. S2a) yields a different “shape” of model parameter space for which good fits to the climate record can be obtained, compared to the other training periods. The different shape for this shorter training period is due to two factors. First, the formulation of the ocean component of our model for the training period that stops in 1989 uses 35 years of the observed OHC record. We are able to calculate good fits to the

OHC record over this shorter time period that diverge from the OHC record after 1989. Also, for this shorter
35 time period, aerosol radiative forcing of climate cools in a manner that nearly mirrors the warming due to
rising GHGs, resulting in a wider range of model parameters that lead to a “good fit” of the climate record,
compared to model simulations constrained by data that extend closer to present-day. The highest values of
 ΔT_{2100} in Fig. S2a are associated with the largest values of λ_{Σ} , which in our model corresponds to excessively
high values of κ that we can rule out, based on OHC data collected during 1990 to 2019.

40 Figure S3 shows the observed (HadCRUT5) and modeled ΔT anomaly from 1945-2060 for the four
different training periods described above. Each panel contains three projections of future ΔT for SSP4-3.4:
projection using the value of climate feedback that provides the best fit to the historical climate record for a
value of $\text{AER RF}_{2011} = -0.9 \text{ W m}^{-2}$, the lowest value of climate feedback that provides a good fit to the
observed ΔT record for a value of $\text{AER RF}_{2011} = -0.1 \text{ W m}^{-2}$, and the highest value of climate feedback that
45 provides a good fit to the historical climate record (the associated value of AER RF_{2011} varies depending on
the training period). As more years are added to the training period, the range of projection for future
temperature decreases (Fig. S3a vs S3d). All of the best fit projections (solid line) and highest value of climate
feedback (upper dashed line) closely follow the mid-point of the data, regardless of the training period. Given
the nature of this test (i.e., predicting GMST out to 2019 for a series of trainings that stop in either 1989,
50 1999, or 2009), Figure S3 supports the quantitative accuracy of our approach for simulating and projecting
future ΔT .

Section 2.2.1 states “We use the uncertainty time series from HadCRUT4 for all GMST records (see
the supplement, Figs. S4 and S5, and Table S1 for more information)”. Figure S4 shows values of ΔT based
55 on the seven individual GMST records (GISTEMP, BEG, HadCRUT4, CW14, HadCRUT5, NOAAAGT, and
JMA) with their corresponding 1σ and 2σ uncertainties. A horizontal line at zero denotes the time period of
the baseline for each ΔT record. The multi-record mean, excluding the data set that is plotted, is also shown.
Since the multi-record mean and individual ΔT record are plotted on the same baseline, these two quantities
closely match over this time period. Panels (a), (b), (e), and (f) illustrate that the uncertainties for these GMST
60 records are not large enough to encompass the multi-record mean over 1850-2019. The multi-record mean in
panel (a) is below the GISTEMP 1σ uncertainty range between 1880 and 1900, and again between 1980 to
2019. In panel (b), the multi-record mean is above the BEG 1σ range from 1850 until 1865, 1880 to 1895,
and below the 1σ uncertainty range from 2000 to 2019. The multi-record mean in panel (e) is below the
HadCRUT5 1σ uncertainty range from 1990 until 2019. In panel (f), the multi-record mean is above the
65 NOAAAGT 1σ uncertainty range from 1920 until 1955. The JMA GMST record does not provide an
uncertainty estimate. We therefore use the HadCRUT4 combined uncertainty (measurement, sampling, bias,

and coverage uncertainties (Morice et al., 2012)) estimate for JMA in panel (g). The multi-record mean of ΔT for all data sets other than JMA lies at the edge of the 1σ uncertainty range from 1891 until 2000. After 2000, the multi-record mean falls above both the 1σ and 2σ HadCRUT4 uncertainty range. The HadCRUT4 uncertainty time series shown in panel (c) is the only uncertainty estimate large enough to cover the spread in the various GMST records.

Figure S5 shows ΔT based on all seven GMST records and the multi-record mean relative to three baseline periods. The 1σ and 2σ uncertainties from HadCRUT4 are plotted about the multi-record mean. Panels (a) and (d) show the GMST records relative to 1891-1920, which are the first 30 years all of the data sets have in common. Between 1850-1970, all of the data sets fall within the 1σ HadCRUT4 uncertainty. After 1970, the GMST records start to deviate and some fall outside of the 1σ uncertainty but within the 2σ uncertainty, and JMA falls outside of the 2σ uncertainty. Panels (b) and (e) show the GMST records relative to the HadCRUT baseline period of 1961-1990. We see similar behavior as in panels (a) and (d), where the GMST records largely fall within the HadCRUT4 1σ uncertainty until about 1970. Panels (c) and (f) show the GMST records forced to match HadCRUT5 from 2010-2019, which is baselined to 1961-1990. In these two panels, we see a large spread between the GMST records from the beginning of the time period until 2005.

Table S1 shows the percentage of ΔT data points that lie within the 1σ or 2σ HadCRUT4 uncertainty about the multi-record mean for all seven data records since 1940. Year 1940 is used to be consistent with the definition of our χ^2_{RECENT} parameter. Depending on the choice of baseline period, the number of data points within the uncertainty range varies. For a baseline of 1891-1920, 80% of the data points for all seven records are within the 1σ uncertainty and 95% of the data points are within the 2σ . For a baseline of 1961-1990, 88% and 93% of data points are within the 1σ and 2σ HadCRUT4 uncertainties, respectively. If the ΔT records are forced to match the average value of the HadCRUT5 data set over the last decade, 72% of the data points are within the 1σ uncertainty and 88% are within the 2σ uncertainty. This analysis shows that depending on which baseline is used, the percentage of points within the 1σ or 2σ uncertainty ranges varies. Overall, these comparisons support the utility of the HadCRUT4 uncertainty for the GMST, since the 1σ and 2σ uncertainty ranges capture a percentage of points approximately correct for a pure Gaussian distribution. Therefore, we have adopted the HadCRUT4 uncertainties in GMST for all of the analyses in the main paper. The uncertainties published by other data centers tend to be smaller than the HadCRUT4 uncertainties. Since only the HadCRUT4 uncertainties span the range of values for ΔT from the seven data records in a somewhat realistic fashion, we have decided to use these uncertainties uniformly throughout the analysis.

Section 2.2.1 also says “We then adjust each data set to the HadCRUT5 pre-industrial baseline as

described in the supplement”. The mean of the HadCRUT5 GMST record from 1850-1900 is -0.3589°C . We add 0.3589°C to each value of the HadCRUT5 record to adjust the data set onto the pre-industrial baseline. We use this same offset for all of the other data sets. We add 0.3589°C to each value of ΔT from the six data sets to match the HadCRUT5 1850-1900 baseline.

Section 2.2.3 states “Figure S6 shows the ozone RF time series used in this analysis and the supplement provides more information about the creation of the time series for the RF due to O_3^{TROP} ”.

Figure S6 displays the time series of tropospheric ozone RF used in our analysis for the various SSPs. Tropospheric ozone is an important GHG that rivals nitrous oxide as the third most important anthropogenic GHG. We include the RF due to tropospheric ozone (O_3^{TROP}) in our model for completion, even though the SSP database does not provide RF estimates for the various SSPs. We use values from the RCP scenarios provided by the Potsdam Institute for Climate Impact Research (Meinshausen et al., 2011). The values of the RF due to O_3^{TROP} for SSP1-1.9 and SSP1-2.6 are from the RCP2.6 pathway. The RCP4.5 time series of O_3^{TROP} is used for SSP2-4.5, the RCP6.0 time series is used for SSP4-6.0, and the RCP8.5 time series is used for SSP5-8.5. We create linear combinations of RCP2.6 and RCP8.5 to generate two new time series of the RF due to O_3^{TROP} for SSP4-3.4 and SSP3-7.0. There is a large gap between the time series of the RF due to O_3^{TROP} for RCP6.0 (shown as SSP4-6.0) and RCP8.5 (shown as SSP5-8.5) in Fig. S6. We created a time series that would split the difference between the two RCPs to represent the RF due to O_3^{TROP} for SSP3-7.0. The SSP4-3.4 time series of the RF due to O_3^{TROP} that was created lies in between the RCP2.6 (shown as SSP1-2.6) and RCP4.5 (shown as SSP2-4.5) time series in Fig. S6.

Section 2.2.8 states “Figure S9 shows the five OHC records as well as the multi-measurement

average”. Figure S9 displays the five OHC content data sets, as well as the multi-measurement average, plotted as a function of time and normalized to year 1986. This figure illustrates how the shapes of the different OHC records compare. Each of the time series represents the amount of heat stored in the top 700 m of the world’s oceans for that specific data set. Carton et al. (2018) is the shortest data set, and only spans 36 years (1982-2017). The second shortest record is Balmaseda et al. (2013a), which spans 52 years (1958.5-2009.5). Ishii et al. (2017) is the record in the middle with a range of 63 years (1955-2017). Both Cheng et al. (2017) and Levitus et al. (2012) have records that span 65 years (1955-2019). The length of the data set and the shape of the curve affect the estimate of ocean heat export (OHE), because we calculate OHE by taking a linear fit to the full OHC time series. Balmaseda et al. (2013a) has the lowest estimate of OHE because the slope of the curve is relatively shallow, due to the fact that it slightly rises, then decreases at the

start of the record. Carton et al. (2018) has the highest estimate of OHE because the slope of the curve is the steepest of the five records.

Section 2.2.8 also says “For these five OHC data sets, uncertainty estimates are not always provided. Furthermore, some studies that do provide uncertainties give estimates that seem unreasonably small (see Fig S10 and the supplement)” and “Figure S10 and the supplement provide more detail on the creation of this time dependent uncertainty estimate for OHC”. Figure S10 shows the multi-measurement average as well as the five OHC data records as a function of time, the uncertainty for each corresponding data set, and the combined uncertainty used in this analysis. Panel (a) shows the multi-measurement OHC average with the standard deviation of the mean plotted around the average time series. The standard deviation is large at the beginning of the time series, due to the spread in the estimates of OHC between the different records (illustrated in Fig. S9). The standard deviation decreases as the various OHC records converge near a similar estimate. The standard deviation is zero in 1986 because we normalized all of the time series to zero in this year to create the multi-measurement average. Because of this normalization, the standard deviation of the mean is not a realistic measure of uncertainty for the five OHC time series.

Panels (b), (c), (d), (e), and (f) display the uncertainty estimates for the five OHC data records. We use the standard deviation of the mean of five ensemble members of the European Centre for Medium-Range Weather Forecasts Ocean ReAnalysis System 4 (ORSA) (Balmaseda et al., 2013b) for the Balmaseda et al. (2013a) record. The standard deviation is plotted in panel (b) as the dotted blue line. The standard deviation is small at the beginning of the record, because the five ensemble members started at similar values of OHC in 1958 and diverged over time. The combined uncertainty of the standard deviation of the average of the five OHC records and the Cheng et al. (2017) estimate is plotted as a dashed blue line. Panel (c) shows the Levitus et al. (2012) time series for the top 700 m updated to the end of 2019. The Levitus time series utilizes the standard error over the whole ocean for their uncertainty estimate and is plotted as the dotted light blue line. The standard error is a very small uncertainty estimate compared to the other OHC data records, which is unreasonable considering the large variations in OHC between the different records. We use the standard deviation of eight reanalysis experiments to represent the uncertainty associated with the Carton et al. (2018) OHC record and is plotted as a dotted orange line in panel (e). The standard deviation of the eight reanalysis experiments is rather small, which also is unrealistic. Panel (f) displays the Cheng et al. (2017) OHC record updated through the end of 2019 with the 1σ uncertainty. This uncertainty does not vary much throughout the data record, making it more realistic as an estimate for such an uncertain quantity as OHC. We created the combined uncertainty estimate of the standard deviation of the average of the five OHC records and the Cheng et al. (2017) 1σ uncertainty to have the largest uncertainty possible due to the fact that OHC varies between the different records. The EM-GC cannot achieve $\chi^2_{\text{OCEAN}} \leq 2$ for Balmaseda et al. (2013a), Levitus

et al (2012), and Carton et al. (2018) using their own respective estimates of uncertainty. Creating one uncertainty estimate to be used for all of the OHC records provides consistency and allows the EM-GC to achieve good fits between the observed and modeled OHC.

Section 2.3 states “Figure S12 illustrates the REG method used to determine AAWR from the CMIP6 GCMs”. Figure S12 shows the change in ΔT from 1975-2014 from the CMIP6 GCMs and the contribution of SAOD from 1975-2014. There was about a 6 month lag between the response of ΔT and enhancements of SAOD following the eruption of Mount Pinatubo in June 1991 (Douglass and Knox, 2005; Thompson et al., 2009); a 6 month delay for the response of ΔT to SAOD is commonly used in regression analyses of the actual temperature record (Foster and Rahmstorf, 2011; Lean and Rind, 2008). The time needed for ΔT to respond to a change in the aerosol loading in the stratosphere due to a volcanic eruption in each GCM can exhibit a significant difference compared to this empirically determined response time. Therefore, a lag was determined for each GCM by calculating the value of the monthly delay that resulted in the largest regression coefficient for SAOD (versus ΔT). Due to the difference in model physics between the various GCMs, the value of the delay between the volcanic forcing and surface temperature response ranged from 0 to 11 months. The effect of SAOD on ΔT for the 50 GCMs is shown in Fig. S12d. Figure S12b shows the residual in ΔT after removing the influence of SOAD, and the median value of AAWR from the CMIP6 multi-model ensemble is plotted as a linear line. Figure S12c shows the human component of global warming, $\Delta T_{\text{ATM,HUMAN}}$, from the EM-GC. A linear fit and quadratic fit are shown to illustrate that $\Delta T_{\text{ATM,HUMAN}}$ is almost nearly linear from 1975-2014, supporting the approximation of $\Delta T_{\text{ATM,HUMAN}}$ as a linear function from 1975-2014 for the REG calculation.

Section 2.3 also states “Figure S13 and the supplement compare values of AAWR found using the REG method applied to EM-GC output with values of AAWR found using Eq. (9), as support for the validity of using the REG method to determine AAWR from CMIP6 output”. We applied the REG method to the EM-GC simulations to check the validity of the REG method. We regressed the modeled ΔT time series from the EM-GC for an AER $\text{RF}_{2011} = -0.9 \text{ W m}^{-2}$ simulation with SAOD and applied a 6 month lag. A linear function is used to represent the anthropogenic effect on temperature from 1975-2014. Fig. S13 shows the results of using the REG method on output of the EM-GC.

The value of AAWR from the EM-GC determined using the REG method is $0.188^{\circ}\text{C} \frac{\text{decade}^{-1}}{\text{decade}}$, compared to $0.167^{\circ}\text{C} \frac{\text{decade}^{-1}}{\text{decade}}$ using Eq. (9) (Fig. S13c and Fig. 1). There is a $0.021^{\circ}\text{C} \frac{\text{decade}^{-1}}{\text{decade}}$ difference between the two methods. This difference arises because the REG method, when applied to the EM-GC modeled ΔT time series, includes the contribution of AMOC in the value of AAWR

(Fig. S13c). Figure 1 of our paper illustrates that AMOC contributes about $0.025^{\circ}\text{C}_{\text{decade}^{-1}/\text{decade}}$ to the rise in ΔT . If we include AMOC as a regressor variable to the REG method, we obtain a value of AAWR of $0.161^{\circ}\text{C}_{\text{decade}^{-1}/\text{decade}}$ from the output of the EM-GC (Fig. S13g).

The close agreement of values of AAWR from the REG method once we account for AMOC and Eq. (9) supports the validity of the REG method to determine AAWR from CMIP6 output. We do not explicitly use AMOC as a regressor variable when applying the REG method to CMIP6 GCMs for two reasons. The first reason is that GCMs have been shown to underestimate key aspects of the Atlantic multidecadal oscillation and are unable to simulate the many oceanic and atmospheric footprints of AMOC (Kavvada et al., 2013). The second reason is that CMIP6 GCM historical runs do not use prescribed SSTs. If the CMIP6 GCMs are representing AMOC, it is a random signal that is averaged out when we analyze the 50 GCMs in order to calculate AAWR.

Section 2.3 also says “Analysis of AAWR for these 50 GCMs of LIN versus REG (see Fig. S14)...”. Figure S14 shows the similarity between the values of AAWR determined using the LIN and REG methods. The ratio between the values of AAWR determined utilizing LIN and REG is 1.009, indicating there is only about a 0.9% difference in the values of AAWR using the two methods. Figure S14 also shows the values of AAWR that are below the maximum value of AAWR determined by the EM-GC utilizing the HadCRUT5 temperature record (blue) and the values that are above the maximum (red). Less than half of the GCMs result in values of AAWR less than the maximum value from the EM-GC and more than half of the GCMs result in values of AAWR greater than the maximum value from the EM-GC utilizing the HadCRUT5 GMST record.

Section 2.4 states “For the estimate of $\text{ECS}_{\text{climate sensitivity}}$ from the CMIP6 multi-model ensemble, we use the method described by Gregory et al. (2004) (See the supplement and Fig. S15 for more information)”. To use the Gregory method, near surface air temperature output from the Abrupt $4\times\text{CO}_2$ and piControl simulations, as well as net downward radiative flux output from the Abrupt $4\times\text{CO}_2$ simulation is used to calculate ECS. The near surface air temperature and net downward radiative flux was converted from monthly gridded output to annual global averages. We calculate the temperature change for the Abrupt $4\times\text{CO}_2$ simulation by subtracting the piControl near surface air temperature (Chen et al., 2019) (Fig. S15). This computed temperature anomaly is then regressed against the net downward radiative flux, with the x-intercept yielding the $\text{equilibrium-response}$ of ΔT to a quadrupling of CO_2 . This $\text{equilibrium-response}$ is then divided by two (Jones et al., 2019) to arrive at the $\text{equilibrium-effective}$ climate sensitivity (Fig. S15).

Section 2.5 states “See Fig. S16 for unweighted ECS values and Section 3.2 states “See Fig S16 for results without aerosol weighting”. Figure S16 displays the values of ECS using the EM-GC and the CMIP6 multi-model ensemble. The EM-GC box contains the 25th, 50th, and 75th percentiles, the whiskers denote the 5th and 95th percentiles, and the stars represent the minimum and maximum values of ECS. The box labeled CMIP6 is unchanged from Fig. 7. The values of ECS are not treated with the aerosol weighting described in Sect. 2.5. This figure shows that most of the estimates of ECS found using the EM-GC are concentrated towards small values of ECS, due to the fact that the majority of the EM-GC model runs with good fits to the climate record (χ^2_{ATM} , χ^2_{RECENT} , and χ^2_{OCEAN}) have weak aerosol cooling and low values of λ_{Σ} (Fig. 5b). We use the aerosol weighting method to assign the same weights for the IPCC 2013 “likely” range limits of AER RF₂₀₁₁ of -0.4 and -1.5 W m^{-2} at the one sigma values of a Gaussian, and the -0.1 and -1.9 W m^{-2} are at the two sigma values of a Gaussian. Using the aerosol weighting method adjusts our estimates of ECS so that the calculated percentiles occur at higher values.

Section 3.2 in the Fig. 8 caption says, “See supplement for the confidence intervals plotted for each study”. All of the studies except Dessler et al. (2018), Rugenstein et al. (2020), IPCC 2013, and Zelinka et al. (2020) have the 5 to 95% confidence intervals shown. The 66% confidence intervals are shown for IPCC 2013, and the minimum and maximum are shown for Dessler et al. (2020), Rugenstein et al. (2020) and Zelinka et al. (2020).

The Fig. 8 caption in Sect. 3.2 also refers to the supplement for information about which studies are estimating effective climate sensitivity or equilibrium climate sensitivity. We designate each study based on information found in their manuscripts if their analysis uses the Gregory et al. (2004) method or infers climate feedback from the historical climate record will persist until equilibrium. The use of either of these two factors results in our designation of effective climate sensitivity (Gregory et al., 2004; Sherwood et al., 2020; Tokarska et al., 2020a; Zelinka et al., 2020). Based on our examination of IPCC 2013, it seems their estimate is a combination of effective climate sensitivity and equilibrium climate sensitivity.

Section 3.3.4 states “see Fig. S21 and the supplement” and “see the supplement for more information”. Figure S21 shows the rise in ΔT from pre-industrial for SSP5-8.5 versus the cumulative emissions of CO₂, in Gt C, since 1870. The colored lines denote the probability of reaching at least that temperature by the end of century. The large spread in projections of future ΔT is driven by the uncertainty in AER RF. The computed probabilities are based on the aerosol weighting method, so the uncertainty in

AER RF is considered when determining the likelihood of achieving the Paris Agreement target of 1.5°C and upper limit of 2.0°C for the cumulative carbon emissions.

We use the uncertainty suggested by coupled atmospheric / carbon cycle models in how atmospheric CO₂ will respond to the prescribed carbon emissions. Examination of Fig. 2 and Table 3 from Friedlingstein et al. (2014) and Fig. 9b from Murphy et al. (2014) led to our determination that the uncertainty in estimates of atmospheric CO₂ from emissions driven runs of CMIP5 coupled atmospheric / carbon cycle models is about 10% (1σ). We include this 10% uncertainty in our determination of the carbon budgets for each probability of achieving the Paris Agreement target and upper limit shown in Table 2.

Section 3.3.6 states “Figure S23 is identical to Fig. 14, except for the use of no delay between the RF perturbations and the response of climate feedback, see Fig. S23 and the supplement for results without the time delay”. Figure S23 shows the effect of time variant λ^{-1} , assuming with an instantaneous response between λ^{-1} and a change in radiative forcing for a simulation using a value of AER RF₂₀₁₁ = -0.9 W m⁻². The instantaneous response causes the modeled ΔT to deviate more from the observed temperature than ~~the~~ results found using the ~~20-year~~32.5-year delay in the response (Fig. S23g, h versus Fig. 14g, h). The deviation between the modeled and observed ΔT does not allow for a large change in λ^{-1} over time to still achieve the $\chi^2_{\text{ATM}} \leq 2$ and $\chi^2_{\text{RECENT}} \leq 2$ constraints. The deviation between modeled and observed ΔT in Fig. S23d resembles the behavior of some CMIP6 GCMs (see Fig. 9 and Tokarska et al. (2020b)).

Section 3.3.6 also states “In Figs. 14 and S23 we also analyze a RF scenario termed SSP2-4.5' that serves as a doubled CO₂ scenario (dotted lines)”. In the SSP2-4.5' simulation, only CO₂ is allowed to change after the end of 2019. All other GHGs and aerosols are kept constant at their December 2019 values. This simulation allows us to examine the effect of time variant λ^{-1} on changes in ΔT due only to the future rise in CO₂. In the SSP2-4.5 scenario, CH₄, tropospheric O₃, and ODSs decrease after 2019 leading to a future decline in RF, whereas N₂O and tropospheric aerosols result in a future increase in RF. When all of these RF are kept constant in the SSP2-4.5' scenario for the AER RF₂₀₁₁ = -0.9 W m⁻² scaling assumption, the terms result in a near balance out to 2100. For the weaker aerosol cooling scenario (AER RF₂₀₁₁ = -0.4 W m⁻²), the value of RF due to tropospheric aerosols is not large enough to completely offset the other GHGs that are held constant. Consequently, the SSP2-4.5' simulation (dotted line) results in slightly larger total RF and associated warming than the SSP2-4.5 scenario (solid line) shown in Fig. S24. For the stronger aerosol cooling scenario (AER RF₂₀₁₁ = -1.5 W m⁻²), the value of RF due to tropospheric aerosols is larger than the RF due to the other GHGs that are held constant, resulting in the SSP2-4.5' having a slightly lower total RF and associated warming than the SSP2-4.5 scenario (Fig. S25).

The effect of the uncertainty in AER RF₂₀₁₁ on ECS found using time dependent climate feedback (ECS _{$\lambda(t)$} in Main) is based on results shown in Figs. 14b, 24b, and 25c. If we apply the χ^2_{RECENT} constraint equally to the -0.4, -0.9, and -1.5 W m⁻² simulations, our new estimate of ECS _{$\lambda(t)$} is 3.52°C (range of 2.71 to 5.53°C)

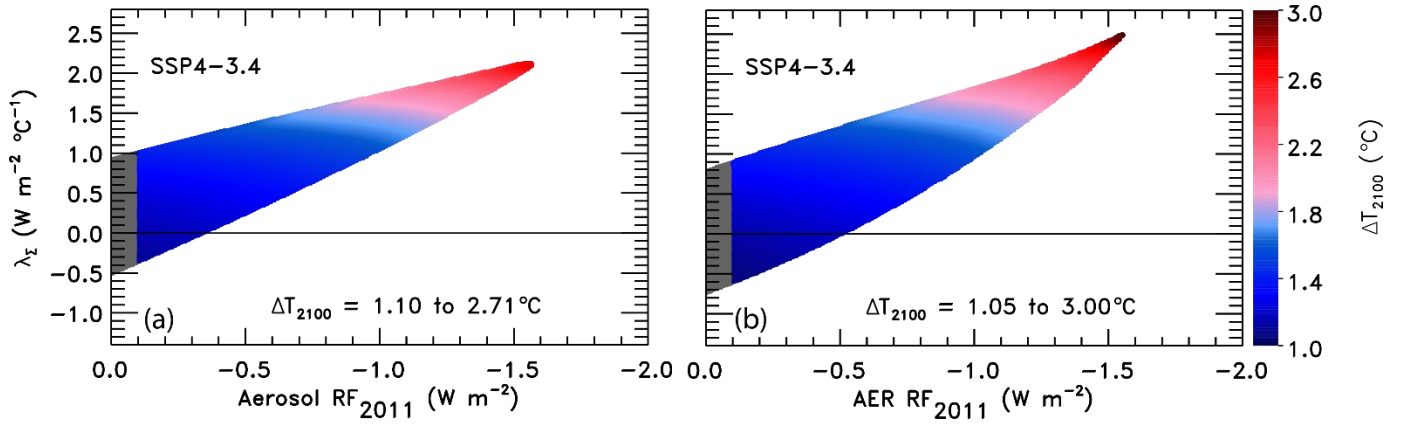


Figure S1. GMST anomaly in 2100 relative to pre-industrial (ΔT_{2100}) as a function of climate feedback parameter and $AER RF_{2011}$ for two versions of the EM-GC trained with the HadCRUT4 ΔT record. (a) The change in ΔT_{2100} for SSP4-3.4 using the original formulation of Eq. (2) where Q_{OCEAN} is subtracted outside of the feedback multiplicative term. (b) The change in ΔT_{2100} for SSP4-3.4 using the updated formulation of Eq. (2) where Q_{OCEAN} is subtracted within the feedback multiplicative term similar to Bony et al. (2006) and Schwartz (2012). The EM-GC is able to fit higher values of λ_{Σ} at strong aerosol cooling (around $-1.5 W m^{-2}$) for the new Eq. (2) compared to the original formulation in Canty et al. (2013) and Hope et al. (2017). The maximum value of future warming has increased due to the higher λ_{Σ} values.

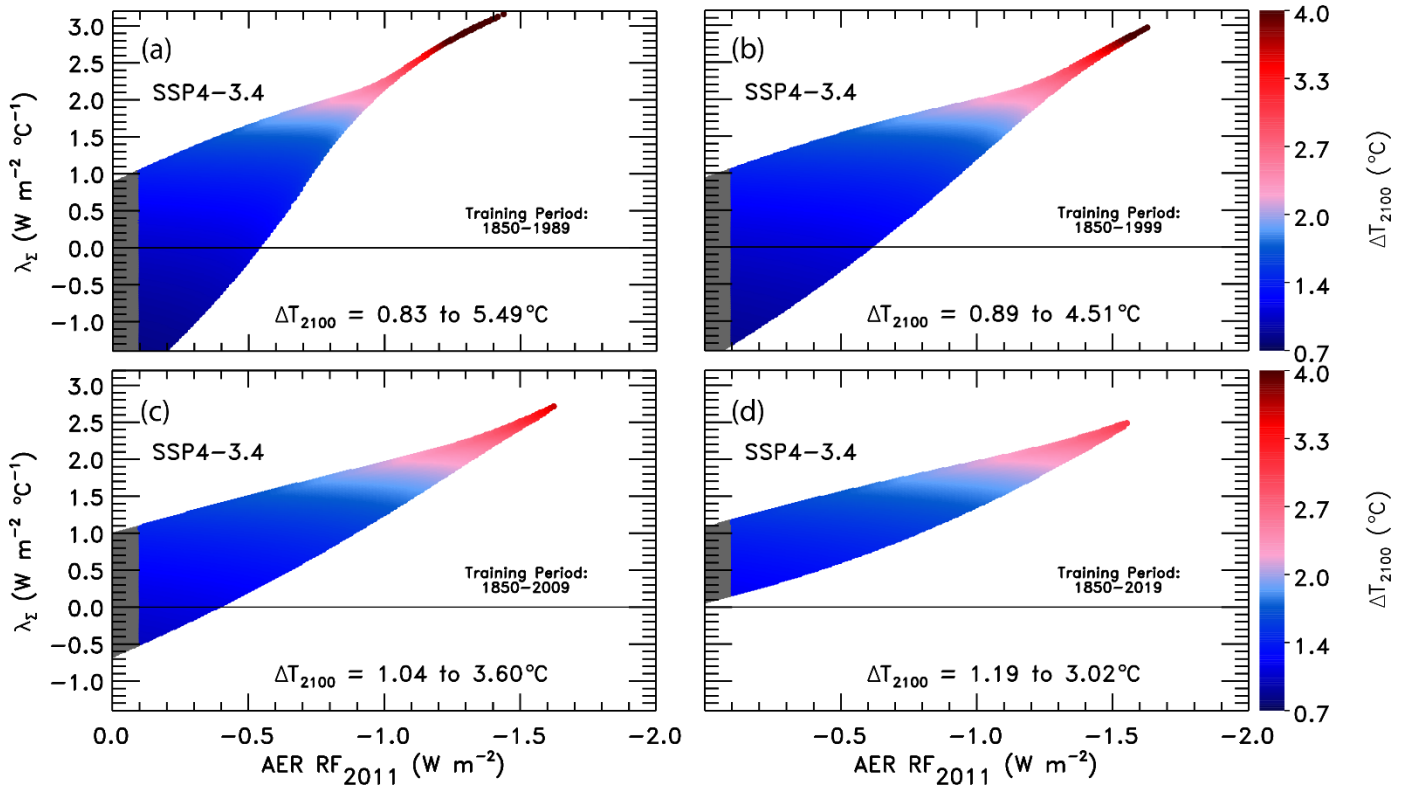


Figure S2. ΔT_{2100} as a function of climate feedback parameter and tropospheric aerosol radiative forcing in 2011 using the EM-GC trained with the HadCRUT5 ΔT record for SSP4-3.4. (a) Training period of 1850-1989. The region outside of the AER RF_{2011} range provided by IPCC 2013 is shaded (grey). Colors denote the GMST change in year 2100 relative to pre-industrial. The color bar is the same across all four panels for comparison. (b) Training period of 1850-1999. (c) Training period of 1850-2009. (d) Training period of 1850-2019, which is the normal training period used in our analysis.

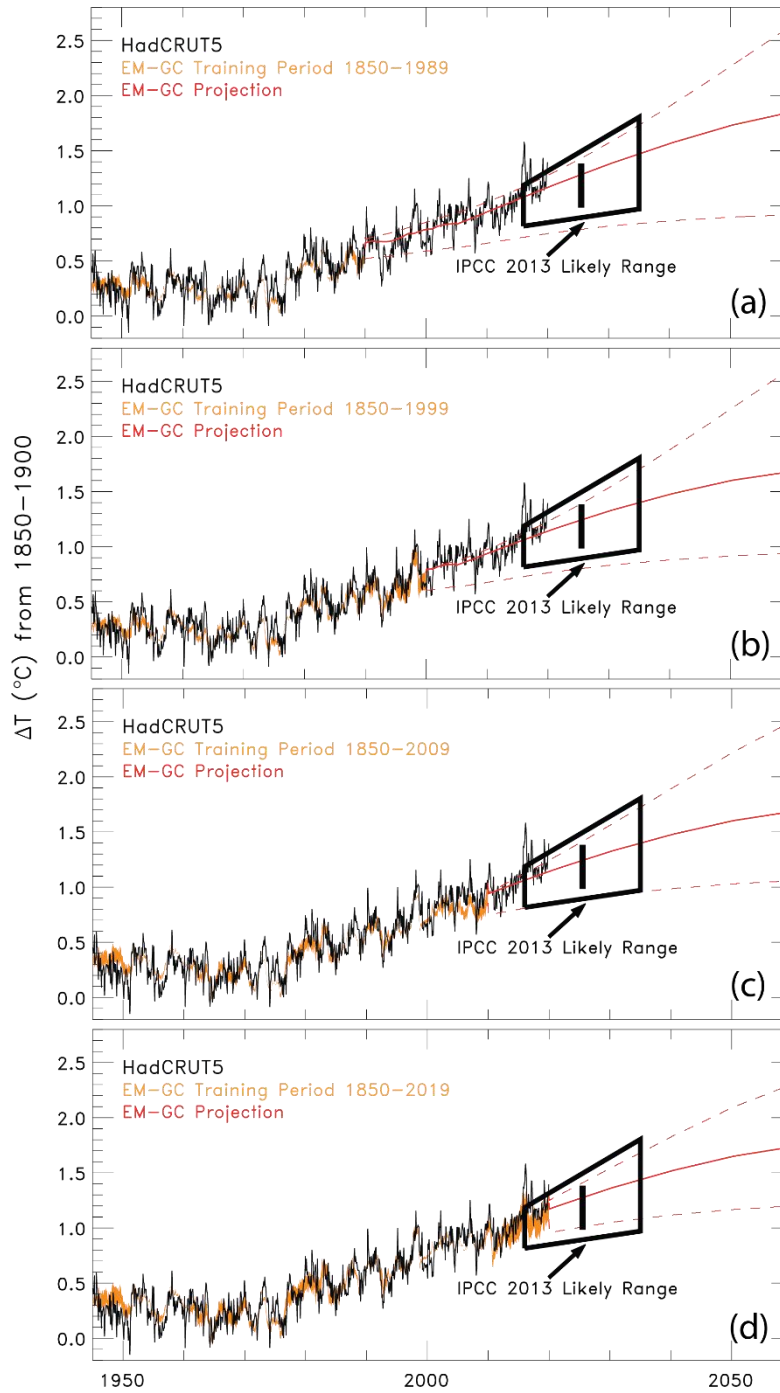


Figure S3. Observed and modeled GMST anomaly relative to 1850-1900 from 1945-2060 for four training periods. (a) Observations from HadCRUT5 (black), the EM-GC ΔT simulation for a training period of 1850-1989 (orange) of HadCRUT5, and the EM-GC projections for SSP4-3.4 out to 2060. Three EM-GC projections are shown in red: The best estimate of climate feedback for $\text{AER RF}_{2011} = -0.9 \text{ W m}^{-2}$, the lowest value of climate feedback that satisfies the χ^2 constraints for $\text{AER RF}_{2011} = -0.1 \text{ W m}^{-2}$, and the highest value of climate feedback that satisfies the χ^2 constraints (the value of AER RF_{2011} varies for each training period). The IPCC 2013 likely range of warming is denoted as the black trapezoid. (b) Training period of 1850-1999. (c) Training period of 1850-2009. (d) Training period of 1850-2019.

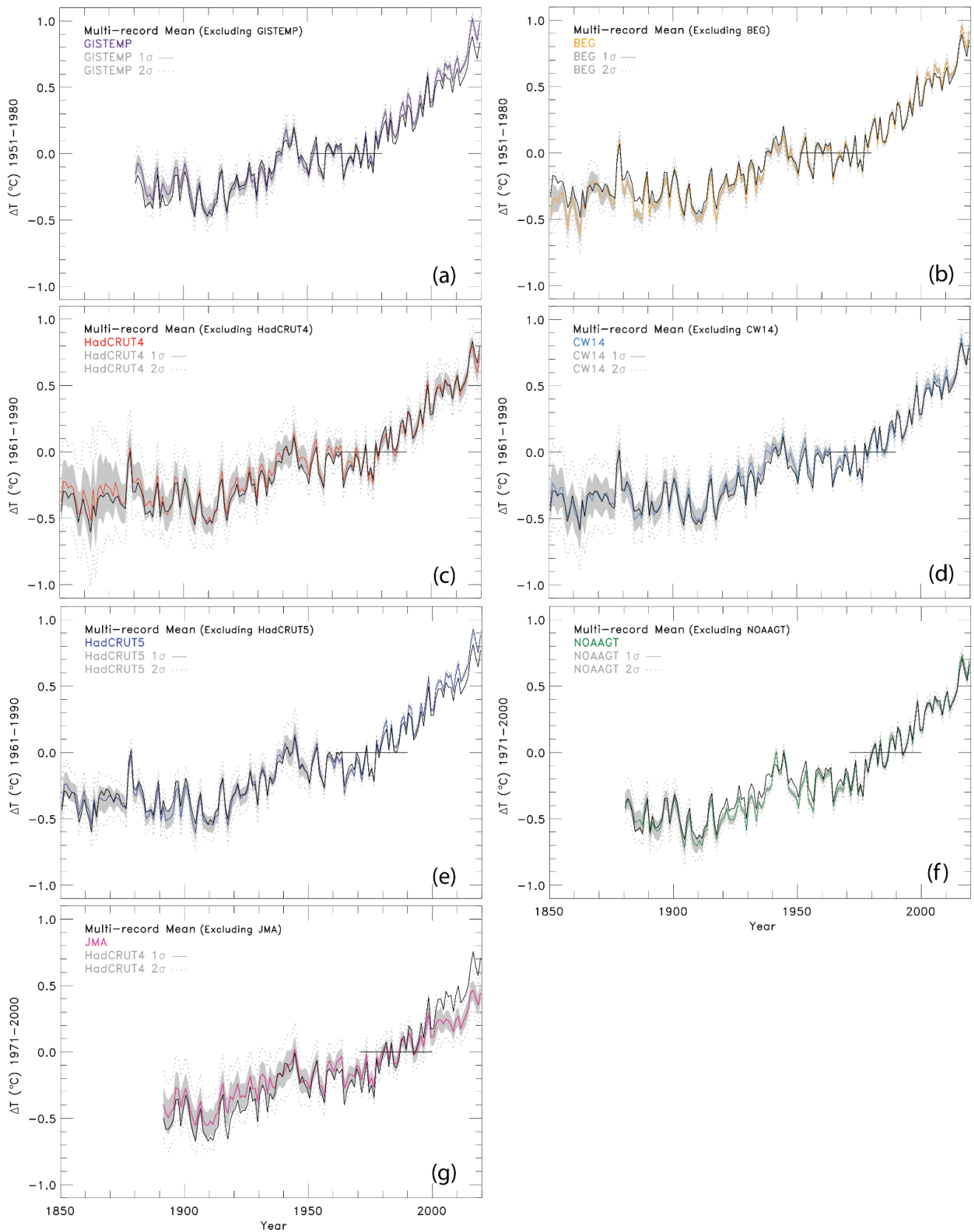


Figure S4. Annual GMST (ΔT) anomaly for seven data records relative to their individual baseline and the multi-record mean. The multi-record mean does not include the data set that is being shown. The 1 σ and 2 σ uncertainties for each GMST record are shown, and the horizontal line for $\Delta T=0$ spans the baseline used for the specific panel. (a) GISTEMP. (b) BEG. (c) HadCRUT4. (d) CW14. (e) HadCRUT5. (f) NOAAAGT. (g) JMA. Since the JMA data provider does not provide an uncertainty time series, the HadCRUT4 uncertainty is used.

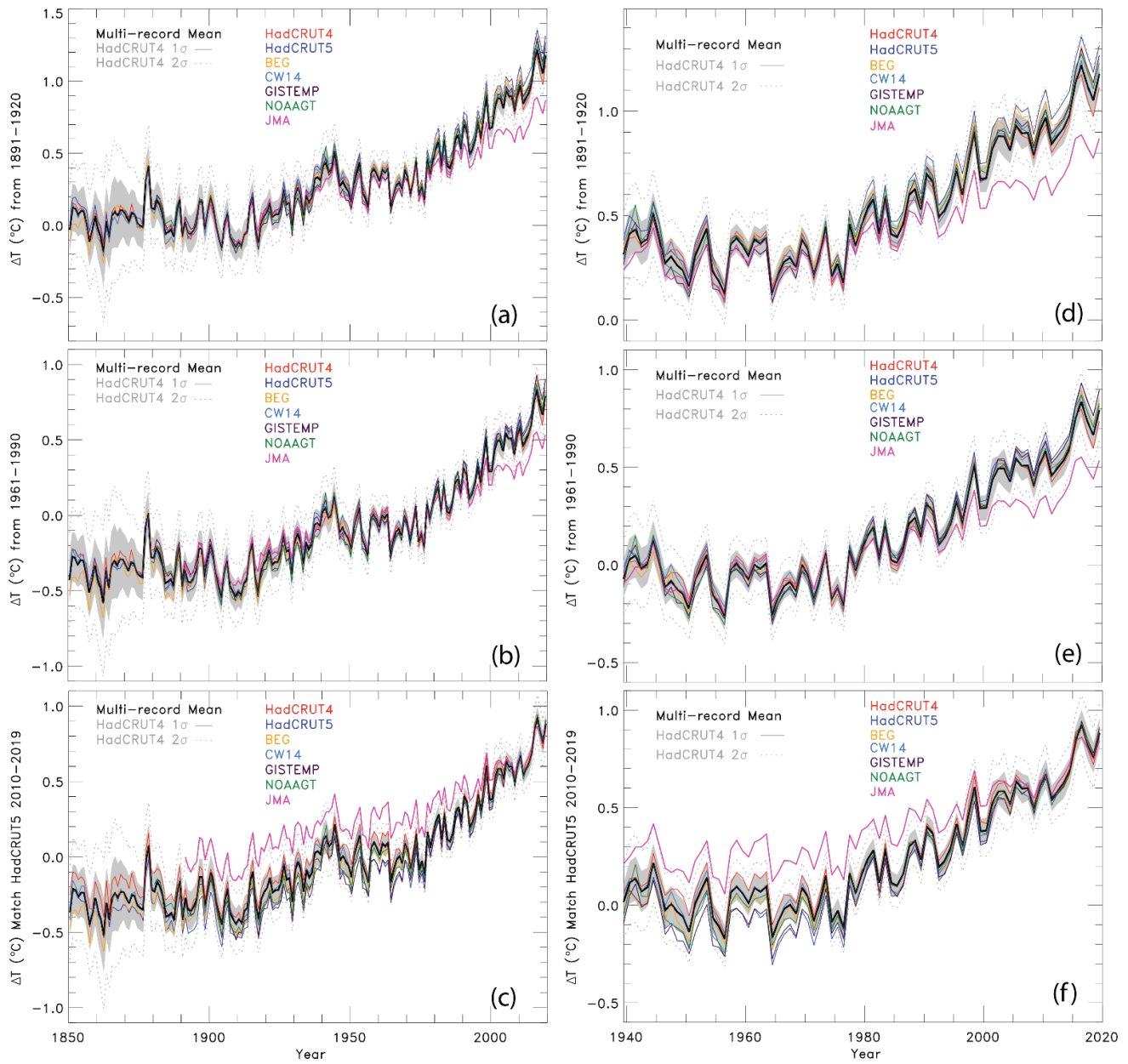


Figure S5. Annual GMST (ΔT) anomaly relative to several baseline periods for seven data records. The 1σ (shaded grey) and 2σ (dotted grey) HadCRUT4 uncertainties are plotted about the multi-model record mean (black). (a) Baseline of 1891-1920 plotted from 1850-2019. (b) Same as (a) using a baseline of 1961-1990. (c) Same as (a) except all of the ΔT records are forced to match the average ΔT anomaly over 2010-2019 given by HadCRUT5 that is relative to 1961-1990. (d) – (f) Same as (a) – (c) except plotted from 1940-2019.

Table S1. Percentage of annual values between 1940-2019 of the GMST record within the 1 sigma or 2 sigma HadCRUT4 uncertainties about the multi-record mean for each baseline period.

Baseline: 1891-1920			1σ			2σ		
	N _{WITHIN}	N _{TOTAL}	%	N _{WITHIN}	N _{TOTAL}	%		
HadCRUT4	77	80	96	80	80	100		
HadCRUT5	42	80	53	80	80	100		
CW14	80	80	100	80	80	100		
BEG	71	80	89	80	80	100		
GISTEMP	73	80	91	80	80	100		
NOAAGT	76	80	95	80	80	100		
JMA	29	80	36	54	80	68		
AVERAGE			80%			95%		

Baseline: 1961-1990								
HadCRUT4	80	80	100	80	80	100		
HadCRUT5	68	80	85	80	80	100		
CW14	80	80	100	80	80	100		
BEG	80	80	100	80	80	100		
GISTEMP	75	80	94	80	80	100		
NOAAGT	80	80	100	80	80	100		
JMA	27	80	34	48	80	60		
AVERAGE			88%			93%		

Match 2010-2019								
HadCRUT4	68	80	86	80	80	100		
HadCRUT5	47	80	59	76	80	95		
CW14	78	80	98	80	80	100		
BEG	77	80	96	80	80	100		
GISTEMP	47	80	59	79	80	99		
NOAAGT	73	80	61	80	80	100		
JMA	11	80	14	18	80	23		
AVERAGE			72%			88%		

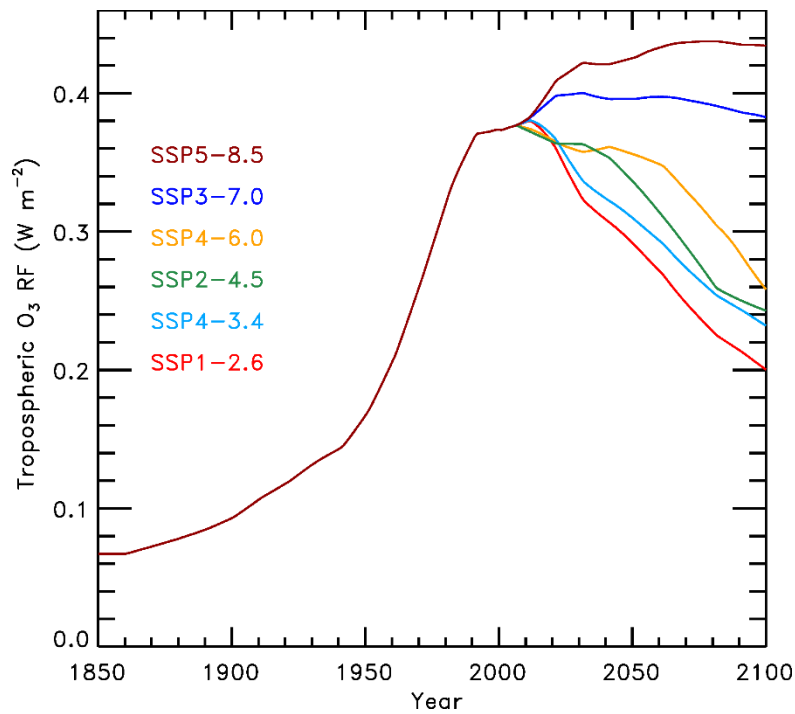


Figure S6. Radiative forcing of tropospheric ozone for the various SSPs analyzed in our study. The time series labeled SSP1-2.6, SSP2-4.5, SSP4-6.0, and SSP5-8.5 are from the corresponding RCP scenarios. We created the time series from SSP4-3.4 and SSP3-7.0 using linear combinations of the SSP1-2.6 and SSP5-8.5 time series.

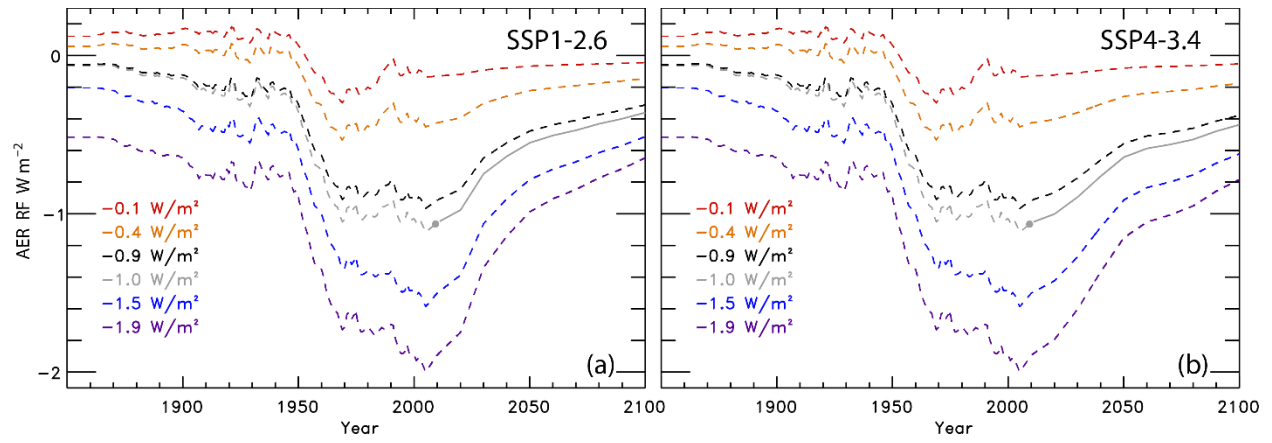


Figure S7. Radiative forcing time series due to tropospheric aerosols. (a) The RF time series due to tropospheric aerosols for SSP1-2.6. The solid grey circle denotes the value of AER RF₂₀₁₁ given by the SSP database. The solid grey lined labeled the -1.0 W m^{-2} time series is the AER RF time series given by the SSP database for SSP1-2.6. We appended a historical AER RF time series from the RCP scenarios and created five additional AER RF time series as described in Sect. 2.2.4. (b) Anthropogenic aerosol radiative forcing time series for SSP4-3.4.

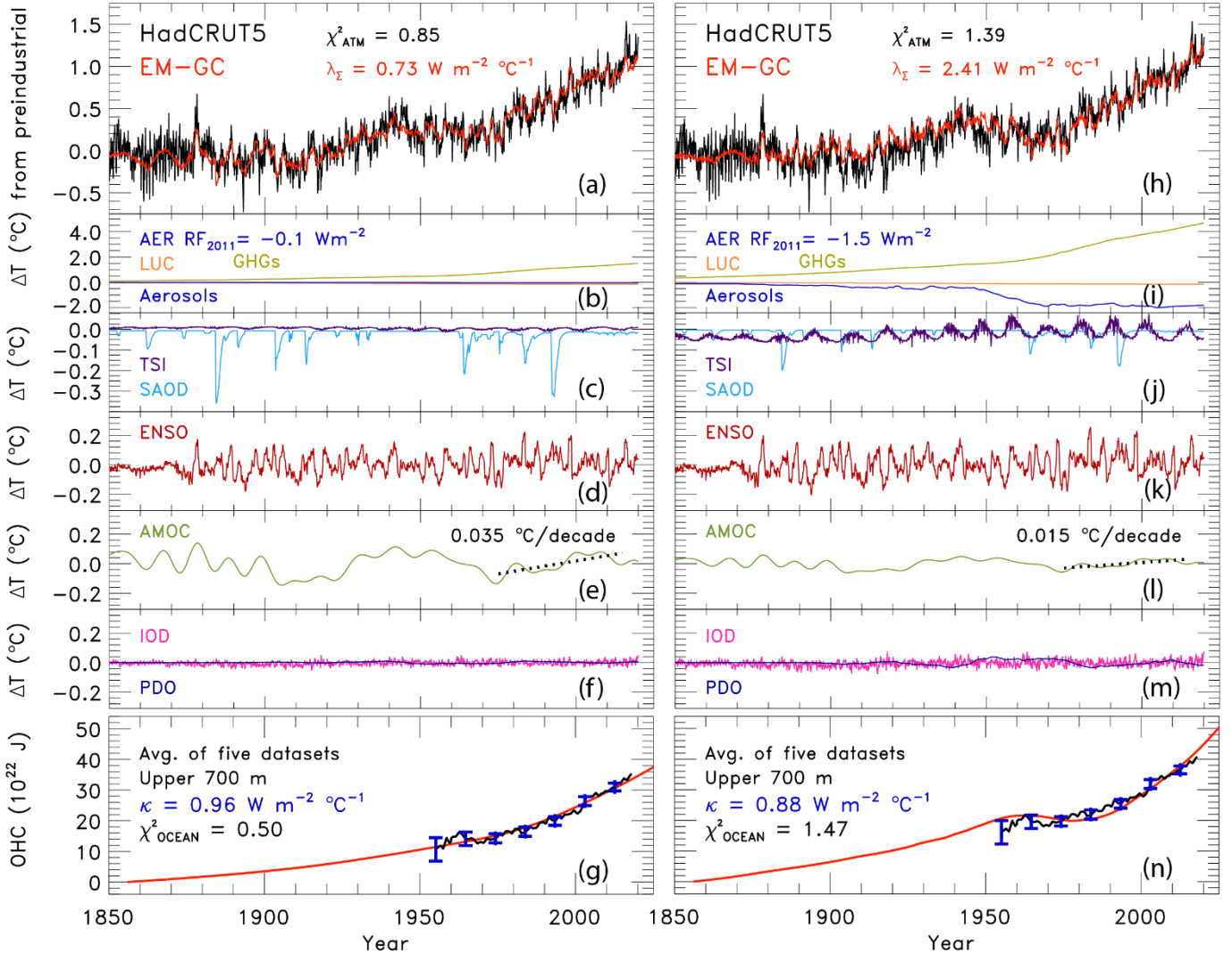


Figure S8. Measured (HadCRUT5) and modeled GMST anomaly (ΔT) relative to a pre-industrial (1850-1900) baseline for an $\text{AER RF}_{2011} = -0.1 \text{ W m}^{-2}$ and -1.5 W m^{-2} . (a) Observed (black) and modeled (red) ΔT from 1850-2019. This panel also displays the values of λ_{Σ} and χ^2_{ATM} (see text) for this best-fit simulation. (b) Contributions from total human activity. This panel also denotes the numerical value of the attributable anthropogenic warming rate from 1975-2014 (black dashed) as well as the 2σ uncertainty in the slope. (c) Solar irradiance (light blue) and major volcanoes (purple). (d) Influences from ENSO on ΔT . (e) Contributions from AMOC to ΔT and to observed warming from 1975-2014. (f) Influences from PDO (blue) and IOD (pink) on ΔT . (g) Measured (black) and modeled (red) ocean heat content (OHC) as a function of time for the average of five data sets (see text), the value of χ^2_{OCEAN} for this run, as well as the ocean heat uptake efficiency, κ , needed to provide the best-fit to the OHC record. The error bars (blue) denote the uncertainty in OHC used in this analysis (see Sect. 2.2.8). (h)-(n) Same as (a)-(g), except for $\text{AER RF}_{2011} = -1.5 \text{ W m}^{-2}$.

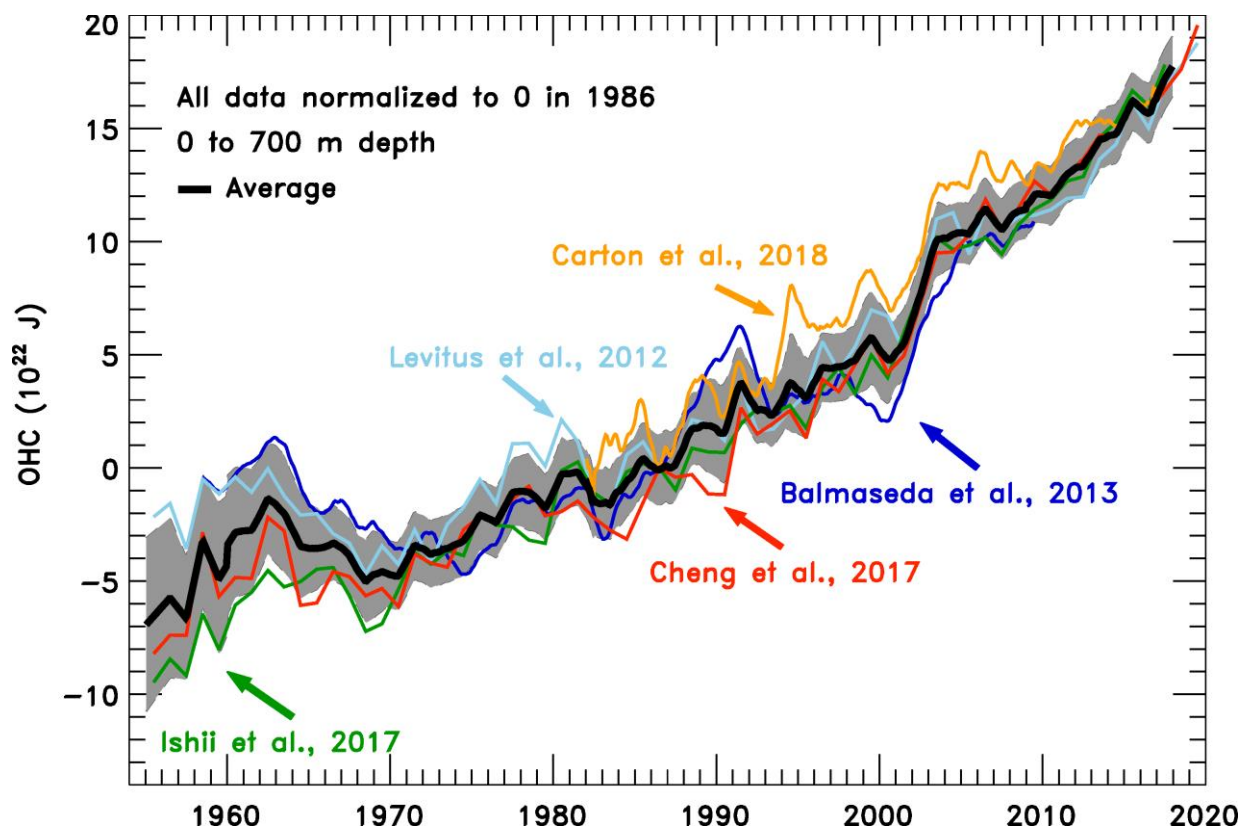


Figure S9. Ocean heat content time series. The five ocean heat content data records used in this analysis, normalized to the year 1986 because this year is in the middle of the average time series. The grey shaded region is the combined uncertainty estimate used in this analysis, centered around the average of the five data sets. The average of the ocean heat content records (1955 – 2017) is computed when there are three or more data sets available for a given year.

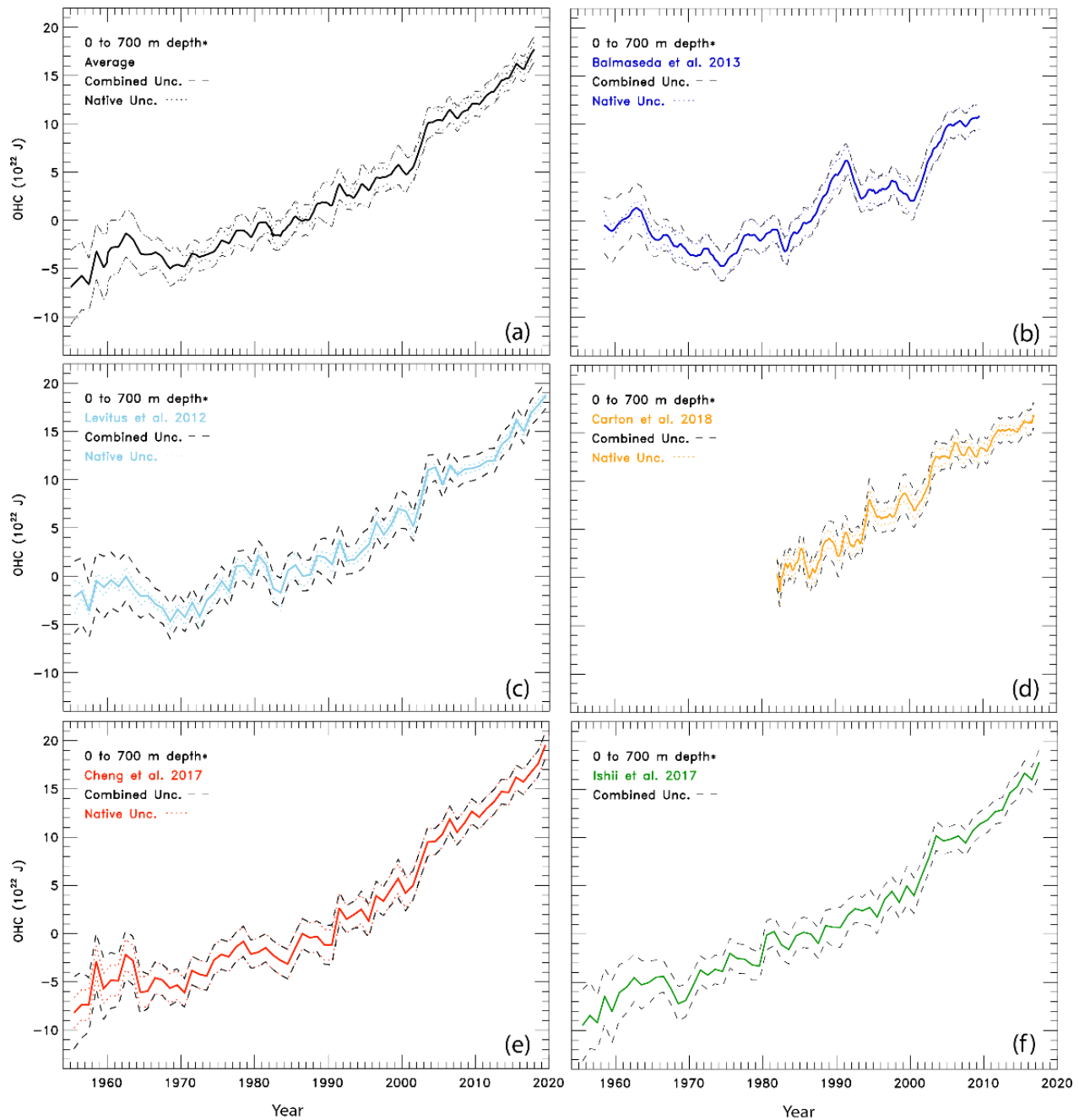


Figure S10. The ocean heat content records and uncertainty estimates analyzed in this study. (a) The average OHC record along with the standard deviation of the mean represented by the dotted black line, and the combined uncertainty of the 1σ standard deviation of the average of the five OHC records and the Cheng et al. (2017) estimates shown as the dashed black line. (b) Balmaseda OHC record with the standard deviation of the five ORSA ensemble members as the dotted line, and the combined uncertainty as the dashed line. (c) Levitus OHC record with the standard error as the native uncertainty, and the combined uncertainty. (d) Carton OHC record with the standard deviation of the mean of multiple ensemble members, and the combined uncertainty. (e) Cheng OHC record with the 1σ native uncertainty and the combined uncertainty. (f) Ishii OHC record with the combined uncertainty as the dashed line.

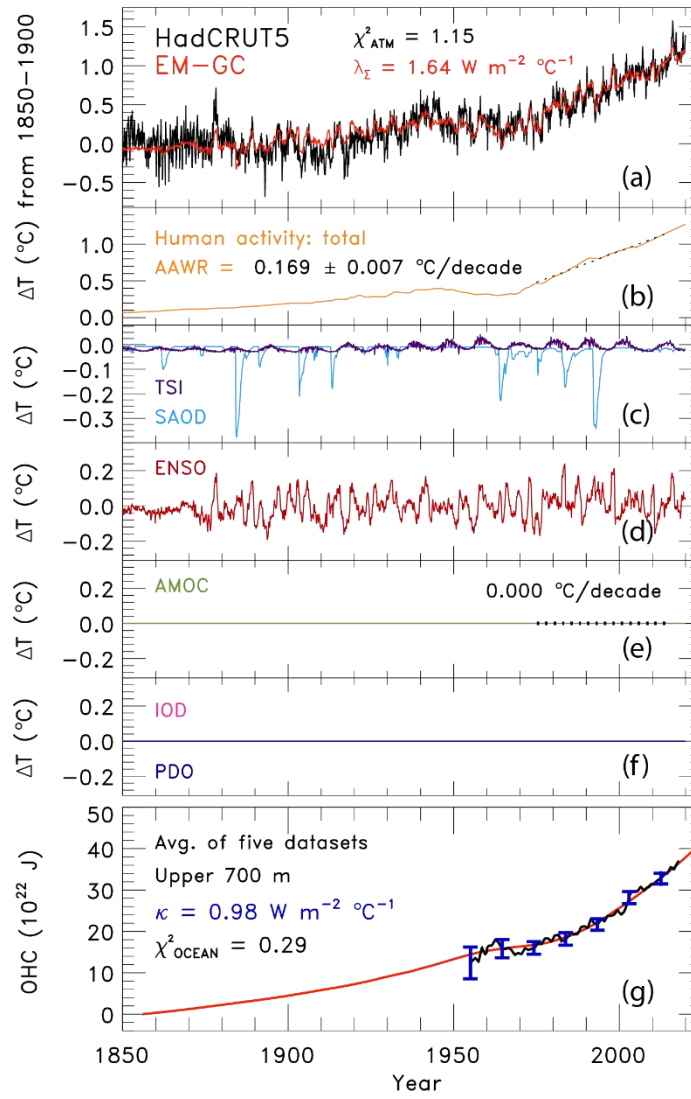


Figure S11. Measured (HadCRUT5) and modeled GMST anomaly (ΔT) relative to a pre-industrial (1850-1900) baseline without AMOC, PDO, and IOD. (a) Observed (black) and modeled (red) ΔT from 1850-2019. This panel also displays the values of λ_{Σ} and χ^2_{ATM} (see text) for this best-fit simulation. (b) Contributions from total human activity. This panel also denotes the numerical value of the attributable anthropogenic warming rate from 1975-2014 (black dashed) as well as the 2σ uncertainty in the slope. The estimates of AAWR show similar results if AMOC is or is not included (see Fig. 1b). (c) Solar irradiance (light blue) and major volcanoes (purple). (d) Influences from ENSO on ΔT . (e-f) Contributions from AMOC, PDO, and IOD to ΔT are set to zero (g) Measured (black) and modeled (red) ocean heat content (OHC) as a function of time for the average of five data sets (see text), the value of χ^2_{OCEAN} for this run, as well as the ocean heat uptake efficiency, κ , needed to provide the best-fit to the OHC record. The error bars (blue) denote the uncertainty in OHC used in this analysis (see Sect. 2.2.8).

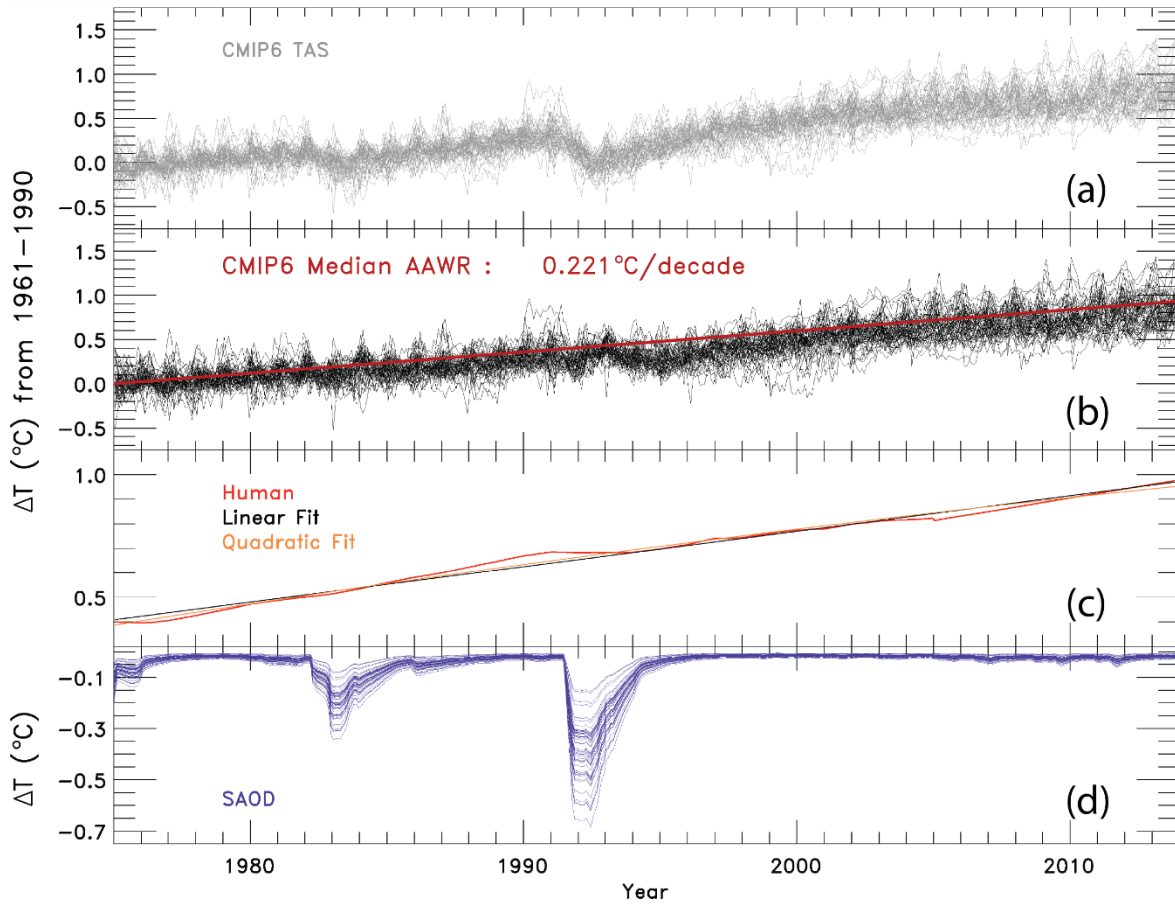


Figure S12. The change in GMST (ΔT) relative to 1961-1990 from the CMIP6 GCMs and the contribution from SAOD from 1975-2014. (a) ΔT from the 50 CMIP6 GCMs. (b) The residual in the change of GMST from the 50 CMIP6 GCMs after subtracting the contribution of SAOD determined by the updated REG method. The median value of AAWR is written on this panel and plotted in red. (c) The human component of global warming, $\Delta T_{\text{ATM,HUMAN}}$, from the EM-GC. A linear fit (black) and quadratic fit (red) are plotted on top to show that $\Delta T_{\text{ATM,HUMAN}}$ is almost exactly linear. (d) The contribution of SAOD in the 50 CMIP6 GCMs using a lag month calculated for each model.

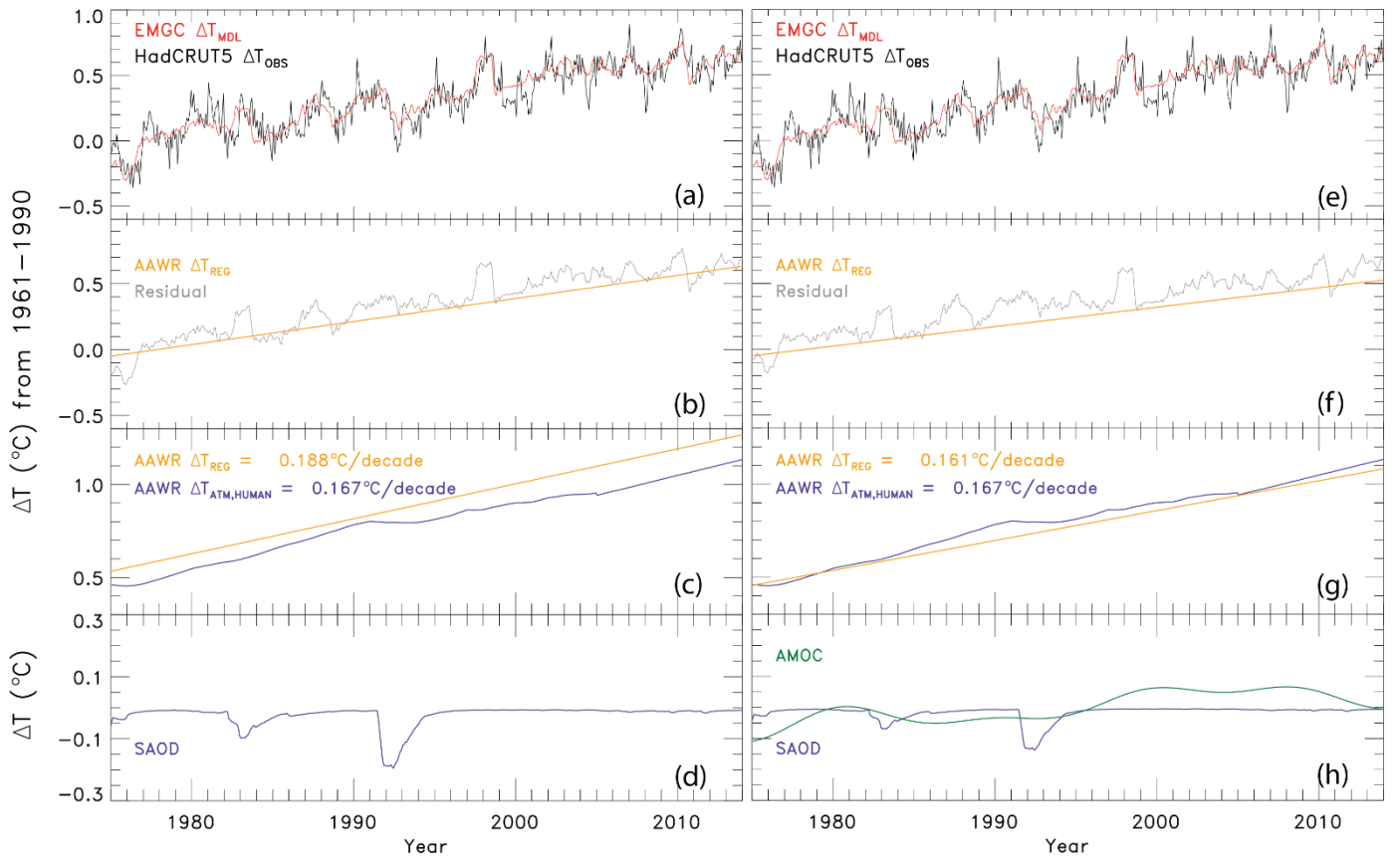


Figure S13. The change in GMST (ΔT) relative to 1961-1990 from observations and modeled output. (a) ΔT from HadCRUT5 and EM-GC simulation. (b) The residual in ΔT from the EM-GC simulation after subtracting the contribution of SAOD determined by the REG method (grey) and ΔT due to humans from the REG method (orange). (c) ΔT due to humans from the REG method (orange) and from the EM-GC (blue). The values of AAWR determined using the REG method and Eq. (9) are shown. (d) The contribution of SAOD to ΔT . (e) Same as (a). (f) Same as (b) but also subtracting the contribution of AMOC determined by the REG method. (g) Same as (c) but using AMOC as a regressor. (h) Same as (d) also showing the contribution of AMOC to ΔT found using the REG method.

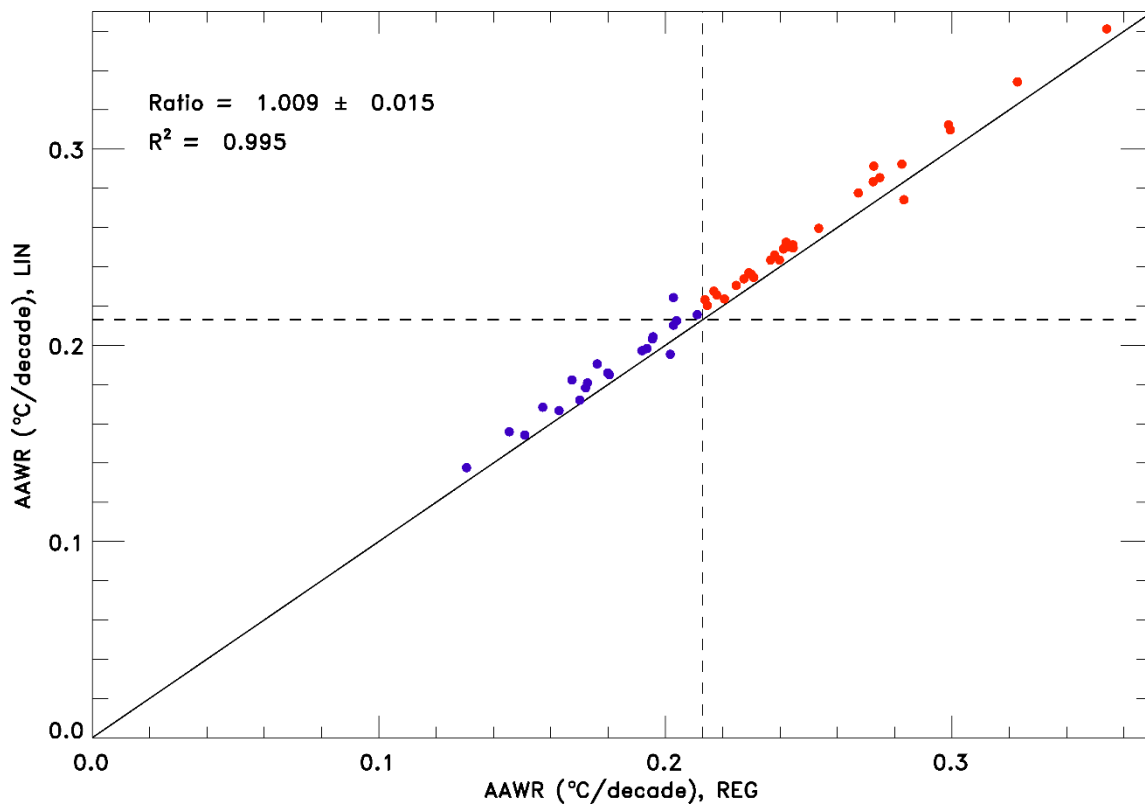


Figure S14. Values of AAWR for 50 CMIP6 GCMs using the LIN and REG methods. The solid black line is the 1:1 line and the vertical and horizontal dashed lines are the maximum value of AAWR determined using the EM-GC and the HadCRUT temperature record. The CMIP6 GCMs that have values of AAWR less than the maximum value from the EM-GC are blue, and the CMIP6 GCMs that have values of AAWR greater than the maximum value from the EM-GC are red. The slope, 1σ standard deviation, and R^2 of the values of AAWR from the CMIP6 GCMs are shown.

420

Table S2. Values of AAWR calculated using the EM-GC as a function of start and end year. The value of AAWR from 1975-2014 used in the main manuscript is shown in red. Each model run uses the best estimate of AER RF₂₀₁₁ (-0.9 W m^{-2}), the average of five OHC records, and the HadCRUT5 GMST record. The impact on varying the start and end year on AAWR is slight, except when a short record is used (i.e., 1984-2004, a 21-year span). A two-decade time span is not long enough to calculate an accurate estimate of AAWR. The value of AAWR is more sensitive to the choice of OHC or temperature record used than the chosen time span.

		Start Year					
End Year	AAWR ($^{\circ}\text{C}$ $\text{decade}^{-1}/\text{decade}$)	1970	1973	1975	1979	1982	1984
	2004	0.181 \pm 0.007	0.180 \pm 0.009	0.180 \pm 0.010	0.169 \pm 0.011	0.159 \pm 0.013	0.149 \pm 0.012
	2006	0.177 \pm 0.008	0.175 \pm 0.009	0.174 \pm 0.010	0.163 \pm 0.011	0.153 \pm 0.012	0.143 \pm 0.011
	2008	0.173 \pm 0.007	0.171 \pm 0.008	0.169 \pm 0.009	0.159 \pm 0.010	0.150 \pm 0.010	0.141 \pm 0.009
	2010	0.172 \pm 0.007	0.169 \pm 0.008	0.167 \pm 0.008	0.158 \pm 0.008	0.150 \pm 0.009	0.143 \pm 0.008
	2012	0.171 \pm 0.006	0.168 \pm 0.007	0.167 \pm 0.008	0.158 \pm 0.008	0.152 \pm 0.008	0.145 \pm 0.007
	2014	0.171 \pm 0.005	0.168 \pm 0.006	0.167 \pm 0.007	0.160 \pm 0.007	0.154 \pm 0.007	0.149 \pm 0.007
	2016	0.171 \pm 0.005	0.169 \pm 0.006	0.168 \pm 0.006	0.161 \pm 0.006	0.157 \pm 0.007	0.153 \pm 0.007
	2018	0.171 \pm 0.005	0.170 \pm 0.005	0.169 \pm 0.006	0.163 \pm 0.006	0.159 \pm 0.006	0.156 \pm 0.006

425

430

Table S3. Average values of AAWR calculated from the CMIP6 multi-model results using the regression method as a function of start and end year. The uncertainty corresponds to the 1σ standard deviation of AAWR found from the 50 GCMs. The value of AAWR from 1975-2014 used in the main manuscript is shown in red. The values of AAWR from the CMIP6 multi-model ensemble is more sensitive to the choice of start and end year than the EM-GC due to the small number of models. We use the same start and end year, 1975-2014, for the determination of AAWR for both the EM-GC and the CMIP6 multi-model ensemble for consistency.

		Start Year					
End Year	AAWR ($^{\circ}\text{C}$ <u>decade⁻¹/decade</u>)	1970	1973	1975	1979	1982	1984
	2004	0.185	0.196	0.200	0.208	0.224	0.230
	2006	0.192	0.203	0.207	0.216	0.232	0.238
	2008	0.196	0.207	0.211	0.220	0.234	0.241
	2010	0.200	0.209	0.214	0.222	0.236	0.241
	2012	0.204	0.213	0.218	0.226	0.239	0.244
	2014	0.208	0.217	0.222	0.230	0.242	0.247

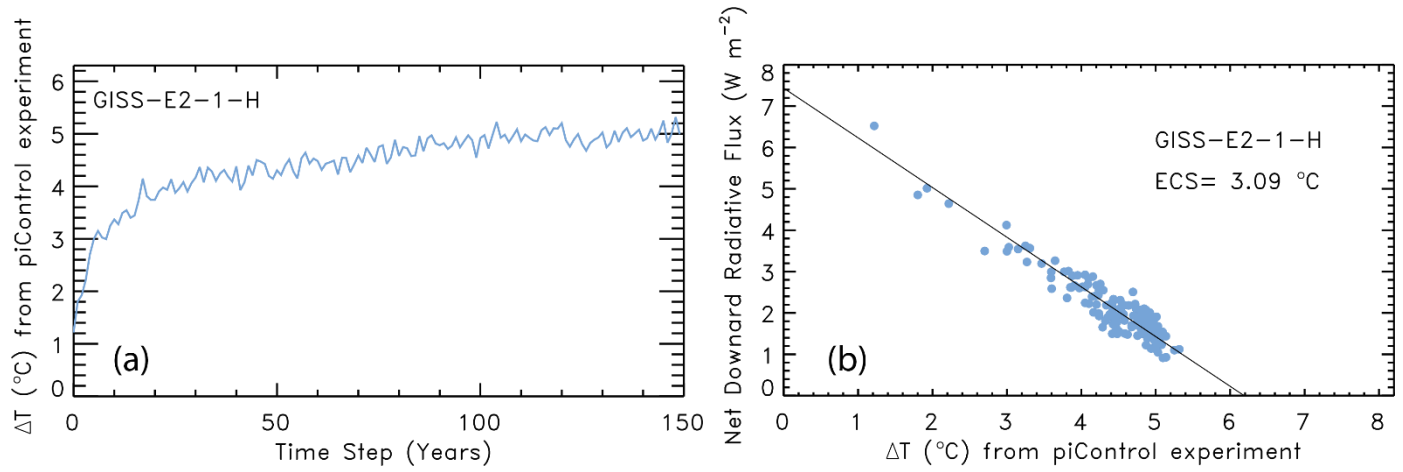


Figure S15. Steps for the calculation of ECS using the Gregory et al. (2004) method, using GISS-E2-1-H (Kelley et al., 2020) as an example. (a) The change in Abrupt 4xCO₂ GMST (variable: tas) from the piControl experiment for 150 years. (b) Abrupt 4xCO₂ net downward radiative flux (variable: rtmt) versus the Abrupt 4xCO₂ GMST change from the piControl experiment for 150 years. The x-intercept of the orthogonal linear least squares fit of the GCM output shown in panel (b), divided by two yields the equilibrium-effective climate sensitivity, which in this case is 3.09°C.

Table S4. Values of AAWR from 1975-2014 for the 50 CMIP6 multi-model Historical simulations available at time of the analysis (April 2020) for both the REG and LIN methods. The asterisk symbol (*) indicates there is only one run used to compute the value of AAWR for that GCM. No asterisk indicates the AAWR value shown in the table is the average of the values of AAWR for all runs of that model. The average ratio of LIN to REG for all 50 models is 1.009 ± 0.015 , shown at the bottom of the table and in Fig. S14. The correlation coefficient (r^2) of 0.995 is also shown. We conclude our determination of AAWR from the CMIP6 multi-model ensemble is accurate to $\pm 1\%$, which is much smaller than the difference between the CMIP6 multi-model ensemble values of AAWR and those found using the EM-GC framework.

Model	AAWR, REG (°C $\text{decade}^{-1}/\text{decade}$ de)	AAWR, LIN (°C $\text{decade}^{-1}/\text{decade}$ de)	Model	AAWR, REG (°C $\text{decade}^{-1}/\text{decade}$ de)	AAWR, LIN (°C $\text{decade}^{-1}/\text{decade}$ de)
ACCESS-CM2	0.211	0.216	GFDL-CM4*	0.243	0.250
ACCESS-ESM1-5	0.238	0.246	GFDL-ESM4	0.203	0.224
AWI-CM-1-1-MR	0.215	0.220	GISS-E2-1-G	0.194	0.198
BCC-CSM2-MR	0.217	0.228	GISS-E2-1-G-CC	0.204	0.213
BCC-ESM1	0.241	0.249	GISS-E2-1-H	0.237	0.244
CAMS-CSM1-0	0.131	0.138	HadGEM3-GC31-LL	0.283	0.292
CanESM5	0.354	0.361	HadGEM3-GC31-MM	0.227	0.234
CanESM5-CanOE	0.323	0.334	INM-CM4-8*	0.173	0.181
CAS-ESM2-0	0.196	0.204	INM-CM5-0	0.146	0.156
CESM2	0.240	0.243	IPSL-CM6A-LR	0.230	0.236
CESM2-FV2	0.221	0.224	KACE-1-0-G	0.254	0.260
CESM2-WACCM	0.273	0.291	MCM-UA-1-0	0.225	0.231
CESM2-WACCM-FV2	0.231	0.235	MIROC6	0.157	0.168
CIESM	0.245	0.251	MIROC-ES2L	0.163	0.167
CNRM-CM6-1	0.202	0.196	MPI-ESM1-2-HAM	0.180	0.186
CNRM-CM6-1-HR*	0.172	0.178	MPI-ESM1-2-HR	0.195	0.203
CNRM-ESM2-1	0.170	0.172	MPI-ESM1-2-LR	0.192	0.197
E3SM-1-0	0.267	0.278	MRI-ESM2-0	0.203	0.210
E3SM-1-1*	0.283	0.285	NESM3	0.242	0.253
E3SM-1-1-ECA*	0.275	0.274	NorCPM1	0.180	0.185
EC-Earth3*	0.299	0.310	NorESM2-LM	0.167	0.182
EC-Earth3-Veg*	0.214	0.223	NorESM2-MM*	0.151	0.154
FGOALS-f3-L	0.218	0.226	SAM0-UNICON*	0.245	0.250
FGOALS-g3	0.176	0.191	TaiESM1*	0.273	0.283
FIO-ESM-2-0	0.229	0.237	UKESM1-0-LL	0.299	0.312
Ratio = 1.009 ± 0.015			$R^2 = 0.995$		

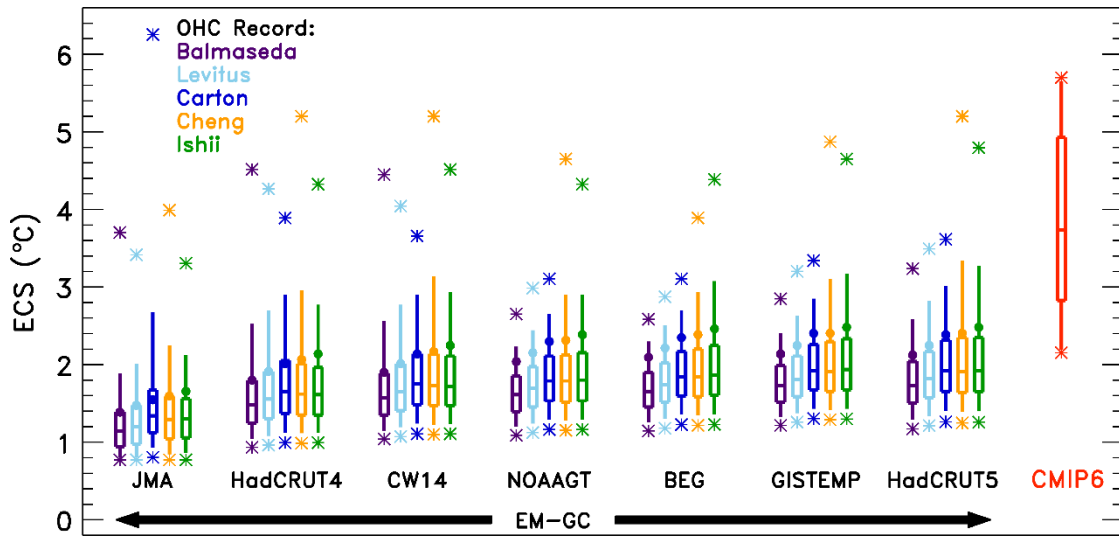


Figure S16. Values of ECS found using the EM-GC and the CMIP6 multi-model ensemble without the aerosol weighting method. Values of ECS utilizing the EM-GC are calculated using seven temperature data sets and five ocean heat content records (as indicated). The box represents the 25th, 50th, and 75th percentiles of the values of ECS and the whiskers denote the 5th and 95th percentiles for the different OHC records and each temperature record without using the aerosol weighting method (unweighted). The stars indicate the minimum and maximum values of ECS. The circles are the values of ECS associated with the best estimate of AER RF₂₀₁₁ of -0.9 W m^{-2} . The box labeled CMIP6 is the 25th, 50th, and 75th percentiles of the values of ECS from the CMIP6 multi-model ensemble, the whiskers indicate the 5th and 95th percentiles, and the stars represent the minimum and maximum values of ECS from the CMIP6 multi-model ensemble.

465 **Table S5.** Equilibrium-Effective climate sensitivity (ECS) from 28 CMIP6 GCMs. We can only calculate ECS for GCMs that provide Abrupt 4×CO₂ near surface air temperature (output variable: tas), net downward radiative flux (output variable: rtmt), and piControl near surface air temperature (output variable: tas) to the CMIP6 archive at time of the analysis (April 2020). All estimates are for one model run except for CanESM5, which is the average of two runs.

Model	ECS (K)
ACCESS-CM2	4.93
ACCESS-ESM1-5	3.63
BCC-CSM2-MR	3.16
BCC-ESM1	3.74
CanESM5	5.70
CESM2	5.32
CESM2-FV2	5.06
CESM2-WACCM	4.73
CESM2-WACCM-FV2	4.56
E3SM-1-0	5.28
EC-Earth3-Veg	4.34
GFDL-CM4	3.78
GFDL-ESM4	2.61
GISS-E2-1-G	2.71
GISS-E2-2-G	2.25
GISS-E2-1-H	3.09
HadGEM3-GC31-LL	5.65
INM-CM4-8	2.32
INM-CM5-0	2.39
IPSL-CM6A-LR	4.97
MCM-UA-1-0	3.68
MIROC6	2.84
MIROC-ES2L	2.83
NorESM2-LM	2.19
NorESM2-MM	2.15
SAM0-UNICON	3.53
TaiESM1	4.33
UKESM1-0-LL	5.40

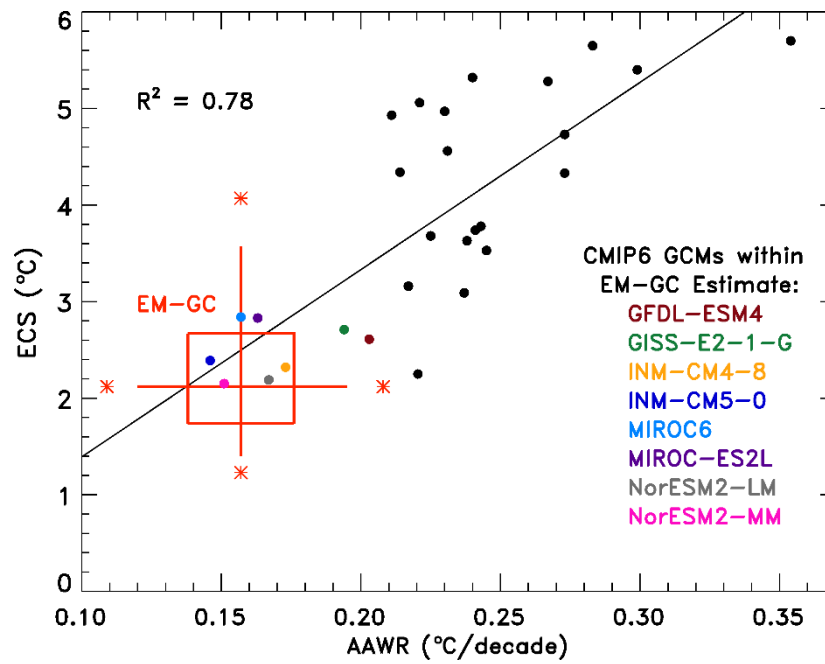
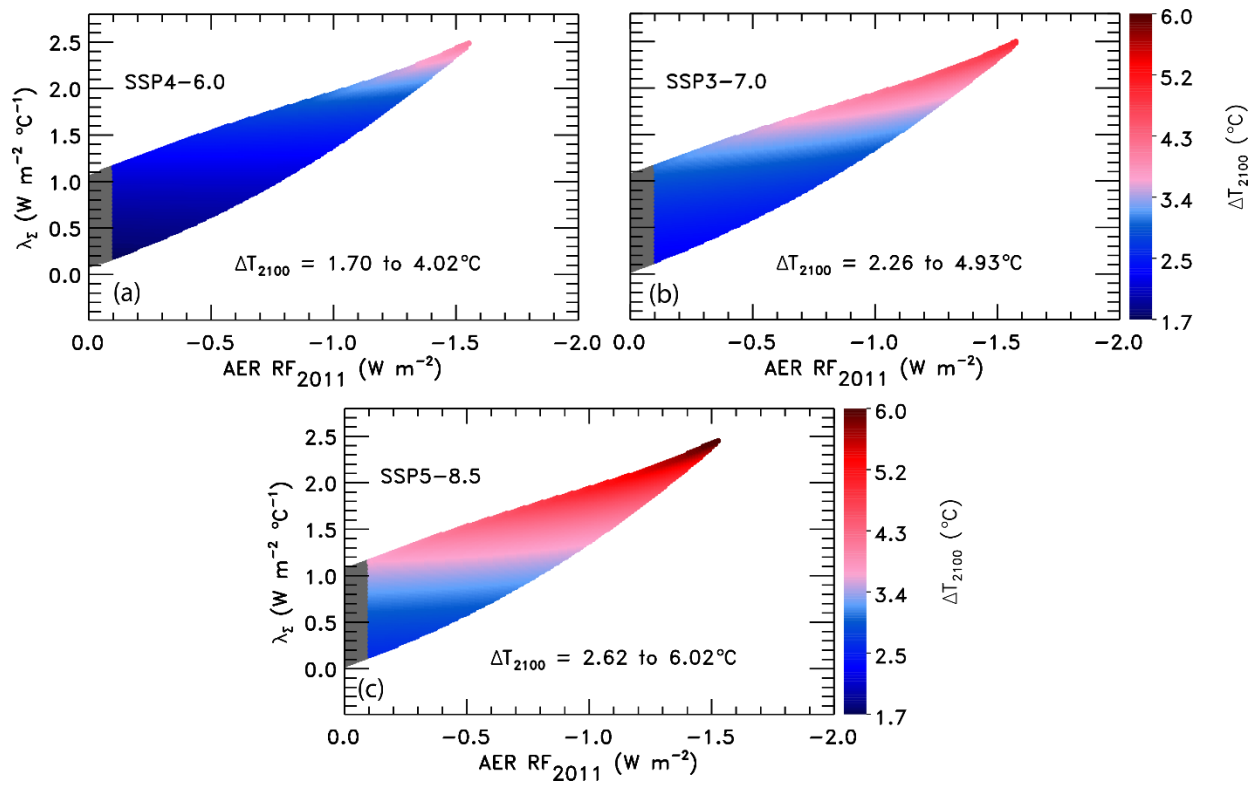


Figure S17. Values of ECS versus AAWR for the CMIP6 multi-model ensemble. The EM-GC estimates of AAWR and ECS based on training to the HadCRUT5 GMST record are plotted as a box and whisker. The box shows the average 25th, 50th, and 75th percentiles for the five OHC records shown for HadCRUT5 in Fig. 6 and Fig. 7. The whiskers represent the average 5th and 95th percentiles. The stars denote the average minimum and maximum values of AAWR or ECS. The eight CMIP6 GCMs that obtain values of AAWR and ECS that are both within the minimum and maximum estimates provided by the EM-GC are identified on the figure. Values of AAWR explain about 78% of the variance in ECS among the CMIP6 GCMs.



480 **Figure S18.** GMST anomaly in 2100 from pre-industrial (ΔT_{2100}) as a function of climate feedback parameter and AER RF_{2011} found using the EM-GC trained with ΔT from HadCRUT5. (a) ΔT_{2100} for SSP4-6.0. The region outside of the tropospheric aerosol radiative forcing range provided by IPCC 2013 (Myhre et al., 2013) is shaded grey. Colors denote the change in ΔT_{2100} . (b) ΔT_{2100} for SSP3-7.0. (c) ΔT_{2100} for SSP5-8.5.

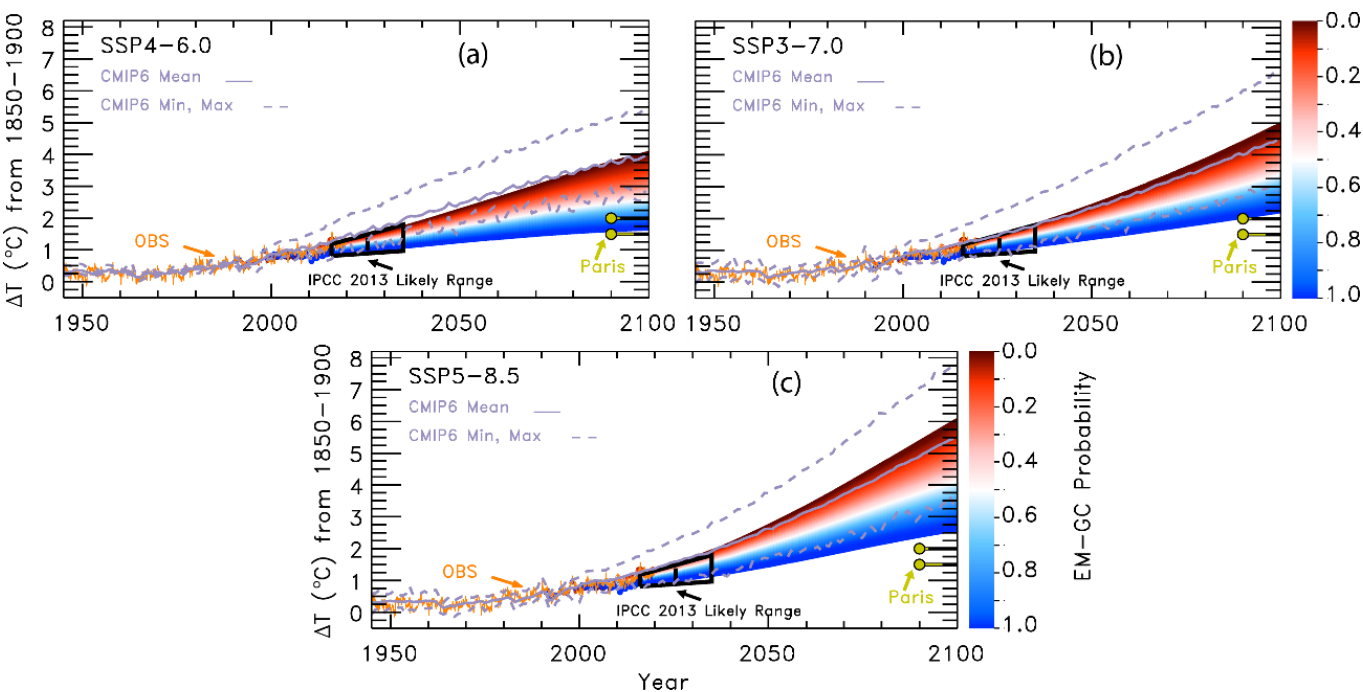


Figure S19. Probabilistic forecasts of future projections of ΔT using the EM-GC trained with ΔT from HadCRUT5 for the SSP4-6.0, SSP3-7.0, and SSP5-8.5 scenarios. (a) Future projections of ΔT for SSP4-6.0. Observations (orange) are from HadCRUT5. The IPCC 2013 likely range of warming (black) is from Figure 11.25b of chapter 11 of the IPCC 2013 report. The Paris Agreement target and upper limit (yellow) are shown for comparison to projections of ΔT using the EM-GC. The CMIP6 minimum, multi-model mean, and maximum values of the rise in ΔT are shown to compare to projections from the EM-GC. Colors denote the probability of reaching at least that temperature by the end of the century and are computed using the aerosol weighting method (see Sect. 2.5). (b) Future projections of ΔT for SSP3-7.0. (c) Future projections of ΔT for SSP5-8.5.

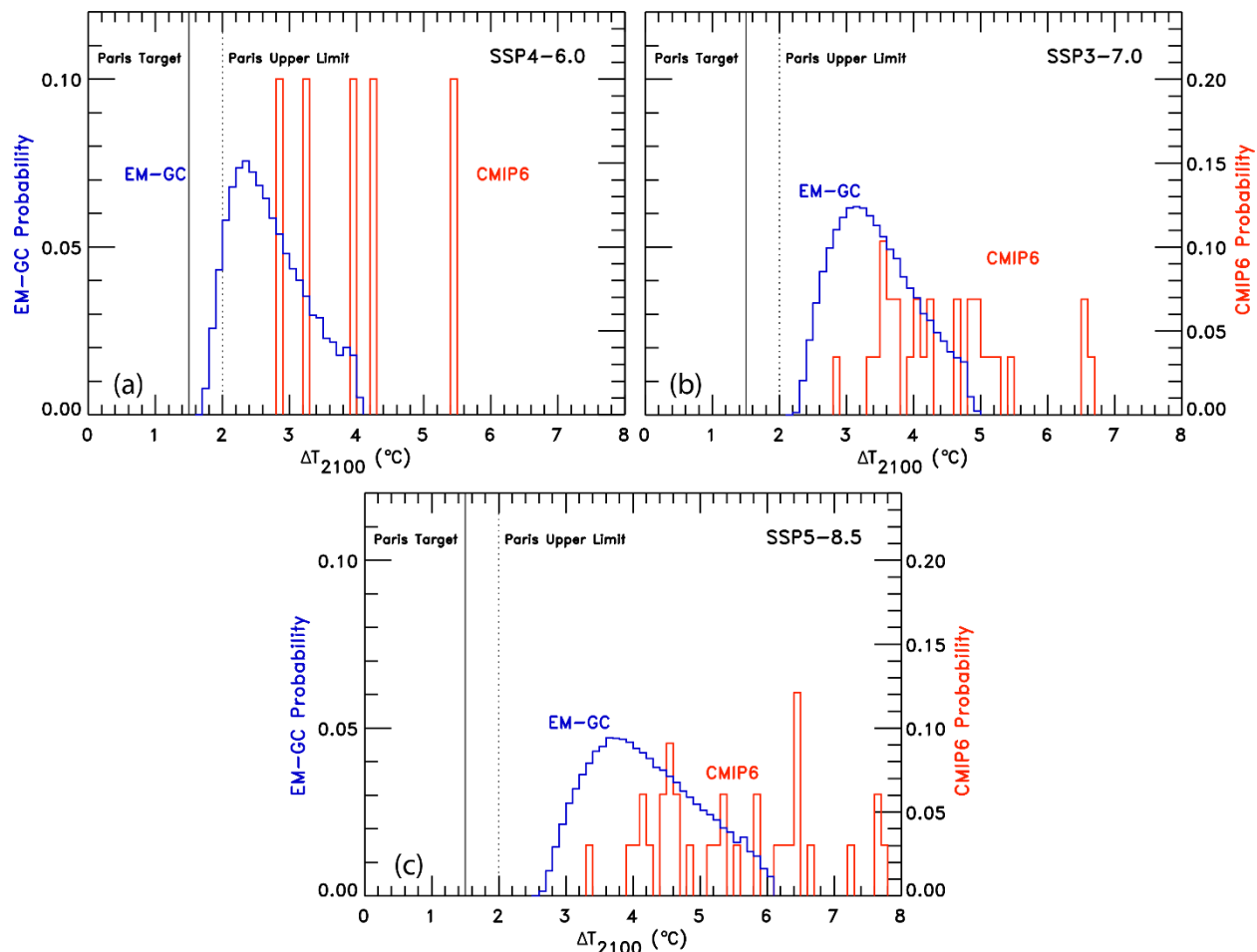


Figure S20. Probability density functions (PDF) for the increase in ΔT_{2100} using the EM-GC and the CMIP6 multi-model ensemble. (a) PDF for EM-GC (blue) results trained with ΔT from HadCRUT5 and CMIP6 multi-model results (red) for SSP4-6.0. The left-hand y-axis is for EM-GC probabilities and the righthand y-axis is for GCM probabilities. (b) PDF for SSP3-7.0. (c) PDF for SSP5-8.5.

Table S6. Probabilities of achieving the Paris Agreement target and upper limit for the various SSP scenarios based on the EM-GC using the HadCRUT4 or HadCRUT5 GMST data set and the CMIP6 multi-model ensemble. The probabilities using the EM-GC are computed using the aerosol weighting method. The probabilities using the CMIP6 GCMs are computed by calculating how many of the models for that scenario are below the temperature limits compared to the total number of models.

	Probability of Staying at or Below 1.5°C			Probability of Staying at or Below 2.0°C		
	HadCRUT4	HadCRUT5	CMIP6	HadCRUT4	HadCRUT5	CMIP6
SSP1-1.9	84%	81%	50%	99%	98%	80%
SSP1-2.6	64%	53%	18%	90%	86%	47%
SSP4-3.4	35%	19%	0%	74%	64%	17%
SSP2-4.5	9%	0%	0%	52%	33%	3%
SSP4-6.0	0%	0%	0%	26%	8%	0%
SSP3-7.0	0%	0%	0%	1%	0%	0%
SSP5-8.5	0%	0%	0%	0%	0%	0%

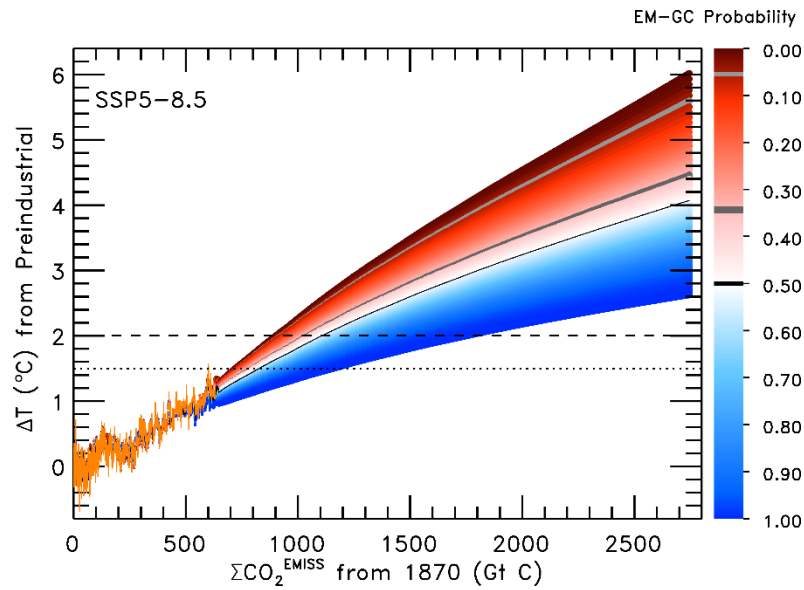


Figure S21. Transient climate response to cumulative CO₂ emissions for SSP5-8.5 using the EM-GC trained with the HadCRUT5 ΔT record. Simulations of the rise in ΔT versus cumulative CO₂ emissions in units of Gt C. The orange line is observations of ΔT from HadCRUT5 plotted against cumulative carbon emissions from the Global Carbon Budget project (Friedlingstein et al., 2019). The dotted and dashed lines denote the Paris Agreement target and upper limit, respectively. The EM-GC projections represent the probability that the future value of ΔT will rise to the indicated level, considering only acceptable fits to the climate record. The probabilities were determined using the aerosol weighting method. The light grey, dark grey, and black curves denote the 95, 66, and 50% probabilities of either the Paris target (intersection of dotted horizontal lines) or upper limit (intersection of dashed lines with curves) being achieved.

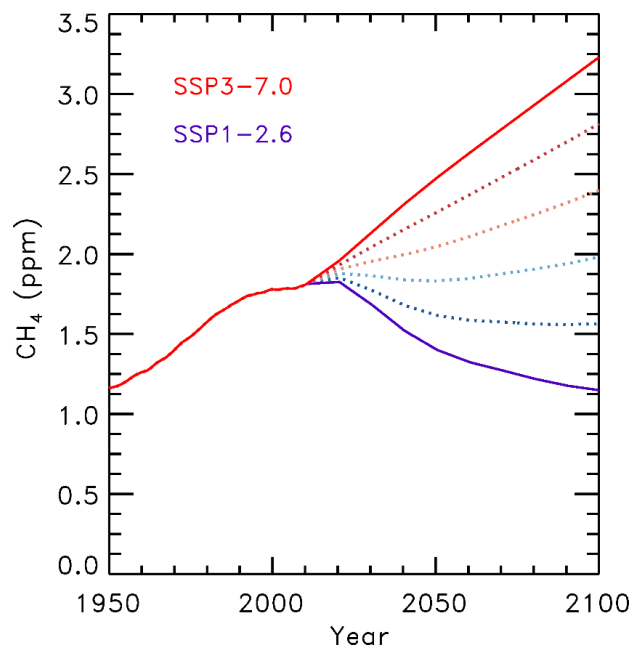


Figure S22. Blended methane mixing ratios. The dotted lines are linear combinations of the time series of methane abundances using SSP1-2.6 and SSP3-7.0 to span the range of values of future methane. The solid lines are the SSP1-2.6 and SSP3-7.0 methane mixing ratio time series.

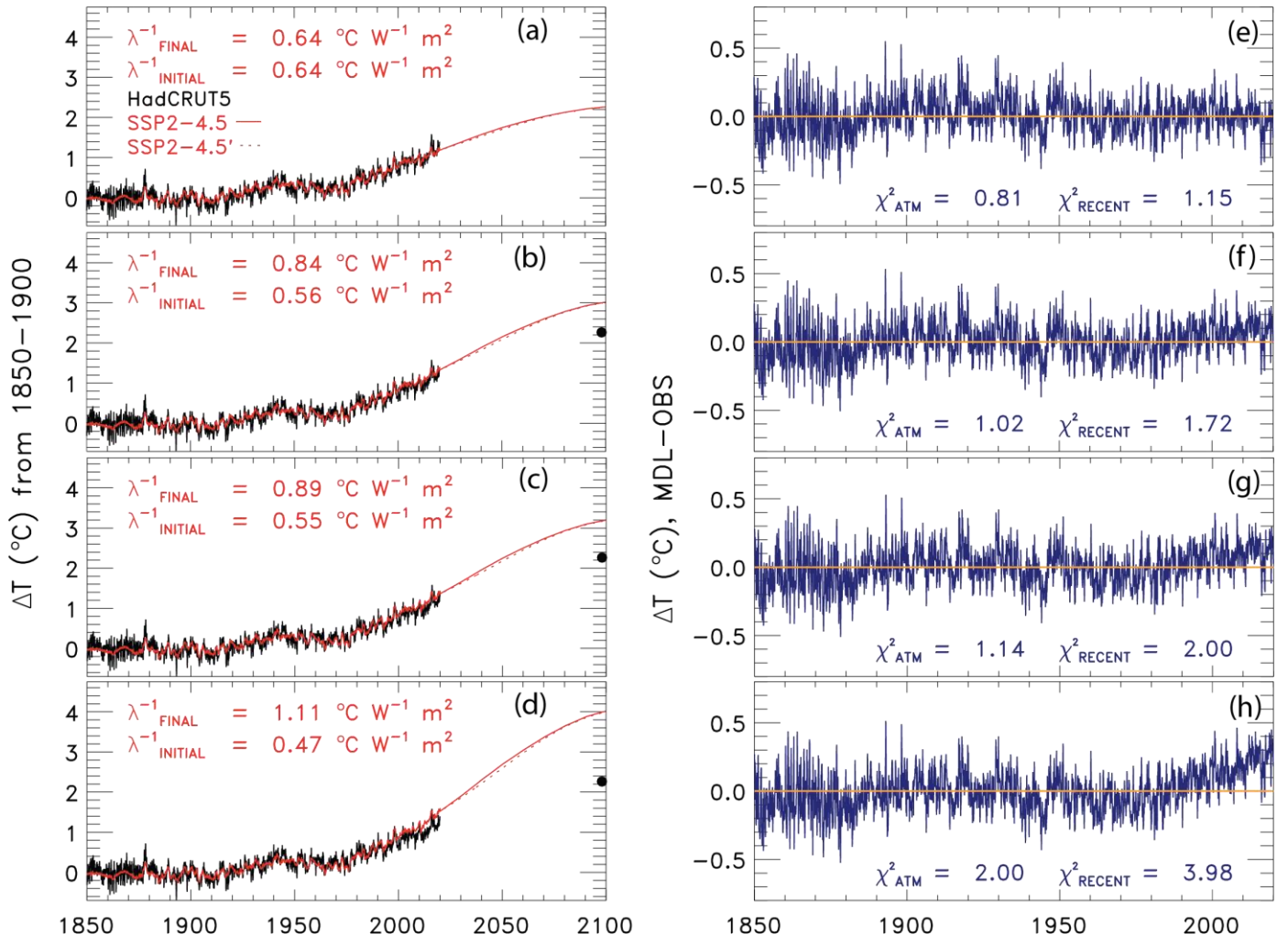


Figure S23. Change in GMST (ΔT) from 1850-2019 for observations from HadCRUT5 (black) and 1850-2100 for modeled (red) using SSP4-3.4-2-4.5 and a value of $AER\ RF_{2011} = -0.9\ W\ m^{-2}$ and the residual between modeled and observations using an instantaneous time variant λ^{-1} . The solid line denotes a simulation for the original SSP2-4.5 scenario and the dashed line indicates the SSP2-4.5' simulation (see Sect. 3.3.6). (a) ΔT assuming a constant value of λ^{-1} . (b) ΔT allowing λ^{-1} to increase by 50%. (c) ΔT allowing λ^{-1} to vary while the value of χ^2_{RECENT} is kept below 2. (d) ΔT allowing λ^{-1} to vary while the value of χ^2_{ATM} is kept below 2. (e) Residual between modeled and observed ΔT from 1850-2019 for constant λ^{-1} . (f) Same as (e) but for increasing λ^{-1} by 50%. (g) Same as (f) but for varying λ^{-1} while the value of χ^2_{RECENT} is kept below 2. (h) same as (g) but for varying λ^{-1} while the value of χ^2_{ATM} is kept below 2.

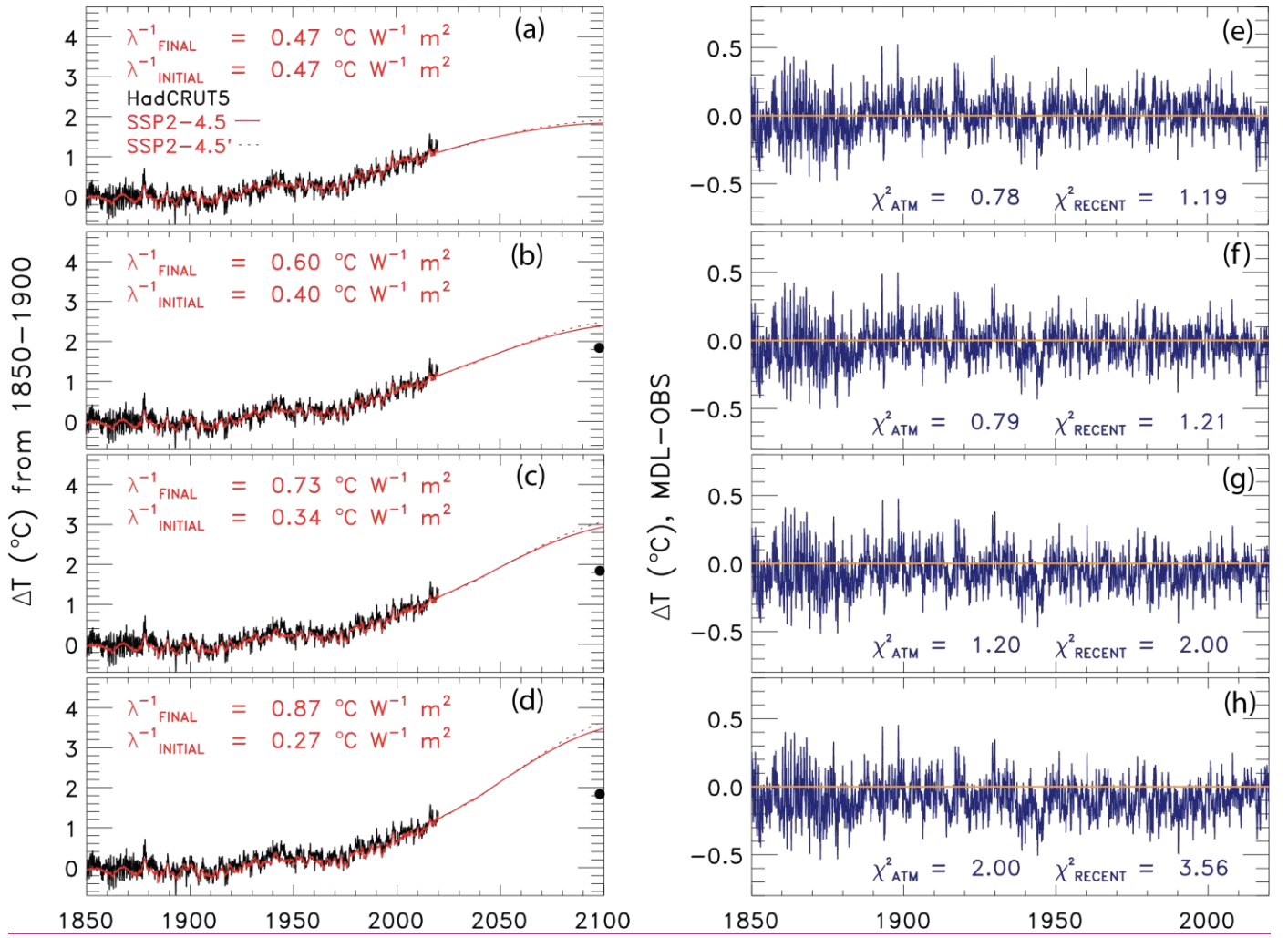


Figure S24. Change in GMST (ΔT) from 1850-2019 for observations from HadCRUT5 (black) and 1850-2100 for modeled (red) using SSP2-4.5 and a value of AER $\text{RF}_{2011} = -0.4 \text{ W m}^{-2}$ and the residual between modeled and observations incorporating a 32.5-year delay between λ^{-1} and a change in RF. The solid line denotes a simulation for the original SSP2-4.5 scenario and the dashed line indicates the SSP2-4.5' simulation (see Sect. 3.3.6). (a) ΔT assuming a constant value of λ^{-1} . (b) ΔT allowing λ^{-1} to increase by 50%. (c) ΔT allowing λ^{-1} to vary while the value of χ^2_{RECENT} is kept below 2. (d) ΔT allowing λ^{-1} to vary while the value of χ^2_{ATM} is kept below 2. (e) Residual between modeled and observed ΔT from 1850-2019 for constant λ^{-1} . (f) Same as (e) but for increasing λ^{-1} by 50%. (g) Same as (f) but for varying λ^{-1} while the value of χ^2_{RECENT} is kept below 2. (h) same as (g) but for varying λ^{-1} while the value of χ^2_{ATM} is kept below 2.

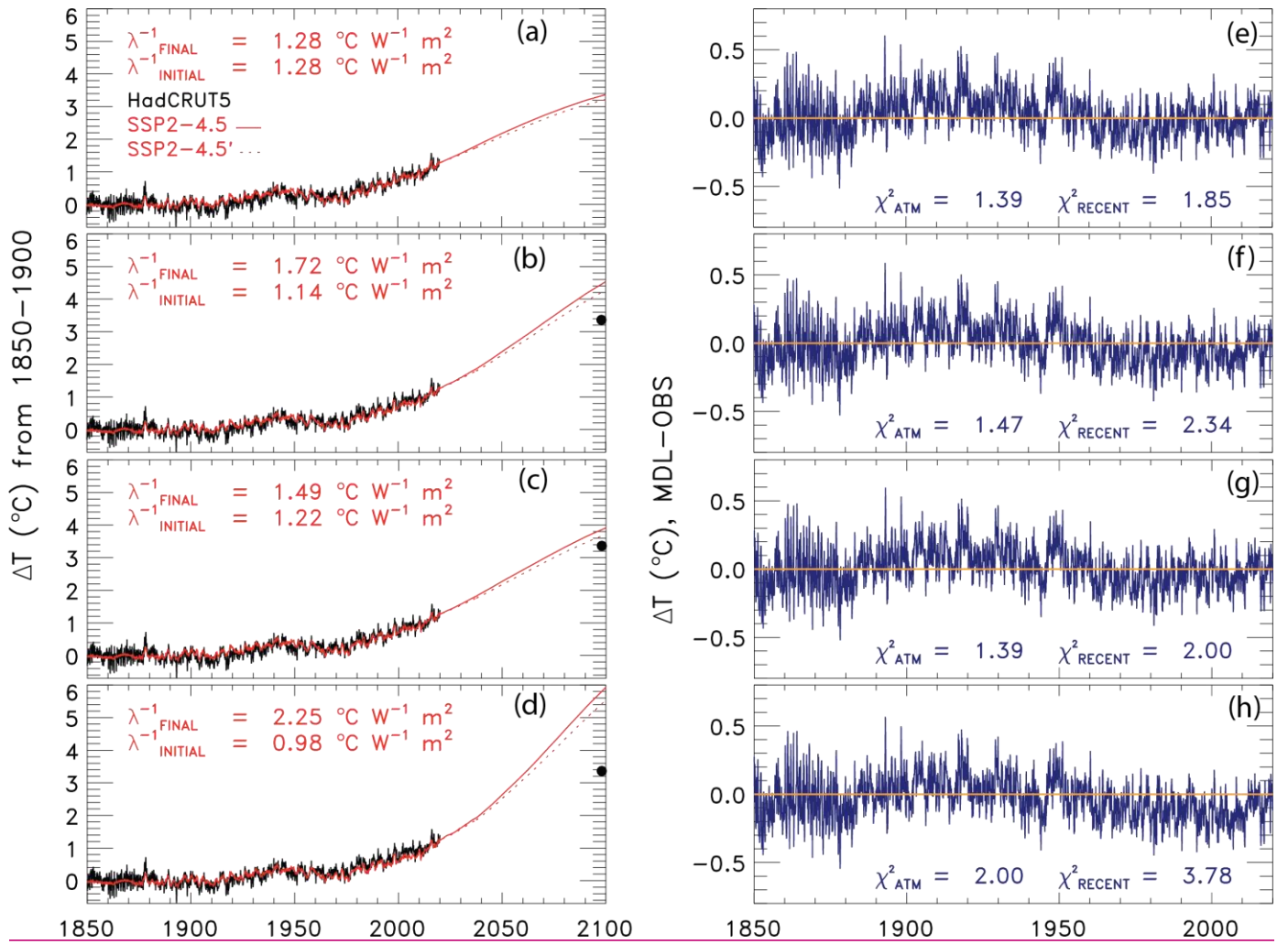


Figure S25. Change in GMST (ΔT) from 1850-2019 for observations from HadCRUT5 (black) and 1850-2100 for modeled (red) using SSP2-4.5 and a value of AER $\text{RF}_{2011} = -1.5 \text{ W m}^{-2}$ and the residual between modeled and observations incorporating a 32.5-year delay between λ^{-1} and a change in RF. The solid line denotes a simulation for the original SSP2-4.5 scenario and the dashed line indicates the SSP2-4.5' simulation (see Sect. 3.3.6). (a) ΔT assuming a constant value of λ^{-1} . (b) ΔT allowing λ^{-1} to increase by 50%. (c) ΔT allowing λ^{-1} to vary while the value of χ^2_{RECENT} is kept below 2. (d) ΔT allowing λ^{-1} to vary while the value of χ^2_{ATM} is kept below 2. (e) Residual between modeled and observed ΔT from 1850-2019 for constant λ^{-1} . (f) Same as (e) but for increasing λ^{-1} by 50%. (g) Same as (f) but for varying λ^{-1} while the value of χ^2_{RECENT} is kept below 2. (h) same as (g) but for varying λ^{-1} while the value of χ^2_{ATM} is kept below 2.

Table S7. Details of the CMIP6 GCMs used in this study.

Institution	Model	Model Output
AS-RCEC	TaiESM1	No reference provided
AWI	AWI-CM-1-1-MR	(Semmler et al., 2018a, 2018b, 2018c, 2019a, 2019b)
BCC	BCC-CSM2-MR	(Wu et al., 2018a, 2018b, 2018c; Xin et al., 2019a, 2019b, 2019c, 2019d)
	BCC-ESM1	(Zhang et al., 2018a, 2018b, 2019)
CAMS	CAMS-CSM1-0	(Rong, 2019a, 2019b, 2019c, 2019d, 2019e, 2019f)
	CAS-ESM2-0	(Chai, 2019)
CAS	FGOALS-f3-L	(YU, 2019a, 2019b, 2019c, 2019d, 2019e)
	FGOALS-g3	(Li, 2019a, 2019b, 2019c, 2019d, 2019e)
CCCma	CanESM5	(Swart et al., 2019f, 2019g, 2019h, 2019i, 2019j, 2019k, 2019l, 2019m, 2019n, 2019o)
	CanESM5-CanOE	(Swart et al., 2019a, 2019b, 2019c, 2019d, 2019e)
	CNRM-CM6-1	(Voldoire, 2018, 2019c, 2019d, 2019e, 2019f)
CNRM-CERFACS	CNRM-CM6-1-HR	(Voldoire, 2019a, 2019b, 2020a, 2020b)
	CNRM-ESM2-1	(Seferian, 2018; Voldoire, 2019g, 2019h, 2019i, 2019j, 2019k, 2019l)
CSIRO	ACCESS-ESM1-5	(Ziehn et al., 2019a, 2019b, 2019c, 2019d, 2019e, 2019f, 2019g)
CSIRO-ARCCSS	ACCESS-CM2	(Dix et al., 2019a, 2019b, 2019c, 2019d, 2019e, 2019f, 2019g)
E3SM-Project	E3SM-1-0	(Bader et al., 2018, 2019a, 2019b)
	E3SM-1-1-ECA	(Bader et al., 2020)
E3SM-Project RUBISCO	E3SM-1-1	(Bader et al., 2019c)
EC-Earth-Consortium	EC-Earth3	(EC-Earth Consortium (EC-Earth), 2019i, 2019j, 2019k, 2019l, 2019m)
	EC-Earth3-Veg	(EC-Earth Consortium (EC-Earth), 2019a, 2019b, 2019c, 2019d, 2019e, 2019f, 2019g, 2019h)

FIO-QLNM	FIO-ESM-2-0	(Song et al., 2019a, 2019b, 2019c, 2019d)
HAMMOZ-Consortium	MPI-ESM1-2-HAM	(Neubauer et al., 2019)
	INM-CM4-8	(Volodin et al., 2019a, 2019b, 2019c, 2019d, 2019e, 2019f, 2019g)
	INM-CM5-0	(Volodin et al., 2019m, 2019h, 2019n, 2019i, 2019j, 2019k, 2019l)
IPSL	IPSL-CM6A-LR	(Boucher et al., 2018a, 2018b, 2018c, 2019a, 2019b, 2019c, 2019d, 2019e, 2019f, 2019g)
MIROC	MIROC6	(Shiogama et al., 2019a, 2019b, 2019c, 2019d, 2019e, 2019f, 2019g; Tatebe and Watanabe, 2018a, 2018b, 2018c)
	MIROC-ES2L	(Hajima et al., 2019; Tachiiri et al., 2019a, 2019b, 2019c, 2019d, 2019e)
MOHC	HadGEM3-GC31-MM	(Ridley et al., 2019c)
MOHC NERC	HadGEM3-GC31-LL	(Good, 2019, 2020a, 2020b; Ridley et al., 2018, 2019a, 2019b)
MOHC, NERC, NIMS-KMA, NIWA	UKESM1-0-LL	(Byun, 2020; Good et al., 2019a, 2019b, 2019c, 2019d, 2019e, 2019f; Tang et al., 2019a, 2019b, 2019c)
MPI-M AWI	MPI-ESM1-2-LR	(Wieners et al., 2019a, 2019b, 2019c, 2019d, 2019e)
MPI-M DWD DKRZ	MPI-ESM1-2-HR	(Jungclaus et al., 2019; Schupfner et al., 2019a, 2019b, 2019c, 2019d; Steger et al., 2019)
MRI	MRI-ESM2-0	(Yukimoto et al., 2019a, 2019b, 2019c, 2019d, 2019e, 2019f, 2019g, 2019h)
	GISS-E2-1-G	(NASA Goddard Institute for Space Studies (NASA/GISS), 2018a, 2018b, 2018c, 2020a, 2020b, 2020c, 2020d)
	GISS-E2-1-G-CC	No reference provided
NASA-GISS	GISS-E2-2-G	(NASA Goddard Institute for Space Studies (NASA/GISS), 2019a)
	GISS-E2-1-H	(NASA Goddard Institute for Space Studies (NASA/GISS), 2018d, 2019b, 2019c)
NCAR	CESM2-WACCM-FV2	(Danabasoglu, 2019d, 2019e, 2020a)

NCC	CESM2	(Danabasoglu, 2019c, 2019d, 2019e, 2019f, 2019g, 2019h; Danabasoglu et al., 2019)
	CESM2-FV2	(Danabasoglu, 2019b, 2019c, 2020b)
	CESM2-WACCM	(Danabasoglu, 2019f, 2019g, 2019h, 2019a, 2019i, 2019j, 2019k)
	NorCPM1	(Bethke et al., 2019a, 2019b, 2019c)
	NorESM2-LM	(Seland et al., 2019a, 2019b, 2019c, 2019d, 2019e, 2019f, 2019g)
NIMS-KMA	NorESM2-MM	(Bentsen et al., 2019a, 2019b, 2019c, 2019d, 2019e, 2019f, 2019g)
	KACE-1-0-G	(Byun et al., 2019a, 2019b, 2019c, 2019d, 2019e)
NOAA-GFDL	GFDL-CM4	(Guo et al., 2018a, 2018b, 2018c, 2018d, 2018e)
	GFDL-ESM4	(John et al., 2018a, 2018b, 2018c, 2018d, 2018e; Krasting et al., 2018a, 2018b, 2018c)
NUIST	NESM3	(Cao, 2019a, 2019b, 2019c; Cao and Wang, 2019)
SNU	SAM0-UNICON	(Park and Shin, 2019a, 2019b, 2019c)
THU	CIESM	(Huang, 2019a, 2019b, 2020a, 2020b)
UA	MCM-UA-1-0	(Stouffer, 2019a, 2019b, 2019c, 2019d, 2019e, 2019f, 2019g)

- Bader, D. C., Leung, R., Taylor, M. and McCoy, R. B.: E3SM-Project E3SM1.0 model output prepared for CMIP6 CMIP piControl, Earth System Grid Federation, , doi:<https://doi.org/10.22033/ESGF/CMIP6.4499>, 2018.
- Bader, D. C., Leung, R., Taylor, M. and McCoy, R. B.: E3SM-Project E3SM1.0 model output prepared for CMIP6 CMIP abrupt-4xCO2, Earth System Grid Federation, , doi:<https://doi.org/10.22033/ESGF/CMIP6.4491>,
570 2019a.
- Bader, D. C., Leung, R., Taylor, M. and McCoy, R. B.: E3SM-Project E3SM1.0 model output prepared for CMIP6 CMIP historical, Earth System Grid Federation, , doi:<https://doi.org/10.22033/ESGF/CMIP6.4497>, 2019b.
- Bader, D. C., Leung, R., Taylor, M. and McCoy, R. B.: E3SM-Project E3SM1.1 model output prepared for CMIP6 CMIP historical, Earth System Grid Federation, , doi:<https://doi.org/10.22033/ESGF/CMIP6.11485>, 2019c.
- 575 Bader, D. C., Leung, R., Taylor, M. and McCoy, R. B.: E3SM-Project E3SM1.1ECA model output prepared for CMIP6 CMIP historical, Earth System Grid Federation, , doi:<https://doi.org/10.22033/ESGF/CMIP6.11486>, 2020.
- Balmaseda, M. A., Trenberth, K. E. and Källén, E.: Distinctive climate signals in reanalysis of global ocean heat content, *Geophys. Res. Lett.*, 40(9), 1754–1759, doi:10.1002/grl.50382, 2013a.
- 580 Balmaseda, M. A., Mogensen, K. and Weaver, A. T.: Evaluation of the ECMWF ocean reanalysis system ORAS4, *Q. J. R. Meteorol. Soc.*, 139(674), 1132–1161, doi:10.1002/qj.2063, 2013b.
- Bentsen, M., Olivieri, D. J. L., Seland, Ø., Toniazzi, T., Gjermundsen, A., Graff, L. S., Debernard, J. B., Gupta, A. K., He, Y., Kirkevåg, A., Schwinger, J., Tjiputra, J., Aas, K. S., Bethke, I., Fan, Y., Griesfeller, J., Grini, A., Guo, C., Ilicak, M., Karset, I. H. H., Landgren, O. A., Liakka, J., Moseid, K. O., Nummelin, A., Spensberger, C., Tang, H., Zhang, Z., Heinze, C., Iversen, T. and Schulz, M.: NCC NorESM2-MM model output prepared for CMIP6 CMIP abrupt-4xCO2, Earth System Grid Federation, ,
585 doi:<https://doi.org/10.22033/ESGF/CMIP6.7840>, 2019a.
- Bentsen, M., Olivieri, D. J. L., Seland, Ø., Toniazzi, T., Gjermundsen, A., Graff, L. S., Debernard, J. B., Gupta, A. K., He, Y., Kirkevåg, A., Schwinger, J., Tjiputra, J., Aas, K. S., Bethke, I., Fan, Y., Griesfeller, J., Grini, A., Guo, C., Ilicak, M., Karset, I. H. H., Landgren, O. A., Liakka, J., Moseid, K. O., Nummelin, A., Spensberger, C., Tang, H., Zhang, Z., Heinze, C., Iversen, T. and Schulz, M.: NCC NorESM2-MM model output prepared for CMIP6 CMIP historical, Earth System Grid Federation, ,
590 doi:<https://doi.org/10.22033/ESGF/CMIP6.8040>, 2019b.
- Bentsen, M., Olivieri, D. J. L., Seland, Ø., Toniazzi, T., Gjermundsen, A., Graff, L. S., Debernard, J. B., Gupta, A. K., He, Y., Kirkevåg, A., Schwinger, J., Tjiputra, J., Aas, K. S., Bethke, I., Fan, Y., Griesfeller, J., Grini, A., Guo, C., Ilicak, M., Karset, I. H. H., Landgren, O. A., Liakka, J., Moseid, K. O., Nummelin, A., Spensberger, C., Tang, H., Zhang, Z., Heinze, C., Iversen, T. and Schulz, M.: NCC NorESM2-MM model output prepared for CMIP6 CMIP piControl, Earth System Grid Federation, ,
595 doi:<https://doi.org/10.22033/ESGF/CMIP6.8221>, 2019c.
- 600 Bentsen, M., Olivieri, D. J. L., Seland, Ø., Toniazzi, T., Gjermundsen, A., Graff, L. S., Debernard, J. B., Gupta, A. K., He, Y., Kirkevåg, A., Schwinger, J., Tjiputra, J., Aas, K. S., Bethke, I., Fan, Y., Griesfeller, J., Grini, A., Guo, C., Ilicak, M., Karset, I. H. H., Landgren, O. A., Liakka, J., Moseid, K. O., Nummelin, A., Spensberger, C., Tang, H., Zhang, Z., Heinze, C., Iversen, T. and Schulz, M.: NCC NorESM2-MM model output prepared for CMIP6 ScenarioMIP ssp126, Earth System Grid Federation, ,
605 doi:<https://doi.org/10.22033/ESGF/CMIP6.8250>, 2019d.
- Bentsen, M., Olivieri, D. J. L., Seland, Ø., Toniazzi, T., Gjermundsen, A., Graff, L. S., Debernard, J. B., Gupta, A. K., He, Y., Kirkevåg, A., Schwinger, J., Tjiputra, J., Aas, K. S., Bethke, I., Fan, Y., Griesfeller, J., Grini, A.,

- 610 Guo, C., Ilicak, M., Karset, I. H. H., Landgren, O. A., Liakka, J., Moseid, K. O., Nummelin, A., Spensberger, C., Tang, H., Zhang, Z., Heinze, C., Iversen, T. and Schulz, M.: NCC NorESM2-MM model output prepared for CMIP6 ScenarioMIP ssp245, Earth System Grid Federation, , doi:<https://doi.org/10.22033/ESGF/CMIP6.8255>, 2019e.
- 615 Bentsen, M., Olivieri, D. J. L., Seland, Ø., Toniazzi, T., Gjermundsen, A., Graff, L. S., Debernard, J. B., Gupta, A. K., He, Y., Kirkevåg, A., Schwinger, J., Tjiputra, J., Aas, K. S., Bethke, I., Fan, Y., Griesfeller, J., Grini, A., Guo, C., Ilicak, M., Karset, I. H. H., Landgren, O. A., Liakka, J., Moseid, K. O., Nummelin, A., Spensberger, C., Tang, H., Zhang, Z., Heinze, C., Iversen, T. and Schulz, M.: NCC NorESM2-MM model output prepared for CMIP6 ScenarioMIP ssp370, Earth System Grid Federation, , doi:<https://doi.org/10.22033/ESGF/CMIP6.8270>, 2019f.
- 620 Bentsen, M., Olivieri, D. J. L., Seland, Ø., Toniazzi, T., Gjermundsen, A., Graff, L. S., Debernard, J. B., Gupta, A. K., He, Y., Kirkevåg, A., Schwinger, J., Tjiputra, J., Aas, K. S., Bethke, I., Fan, Y., Griesfeller, J., Grini, A., Guo, C., Ilicak, M., Karset, I. H. H., Landgren, O. A., Liakka, J., Moseid, K. O., Nummelin, A., Spensberger, C., Tang, H., Zhang, Z., Heinze, C., Iversen, T. and Schulz, M.: NCC NorESM2-MM model output prepared for CMIP6 ScenarioMIP ssp585, Earth System Grid Federation, , doi:<https://doi.org/10.22033/ESGF/CMIP6.8321>, 2019g.
- 625 Bethke, I., Wang, Y., Counillon, F., Kimmritz, M., Fransner, F., Samuelsen, A., Langehaug, H. R., Chiu, P.-G., Bentsen, M., Guo, C., Tjiputra, J., Kirkevåg, A., Olivieri, D. J. L., Seland, Ø., Fan, Y., Lawrence, P., Eldevik, T. and Keenlyside, N.: NCC NorCPM1 model output prepared for CMIP6 CMIP abrupt-4xCO2, Earth System Grid Federation, , doi:<https://doi.org/10.22033/ESGF/CMIP6.10862>, 2019a.
- 630 Bethke, I., Wang, Y., Counillon, F., Kimmritz, M., Fransner, F., Samuelsen, A., Langehaug, H. R., Chiu, P., Bentsen, M., Guo, C., Tjiputra, J., Kirkevåg, A., Olivieri, D. J. L., Seland, Ø., Fan, Y., Lawrence, P., Eldevik, T. and Keenlyside, N.: NCC NorCPM1 model output prepared for CMIP6 CMIP historical, Earth System Grid Federation, , doi:<https://doi.org/10.22033/ESGF/CMIP6.10894>, 2019b.
- 635 Bethke, I., Wang, Y., Counillon, F., Kimmritz, M., Fransner, F., Samuelsen, A., Langehaug, H. R., Chiu, P.-G., Bentsen, M., Guo, C., Tjiputra, J., Kirkevåg, A., Olivieri, D. J. L., Seland, Ø., Fan, Y., Lawrence, P., Eldevik, T. and Keenlyside, N.: NCC NorCPM1 model output prepared for CMIP6 CMIP piControl, Earth System Grid Federation, , doi:<https://doi.org/10.22033/ESGF/CMIP6.10896>, 2019c.
- Bony, S., Colman, R., Kattsov, V. M., Allan, R. P., Bretherton, C. S., Dufresne, J. L., Hall, A., Hallegatte, S., Holland, M. M., Ingram, W., Randall, D. A., Soden, B. J., Tselioudis, G. and Webb, M. J.: How well do we understand and evaluate climate change feedback processes?, *J. Clim.*, 19(15), 3445–3482, doi:10.1175/JCLI3819.1, 2006.
- 640 Boucher, O., Denvil, S., Caubel, A. and Foujols, M. A.: IPSL IPSL-CM6A-LR model output prepared for CMIP6 CMIP abrupt-4xCO2, Earth System Grid Federation, , doi:<https://doi.org/10.22033/ESGF/CMIP6.5109>, 2018a.
- Boucher, O., Denvil, S., Caubel, A. and Foujols, M. A.: IPSL IPSL-CM6A-LR model output prepared for CMIP6 CMIP historical, Earth System Grid Federation, , doi:<https://doi.org/10.22033/ESGF/CMIP6.5195>, 2018b.
- 645 Boucher, O., Denvil, S., Caubel, A. and Foujols, M. A.: IPSL IPSL-CM6A-LR model output prepared for CMIP6 CMIP piControl, Earth System Grid Federation, , doi:<https://doi.org/10.22033/ESGF/CMIP6.5251>, 2018c.
- Boucher, O., Denvil, S., Caubel, A. and Foujols, M. A.: IPSL IPSL-CM6a-LR model output prepared for CMIP6 ScenarioMIP ssp119, Earth System Grid Federation, , doi:<https://doi.org/10.22033/ESGF/CMIP6.5261>, 2019a.
- 650 Boucher, O., Denvil, S., Caubel, A. and Foujols, M. A.: IPSL IPSL-CM6A-LR model output prepared for CMIP6 ScenarioMIP ssp126, Earth System Grid Federation, , doi:<https://doi.org/10.22033/ESGF/CMIP6.5262>,

2019b.

- 655 Boucher, O., Denvil, S., Caubel, A. and Foujols, M. A.: IPSL IPSL-CM6A-LR model output prepared for CMIP6 ScenarioMIP ssp370, Earth System Grid Federation, , doi:<https://doi.org/10.22033/ESGF/CMIP6.5265>, 2019c.
- Boucher, O., Denvil, S., Caubel, A. and Foujols, M. A.: IPSL IPSL-CM6A-LR model output prepared for CMIP6 ScenarioMIP ssp434, Earth System Grid Federation, , doi:<https://doi.org/10.22033/ESGF/CMIP6.5267>, 2019d.
- 660 Boucher, O., Denvil, S., Caubel, A. and Foujols, M. A.: IPSL IPSL-CM6A-LR model output prepared for CMIP6 ScenarioMIP ssp460, Earth System Grid Federation, , doi:<https://doi.org/10.22033/ESGF/CMIP6.5268>, 2019e.
- Boucher, O., Denvil, S., Caubel, A. and Foujols, M. A.: IPSL IPSL-CM6A-LR model output prepared for CMIP6 ScenarioMIP ssp585, Earth System Grid Federation, , doi:<https://doi.org/10.22033/ESGF/CMIP6.5271>, 2019f.
- 665 Boucher, O., Denvil, S., Caubel, A. and Foujols, M. A.: PSL IPSL-CM6A-LR model output prepared for CMIP6 ScenarioMIP ssp245, Earth System Grid Federation, , doi:<https://doi.org/10.22033/ESGF/CMIP6.5264>, 2019g.
- Byun, Y.-H.: NIMS-KMA UKESM1.0-LL model output prepared for CMIP6 CMIP historical, Earth System Grid Federation, , doi:<https://doi.org/10.22033/ESGF/CMIP6.8379>, 2020.
- 670 Byun, Y.-H., Lim, Y.-J., Sung, H. M., Kim, J., Sun, M. and Kim, B.-H.: NIMS-KMA KACE1.0-G model output prepared for CMIP6 CMIP historical, Earth System Grid Federation, , doi:<https://doi.org/10.22033/ESGF/CMIP6.8378>, 2019a.
- Byun, Y.-H., Lim, Y.-J., Shim, S., Sung, H. M., Sun, M., Kim, J., Kim, B.-H., Lee, J.-H. and Moon, H.: NIMS-KMA KACE1.0-G model output prepared for CMIP6 ScenarioMIP ssp126, Earth System Grid Federation, , doi:<https://doi.org/10.22033/ESGF/CMIP6.8432>, 2019b.
- 675 Byun, Y.-H., Lim, Y.-J., Shim, S., Sung, H. M., Sun, M., Kim, J., Kim, B.-H., Lee, J.-H. and Moon, H.: NIMS-KMA KACE1.0-G model output prepared for CMIP6 ScenarioMIP ssp245, Earth System Grid Federation, , doi:<https://doi.org/10.22033/ESGF/CMIP6.8435>, 2019c.
- Byun, Y.-H., Lim, Y.-J., Shim, S., Sung, H. M., Sun, M., Kim, J., Kim, B.-H., Lee, J.-H. and Moon, H.: NIMS-KMA KACE1.0-G model output prepared for CMIP6 ScenarioMIP ssp370, Earth System Grid Federation, , doi:<https://doi.org/10.22033/ESGF/CMIP6.8437>, 2019d.
- 680 Byun, Y.-H., Lim, Y.-J., Shim, S., Sung, H. M., Sun, M., Kim, J., Kim, B.-H., Lee, J.-H. and Moon, H.: NIMS-KMA KACE1.0-G model output prepared for CMIP6 ScenarioMIP ssp585, Earth System Grid Federation, , doi:<https://doi.org/10.22033/ESGF/CMIP6.8456>, 2019e.
- 685 Canty, T., Mascioli, N. R., Smarte, M. D. and Salawitch, R. J.: An empirical model of global climate – Part 1: A critical evaluation of volcanic cooling, Atmos. Chem. Phys., 13(8), 3997–4031, doi:10.5194/acp-13-3997-2013, 2013.
- Cao, J.: NUIST NESMv3 model output prepared for CMIP6 ScenarioMIP ssp126, Earth System Grid Federation, , doi:<https://doi.org/10.22033/ESGF/CMIP6.8780>, 2019a.
- 690 Cao, J.: NUIST NESMv3 model output prepared for CMIP6 ScenarioMIP ssp245, Earth System Grid Federation, , doi:<https://doi.org/10.22033/ESGF/CMIP6.8781>, 2019b.

- Cao, J.: NUIST NESMv3 model output prepared for CMIP6 ScenarioMIP ssp585, Earth System Grid Federation, , doi:<https://doi.org/10.22033/ESGF/CMIP6.8790>, 2019c.
- 695 Cao, J. and Wang, B.: NUIST NESMv3 model output prepared for CMIP6 CMIP historical, , doi:<https://doi.org/10.22033/ESGF/CMIP6.8769>, 2019.
- Carton, J. A., Chepurin, G. A. and Chen, L.: SODA3: A New Ocean Climate Reanalysis, *J. Clim.*, 31(17), 6967–6983, doi:10.1175/jcli-d-18-0149.1, 2018.
- Chai, Z.: CAS CAS-ESM1.0 model output prepared for CMIP6 CMIP historical, Earth System Grid Federation, , doi:<https://doi.org/10.22033/ESGF/CMIP6.3353>, 2019.
- 700 Chen, X., Guo, Z., Zhou, T., Li, J., Rong, X., Xin, Y., Chen, H. and Su, J.: Climate Sensitivity and Feedbacks of a New Coupled Model CAMS-CSM to Idealized CO₂ Forcing: A Comparison with CMIP5 Models, *J. Meteorol. Res.*, 33(1), 31–45, doi:10.1007/s13351-019-8074-5, 2019.
- Cheng, L., Trenberth, K. E., Fasullo, J., Boyer, T., Abraham, J. and Zhu, J.: Improved estimates of ocean heat content from 1960 to 2015, *Sci. Adv.*, 3(3), 1–11, doi:10.1126/sciadv.1601545, 2017.
- 705 Danabasoglu, G.: NCAR CESM2-WACCM model output prepared for CMIP6 ScenarioMIP ssp126, Earth System Grid Federation, , doi:<https://doi.org/10.22033/ESGF/CMIP6.10100>, 2019a.
- Danabasoglu, G.: NCAR CESM2-FV2 model output prepared for CMIP6 CMIP historical, Earth System Grid Federation, , doi:<https://doi.org/10.22033/ESGF/CMIP6.11297>, 2019b.
- Danabasoglu, G.: NCAR CESM2-FV2 model output prepared for CMIP6 CMIP piControl, Earth System Grid Federation, , doi:<https://doi.org/10.22033/ESGF/CMIP6.11301>, 2019c.
- 710 Danabasoglu, G.: NCAR CESM2-WACCM-FV2 model output prepared for CMIP6 CMIP historical, Earth System Grid Federation, , doi:<https://doi.org/10.22033/ESGF/CMIP6.11298>, 2019d.
- Danabasoglu, G.: NCAR CESM2-WACCM-FV2 model output prepared for CMIP6 CMIP piControl, Earth System Grid Federation, , doi:<https://doi.org/10.22033/ESGF/CMIP6.11302>, 2019e.
- 715 Danabasoglu, G.: NCAR CESM2-WACCM model output prepared for CMIP6 CMIP abrupt-4xCO₂, Earth System Grid Federation, , doi:<https://doi.org/10.22033/ESGF/CMIP6.10039>, 2019f.
- Danabasoglu, G.: NCAR CESM2-WACCM model output prepared for CMIP6 CMIP historical, Earth System Grid Federation, , doi:<https://doi.org/10.22033/ESGF/CMIP6.10071>, 2019g.
- Danabasoglu, G.: NCAR CESM2-WACCM model output prepared for CMIP6 CMIP piControl, Earth System Grid Federation, , doi:<https://doi.org/10.22033/ESGF/CMIP6.10094>, 2019h.
- 720 Danabasoglu, G.: NCAR CESM2-WACCM model output prepared for CMIP6 ScenarioMIP ssp245, Earth System Grid Federation, , doi:<https://doi.org/10.22033/ESGF/CMIP6.10101>, 2019i.
- Danabasoglu, G.: NCAR CESM2-WACCM model output prepared for CMIP6 ScenarioMIP ssp370, Earth System Grid Federation, , doi:<https://doi.org/10.22033/ESGF/CMIP6.10102>, 2019j.
- 725 Danabasoglu, G.: NCAR CESM2-WACCM model output prepared for CMIP6 ScenarioMIP ssp585, Earth System Grid Federation, , doi:<https://doi.org/10.22033/ESGF/CMIP6.10115>, 2019k.
- Danabasoglu, G.: NCAR CESM2 model output prepared for CMIP6 CMIP abrupt-4xCO₂, Earth System Grid Federation, , doi:<https://doi.org/10.22033/ESGF/CMIP6.7519>, 2019l.
- Danabasoglu, G.: NCAR CESM2 model output prepared for CMIP6 CMIP historical, Earth System Grid Federation,

- 730 , doi:<https://doi.org/10.22033/ESGF/CMIP6.7627>, 2019m.
- Danabasoglu, G.: NCAR CESM2 model output prepared for CMIP6 ScenarioMIP ssp126, Earth System Grid Federation, , doi:<https://doi.org/10.22033/ESGF/CMIP6.7746>, 2019n.
- Danabasoglu, G.: NCAR CESM2 model output prepared for CMIP6 ScenarioMIP ssp245, Earth System Grid Federation, , doi:<https://doi.org/10.22033/ESGF/CMIP6.7748>, 2019o.
- 735 Danabasoglu, G.: NCAR CESM2 model output prepared for CMIP6 ScenarioMIP ssp370, Earth System Grid Federation, , doi:<https://doi.org/10.22033/ESGF/CMIP6.7753>, 2019p.
- Danabasoglu, G.: NCAR CESM2 model output prepared for CMIP6 ScenarioMIP ssp585, Earth System Grid Federation, , doi:<https://doi.org/10.22033/ESGF/CMIP6.7768>, 2019q.
- 740 Danabasoglu, G.: CAR CESM2-WACCM-FV2 model output prepared for CMIP6 CMIP abrupt-4xCO2, Earth System Grid Federation, , doi:<https://doi.org/10.22033/ESGF/CMIP6.11286>, 2020a.
- Danabasoglu, G.: NCAR CESM2-FV2 model output prepared for CMIP6 CMIP abrupt-4xCO2, Earth System Grid Federation, , doi:<https://doi.org/10.22033/ESGF/CMIP6.11285>, 2020b.
- Danabasoglu, G., Lawrence, D., Lindsay, K., Lipscomb, W. and Strand, G.: NCAR CESM2 model output prepared for CMIP6 CMIP piControl, Earth System Grid Federation, , doi:<https://doi.org/10.22033/ESGF/CMIP6.7733>, 2019.
- 745
- Dix, M., Bi, D., Dobrohotoff, P., Fiedler, R., Harman, I., Law, R., Mackallah, C., Marsland, S., O'Farrell, S., Rashid, H., Srbinovsky, J., Sullivan, A., Trenham, C., Vohralik, P., Watterson, I., Williams, G., Woodhouse, M., Bodman, R., Dias, F. B., Domingues, C., Hannah, N., Heerdegen, A., Savita, A., Wales, S., Allen, C., Druken, K., Evans, B., Richards, C., Ridzwan, S. M., Roberts, D., Smillie, J., Snow, K., Ward, M. and Yang, R.: CSIRO-ARCCSS ACCESS-CM2 model output prepared for CMIP6 CMIP abrupt-4xCO2, Earth System Grid Federation, , doi:<https://doi.org/10.22033/ESGF/CMIP6.4237>, 2019a.
- 750
- Dix, M., Bi, D., Dobrohotoff, P., Fiedler, R., Harman, I., Law, R., Mackallah, C., Marsland, S., O'Farrell, S., Rashid, H., Srbinovsky, J., Sullivan, A., Trenham, C., Vohralik, P., Watterson, I., Williams, G., Woodhouse, M., Bodham, R., Dias, F. B., Domingues, C. M., Hannah, N., Heerdegen, A., Savita, A., Wales, S., Allen, C., Druken, K., Evans, B., Richards, C., Ridzwan, S. M., Robers, D., Smillie, J., Snow, K., Ward, M. and Yang, R.: CSIRO-ARCCSS ACCESS-CM2 model output prepared for CMIP6 CMIP historical, Earth System Grid Federation, , doi:<https://doi.org/10.22033/ESGF/CMIP6.4271>, 2019b.
- 755
- Dix, M., Bi, D., Dobrohotoff, P., Fiedler, R., Harman, I., Law, R., Mackallah, C., Marsland, S., O'Farrell, S., Rashid, H., Srbinovsky, J., Sullivan, A., Trenham, C., Vohralik, P., Watterson, I., Williams, G., Woodhouse, M., Bodman, R., Dias, F. B., Domingues, C., Hannah, N., Heerdegen, A., Savita, A., Wales, S., Allen, C., Druken, K., Evans, B., Richards, C., Ridzwan, S. M., Roberts, D., Smillie, J., Snow, K., Ward, M. and Yang, R.: CSIRO-ARCCSS ACCESS-CM2 model output prepared for CMIP6 CMIP piControl, Earth System Grid Federation, , doi:<https://doi.org/10.22033/ESGF/CMIP6.4311>, 2019c.
- 760
- Dix, M., Bi, D., Dobrohotoff, P., Fiedler, R., Harman, I., Law, R., Mackallah, C., Marsland, S., O'Farrell, S., Rashid, H., Srbinovsky, J., Sullivan, A., Trenham, C., Vohralik, P., Watterson, I., Williams, G., Woodhouse, M., Bodman, R., Dias, F. B., Domingues, C. M., Hannah, N., Heerdegen, A., Savita, A., Wales, S., Allen, C., Druken, K., Evans, B., Richards, C., Ridzwan, S. M., Roberts, D., Smillie, J., Snow, K., Ward, M. and Yang, R.: CSIRO-ARCCSS ACCESS-CM2 model output prepared for CMIP6 ScenarioMIP ssp126, Earth System Grid Federation, , doi:<https://doi.org/10.22033/ESGF/CMIP6.4319>, 2019d.
- 765
- 770 Dix, M., Bi, D., Dobrohotoff, P., Fiedler, R., Harman, I., Law, R., Mackallah, C., Marsland, S., O'Farrell, S., Rashid, H., Srbinovsky, J., Sullivan, A., Trenham, C., Vohralik, P., Watterson, I., Williams, G., Woodhouse, M., Bodman, R., Dias, F. B., Domingues, C., Hannah, N., Heerdegen, A., Savita, A., Wales, S., Allen, C.,

- 775 Druken, K., Evans, B., Richards, C., Ridzwan, S. M., Roberts, D., Smillie, J., Snow, K., Ward, M. and Yang, R.: CSIRO-ARCCSS ACCESS-CM2 model output prepared for CMIP6 ScenarioMIP ssp245, Earth System Grid Federation, , doi:<https://doi.org/10.22033/ESGF/CMIP6.4321>, 2019e.
- 780 Dix, M., Bi, D., Dobrohotoff, P., Fiedler, R., Harman, I., Law, R., Mackallah, C., Marsland, S., O'Farrell, S., Rashid, H., Srbinovsky, J., Sullivan, A., Trenham, C., Vohralik, P., Watterson, I., Williams, G., Woodhouse, M., Bodman, R., Dias, F. B., Domingues, C., Hannah, N., Heerdegen, A., Savita, A., Wales, S., Allen, C., Druken, K., Evans, B., Richards, C., Ridzwan, S. M., Roberts, D., Smillie, J., Snow, K., Ward, M. and Yang, R.: CSIRO-ARCCSS ACCESS-CM2 model output prepared for CMIP6 ScenarioMIP ssp370, Earth System Grid Federation, , doi:<https://doi.org/10.22033/ESGF/CMIP6.4323>, 2019f.
- 785 Dix, M., Bi, D., Dobrohotoff, P., Fiedler, R., Harman, I., Law, R., Mackallah, C., Marsland, S., O'Farrell, S., Rashid, H., Srbinovsky, J., Sullivan, A., Trenham, C., Vohralik, P., Watterson, I., Williams, G., Woodhouse, M., Bodman, R., Dias, F. B., Domingues, C., Hannah, N., Heerdegen, A., Savita, A., Wales, S., Allen, C., Druken, K., Evans, B., Richards, C., Ridzwan, S. M., Roberts, D., Smillie, J., Snow, K., Ward, M. and Yang, R.: CSIRO-ARCCSS ACCESS-CM2 model output prepared for CMIP6 ScenarioMIP ssp585, Earth System Grid Federation, , doi:<https://doi.org/10.22033/ESGF/CMIP6.4332>, 2019g.
- Douglass, D. H. and Knox, R. S.: Climate forcing by the volcanic eruption of Mount Pinatubo, *Geophys. Res. Lett.*, 32(5), 1–5, doi:[10.1029/2004GL022119](https://doi.org/10.1029/2004GL022119), 2005.
- 790 EC-Earth Consortium (EC-Earth): EC-Earth-Consortium EC-Earth3-Veg model output prepared for CMIP6 CMIP, Earth System Grid Federation, , doi:<https://doi.org/10.22033/ESGF/CMIP6.4706>, 2019a.
- EC-Earth Consortium (EC-Earth): EC-Earth-Consortium EC-Earth3-Veg model output prepared for CMIP6 CMIP abrupt-4xCO₂, Earth System Grid Federation, , doi:<https://doi.org/10.22033/ESGF/CMIP6.4524>, 2019b.
- 795 EC-Earth Consortium (EC-Earth): EC-Earth-Consortium EC-Earth3-Veg model output prepared for CMIP6 CMIP piControl, Earth System Grid Federation, , doi:<https://doi.org/10.22033/ESGF/CMIP6.4848>, 2019c.
- EC-Earth Consortium (EC-Earth): EC-Earth-Consortium EC-Earth3-Veg model output prepared for CMIP6 ScenarioMIP ssp119, Earth System Grid Federation, , doi:<https://doi.org/10.22033/ESGF/CMIP6.4872>, 2019d.
- 800 EC-Earth Consortium (EC-Earth): EC-Earth-Consortium EC-Earth3-Veg model output prepared for CMIP6 ScenarioMIP ssp126, Earth System Grid Federation, , doi:<https://doi.org/10.22033/ESGF/CMIP6.4876>, 2019e.
- EC-Earth Consortium (EC-Earth): EC-Earth-Consortium EC-Earth3-Veg model output prepared for CMIP6 ScenarioMIP ssp245, Earth System Grid Federation, , doi:<https://doi.org/10.22033/ESGF/CMIP6.4882>, 2019f.
- 805 EC-Earth Consortium (EC-Earth): EC-Earth-Consortium EC-Earth3-Veg model output prepared for CMIP6 ScenarioMIP ssp370, Earth System Grid Federation, , doi:<https://doi.org/10.22033/ESGF/CMIP6.4886>, 2019g.
- EC-Earth Consortium (EC-Earth): EC-Earth-Consortium EC-Earth3-Veg model output prepared for CMIP6 ScenarioMIP ssp585, Earth System Grid Federation, , doi:<https://doi.org/10.22033/ESGF/CMIP6.4914>, 2019h.
- 810 EC-Earth Consortium (EC-Earth): EC-Earth-Consortium EC-Earth3 model output prepared for CMIP6 CMIP abrupt-4xCO₂, Earth System Grid Federation, , doi:<https://doi.org/10.22033/ESGF/CMIP6.4518>, 2019i.
- EC-Earth Consortium (EC-Earth): EC-Earth-Consortium EC-Earth3 model output prepared for CMIP6 CMIP historical, Earth System Grid Federation, , doi:<https://doi.org/10.22033/ESGF/CMIP6.4700>, 2019j.

- 815 EC-Earth Consortium (EC-Earth): EC-Earth-Consortium EC-Earth3 model output prepared for CMIP6 CMIP
piControl, Earth System Grid Federation, , doi:<https://doi.org/10.22033/ESGF/CMIP6.4842>, 2019k.
- EC-Earth Consortium (EC-Earth): EC-Earth-Consortium EC-Earth3 model output prepared for CMIP6 ScenarioMIP
ssp126, Earth System Grid Federation, , doi:<https://doi.org/10.22033/ESGF/CMIP6.4874>, 2019l.
- 820 EC-Earth Consortium (EC-Earth): EC-Earth-Consortium EC-Earth3 model output prepared for CMIP6 ScenarioMIP
ssp370, Earth System Grid Federation, , doi:<https://doi.org/10.22033/ESGF/CMIP6.4884>, 2019m.
- Foster, G. and Rahmstorf, S.: Global temperature evolution 1979–2010, *Environ. Res. Lett.*, 6(4), 044022,
doi:[10.1088/1748-9326/6/4/044022](https://doi.org/10.1088/1748-9326/6/4/044022), 2011.
- Friedlingstein, P., Meinshausen, M., Arora, V. K., Jones, C. D., Anav, A., Liddicoat, S. K. and Knutti, R.:
825 Uncertainties in CMIP5 climate projections due to carbon cycle feedbacks, *J. Clim.*, 27(2), 511–526,
doi:[10.1175/JCLI-D-12-00579.1](https://doi.org/10.1175/JCLI-D-12-00579.1), 2014.
- Friedlingstein, P., Jones, M. W., Sullivan, M. O., Andrew, R. M., Hauck, J., Peters, G. P., Peters, W., Pongratz, J.,
Sitch, S., Quéré, C. Le, Bakker, D. C. E., Canadell, J. G., Ciais, P., Jackson, R. B., Anthoni, P., Barbero, L.,
Bastos, A., Bastrikov, V., Becker, M., Bopp, L., Buitenhuis, E., Chandra, N., Chevallier, F., Chini, L. P.,
830 Currie, K., Feely, R. A., Gehlen, M., Gilfillan, D., Gkritzalis, T., Goll, D. S., Gruber, N., Gutekunst, S.,
Harris, I., Haverd, V., Houghton, R. A., Hurtt, G., Ilyina, T., Jain, A. K., Joetzjer, E., Kaplan, J. O., Kato, E.,
Goldewijk, K. K., Korsbakken, J. I., Landschützer, P., Lauvset, S. K., Lefevre, N., Lenton, A., Lienert, S.,
Lombardozzi, D., Marland, G., McGuire, P. C., Melton, J. R., Metzl, N., Munro, D. R., Nabel, J. E. M. S.,
Nakaoka, S., Neill, C., Omar, A. M., Ono, T., Peregon, A., Pierrot, D., Poulter, B., Rehder, G., Resplandy,
835 L., Robertson, E., Rodenbeck, C., Seferian, R., Schwinger, J., Smith, N., Tans, P. P., Tian, H., Tilbrook, B.,
Tubiello, F. N., Van Der Werf, G. R., Wiltshire, A. J. and Zaehle, S.: Global Carbon Budget 2019, *Earth
Syst. Sci. Data*, (11), 1783–1838, 2019.
- Good, P.: MOHC HadGEM3-GC31-LL model output prepared for CMIP6 ScenarioMIP ssp245, Earth System Grid
Federation, , doi:<https://doi.org/10.22033/ESGF/CMIP6.10851>, 2019.
- 840 Good, P.: MOHC HadGEM3-GC31-LL model output prepared for CMIP6 ScenarioMIP ssp126, Earth System Grid
Federation, , doi:<https://doi.org/10.22033/ESGF/CMIP6.10849>, 2020a.
- Good, P.: MOHC HadGEM3-GC31-LL model output prepared for CMIP6 ScenarioMIP ssp585, Earth System Grid
Federation, , doi:<https://doi.org/10.22033/ESGF/CMIP6.10901>, 2020b.
- 845 Good, P., Sellar, A., Tang, Y., Rumbold, S., Ellis, R., Kelley, D. and Kuhlbrodt, T.: MOHC UKESM1.0-LL model
output prepared for CMIP6 ScenarioMIP ssp119, Earth System Grid Federation, ,
doi:<https://doi.org/10.22033/ESGF/CMIP6.6329>, 2019a.
- Good, P., Sellar, A., Tang, Y., Rumbold, S., Ellis, R., Kelley, D. and Kuhlbrodt, T.: MOHC UKESM1.0-LL model
output prepared for CMIP6 ScenarioMIP ssp126, Earth System Grid Federation, ,
doi:<https://doi.org/10.22033/ESGF/CMIP6.6333>, 2019b.
- 850 Good, P., Sellar, A., Tang, Y., Rumbold, S., Ellis, R., Kelley, D. and Kuhlbrodt, T.: MOHC UKESM1.0-LL model
output prepared for CMIP6 ScenarioMIP ssp245, Earth System Grid Federation, ,
doi:<https://doi.org/10.22033/ESGF/CMIP6.6339>, 2019c.
- Good, P., Sellar, A., Tang, Y., Rumbold, S., Ellis, R., Kelley, D. and Kuhlbrodt, T.: MOHC UKESM1.0-LL model
output prepared for CMIP6 ScenarioMIP ssp370, Earth System Grid Federation, ,
doi:<https://doi.org/10.22033/ESGF/CMIP6.6347>, 2019d.
- 855 Good, P., Sellar, A., Tang, Y., Rumbold, S., Ellis, R., Kelley, D. and Kuhlbrodt, T.: MOHC UKESM1.0-LL model
output prepared for CMIP6 ScenarioMIP ssp434, Earth System Grid Federation, ,

- Good, P., Sellar, A., Tang, Y., Rumbold, S., Ellis, R., Kelley, D. and Kuhlbrodt, T.: MOHC UKESM1.0-LL model
860 output prepared for CMIP6 ScenarioMIP ssp585, Earth System Grid Federation, ,
doi:<https://doi.org/10.22033/ESGF/CMIP6.6405>, 2019f.
- Gregory, J. M., Ingram, W. J., Palmer, M. A., Jones, G. S., Stott, P. A., Thorpe, R. B., Lowe, J. A., Johns, T. C. and
Williams, K. D.: A new method for diagnosing radiative forcing and climate sensitivity, *Geophys. Res. Lett.*,
31(3), 2–5, doi:10.1029/2003GL018747, 2004.
- Guo, H., John, J. G., Blanton, C., McHugh, C., Nikonov, S., Radhakrishnan, A., Zadeh, N. T., Balaji, V., Durachta,
865 J., Dupuis, C., Menzel, R., Robinson, T., Underwood, S., Vahlenkamp, H., Dunne, K. A., Gauthier, P. P.,
Ginoux, P., Griffies, S. M., Hallberg, R., Harrison, M., Hurlin, W., Malyshev, S., Naik, V., Paulot, F.,
Paynter, D. J., Ploshay, J., Schwarzkopf, D. M., Seman, C. J., Shao, A., Silvers, L., Wyman, B., Zeng, Y.,
Adcroft, A., Dunne, J. P., Held, I. M., Krasting, J. P., Horowitz, L. W., Milly, P. C. ., Shevliakova, E.,
870 Winton, M. and Zhao, M.: NOAA-GFDL GFDL-CM4 model output prepared for CMIP6 CMIP abrupt-
4xCO₂, Earth System Grid Federation, , doi:<https://doi.org/10.22033/ESGF/CMIP6.8486>, 2018a.
- Guo, H., John, J. G., Blanton, C., McHugh, C., Nikonov, S., Radhakrishnan, A., Zadeh, N. T., Balaji, V., Durachta,
J., Dupuis, C., Menzel, R., Robinson, T., Underwood, S., Vahlenkamp, H., Dunne, K. A., Gauthier, P. P.,
Ginoux, P., Griffies, S. M., Hallberg, R. W., Harrison, M., Hurlin, W., Malyshev, S., Naik, V., Paulot, F.,
875 Paynter, D. J., Ploshay, J., Schwarzkopf, D. M., Seman, C. J., Shao, A., Silvers, L. G., Wyman, B., Zeng, Y.,
Adcroft, A. J., Dunne, J. P., Held, I. M., Krasting, J. P., Horowitz, L. W., Milly, P. C. ., Shevliakova, E.,
Winton, M. and Zhao, M.: NOAA-GFDL GFDL-CM4 model output prepared for CMIP6 CMIP historical,
Earth System Grid Federation, , doi:<https://doi.org/10.22033/ESGF/CMIP6.8594>, 2018b.
- Guo, H., John, J. G., Blanton, C., McHugh, C., Nikonov, S., Radhakrishnan, A., Zadeh, N. T., Balaji, V., Durachta,
J., Dupuis, C., Menzel, R., Robinson, T., Underwood, S., Vahlenkamp, H., Dunne, K. A., Gauthier, P. P.,
880 Ginoux, P., Griffies, S. M., Hallberg, R., Harrison, M., Hurlin, W., Malyshev, S., Naik, V., Paulot, F.,
Paynter, D. J., Ploshay, J., Rand, K., Schwarzkopf, D. M., Seman, C. J., Shao, A., Silvers, L., Wyman, B.,
Zeng, Y., Adcroft, A., Dunne, J. P., Held, I. M., Krasting, J. P., Horowitz, L. W., Milly, C., Shevliakova, E.,
Winton, M., Zhao, M., Yan, X. and Zhang, R.: NOAA-GFDL GFDL-CM4 model output prepared for
CMIP6 ScenarioMIP ssp245, Earth System Grid Federation, ,
885 doi:<https://doi.org/10.22033/ESGF/CMIP6.9263>, 2018c.
- Guo, H., John, J. G., Blanton, C., McHugh, C., Nikonov, S., Radhakrishnan, A., Zadeh, N. T., Balaji, V., Durachta,
J., Dupuis, C., Menzel, R., Robinson, T., Underwood, S., Vahlenkamp, H., Dunne, K. A., Gauthier, P. P.,
Ginoux, P., Griffies, S. M., Hallberg, R., Harrison, M., Hurlin, W., Malyshev, S., Naik, V., Paulot, F.,
890 Paynter, D. J., Ploshay, J., Rand, K., Schwarzkopf, D. M., Seman, C. J., Shao, A., Silvers, L., Wyman, B.,
Zeng, Y., Adcroft, A., Dunne, J. P., Held, I. M., Krasting, J. P., Horowitz, L. W., Milly, C., Shevliakova, E.,
Winton, M., Zhao, M., Yan, X. and Zhang, R.: NOAA-GFDL GFDL-CM4 model output prepared for
CMIP6 ScenarioMIP ssp585, Earth System Grid Federation, ,
doi:<https://doi.org/10.22033/ESGF/CMIP6.9268>, 2018d.
- Guo, H., John, J. G., Blanton, C., McHugh, C., Nikonov, S., Radhakrishnan, A., Zadeh, N. T., Balaji, V., Durachta,
895 J., Dupuis, C., Menzel, R., Robinson, T., Underwood, S., Vahlenkamp, H., Dunne, K. A., Gauthier, P. P.,
Ginoux, P., Griffies, S. M., Hallberg, R., Harrison, M., Hurlin, W., Malyshev, S., Naik, V., Paulot, F.,
Paynter, D. J., Ploshay, J., Schwarzkopf, D. M., Seman, C. J., Shao, A., Silvers, L., Wyman, B., Zeng, Y.,
Adcroft, A., Dunne, J. P., Held, I. M., Krasting, J. P., Horowitz, L. W., Milly, P. C. ., Shevliakova, E.,
900 Winton, M. and Zhao, M.: NOAA-GFDL GFDL-CM4 piControl model output, Earth System Grid
Federation, , doi:<https://doi.org/10.22033/ESGF/CMIP6.8666>, 2018e.
- Hajima, T., Abe, M., Arakawa, O., Suzuki, T., Komuro, Y., Ogura, T., Ogochi, K., Watanabe, M., Yamamoto, A.,
Tatebe, H., Noguchi, M. A., Ohgaito, R., Ito, A., Yamazaki, D., Ito, A., Takata, K., Watanabe, S.,
Kawamiya, M. and Tachiiri, K.: MIROC MIROC-ES2L model output prepared for CMIP6 CMIP historical,

- 905 Hope, A. P., Canty, T. P., Salawitch, R. J., Tribett, W. R. and Bennett, B. F.: Forecasting Global Warming, in Paris Climate Agreement: Beacon of Hope, pp. 51–114, Springer Climate., 2017.
- Huang, W.: THU CIESM model output prepared for CMIP6 CMIP historical, Earth System Grid Federation, , doi:<https://doi.org/10.22033/ESGF/CMIP6.7789>, 2019a.
- Huang, W.: THU CIESM model output prepared for CMIP6 ScenarioMIP ssp126, Earth System Grid Federation, ,
910 doi:<https://doi.org/10.22033/ESGF/CMIP6.8857>, 2019b.
- Huang, W.: THU CIESM model output prepared for CMIP6 ScenarioMIP ssp245, Earth System Grid Federation, , doi:<https://doi.org/10.22033/ESGF/CMIP6.8858>, 2020a.
- Huang, W.: THU CIESM model output prepared for CMIP6 ScenarioMIP ssp585, Earth System Grid Federation, , doi:<https://doi.org/10.22033/ESGF/CMIP6.8863>, 2020b.
- 915 Ishii, M., Fukuda, Y., Hirahara, S., Yasui, S., Suzuki, T. and Sato, K.: Accuracy of Global Upper Ocean Heat Content Estimation Expected from Present Observational Data Sets, *Sci. Online Lett. Atmos.*, 13(0), 163–167, doi:10.2151/sola.2017-030, 2017.
- John, J. G., Blanton, C., McHugh, C., Nikonov, S., Radhakrishnan, A., Rand, K., Vahlenkamp, H., Zadeh, N. T., Gauthier, P. P., Ginoux, P., Harrison, M., Horowitz, L. W., Malyshev, S., Naik, V., Paynter, D. J., Ploshay, J., Silvers, L. G., Stock, C., Winton, M., Zeng, Y. and Dunne, J. P.: NOAA-GFDL GFDL-ESM4 model
920 output prepared for CMIP6 ScenarioMIP ssp119, Earth System Grid Federation, , doi:<https://doi.org/10.22033/ESGF/CMIP6.8683>, 2018a.
- John, J. G., Blanton, C., McHugh, C., Nikonov, S., Radhakrishnan, A., Rand, K., Vahlenkamp, H., Zadeh, N. T., Gauthier, P. P., Ginoux, P., Harrison, M., Horowitz, L. W., Malyshev, S., Naik, V., Paynter, D. J., Ploshay, J., Silvers, L. G., Stock, C., Winton, M., Zeng, Y. and Dunne, J. P.: NOAA-GFDL GFDL-ESM4 model
925 output prepared for CMIP6 ScenarioMIP ssp126, Earth System Grid Federation, , doi:<https://doi.org/10.22033/ESGF/CMIP6.8684>, 2018b.
- John, J. G., Blanton, C., McHugh, C., Radhakrishnan, A., Rand, K., Vahlenkamp, H., Wilson, C., Zadeh, N. T., Gauthier, P. P., Dunne, J. P., Dussin, R., Horowitz, L. W., Lin, P., Malyshev, S., Naik, V., Ploshay, J., Silvers, L., Stock, C., Winton, M. and Zeng, Y.: NOAA-GFDL GFDL-ESM4 model output prepared for
930 CMIP6 ScenarioMIP ssp245, Earth System Grid Federation, , doi:<https://doi.org/10.22033/ESGF/CMIP6.8686>, 2018c.
- John, J. G., Blanton, C., McHugh, C., Nikonov, S., Radhakrishnan, A., Rand, K., Vahlenkamp, H., Zadeh, N. T., Gauthier, P. P., Ginoux, P., Harrison, M., Horowitz, L. W., Malyshev, S., Naik, V., Paynter, D. J., Ploshay, J., Silvers, L., Stock, C., Winton, M., Zeng, Y. and Dunne, J. P.: NOAA-GFDL GFDL-ESM4 model output
935 prepared for CMIP6 ScenarioMIP ssp370, Earth System Grid Federation, , doi:<https://doi.org/10.22033/ESGF/CMIP6.8691>, 2018d.
- John, J. G., Blanton, C., McHugh, C., Nikonov, S., Radhakrishnan, A., Rand, K., Vahlenkamp, H., Zadeh, N. T., Gauthier, P. P., Ginoux, P., Harrison, M., Horowitz, L. W., Malyshev, S., Naik, V., Paynter, D. J., Ploshay, J., Silvers, L., Stock, C., Winton, M., Zeng, Y. and Dunne, J. P.: NOAA-GFDL GFDL-ESM4 model output
940 prepared for CMIP6 ScenarioMIP ssp585, Earth System Grid Federation, , doi:<https://doi.org/10.22033/ESGF/CMIP6.8706>, 2018e.
- Jones, C., Sellar, A., Tang, Y. and Rumbold, S.: Results from the UKESM1 CMIP6 DECK and historical simulations, UKESM [online] Available from: <https://ukesm.ac.uk/portfolio-item/ukesm1-cmip6-deck-and-historical/#> (Accessed 9 October 2019), 2019.
945

- 950 Jungclaus, J. H., Bittner, M., Wieners, K.-H., Wachsmann, F., Schupfner, M., Legutke, S., Giorgetta, M., Reick, C., Gayler, V., Haak, H., de Vrese, P., Raddatz, T., Esch, M., Mauritsen, T., von Storch, J.-S., Behrens, J., Brovkin, V., Claussen, M., Crueger, T., Fast, I., Fiedler, S., Hagemann, S., Hohenegger, C., Jahns, T., Kloster, S., Kinne, S., Lasslop, G., Kornbluh, L., Marotzke, J., Matali, D., Meraner, K., Mikolajewicz, U., Modali, K., Muller, W., Nabel, J., Notz, D., Peters, K., Pincus, R., Pohlmann, H., Pongratz, J., Rast, S., Schmidt, H., Schnur, R., Schulzweida, U., Six, K., Stevens, B., Voigt, A. and Roeckner, E.: MPI-M MPI-ESM1.2-HR model output prepared for CMIP6 CMIP historical, Earth System Grid Federation, , doi:<https://doi.org/10.22033/ESGF/CMIP6.6594>, 2019.
- 955 Kavvada, A., Ruiz-Barradas, A. and Nigam, S.: AMO's structure and climate footprint in observations and IPCC AR5 climate simulations, *Clim. Dyn.*, 41(5–6), 1345–1364, doi:[10.1007/s00382-013-1712-1](https://doi.org/10.1007/s00382-013-1712-1), 2013.
- 960 Kelley, M., Schmidt, G., Nazarenko, L., Bauer, S., Ruedy, R., Russell, G., Ackerman, A., Aleinov, I., Bauer, M., Bleck, R., Canuto, V., Cesana, G., Cheng, Y., Clune, T., Cook, B., Cruz, C., Del Genio, A., Elsaesser, G., Faluvegi, G., Kiang, N., Kim, D., Lacis, A., Leboissetier, A., LeGrande, A., Lo, K., Marshall, J., Matthews, E., McDermid, S., Mezuman, K., Miller, R., Murray, L., Oinas, V., Orbe, C., Pérez García-Pando, C., Perlwitz, J., Puma, M., Rind, D., Romanou, A., Shindell, D., Sun, S., Tausnev, N., Tsigaridis, K., Tselioudis, G., Weng, E., Wu, J. and Yao, M.: GISS-E2.1: Configurations and Climatology, *J. Adv. Model. Earth Syst.*, 2018(Phase 6), doi:[10.1029/2019MS002025](https://doi.org/10.1029/2019MS002025), 2020.
- 965 Krasting, J. P., John, J. G., Blanton, C., McHugh, C., Nikonov, S., Radhakrishnan, A., Rand, K., Zadeh, N. T., Balaji, V., Durachta, J., Dupuis, C., Menzel, R., Robinson, T., Underwood, S., Vahlenkamp, H., Dunne, K. A., Gauthier, P. P., Ginoux, P., Griffies, S. M., Hallberg, R., Harrison, M., Hurlin, W., Malyshev, S., Naik, V., Paulot, F., Paynter, D. J., Ploshay, J., Schwarzkopf, D. M., Seman, C. J., Silvers, L., Wyman, B., Zeng, Y., Adcroft, A., Dunne, J. P., Guo, H., Held, I. M., Horowitz, L. W., Milly, P. C. ., Shevliakova, E., Stock, C., Winton, M. and Zhao, M.: NOAA-GFDL GFDL-ESM4 model output prepared for CMIP6 CMIP abrupt-4xCO₂, Earth System Grid Federation, , doi:<https://doi.org/10.22033/ESGF/CMIP6.8489>, 2018a.
- 970 Krasting, J. P., John, J. G., Blanton, C., McHugh, C., Nikonov, S., Radhakrishnan, A., Rand, K., Zadeh, N. T., Balaji, V., Durachta, J., Dupuis, C., Menzel, R., Robinson, T., Underwood, S., Vahlenkamp, H., Dunne, K. A., Gauthier, P. P., Ginoux, P., Griffies, S. M., Hallberg, R. W., Harrison, M., Hurlin, W., Malyshev, S., Naik, V., Paulot, F., Paynter, D. J., Ploshay, J., Schwarzkopf, D. M., Seman, C. J., Silvers, L. G., Wyman, B., Zeng, Y., Adcroft, A. J., Dunne, J. P., Guo, H., Held, I. M., Horowitz, L. W., Milly, P. C. ., Shevliakova, E., Stock, C., Winton, M. and Zhao, M.: NOAA-GFDL GFDL-ESM4 model output prepared for CMIP6 CMIP historical, Earth System Grid Federation, , doi:<https://doi.org/10.22033/ESGF/CMIP6.8597>, 2018b.
- 975 Krasting, J. P., John, J. G., Blanton, C., McHugh, C., Nikonov, S., Radhakrishnan, A., Rand, K., Zadeh, N. T., Balaji, V., Durachta, J., Dupuis, C., Menzel, R., Robinson, T., Underwood, S., Vahlenkamp, H., Dunne, K. A., Gauthier, P. P., Ginoux, P., Griffies, S. M., Hallberg, R., Harrison, M., Hurlin, W., Malyshev, S., Naik, V., Paulot, F., Paynter, D. J., Ploshay, J., Schwarzkopf, D. M., Seman, C. J., Silvers, L., Wyman, B., Zeng, Y., Adcroft, A., Dunne, J. P., Guo, H., Held, I. M., Horowitz, L. W., Milly, P. C. ., Shevliakova, E., Stock, C., Winton, M. and Zhao, M.: NOAA-GFDL GFDL-ESM4 model output prepared for CMIP6 CMIP piControl, Earth System Grid Federation, , doi:<https://doi.org/10.22033/ESGF/CMIP6.8669>, 2018c.
- 980 Krasting, J. P., John, J. G., Blanton, C., McHugh, C., Nikonov, S., Radhakrishnan, A., Rand, K., Zadeh, N. T., Balaji, V., Durachta, J., Dupuis, C., Menzel, R., Robinson, T., Underwood, S., Vahlenkamp, H., Dunne, K. A., Gauthier, P. P., Ginoux, P., Griffies, S. M., Hallberg, R., Harrison, M., Hurlin, W., Malyshev, S., Naik, V., Paulot, F., Paynter, D. J., Ploshay, J., Schwarzkopf, D. M., Seman, C. J., Silvers, L., Wyman, B., Zeng, Y., Adcroft, A., Dunne, J. P., Guo, H., Held, I. M., Horowitz, L. W., Milly, P. C. ., Shevliakova, E., Stock, C., Winton, M. and Zhao, M.: NOAA-GFDL GFDL-ESM4 model output prepared for CMIP6 CMIP piControl, Earth System Grid Federation, , doi:<https://doi.org/10.22033/ESGF/CMIP6.8669>, 2018c.
- 985 Lean, J. L. and Rind, D. H.: How natural and anthropogenic influences alter global and regional surface temperatures: 1889 to 2006, *Geophys. Res. Lett.*, 35(18), 1–6, doi:[10.1029/2008GL034864](https://doi.org/10.1029/2008GL034864), 2008.
- Levitus, S., Antonov, J. I., Boyer, T. P., Baranova, O. K., Garcia, H. E., Locarnini, R. A., Mishonov, A. V., Reagan, J. R., Seidov, D., Yarosh, E. S. and Zweng, M. M.: World ocean heat content and thermocline sea level change (0–2000m), 1955–2010, *Geophys. Res. Lett.*, 39(10), 1–5, doi:[10.1029/2012GL051106](https://doi.org/10.1029/2012GL051106), 2012.
- 990 Li, L.: CAS FGOALS-g3 model output prepared for CMIP6 CMIP historical, Earth System Grid Federation, , doi:<https://doi.org/10.22033/ESGF/CMIP6.3356>, 2019a.
- Li, L.: CAS FGOALS-g3 model output prepared for CMIP6 ScenarioMIP ssp126, Earth System Grid Federation, ,

doi:<https://doi.org/10.22033/ESGF/CMIP6.3465>, 2019b.

Li, L.: CAS FGOALS-g3 model output prepared for CMIP6 ScenarioMIP ssp245, Earth System Grid Federation, , doi:<https://doi.org/10.22033/ESGF/CMIP6.3469>, 2019c.

995 Li, L.: CAS FGOALS-g3 model output prepared for CMIP6 ScenarioMIP ssp370, Earth System Grid Federation, , doi:<https://doi.org/10.22033/ESGF/CMIP6.3480>, 2019d.

Li, L.: CAS FGOALS-g3 model output prepared for CMIP6 ScenarioMIP ssp585, Earth System Grid Federation, , doi:<https://doi.org/10.22033/ESGF/CMIP6.3503>, 2019e.

1000 Meinshausen, M., Smith, S. J., Calvin, K., Daniel, J. S., Kainuma, M. L. T., Lamarque, J., Matsumoto, K., Montzka, S. A., Raper, S. C. B., Riahi, K., Thomson, A., Velders, G. J. M. and van Vuuren, D. P. P.: The RCP greenhouse gas concentrations and their extensions from 1765 to 2300, *Clim. Change*, 109(1), 213–241, doi:10.1007/s10584-011-0156-z, 2011.

1005 Morice, C. P., Kennedy, J. J., Rayner, N. A. and Jones, P. D.: Quantifying uncertainties in global and regional temperature change using an ensemble of observational estimates: The HadCRUT4 data set, *J. Geophys. Res. Atmos.*, 117(8), 1–22, doi:10.1029/2011JD017187, 2012.

Murphy, J. M., Booth, B. B. B., Boulton, C. A., Clark, R. T., Harris, G. R., Lowe, J. A. and Sexton, D. M. H.: Transient climate changes in a perturbed parameter ensemble of emissions-driven earth system model simulations, *Clim. Dyn.*, 43(9–10), 2855–2885, doi:10.1007/s00382-014-2097-5, 2014.

1010 Myhre, G., Shindell, D., Bréon, F.-M., Collins, W., Fuglestedt, J., Huang, J., Koch, D., Lamarque, J.-F., Lee, D., Mendoza, B., Nakajima, T., Robock, A., Stephens, G., Takemura, T. and Zhang, H.: Anthropogenic and Natural Radiative Forcing, *Clim. Chang. 2013 Phys. Sci. Basis. Contrib. Work. Gr. I to Fifth Assess. Rep. Intergov. Panel Clim. Chang.*, 659–740, doi:10.1017/CBO9781107415324.018, 2013.

1015 NASA Goddard Institute for Space Studies (NASA/GISS): NASA-GISS GISS-E2.1G model output prepared for CMIP6 CMIP abrupt-4xCO2, Earth System Grid Federation, , doi:<https://doi.org/10.22033/ESGF/CMIP6.6976>, 2018a.

NASA Goddard Institute for Space Studies (NASA/GISS): NASA-GISS GISS-E2.1G model output prepared for CMIP6 CMIP historical, Earth System Grid Federation, , doi:<https://doi.org/10.22033/ESGF/CMIP6.7127>, 2018b.

1020 NASA Goddard Institute for Space Studies (NASA/GISS): NASA-GISS GISS-E2.1G model output prepared for CMIP6 CMIP piControl, Earth System Grid Federation, , doi:<https://doi.org/10.22033/ESGF/CMIP6.7380>, 2018c.

NASA Goddard Institute for Space Studies (NASA/GISS): NASA-GISS GISS-E2.1H model output prepared for CMIP6 CMIP piControl, Earth System Grid Federation, , doi:<https://doi.org/10.22033/ESGF/CMIP6.7381>, 2018d.

1025 NASA Goddard Institute for Space Studies (NASA/GISS): NASA-GISS GISS-E2-2-G model output prepared for CMIP6 CMIP abrupt-4xCO2, Earth System Grid Federation, , doi:<https://doi.org/10.22033/ESGF/CMIP6.6978>, 2019a.

1030 NASA Goddard Institute for Space Studies (NASA/GISS): NASA-GISS GISS-E2.1H model output prepared for CMIP6 CMIP abrupt-4xCO2, Earth System Grid Federation, , doi:<https://doi.org/10.22033/ESGF/CMIP6.6977>, 2019b.

NASA Goddard Institute for Space Studies (NASA/GISS): NASA-GISS GISS-E2.1H model output prepared for CMIP6 CMIP historical, Earth System Grid Federation, , doi:<https://doi.org/10.22033/ESGF/CMIP6.7128>,

2019c.

- 1035 NASA Goddard Institute for Space Studies (NASA/GISS): NASA-GISS GISS-E2.1G model output prepared for CMIP6 ScenarioMIP ssp126, Earth System Grid Federation, , doi:<https://doi.org/10.22033/ESGF/CMIP6.7410>, 2020a.
- NASA Goddard Institute for Space Studies (NASA/GISS): NASA-GISS GISS-E2.1G model output prepared for CMIP6 ScenarioMIP ssp245, Earth System Grid Federation, , doi:<https://doi.org/10.22033/ESGF/CMIP6.7415>, 2020b.
- 1040 NASA Goddard Institute for Space Studies (NASA/GISS): NASA-GISS GISS-E2.1G model output prepared for CMIP6 ScenarioMIP ssp370, Earth System Grid Federation, , doi:<https://doi.org/10.22033/ESGF/CMIP6.7426>, 2020c.
- NASA Goddard Institute for Space Studies (NASA/GISS): NASA-GISS GISS-E2.1G model output prepared for CMIP6 ScenarioMIP ssp585, Earth System Grid Federation, , doi:<https://doi.org/10.22033/ESGF/CMIP6.7460>, 2020d.
- 1045
- Neubauer, D., Ferrachat, S., Siegenthaler-Le Drian, C., Stoll, J., Folini, D. S., Tegen, I., Wieners, K.-H., Mauritsen, T., Stemmler, I., Barthel, S., Bey, I., Daskalakis, M., Heinold, B., Kokkola, H., Partridge, D., Rast, S., Schmidt, H., Schutgens, N., Stanelle, T., Stier, P., Watson-Parrs, D. and Lohmann, U.: HAMMOZ-Consortium MPI-ESM1.2-HAM model output prepared for CMIP6 CMIP6 historical, Earth System Grid Federation, , doi:<https://doi.org/10.22033/ESGF/CMIP6.5016>, 2019.
- 1050
- Nicholls, Z., Meinshausen, M., Lewis, J., Corradi, M. R., Dorheim, K., Gasser, T., Gieseke, R., Hope, A. P., Leach, N. J., McBride, L. A., Quilcaille, Y., Rogelj, J., Salawitch, R. J., Samset, B. H., Sandstad, M., Shiklomanov, A., Skeie, R. B., Smith, C. J., Smith, S. J., Su, X., Tsutsui, J., Vega-Westhoff, B. and Woodward, D.: Reduced Complexity Model Intercomparison Project Phase 2 : Synthesising Earth system knowledge for probabilistic climate projections, Earth's Futur., doi:<https://doi.org/10.1002/essoar.10504793.1>, 2020.
- 1055
- Park, S. and Shin, J.: SNU SAM0-UNICON model output prepared for CMIP6 CMIP abrupt-4xCO2, Earth System Grid Federation, , doi:<https://doi.org/10.22033/ESGF/CMIP6.7783>, 2019a.
- Park, S. and Shin, J.: SNU SAM0-UNICON model output prepared for CMIP6 CMIP historical, Earth System Grid Federation, , doi:<https://doi.org/10.22033/ESGF/CMIP6.7789>, 2019b.
- 1060
- Park, S. and Shin, J.: SNU SAM0-UNICON model output prepared for CMIP6 CMIP piControl, Earth System Grid Federation, , doi:<https://doi.org/10.22033/ESGF/CMIP6.7791>, 2019c.
- Ridley, J., Menary, M., Kuhlbrodt, T., Andrews, M. and Andrews, T.: MOHC HadGEM3-GC31-LL model output prepared for CMIP6 CMIP piControl, Earth System Grid Federation, , doi:<https://doi.org/10.22033/ESGF/CMIP6.6294>, 2018.
- 1065
- Ridley, J., Menary, M., Kuhlbrodt, T., Andrews, M. and Andrews, T.: MOHC HadGEM3-GC31-LL model output prepared for CMIP6 CMIP, Earth System Grid Federation, , doi:<https://doi.org/10.22033/ESGF/CMIP6.6109>, 2019a.
- Ridley, J., Menary, M., Kuhlbrodt, T., Andrews, M. and Andrews, T.: MOHC HadGEM3-GC31-LL model output prepared for CMIP6 CMIP abrupt-4xCO2, Earth System Grid Federation, , doi:<https://doi.org/10.22033/ESGF/CMIP6.5839>, 2019b.
- 1070
- Ridley, J., Menary, M., Kuhlbrodt, T., Andrews, M. and Andrews, T.: MOHC HadGEM3-GC31-MM model output prepared for CMIP6 CMIP historical, Earth System Grid Federation, , doi:<https://doi.org/10.22033/ESGF/CMIP6.6112>, 2019c.

- 1075 Rong, X.: CAMS CAMS-CSM1.0 model output preapred for CMIP6 CMIP historical, Earth System Grid Federation, , doi:<https://doi.org/10.22033/ESGF/CMIP6.9754>, 2019a.
- Rong, X.: CAMS CAMS-CSM1.0 model output prepared for CMIP6 ScenarioMIP ssp119, Earth System Grid Federation, , doi:<https://doi.org/10.22033/ESGF/CMIP6.11045>, 2019b.
- Rong, X.: CAMS CAMS-CSM1.0 model output prepared for CMIP6 ScenarioMIP ssp126, Earth System Grid Federation, , doi:<https://doi.org/10.22033/ESGF/CMIP6.11046>, 2019c.
- 1080 Rong, X.: CAMS CAMS-CSM1.0 model output prepared for CMIP6 ScenarioMIP ssp245, Earth System Grid Federation, , doi:<https://doi.org/10.22033/ESGF/CMIP6.11047>, 2019d.
- Rong, X.: CAMS CAMS-CSM1.0 model output prepared for CMIP6 ScenarioMIP ssp370, Earth System Grid Federation, , doi:<https://doi.org/10.22033/ESGF/CMIP6.11048>, 2019e.
- 1085 Rong, X.: CAMS CAMS-CSM1.0 model output prepared for CMIP6 ScenarioMIP ssp585, Earth System Grid Federation, , doi:<https://doi.org/10.22033/ESGF/CMIP6.11052>, 2019f.
- Schupfner, M., Wieners, K.-H., Wachsmann, F., Steger, C., Bittner, M., Jungclaus, J., Früh, B., Pankatz, K., Giorgetta, M., Reick, C., Legutke, S., Esch, M., Gayler, V., Haak, H., de Vrese, P., Raddatz, T., Mauritsen, T., von Storch, J.-S., Behrens, J., Brovkin, V., Claussen, M., Crueger, T., Fast, I., Fiedler, S., Hagemann, S., Hohenegger, C., Jahns, T., Kloster, S., Kinne, S., Lasslop, G., Kornblueh, L., Marotzke, J., Matei, D., Meraner, K., Mikolajewicz, U., Modali, K., Müller, W., Nabel, J., Notz, D., Peters, K., Pincus, R., Pohlmann, H., Pongratz, J., Rast, S., Schmidt, H., Schnur, R., Schulzweida, U., Six, K., Stevens, B., Voigt, A. and Roeckner, E.: DKRZ MIP-ESM1.2-HR model output prepared for CMIP6 ScenarioMIP ssp126, Earth System Grid Federation, , doi:<https://doi.org/10.22033/ESGF/CMIP6.4397>, 2019a.
- 1090 Schupfner, M., Wieners, K.-H., Wachsmann, F., Steger, C., Bittner, M., Jungclaus, J., Früh, B., Pankatz, K., Giorgetta, M., Reick, C., Legutke, S., Esch, M., Gayler, V., Haak, H., de Vrese, P., Raddatz, T., Mauritsen, T., von Storch, J.-S., Behrens, J., Brovkin, V., Claussen, M., Crueger, T., Fast, I., Fiedler, S., Hagemann, S., Hohenegger, C., Jahns, T., Kloster, S., Kinne, S., Lasslop, G., Kornblueh, L., Marotzke, J., Matei, D., Meraner, K., Mikolajewicz, U., Modali, K., Müller, W., Nabel, J., Notz, D., Peters, K., Pincus, R., Pohlmann, H., Pongratz, J., Rast, S., Schmidt, H., Schnur, R., Schulzweida, U., Six, K., Stevens, B., Voigt, A. and Roeckner, E.: DKRZ MPI-ESM1.2-HR model output prepared for CMIP6 ScenarioMIP ssp245, Earth System Grid Federation, , doi:<https://doi.org/10.22033/ESGF/CMIP6.4398>, 2019b.
- 1095 Schupfner, M., Wieners, K.-H., Wachsmann, F., Steger, C., Bittner, M., Jungclaus, J., Früh, B., Pankatz, K., Giorgetta, M., Reick, C., Legutke, S., Esch, M., Gayler, V., Haak, H., de Vrese, P., Raddatz, T., Mauritsen, T., von Storch, J.-S., Behrens, J., Brovkin, V., Claussen, M., Crueger, T., Fast, I., Fiedler, S., Hagemann, S., Hohenegger, C., Jahns, T., Kloster, S., Kinne, S., Lasslop, G., Kornblueh, L., Marotzke, J., Matei, D., Meraner, K., Mikolajewicz, U., Modali, K., Müller, W., Nabel, J., Notz, D., Peters, K., Pincus, R., Pohlmann, H., Pongratz, J., Rast, S., Schmidt, H., Schnur, R., Schulzweida, U., Six, K., Stevens, B., Voigt, A. and Roeckner, E.: DKRZ MPI-ESM1.2-HR model output prepared for CMIP6 ScenarioMIP ssp370, Earth System Grid Federation, , doi:<https://doi.org/10.22033/ESGF/CMIP6.4399>, 2019c.
- 1100 Schupfner, M., Wieners, K.-H., Wachsmann, F., Steger, C., Bittner, M., Jungclaus, J., Früh, B., Pankatz, K., Giorgetta, M., Reick, C., Legutke, S., Esch, M., Gayler, V., Haak, H., de Vrese, P., Raddatz, T., Mauritsen, T., von Storch, J.-S., Behrens, J., Brovkin, V., Claussen, M., Crueger, T., Fast, I., Fiedler, S., Hagemann, S., Hohenegger, C., Jahns, T., Kloster, S., Kinne, S., Lasslop, G., Kornblueh, L., Marotzke, J., Matei, D., Meraner, K., Mikolajewicz, U., Modali, K., Müller, W., Nabel, J., Notz, D., Peters, K., Pincus, R., Pohlmann, H., Pongratz, J., Rast, S., Schmidt, H., Schnur, R., Schulzweida, U., Six, K., Stevens, B., Voigt, A. and Roeckner, E.: DKRZ MPI-ESM1.2-HR model output prepared for CMIP6 ScenarioMIP ssp585, Earth System Grid Federation, , doi:<https://doi.org/10.22033/ESGF/CMIP6.4403>, 2019d.
- 1105
1115 Schwartz, S. E.: Determination of Earth's Transient and Equilibrium Climate Sensitivities from Observations Over

the Twentieth Century: Strong Dependence on Assumed Forcing, *Surv. Geophys.*, 33(3–4), 745–777, doi:10.1007/s10712-012-9180-4, 2012.

Seferian, R.: CNRM-CERFACS CNRM-ESM2-1 model output prepared for CMIP6 CMIP historical, Earth System Grid Federation, , doi:https://doi.org/10.22033/ESGF/CMIP6.4068, 2018.

Seland, Ø., Bentsen, M., Olivière, D. J. L., Toniazzi, T., Gjermundsen, A., Graff, L. S., Debernard, J. B., Gupta, A. K., He, Y., Kirkevåg, A., Schwinger, J., Tjiputra, J., Aas, K. S., Bethke, I., Fan, Y., Griesfeller, J., Grini, A., Guo, C., Ilicak, M., Karset, I. H. H., Landgren, O. A., Liakka, J., Moseid, K. O., Nummelin, A., Spensberger, C., Tang, H., Zhang, Z., Heinze, C., Iversen, T. and Schulz, M.: NCC NorESM2-LM model output prepared for CMIP6 CMIP abrupt-4xCO2, Earth System Grid Federation, , doi:https://doi.org/10.22033/ESGF/CMIP6.7836, 2019a.

Seland, Ø., Bentsen, M., Olivière, D. J. L., Toniazzi, T., Gjermundsen, A., Graff, L. S., Debernard, J. B., Gupta, A. K., He, Y., Kirkevåg, A., Schwinger, J., Tjiputra, J., Aas, K. S., Bethke, I., Fan, Y., Griesfeller, J., Grini, A., Guo, C., Ilicak, M., Karset, I. H. H., Landgren, O. A., Liakka, J., Moseid, K. O., Nummelin, A., Spensberger, C., Tang, H., Zhang, Z., Heinze, C., Iversen, T. and Schulz, M.: NCC NorESM2-LM model output prepared for CMIP6 CMIP piControl, Earth System Grid Federation, , doi:https://doi.org/10.22033/ESGF/CMIP6.8217, 2019b.

Seland, Ø., Bentsen, M., Olivière, D. J. L., Toniazzi, T., Gjermundsen, A., Graff, L. S., Debernard, J. B., Gupta, A. K., He, Y., Kirkevåg, A., Schwinger, J., Tjiputra, J., Aas, K. S., Bethke, I., Fan, Y., Griesfeller, J., Grini, A., Guo, C., Ilicak, M., Karset, I. H. H., Landgren, O. A., Liakka, J., Moseid, K. O., Nummelin, A., Spensberger, C., Tang, H., Zhang, Z., Heinze, C., Iversen, T. and Schulz, M.: NCC NorESM2-LM model output prepared for CMIP6 ScenarioMIP ssp126, Earth System Grid Federation, , doi:https://doi.org/10.22033/ESGF/CMIP6.8248, 2019c.

Seland, Ø., Bentsen, M., Olivière, D. J. L., Toniazzi, T., Gjermundsen, A., Graff, L. S., Debernard, J. B., Gupta, A. K., He, Y., Kirkevåg, A., Schwinger, J., Tjiputra, J., Aas, K. S., Bethke, I., Fan, Y., Griesfeller, J., Grini, A., Guo, C., Ilicak, M., Karset, I. H. H., Landgren, O. A., Liakka, J., Moseid, K. O., Nummelin, A., Spensberger, C., Tang, H., Zhang, Z., Heinze, C., Iversen, T. and Schulz, M.: NCC NorESM2-LM model output prepared for CMIP6 ScenarioMIP ssp245, Earth System Grid Federation, , doi:https://doi.org/10.22033/ESGF/CMIP6.8253, 2019d.

Seland, Ø., Bentsen, M., Olivière, D. J. L., Toniazzi, T., Gjermundsen, A., Graff, L. S., Debernard, J. B., Gupta, A. K., He, Y., Kirkevåg, A., Schwinger, J., Tjiputra, J., Aas, K. S., Bethke, I., Fan, Y., Griesfeller, J., Grini, A., Guo, C., Ilicak, M., Karset, I. H. H., Landgren, O. A., Liakka, J., Moseid, K. O., Nummelin, A., Spensberger, C., Tang, H., Zhang, Z., Heinze, C., Iversen, T. and Schulz, M.: NCC NorESM2-LM model output prepared for CMIP6 ScenarioMIP ssp370, Earth System Grid Federation, , doi:https://doi.org/10.22033/ESGF/CMIP6.8268, 2019e.

Seland, Ø., Bentsen, M., Olivière, D. J. L., Toniazzi, T., Gjermundsen, A., Graff, L. S., Debernard, J. B., Gupta, A. K., He, Y., Kirkevåg, A., Schwinger, J., Tjiputra, J., Aas, K. S., Bethke, I., Fan, Y., Griesfeller, J., Grini, A., Guo, C., Ilicak, M., Karset, I. H. H., Landgren, O. A., Liakka, J., Moseid, K. O., Nummelin, A., Spensberger, C., Tang, H., Zhang, Z., Heinze, C., Iversen, T. and Schulz, M.: NCC NorESM2-LM model output prepared for CMIP6 ScenarioMIP ssp585, Earth System Grid Federation, , doi:https://doi.org/10.22033/ESGF/CMIP6.8319, 2019f.

Seland, Ø., Bentsen, M., Olivière, D. J. L., Toniazzi, T., Gjermundsen, A., Graff, L. S., Debernard, J. B., Gupta, A. K., He, Y., Kirkevåg, A., Schwinger, J., Tjiputra, J., Aas, K. S., Bethke, I., Fan, Y., Griesfeller, J., Grini, A., Guo, C., Ilicak, M., Karset, I. H. H., Landgren, O. A., Liakka, J., Moseid, K. O., Nummelin, A., Spensberger, C., Tang, H., Zhang, Z., Heinze, C., Iversen, T. and Schulz, M.: NCC NorESM2-LM output prepared for CMIP6 CMIP historical, Earth System Grid Federation, , doi:https://doi.org/10.22033/ESGF/CMIP6.8036, 2019g.

- 1165 Semmler, T., Danilov, S., Rackow, T., Sidorenko, D., Barbi, D., Hegewald, J., Sein, D., Wang, Q. and Jung, T.: AWI AWI-CM1.1MR model output prepared for CMIP6 CMIP historical, Earth System Grid Federation, , doi:<https://doi.org/10.22033/ESGF/CMIP6.2686>, 2018a.
- Semmler, T., Danilov, S., Rackow, T., Sidorenko, D., Barbi, D., Hegewald, J., Pradhan, H. K., Sein, D., Wang, Q. and Jung, T.: AWI AWI-CM1.1MR model output prepared for CMIP6 ScenarioMIP ssp126, Earth System Grid Federation, , doi:<https://doi.org/10.22033/ESGF/CMIP6.2796>, 2018b.
- 1170 Semmler, T., Danilov, S., Rackow, T., Sidorenko, D., Barbi, D., Hegewald, J., Pradhan, H. K., Sein, D., Wang, Q. and Jung, T.: AWI AWI-CM1.1MR model output prepared for CMIP6 ScenarioMIP ssp246, Earth System Grid Federation, , doi:<https://doi.org/10.22033/ESGF/CMIP6.2800>, 2018c.
- Semmler, T., Danilov, S., Rackow, T., Sidorenko, D., Barbi, D., Hegewald, J., Pradhan, H. K., Sein, D., Wang, Q. and Jung, T.: AWI AWI-CM1.1MR model output prepared for CMIP6 ScenarioMIP ssp370, Earth System Grid Federation, , doi:<https://doi.org/10.22033/ESGF/CMIP6.2803>, 2019a.
- 1175 Semmler, T., Danilov, S., Rackow, T., Sidorenko, D., Barbi, D., Hegewald, J., Pradhan, H. K., Sein, D., Wang, Q. and Jung, T.: AWI AWI-CM1.1MR model output prepared for CMIP6 ScenarioMIP ssp585, Earth System Grid Federation, , doi:<https://doi.org/10.22033/ESGF/CMIP6.2817>, 2019b.
- 1180 Sherwood, A. S., Webb, M. J., Annan, J. D., Armour, K. C., Forster, P. M., Hargreaves, J. C., Hegerl, G., Klein, S. A., Marvel, K. D., Rohling, E. J., Watanabe, M., Andrews, T., Braconnot, P., Bretherton, C. S., Foster, G. L., Hausfather, Z., von der Heydt, A. S., Knutti, R., Mauritsen, T., Norris, J. R., Proistosescu, C., Rugenstein, M., Schmidt, G. A. and Tokarska, K. B., Zelinka, M. D.: An assessment of Earth ' s climate sensitivity using multiple lines of evidence, *Rev. Geophys.*, 1–166, 2020.
- 1185 Shiogama, H., Abe, M. and Tatebe, H.: MIROC MIROC6 model output prepared for CMIP6 ScenarioMIP ssp119, Earth System Grid Federation, , doi:<https://doi.org/10.22033/ESGF/CMIP6.5741>, 2019a.
- Shiogama, H., Abe, M. and Tatebe, H.: MIROC MIROC6 model output prepared for CMIP6 ScenarioMIP ssp126, Earth System Grid Federation, , doi:<https://doi.org/10.22033/ESGF/CMIP6.5743>, 2019b.
- Shiogama, H., Abe, M. and Tatebe, H.: MIROC MIROC6 model output prepared for CMIP6 ScenarioMIP ssp245, Earth System Grid Federation, , doi:<https://doi.org/10.22033/ESGF/CMIP6.5746>, 2019c.
- 1190 Shiogama, H., Abe, M. and Tatebe, H.: MIROC MIROC6 model output prepared for CMIP6 ScenarioMIP ssp370, Earth System Grid Federation, , doi:<https://doi.org/10.22033/ESGF/CMIP6.5752>, 2019d.
- Shiogama, H., Abe, M. and Tatebe, H.: MIROC MIROC6 model output prepared for CMIP6 ScenarioMIP ssp434, Earth System Grid Federation, , doi:<https://doi.org/10.22033/ESGF/CMIP6.5764>, 2019e.
- 1195 Shiogama, H., Abe, M. and Tatebe, H.: MIROC MIROC6 model output prepared for CMIP6 ScenarioMIP ssp460, Earth System Grid Federation, , doi:<https://doi.org/10.22033/ESGF/CMIP6.5766>, 2019f.
- Shiogama, H., Abe, M. and Tatebe, H.: MIROC MIROC6 model output prepared for CMIP6 ScenarioMIP ssp585, Earth System Grid Federation, , doi:<https://doi.org/10.22033/ESGF/CMIP6.5771>, 2019g.
- 1200 Song, Z., Qiao, F., Bao, Y., Shu, Q., Song, Y. and Yang, X.: FIO-QLNM FIO-ESM2.0 model output prepared for CMIP6 CMIP historical, Earth System Grid Federation, , doi:<https://doi.org/10.22033/ESGF/CMIP6.9199>, 2019a.
- Song, Z., Qiao, F., Bao, Y., Shu, Q., Song, Y. and Yang, X.: FIO-QLNM FIO-ESM2.0 model output prepared for CMIP6 ScenarioMIP ssp126, Earth System Grid Federation, , doi:<https://doi.org/10.22033/ESGF/CMIP6.9208>, 2019b.

1205 Song, Z., Qiao, F., Bao, Y., Shu, Q., Song, Y. and Yang, X.: FIO-QLNM FIO-ESM2.0 model output prepared for CMIP6 ScenarioMIP ssp245, Earth System Grid Federation, , doi:<https://doi.org/10.22033/ESGF/CMIP6.9209>, 2019c.

Song, Z., Qiao, F., Bao, Y., Shu, Q., Song, Y. and Yang, X.: FIO-QLNM FIO-ESM2.0 model output prepared for CMIP6 ScenarioMIP ssp585, Earth System Grid Federation, , doi:<https://doi.org/10.22033/ESGF/CMIP6.9214>, 2019d.

1210 Steger, C., Schupfner, M., Wieners, K.-H., Wachsmann, F., Bittner, M., Jungclaus, J., Früh, B., Pankatz, K., Giorgetta, M., Reick, C., Legutke, S., Esch, M., Gayler, V., Haak, H., de Vrese, P., Raddatz, T., Mauritsen, T., von Storch, J.-S., Behrens, J., Brovkin, V., Claussen, M., Crueger, T., Fast, I., Fiedler, S., Hagemann, S., Hohenegger, C., Jahns, T., Kloster, S., Kinne, S., Lasslop, G., Kornblueh, L., Marotzke, J., Matei, D., Meraner, K., Mikolajewicz, U., Modali, K., Müller, W., Nabel, J., Notz, D., Peters, K., Pincus, R., Pohlmann, H., Pongratz, J., Rast, S., Schmidt, H., Schnur, R., Schulzweida, U., Ix, K., Stevens, B., Voigt, A. and Roeckner, E.: DWD MPI-ESM1.2-HR model output prepared for CMIP6 ScenarioMIP ssp585, Earth System Grid Federation, , doi:<https://doi.org/10.22033/ESGF/CMIP6.4479>, 2019.

1215 Stouffer, R. J.: UA MCM-UA-1-0 model output prepared for CMIP6 CMIP abrupt-4xCO2, Earth System Grid Federation, , doi:<https://doi.org/10.22033/ESGF/CMIP6.8882>, 2019a.

1220 Stouffer, R. J.: UA MCM-UA-1-0 model output prepared for CMIP6 CMIP historical, Earth System Grid Federation, , doi:<https://doi.org/10.22033/ESGF/CMIP6.8888>, 2019b.

Stouffer, R. J.: UA MCM-UA-1-0 model output prepared for CMIP6 CMIP piControl, Earth System Grid Federation, , doi:<https://doi.org/10.22033/ESGF/CMIP6.8890>, 2019c.

1225 Stouffer, R. J.: UA MCM-UA-1-0 model output prepared for CMIP6 ScenarioMIP ssp245, Earth System Grid Federation, , doi:<https://doi.org/10.22033/ESGF/CMIP6.13896>, 2019d.

Stouffer, R. J.: UA MCM-UA-1-0 model output prepared for CMIP6 ScenarioMIP ssp370, Earth System Grid Federation, , doi:<https://doi.org/10.22033/ESGF/CMIP6.13897>, 2019e.

Stouffer, R. J.: UA MCM-UA-1-0 model output prepared for CMIP6 ScenarioMIP ssp585, Earth System Grid Federation, , doi:<https://doi.org/10.22033/ESGF/CMIP6.13901>, 2019f.

1230 Stouffer, R. J.: UA MCM-UA-1.0 model output prepared for CMIP6 ScenarioMIP ssp126, Earth System Grid Federation, , doi:<https://doi.org/10.22033/ESGF/CMIP6.13895>, 2019g.

Swart, N. C., Jason, N. ., Kharin, V. V., Lazare, M., Scinocca, J. F., Gillett, N. P., Anstey, J., Arora, V. K., Christian, J. R., Jiao, Y., Lee, W. G., Majaess, F., Saenko, O. A., Seiler, C., Seinen, C., Shao, A., Solheim, L., von Salzen, K., Yang, D., Winter, B. and Sigmond, M.: CCCma CanESM5-CanOE model output prepared for CMIP6 CMIP, Earth System Grid Federation, , doi:<https://doi.org/10.22033/ESGF/CMIP6.10260>, 2019a.

1235 Swart, N. C., Cole, J. N. S., Kharin, V. V., Lazare, M., Scinocca, J. F., Gillett, N. P., Anstey, J., Arora, V. K., Christian, J. R., Jiao, Y., Lee, W. G., Majaess, F., Saenko, O. A., Seiler, C., Seinen, C., Shao, A., Solheim, L., von Salzen, K., Yang, D., Winter, B. and Sigmond, M.: CCCma CaneSM5-CanOE model output prepared for CMIP6 ScenarioMIP ssp126, Earth System Grid Federation, , doi:<https://doi.org/10.22033/ESGF/CMIP6.10269>, 2019b.

1240 Swart, N. C., Cole, J. N. S., Kharin, V. V., Lazare, M., Scinocca, J. F., Gillett, N. P., Anstey, J., Arora, V., Christian, J. R., Jiao, Y., Lee, W. G., Majaess, F., Saenko, O. A., Seiler, C., Seinen, C., Shao, A., Solheim, L., von Salzen, K., Yang, D., Winter, B. and Sigmond, M.: CCCma CanESM5-CanOE model output prepared for CMIP6 ScenarioMIP ssp245, Earth System Grid Federation, , doi:<https://doi.org/10.22033/ESGF/CMIP6.10270>, 2019c.

1245

- 1250 Swart, N. C., Cole, J. N. S., Kharin, V. V., Lazare, M., Scinocca, J. F., Gillett, N. P., Anstey, J., Arora, V., Christian, J. R., Jiao, Y., Lee, W. G., Majaess, F., Saenko, O. A., Seiler, C., Seinen, C., Shao, A., Solheim, L., von Salzen, K., Yang, D., Winter, B. and Sigmond, M.: CCCma CanESM5-CanOE model output prepared for CMIP6 ScenarioMIP ssp370, Earth System Grid Federation, , doi:<https://doi.org/10.22033/ESGF/CMIP6.10271>, 2019d.
- 1255 Swart, N. C., Cole, J. N. S., Kharin, V. V., Lazare, M., Scinocca, J. F., Gillett, N. P., Anstey, J., Arora, V., Christian, J. R., Jiao, Y., Lee, W. G., Majaess, F., Saenko, O. A., Seiler, C., Seinen, C., Shao, A., Solheim, L., von Salzen, K., Yang, D., Winter, B. and Sigmond, M.: CCCma CanESM5-CanOE model output prepared for CMIP6 ScenarioMIP ssp585, Earth System Grid Federation, , doi:<https://doi.org/10.22033/ESGF/CMIP6.10276>, 2019e.
- 1260 Swart, N. C., Cole, J. N. S., Kharin, V. V., Lazare, M., Scinocca, J. F., Gillett, N. P., Anstey, J., Arora, V., Christian, J. R., Jiao, Y., Lee, W. G., Majaess, F., Saenko, O. A., Seiler, C., Seinen, C., Shao, A., Solheim, L., von Salzen, K., Yang, D., Winter, B. and Sigmond, M.: CCCma CanESM5 model output prepared for CMIP6 CMIP abrupt-4xCO2, Earth System Grid Federation, , doi:<https://doi.org/10.22033/ESGF/CMIP6.3532>, 2019f.
- 1265 Swart, N. C., Cole, J. N. S., Kharin, V. V., Lazare, M., Scinocca, J. F., Gillett, N. P., Anstey, J., Arora, V. K., Christian, J. R., Jiao, Y., Lee, W. G., Majaess, F., Saenko, O. A., Seiler, C., Seinen, C., Shao, A., Solheim, L., von Salzen, K., Yang, D., Winter, B. and Sigmond, M.: CCCma CanESM5 model output prepared for CMIP6 CMIP historical, Earth System Grid Federation, , doi:<https://doi.org/10.22033/ESGF/CMIP6.3610>, 2019g.
- 1270 Swart, N. C., Cole, J. N. S., Kharin, V. V., Lazare, M., Scinocca, J. F., Gillett, N. P., Anstey, J., Arora, V., Christian, J. R., Jiao, Y., Lee, W. G., Majaess, F., Saenko, O. A., Seiler, C., Seinen, C., Shao, A., Solheim, L., von Salzen, K., Yang, D., Winter, B. and Sigmond, M.: CCCma CanESM5 model output prepared for CMIP6 CMIP piControl, Earth System Grid Federation, , doi:<https://doi.org/10.22033/ESGF/CMIP6.3673>, 2019h.
- 1275 Swart, N. C., Cole, J. N. S., Kharin, V. V., Lazare, M., Scinocca, J. F., Gillett, N. P., Anstey, J., Arora, V. K., Christian, J. R., Jiao, Y., Lee, W. G., Majaess, F., Saenko, O. A., Seiler, C., Seinen, C., Shao, A., Solheim, L., von Salzen, K., Yang, D., Winter, B. and Sigmond, M.: CCCma CanESM5 model output prepared for CMIP6 ScenarioMIP ssp119, Earth System Grid Federation, , doi:<https://doi.org/10.22033/ESGF/CMIP6.3682>, 2019i.
- 1280 Swart, N. C., Cole, J. N. S., Jason, N. ., Kharin, V. V., Lazare, M., Scinocca, J. F., Gillett, N. P., Anstey, J., Arora, V. K., Christian, J. R., Jiao, Y., Lee, W. G., Majaess, F., Saenko, O. A., Seiler, C., Seinen, C., Shao, A., Solheim, L., von Salzen, K., Yang, D., Winter, B. and Sigmond, M.: CCCma CanESM5 model output prepared for CMIP6 ScenarioMIP ssp126, Earth System Grid Federation, , doi:<https://doi.org/10.22033/ESGF/CMIP6.3683>, 2019j.
- 1285 Swart, N. C., Cole, J. N. S., Kharin, V. V., Lazare, M., Scinocca, J. F., Gillett, N. P., Anstey, J., Arora, V., Christian, J. R., Jiao, Y., Lee, W. G., Majaess, F., Saenko, O. A., Seiler, C., Seinen, C., Shao, A., Solheim, L., von Salzen, K., Yang, D., Winter, B. and Sigmond, M.: CCCma CanESM5 model output prepared for CMIP6 ScenarioMIP ssp245, Earth System Grid Federation, , doi:<https://doi.org/10.22033/ESGF/CMIP6.3685>, 2019k.
- 1290 Swart, N. C., Cole, J. N. S., Kharin, V. V., Lazare, M., Scinocca, J. F., Gillett, N. P., Anstey, J., Arora, V., Christian, J. R., Jiao, Y., Lee, W. G., Majaess, F., Saenko, O. A., Seiler, C., Seinen, C., Shao, A., Solheim, L., von Salzen, K., Yang, D., Winter, B. and Sigmond, M.: CCCma CanESM5 model output prepared for CMIP6 ScenarioMIP ssp370, Earth System Grid Federation, , doi:<https://doi.org/10.22033/ESGF/CMIP6.3690>, 2019l.
- Swart, N. C., Cole, J. N. S., Kharin, V. V., Lazare, M., Scinocca, J. F., Gillett, N. P., Anstey, J., Arora, V., Christian, J. R., Jiao, Y., Lee, W. G., Majaess, F., Saenko, O. A., Seiler, C., Seinen, C., Shao, A., Solheim, L., von

Salzen, K., Yang, D., Winter, B. and Sigmond, M.: CCCma CanESM5 model output prepared for CMIP6 ScenarioMIP ssp434, Earth System Grid Federation, , doi:<https://doi.org/10.22033/ESGF/CMIP6.3692>, 2019m.

Swart, N. C., Cole, J. N. S., Kharin, V. V., Lazare, M., Scinocca, J. F., Gillett, N. P., Anstey, J., Arora, V., Christian, J. R., Jiao, Y., Lee, W. G., Majaess, F., Saenko, O. A., Seiler, C., Seinen, C., Shao, A., Solheim, L., von Salzen, K., Yang, D., Winter, B. and Sigmond, M.: CCCma CanESM5 model output prepared for CMIP6 ScenarioMIP ssp460, Earth System Grid Federation, , doi:<https://doi.org/10.22033/ESGF/CMIP6.3693>, 2019n.

Swart, N. C., Cole, J. N. S., Kharin, V. V., Lazare, M., Scinocca, J. F., Gillett, N. P., Anstey, J., Arora, V., Christian, J. R., Jiao, Y., Lee, W. G., Majaess, F., Saenko, O. A., Seiler, C., Seinen, C., Shao, A., Solheim, L., von Salzen, K., Yang, D., Winter, B. and Sigmond, M.: CCCma CanESM5 model output prepared for CMIP6 ScenarioMIP ssp585, Earth System Grid Federation, , doi:<https://doi.org/10.22033/ESGF/CMIP6.3696>, 2019o.

Tachiiri, K., Abe, M., Hajima, T., Arakawa, O., Suzuki, T., Komuro, Y., Ogochi, K., Watanabe, M., Yamamoto, A., Tatebe, H., Noguchi, M. A., Ohgaito, R., Ito, A., Yamazaki, D., Ito, A., Takata, K., Watanabe, S. and Kawamiya, M.: MIROC MIROC-ES2L model output prepared for CMIP6 ScenarioMIP ssp119, Earth System Grid Federation, , doi:<https://doi.org/10.22033/ESGF/CMIP6.5740>, 2019a.

Tachiiri, K., Abe, M., Hajima, T., Arakawa, O., Suzuki, T., Komuro, Y., Ogochi, K., Watanabe, M., Yamamoto, A., Tatebe, H., Noguchi, M. A., Ohgaito, R., Ito, A., Yamazaki, D., Ito, A., Takata, K., Watanabe, S. and Kawamiya, M.: MIROC MIROC-ES2L model output prepared for CMIP6 ScenarioMIP ssp126, , doi:<https://doi.org/10.22033/ESGF/CMIP6.5742>, 2019b.

Tachiiri, K., Abe, M., Hajima, T., Arakawa, O., Suzuki, T., Komuro, Y., Ogochi, K., Watanabe, M., Yamamoto, A., Tatebe, H., Noguchi, M. A., Ohgaito, R., Ito, A., Yamazaki, D., Ito, A., Takata, K., Watanabe, S. and Kawamiya, M.: MIROC MIROC-ES2L model output prepared for CMIP6 ScenarioMIP ssp245, Earth System Grid Federation, , doi:<https://doi.org/10.22033/ESGF/CMIP6.5745>, 2019c.

Tachiiri, K., Abe, M., Hajima, T., Arakawa, O., Suzuki, T., Komuro, Y., Ogochi, K., Watanabe, M., Yamamoto, A., Tatebe, H., Noguchi, M. A., Ohgaito, R., Ito, A., Yamazaki, D., Ito, A., Takata, K., Watanabe, S. and Kawamiya, M.: MIROC MIROC-ES2L model output prepared for CMIP6 ScenarioMIP ssp370, Earth System Grid Federation, , doi:<https://doi.org/10.22033/ESGF/CMIP6.5751>, 2019d.

Tachiiri, K., Abe, M., Hajima, T., Arakawa, O., Suzuki, T., Komuro, Y., Ogochi, K., Watanabe, M., Yamamoto, A., Tatebe, H., Noguchi, M. A., Ohgaito, R., Ito, A., Yamazaki, D., Ito, A., Takata, K., Watanabe, S. and Kawamiya, M.: MIROC MIROC-ES2L model output prepared for CMIP6 ScenarioMIP ssp585, Earth System Grid Federation, , doi:<https://doi.org/10.22033/ESGF/CMIP6.5770>, 2019e.

Tang, Y., Rumbold, S., Ellis, R., Kelley, D., Mulcahy, J., Sellar, A., Walton, J. and Jones, C.: MOHC UKESM1.0-LL model output prepared for CMIP6 CMIP abrupt-4xCO2, Earth System Grid Federation, , doi:<https://doi.org/10.22033/ESGF/CMIP6.5843>, 2019a.

Tang, Y., Rumbold, S., Ellis, R., Kelley, D., Mulcahy, J., Sellar, A., Walton, J. and Jones, C.: MOHC UKESM1.0-LL model output prepared for CMIP6 CMIP piControl, Earth System Grid Federation, , doi:<https://doi.org/10.22033/ESGF/CMIP6.6298>, 2019b.

Tang, Y., Rumbold, S., Ellis, R., Kelley, D., Mulcahy, J., Sellar, A., Walton, J. and Jones, C.: MOHC UKESM1.0LL model output prepared for CMIP6 CMIP historical, Earth System Grid Federation, , doi:<https://doi.org/10.22033/ESGF/CMIP6.6113>, 2019c.

Tatebe, H. and Watanabe, M.: MIROC MIROC6 model output prepared for CMIP6 CMIP abrupt-4xCO2, Earth System Grid Federation, , doi:<https://doi.org/10.22033/ESGF/CMIP6.5411>, 2018a.

- Tatebe, H. and Watanabe, M.: MIROC MIROC6 model output prepared for CMIP6 CMIP historical, Earth System Grid Federation, , doi:<https://doi.org/10.22033/ESGF/CMIP6.5603>, 2018b.
- 1340 Tatebe, H. and Watanabe, M.: MIROC MIROC6 model output prepared for CMIP6 CMIP piControl, Earth System Grid Federation, , doi:<https://doi.org/10.22033/ESGF/CMIP6.5711>, 2018c.
- Thompson, D. W. J., Wallace, J. M., Jones, P. D. and Kennedy, J. J.: Identifying signatures of natural climate variability in time series of global-mean surface temperature: Methodology and insights, *J. Clim.*, 22(22), 6120–6141, doi:10.1175/2009JCLI3089.1, 2009.
- 1345 Tokarska, K. B., Hegerl, G. C., Schurer, A. P., Forster, P. M. and Marvel, K.: Observational constraints on the effective climate sensitivity from the historical period, *IOP Publishing, Environ. Res. Lett.*, 15(3), doi:10.1088/1748-9326/ab738f, 2020a.
- Tokarska, K. B., Stolpe, M. B., Sippel, S., Fischer, E. M., Smith, C. J., Lehner, F. and Knutti, R.: Past warming trend constrains future warming in CMIP6 models, *Sci. Adv.*, 6(12), 1–13, doi:10.1126/sciadv.aaz9549, 2020b.
- 1350 Voldoire, A.: CMIP6 simulations of the CNRM-CERFACS based on CNRM-CM6-1 model for CMIP experiment historical, Earth System Grid Federation, , doi:<https://doi.org/10.22033/ESGF/CMIP6.4066>, 2018.
- Voldoire, A.: CNRM-CERFACS CNRM-CM6-1-HR model output prepared for CMIP6 ScenarioMIP ssp245, Earth System Grid Federation, , doi:<https://doi.org/10.22033/ESGF/CMIP6.4190>, 2019a.
- Voldoire, A.: CNRM-CERFACS CNRM-CM6-1-HR model output prepared for CMIP6 ScenarioMIP ssp585, Earth System Grid Federation, , doi:<https://doi.org/10.22033/ESGF/CMIP6.4225>, 2019b.
- 1355 Voldoire, A.: CNRM-CERFACS CNRM-CM6-1 model output prepared for CMIP6 ScenarioMIP for ssp245, Earth System Grid Federation, , doi:<https://doi.org/10.22033/ESGF/CMIP6.4189>, 2019c.
- Voldoire, A.: CNRM-CERFACS CNRM-CM6-1 model output prepared for CMIP6 ScenarioMIP ssp126, Earth System Grid Federation, , doi:<https://doi.org/10.22033/ESGF/CMIP6.4184>, 2019d.
- 1360 Voldoire, A.: CNRM-CERFACS CNRM-CM6-1 model output prepared for CMIP6 ScenarioMIP ssp370, Earth System Grid Federation, , doi:<https://doi.org/10.22033/ESGF/CMIP6.4197>, 2019e.
- Voldoire, A.: CNRM-CERFACS CNRM-CM6-1 model output prepared for CMIP6 ScenarioMIP ssp585, Earth System Grid Federation, , doi:<https://doi.org/10.22033/ESGF/CMIP6.4224>, 2019f.
- Voldoire, A.: CNRM-CERFACS CNRM-ESM2-1 model output prepared for CMIP6 ScenarioMIP ssp119, Earth System Grid Federation, , doi:<https://doi.org/10.22033/ESGF/CMIP6.4182>, 2019g.
- 1365 Voldoire, A.: CNRM-CERFACS CNRM-ESM2-1 model output prepared for CMIP6 ScenarioMIP ssp126, Earth System Grid Federation, , doi:<https://doi.org/10.22033/ESGF/CMIP6.4186>, 2019h.
- Voldoire, A.: CNRM-CERFACS CNRM-ESM2-1 model output prepared for CMIP6 ScenarioMIP ssp245, Earth System Grid Federation, , doi:<https://doi.org/10.22033/ESGF/CMIP6.4191>, 2019i.
- 1370 Voldoire, A.: CNRM-CERFACS CNRM-ESM2-1 model output prepared for CMIP6 ScenarioMIP ssp370, Earth System Grid Federation, , doi:<https://doi.org/10.22033/ESGF/CMIP6.4199>, 2019j.
- Voldoire, A.: CNRM-CERFACS CNRM-ESM2-1 model output prepared for CMIP6 ScenarioMIP ssp434, Earth System Grid Federation, , doi:<https://doi.org/10.22033/ESGF/CMIP6.4213>, 2019k.
- Voldoire, A.: CNRM-CERFACS CNRM-ESM2-1 model output prepared for CMIP6 ScenarioMIP ssp460, Earth System Grid Federation, , doi:<https://doi.org/10.22033/ESGF/CMIP6.4217>, 2019l.

- 1375 Volodire, A.: CNRM-CERFACS CNRM-CM6-1-HR model output prepared for CMIP6 ScenarioMIP ssp126, Earth System Grid Federation, , doi:<https://doi.org/10.22033/ESGF/CMIP6.4185>, 2020a.
- Volodire, A.: CNRM-CERFACS CNRM-CM6-1-HR model output prepared for CMIP6 ScenarioMIP ssp370, Earth System Grid Federation, , doi:<https://doi.org/10.22033/ESGF/CMIP6.4198>, 2020b.
- 1380 Volodin, E., Mortikov, E., Gritsun, A., Lykossov, V., Galin, V., Diansky, N., Gusev, A., Kostrikin, S., Iakovlev, N., Shestakova, A. and Emelina, S.: INM INM-CM4-8 model output prepared for CMIP6 CMIP abrupt-4xCO2, Earth System Grid Federation, , doi:<https://doi.org/10.22033/ESGF/CMIP6.4931>, 2019a.
- Volodin, E., Mortikov, E., Gritsun, A., Lykossov, V., Galin, V., Diansky, N., Gusev, A., Kostrikin, S., Iakovlev, N., Shestakova, A. and Emelina, S.: INM INM-CM4-8 model output prepared for CMIP6 CMIP historical, Earth System Grid Federation, , doi:<https://doi.org/10.22033/ESGF/CMIP6.5069>, 2019b.
- 1385 Volodin, E., Mortikov, E., Gritsun, A., Lykossov, V., Galin, V., Diansky, N., Gusev, A., Kostrikin, S., Iakovlev, N., Shestakova, A. and Emelina, S.: INM INM-CM4-8 model output prepared for CMIP6 CMIP piControl, Earth System Grid Federation, , doi:<https://doi.org/10.22033/ESGF/CMIP6.5080>, 2019c.
- Volodin, E., Mortikov, E., Gritsun, A., Lykossov, V., Galin, V., Diansky, N., Gusev, A., Kostrikin, S., Iakovlev, N., Shestakova, A. and Emelina, S.: INM INM-CM4-8 model output prepared for CMIP6 ScenarioMIP ssp126, Earth System Grid Federation, , doi:<https://doi.org/10.22033/ESGF/CMIP6.12325>, 2019d.
- 1390 Volodin, E., Mortikov, E., Gritsun, A., Lykossov, V., Galin, V., Diansky, N., Gusev, A., Kostrikin, S., Iakovlev, N., Shestakova, A. and Emelina, S.: INM INM-CM4-8 model output prepared for CMIP6 ScenarioMIP ssp245, Earth System Grid Federation, , doi:<https://doi.org/10.22033/ESGF/CMIP6.12327>, 2019e.
- Volodin, E., Mortikov, E., Gritsun, A., Lykossov, V., Galin, V., Diansky, N., Gusev, A., Kostrikin, S., Iakovlev, N., Shestakova, A. and Emelina, S.: INM INM-CM4-8 model output prepared for CMIP6 ScenarioMIP ssp370, Earth System Grid Federation, , doi:<https://doi.org/10.22033/ESGF/CMIP6.12329>, 2019f.
- 1395 Volodin, E., Mortikov, E., Gritsun, A., Lykossov, V., Galin, V., Diansky, N., Gusev, A., Kostrikin, S., Iakovlev, N., Shestakova, A. and Emelina, S.: INM INM-CM4-8 model output prepared for CMIP6 ScenarioMIP ssp585, Earth System Grid Federation, , doi:<https://doi.org/10.22033/ESGF/CMIP6.12337>, 2019g.
- 1400 Volodin, E., Mortikov, E., Gritsun, A., Lykossov, V., Galin, V., Diansky, N., Gusev, A., Kostrikin, S., Iakovlev, N., Shestakova, A. and Emelina, S.: INM INM-CM5-0 model output prepared for CMIP6 CMIP historical, Earth System Grid Federation, , doi:<https://doi.org/10.22033/ESGF/CMIP6.5070>, 2019h.
- Volodin, E., Mortikov, E., Gritsun, A., Lykossov, V., Galin, V., Diansky, N., Gusev, A., Kostrikin, S., Iakovlev, N., Shestakova, A. and Emelina, S.: INM INM-CM5-0 model output prepared for CMIP6 ScenarioMIP ssp126, Earth System Grid Federation, , doi:<https://doi.org/10.22033/ESGF/CMIP6.12326>, 2019i.
- 1405 Volodin, E., Mortikov, E., Gritsun, A., Lykossov, V., Galin, V., Diansky, N., Gusev, A., Kostrikin, S., Iakovlev, N., Shestakova, A. and Emelina, S.: INM INM-CM5-0 model output prepared for CMIP6 ScenarioMIP ssp245, Earth System Grid Federation, , doi:<https://doi.org/10.22033/ESGF/CMIP6.12328>, 2019j.
- Volodin, E., Mortikov, E., Gritsun, A., Lykossov, V., Galin, V., Diansky, N., Gusev, A., Kostrikin, S., Iakovlev, N., Shestakova, A. and Emelina, S.: INM INM-CM5-0 model output prepared for CMIP6 ScenarioMIP ssp370, Earth System Grid Federation, , doi:<https://doi.org/10.22033/ESGF/CMIP6.12330>, 2019k.
- 1410 Volodin, E., Mortikov, E., Gritsun, A., Lykossov, V., Galin, V., Diansky, N., Gusev, A., Kostrikin, S., Iakovlev, N., Shestakova, A. and Emelina, S.: INM INM-CM5-0 model output prepared for CMIP6 ScenarioMIP ssp585, Earth System Grid Federation, , doi:<https://doi.org/10.22033/ESGF/CMIP6.12338>, 2019l.
- 1415 Volodin, E., Mortikov, E., Gritsun, A., Lykossov, V., Galin, V., Diansky, N., Gusev, A., Kostrikin, S., Iakovlev, N.,

Shestakova, A. and Emelina, S.: NM INM-CM5-0 model output prepared for CMIP6 CMIP abrupt-4xCO₂, Earth System Grid Federation, , doi:<https://doi.org/10.22033/ESGF/CMIP6.4932>, 2019m.

Volodin, E., Mortikov, E., Gritsun, A., Lykossov, V., Galin, V., Diansky, N., Gusev, A., Kostykin, S., Iakovlev, N., Shestakova, A. and Emelina, S.: NM INM-CM5-0 model output prepared for CMIP6 CMIP piControl, Earth System Grid Federation, , doi:<https://doi.org/10.22033/ESGF/CMIP6.5081>, 2019n.

Wieners, K.-H., Giorgetta, M., Jungclaus, J. H., Reick, C., Esch, M., Bittner, M., Legutke, S., Schupfner, M., Wachsmann, F., Gayler, V., Haak, H., de Vrese, P., Raddatz, T., Mauritsen, T., von Storch, J.-S., Behrens, J., Brovkin, V., Claussen, M., Crueger, T., Fast, I., Fiedler, S., Hagemann, S., Hohenegger, C., Jahns, T., Kloster, S., Kinne, S., Lasslop, G., Kornblueh, L., Marotzke, J., Matei, D., Meraner, K., Mikolajewicz, U., Modali, K., Muller, W., Nabel, J. E. M. S., Notz, D., Peters, K., Pincus, R., Pohlmann, H., Pongratz, J., Rast, S., Schmidt, H., Schnur, R., Schulzweida, U., Six, K., Stevens, B., Voigt, A. and Roeckner, E.: MPI-M MPI-ESM1.2-LR model output prepared for CMIP6 CMIP historical, Earth System Grid Federation, , doi:<https://doi.org/10.22033/ESGF/CMIP6.6595>, 2019a.

Wieners, K.-H., Giorgetta, M., Jungclaus, J., Reick, C., Esch, M., Bittner, M., Gayler, V., Haak, H., de Vrese, P., Raddatz, T., Mauritsen, T., von Storch, J.-S., Behrens, J., Brovkin, V., Claussen, M., Crueger, T., Fast, I., Fiedler, S., Hagemann, S., Hohenegger, C., Jahns, T., Kloster, S., Kinne, S., Lasslop, G., Kornblueh, L., Marotzke, J., Matei, D., Meraner, K., Mikolajewicz, U., Modali, K., Müller, W., Nabel, J., Notz, D., Peters, K., Pincus, R., Pohlmann, H., Pongratz, J., Rast, S., Schmidt, H., Schnur, R., Schulzweida, U., Six, K., Stevens, B., Voigt, A. and Roeckner, E.: MPI-M MPI-ESM1.2-LR model output prepared for CMIP6 ScenarioMIP ssp126, Earth System Grid Federation, , doi:<https://doi.org/10.22033/ESGF/CMIP6.6690>, 2019b.

Wieners, K.-H., Giorgetta, M., Jungclaus, J., Reick, C., Esch, M., Bittner, M., Gayler, V., Haak, H., de Vrese, P., Raddatz, T., Mauritsen, T., von Storch, J.-S., Behrens, J., Brovkin, V., Claussen, M., Crueger, T., Fast, I., Fiedler, S., Hagemann, S., Hohenegger, C., Jahns, T., Kloster, S., Kinne, S., Lasslop, G., Kornblueh, L., Marotzke, J., Matei, D., Meraner, K., Mikolajewicz, U., Modali, K., Müller, W., Nabel, J., Notz, D., Peters, K., Pincus, R., Pohlmann, H., Pongratz, J., Rast, S., Schmidt, H., Schnur, R., Schulzweida, U., Six, K., Stevens, B., Voigt, A. and Roeckner, E.: MPI-M MPI-ESM1.2-LR model output prepared for CMIP6 ScenarioMIP ssp245, Earth System Grid Federation, , doi:<https://doi.org/10.22033/ESGF/CMIP6.6693>, 2019c.

Wieners, K.-H., Giorgetta, M., Jungclaus, J., Reick, C., Esch, M., Bittner, M., Gayler, V., Haak, H., de Vrese, P., Raddatz, T., Mauritsen, T., von Storch, J.-S., Behrens, J., Brovkin, V., Claussen, M., Crueger, T., Fast, I., Fiedler, S., Hagemann, S., Hohenegger, C., Jahns, T., Kloster, S., Kinne, S., Lasslop, G., Kornblueh, L., Marotzke, J., Matei, D., Meraner, K., Mikolajewicz, U., Modali, K., Müller, W., Nabel, J., Notz, D., Peters, K., Pincus, R., Pohlmann, H., Pongratz, J., Rast, S., Schmidt, H., Schnur, R., Schulzweida, U., Six, K., Stevens, B., Voigt, A. and Roeckner, E.: MPI-M MPI-ESM1.2-LR model output prepared for CMIP6 ScenarioMIP ssp370, Earth System Grid Federation, , doi:<https://doi.org/10.22033/ESGF/CMIP6.6695>, 2019d.

Wieners, K.-H., Giorgetta, M., Jungclaus, J., Reick, C., Esch, M., Bittner, M., Gayler, V., Haak, H., de Vrese, P., Raddatz, T., Mauritsen, T., von Storch, J.-S., Behrens, J., Brovkin, V., Claussen, M., Crueger, T., Fast, I., Fiedler, S., Hagemann, S., Hohenegger, C., Jahns, T., Kloster, S., Kinne, S., Lasslop, G., Kornblueh, L., Marotzke, J., Matei, D., Meraner, K., Mikolajewicz, U., Modali, K., Müller, W., Nabel, J., Notz, D., Peters, K., Pincus, R., Pohlmann, H., Pongratz, J., Rast, S., Schmidt, H., Schnur, R., Schulzweida, U., Six, K., Stevens, B., Voigt, A. and Roeckner, E.: MPI-M MPI-ESM1.2-LR model output prepared for CMIP6 ScenarioMIP ssp585, Earth System Grid Federation, , doi:<https://doi.org/10.22033/ESGF/CMIP6.6705>, 2019e.

Wu, T., Chu, M., Dong, M., Fang, Y., Jie, W., Li, J., Li, W., Liu, Q., Shi, X., Xin, X., Yan, J., Zhang, F., Zhang, J., Zhang, L. and Zhang, Y.: BCC BCC-CSM2MR model output prepared for CMIP6 CMIP abrupt-4xCO₂, Earth System Grid Federation, , doi:<https://doi.org/10.22033/ESGF/CMIP6.2845>, 2018a.

- 1465 Wu, T., Chu, M., Dong, M., Fang, Y., Jie, W., Li, J., Li, W., Liu, Q., Shi, X., Xin, X., Yan, J., Zhang, F., Zhang, J., Zhang, L. and Zhang, Y.: BCC BCC-CSM2MR model output prepared for CMIP6 CMIP historical, Earth System Grid Federation, , doi:<https://doi.org/10.22033/ESGF/CMIP6.2948>, 2018b.
- Wu, T., Chu, M., Dong, M., Fang, Y., Jie, W., Li, J., Li, W., Liu, Q., Shi, X., Xin, X., Yan, J., Zhang, F., Zhang, J., Zhang, L. and Zhang, Y.: BCC BCC-CSM2MR model output prepared for CMIP6 CMIP piControl, Earth System Grid Federation, , doi:<https://doi.org/10.22033/ESGF/CMIP6.3016>, 2018c.
- 1470 Xin, X., Wu, T., Shi, X., Zhang, F., Li, J., Chu, M., Liu, Q., Yan, J., Ma, Q. and Wei, M.: BCC BCC-CSM2MR model output prepared for CMIP6 ScenarioMIP ssp126, Earth System Grid Federation, , doi:<https://doi.org/10.22033/ESGF/CMIP6.3028>, 2019a.
- Xin, X., Wu, T., Shi, X., Zhang, F., Li, J., Chu, M., Liu, Q., Yan, J., Ma, Q. and Wei, M.: BCC BCC-CSM2MR model output prepared for CMIP6 ScenarioMIP ssp245, Earth System Grid Federation, , doi:<https://doi.org/10.22033/ESGF/CMIP6.3030>, 2019b.
- 1475 Xin, X., Wu, T., Shi, X., Zhang, F., Li, J., Chu, M., Liu, Q., Yan, J., Ma, Q. and Wei, M.: BCC BCC-CSM2MR model output prepared for CMIP6 ScenarioMIP ssp370, Earth System Grid Federation, , doi:<https://doi.org/10.22033/ESGF/CMIP6.3035>, 2019c.
- Xin, X., Wu, T., Shi, X., Zhang, F., Li, J., Chu, M., Liu, Q., Yan, J., Ma, Q. and Wei, M.: BCC BCC-CSM2MR model output prepared for CMIP6 ScenarioMIP ssp585, Earth System Grid Federation, , doi:<https://doi.org/10.22033/ESGF/CMIP6.3050>, 2019d.
- 1480 YU, Y.: CAS FGOALS-f3-L model output prepared for CMIP6 CMIP historical, Earth System Grid Federation, , doi:<https://doi.org/10.22033/ESGF/CMIP6.3355>, 2019a.
- YU, Y.: CAS FGOALS-f3-L model output prepared for CMIP6 ScenarioMIP ssp126, Earth System Grid Federation, , doi:<https://doi.org/10.22033/ESGF/CMIP6.3464>, 2019b.
- 1485 YU, Y.: CAS FGOALS-f3-L model output prepared for CMIP6 ScenarioMIP ssp245, Earth System Grid Federation, , doi:<https://doi.org/10.22033/ESGF/CMIP6.3468>, 2019c.
- YU, Y.: CAS FGOALS-f3-L model output prepared for CMIP6 ScenarioMIP ssp370, Earth System Grid Federation, , doi:<https://doi.org/10.22033/ESGF/CMIP6.3479>, 2019d.
- 1490 YU, Y.: CAS FGOALS-f3-L model output prepared for CMIP6 ScenarioMIP ssp585, Earth System Grid Federation, , doi:<https://doi.org/10.22033/ESGF/CMIP6.3502>, 2019e.
- Yukimoto, S., Koshiro, T., Kawai, H., Oshima, N., Yoshida, K., Urakawa, S., Tsujino, H., Deushi, M., Tanaka, T., Hosaka, M., Yoshimura, H., Shindo, E., Mizuta, R., Ishii, M., Obata, A. and Adachi, Y.: MRI MRI-ESM2.0 model output prepared for CMIP6 CMIP historical, Earth System Grid Federation, , doi:<https://doi.org/10.22033/ESGF/CMIP6.6842>, 2019a.
- 1495 Yukimoto, S., Koshiro, T., Kawai, H., Oshima, N., Yoshida, K., Urakawa, S., Tsujino, H., Deushi, M., Tanaka, T., Hosaka, M., Yoshimura, H., Shindo, E., Mizuta, R., Ishii, M., Obata, A. and Adachi, Y.: MRI MRI-ESM2.0 model output prepared for CMIP6 ScenarioMIP ssp119, Earth System Grid Federation, , doi:<https://doi.org/10.22033/ESGF/CMIP6.6908>, 2019b.
- 1500 Yukimoto, S., Koshiro, T., Kawai, H., Oshima, N., Yoshida, K., Urakawa, S., Tsujino, H., Deushi, M., Tanaka, T., Hosaka, M., Yoshimura, H., Shindo, E., Mizuta, R., Ishii, M., Obata, A. and Adachi, Y.: MRI MRI-ESM2.0 model output prepared for CMIP6 ScenarioMIP ssp126, Earth System Grid Federation, , doi:<https://doi.org/10.22033/ESGF/CMIP6.6909>, 2019c.
- Yukimoto, S., Koshiro, T., Kawai, H., Oshima, N., Yoshida, K., Urakawa, S., Tsujino, H., Deushi, M., Tanaka, T.,

- 1505 Hosaka, M., Yoshimura, H., Shindo, E., Mizuta, R., Ishii, M., Obata, A. and Adachi, Y.: MRI MRI-ESM2.0 model output prepared for CMIP6 ScenarioMIP ssp245, Earth System Grid Federation, , doi:<https://doi.org/10.22033/ESGF/CMIP6.6910>, 2019d.
- Yukimoto, S., Koshiro, T., Kawai, H., Oshima, N., Yoshida, K., Urakawa, S., Tsujino, H., Deushi, M., Tanaka, T., Hosaka, M., Yoshimura, H., Shindo, E., Mizuta, R., Ishii, M., Obata, A. and Adachi, Y.: MRI MRI-ESM2.0
1510 model output prepared for CMIP6 ScenarioMIP ssp370, Earth System Grid Federation, , doi:<https://doi.org/10.22033/ESGF/CMIP6.6915>, 2019e.
- Yukimoto, S., Koshiro, T., Kawai, H., Oshima, N., Yoshida, K., Urakawa, S., Tsujino, H., Deushi, M., Tanaka, T., Hosaka, M., Yoshimura, H., Shindo, E., Mizuta, R., Ishii, M., Obata, A. and Adachi, Y.: MRI MRI-ESM2.0
1515 model output prepared for CMIP6 ScenarioMIP ssp434, Earth System Grid Federation, , doi:<https://doi.org/10.22033/ESGF/CMIP6.6925>, 2019f.
- Yukimoto, S., Koshiro, T., Kawai, H., Oshima, N., Yoshida, K., Urakawa, S., Tsujino, H., Deushi, M., Tanaka, T., Hosaka, M., Yoshimura, H., Shindo, E., Mizuta, R., Ishii, M., Obata, A. and Adachi, Y.: MRI MRI-ESM2.0
model output prepared for CMIP6 ScenarioMIP ssp460, Earth System Grid Federation, , doi:<https://doi.org/10.22033/ESGF/CMIP6.6926>, 2019g.
- 1520 Yukimoto, S., Koshiro, T., Kawai, H., Oshima, N., Yoshida, K., Urakawa, S., Tsujino, H., Deushi, M., Tanaka, T., Hosaka, M., Yoshimura, H., Shindo, E., Mizuta, R., Ishii, M., Obata, A. and Adachi, Y.: MRI MRI-ESM2.0 model output prepared for CMIP6 ScenarioMIP ssp585, Earth System Grid Federation, , doi:<https://doi.org/10.22033/ESGF/CMIP6.6929>, 2019h.
- 1525 Zelinka, M. D., Myers, T. A., McCoy, D. T., Po-Chedley, S., Caldwell, P. M., Ceppi, P., Klein, S. A. and Taylor, K. E.: Causes of Higher Climate Sensitivity in CMIP6 Models, *Geophys. Res. Lett.*, 47(1), doi:[10.1029/2019GL085782](https://doi.org/10.1029/2019GL085782), 2020.
- Zhang, J., Wu, T., Shi, X., Zhang, F., Li, J., Chu, M., Liu, Q., Yan, J., Ma, Q. and Wei, M.: BCC BCC-ESM1 model output prepared for CMIP6 CMIP historical, Earth System Grid Federation, , doi:<https://doi.org/10.22033/ESGF/CMIP6.2949>, 2018a.
- 1530 Zhang, J., Wu, T., Shi, X., Zhang, F., Li, J., Chu, M., Liu, Q., Yan, J., Ma, Q. and Wei, M.: BCC BCC-ESM1 model output prepared for CMIP6 CMIP piControl, Earth System Grid Federation, , doi:<https://doi.org/10.22033/ESGF/CMIP6.3017>, 2018b.
- Zhang, J., Wu, T., Shi, X., Zhang, F., Li, J., Chu, M., Liu, Q., Yan, J., Ma, Q. and Wei, M.: BCC BCC-ESM1 model output prepared for CMIP6 CMIP abrupt-4xCO2, Earth System Grid Federation, ,
1535 doi:<https://doi.org/10.22033/ESGF/CMIP6.2846>, 2019.
- Ziehn, T., Chamberlain, M., Lenton, A., Law, R., Bodman, R., Dix, M., Wang, Y., Dobrohotoff, P., Srbinovsky, J., Stevens, L., Vohralik, P., Mackallah, C., Sullivan, A., O'Farrell, S. and Druken, K.: CSIRO ACCESS-ESM1.5 model output prepared for CMIP6 CMIP abrupt-4xCO2, Earth System Grid Federation, , doi:<https://doi.org/10.22033/ESGF/CMIP6.4238>, 2019a.
- 1540 Ziehn, T., Chamberlain, M., Lenton, A., Law, R., Bodman, R., Dix, M., Wang, Y., Dobrohotoff, P., Srbinovsky, J., Stevens, L., Vohralik, P., Mackallah, C., Sullivan, A., O'Farrell, S. and Druken, K.: CSIRO ACCESS-ESM1.5 model output prepared for CMIP6 CMIP historical, Earth System Grid Federation, , doi:<https://doi.org/10.22033/ESGF/CMIP6.4272>, 2019b.
- 1545 Ziehn, T., Chamberlain, M., Lenton, A., Law, R., Bodman, R., Dix, M., Wang, Y., Dobrohotoff, P., Srbinovsky, J., Stevens, L., Vohralik, P., Mackallah, C., Sullivan, A., O'Farrell, S. and Druken, K.: CSIRO ACCESS-ESM1.5 model output prepared for CMIP6 CMIP piControl, Earth System Grid Federation, , doi:<https://doi.org/10.22033/ESGF/CMIP6.4312>, 2019c.

- 1550 Ziehn, T., Chamberlain, M., Lenton, A., Law, R., Bodman, R., Dix, M., Wang, Y., Dobrohotoff, P., Srbinovsky, J., Stevens, L., Vohralik, P., Mackallah, C., Sullivan, A., O'Farrell, S. and Druken, K.: CSIRO ACCESS-ESM1.5 model output prepared for CMIP6 ScenarioMIP ssp126, Earth System Grid Federation, , doi:<https://doi.org/10.22033/ESGF/CMIP6.4320>, 2019d.
- 1555 Ziehn, T., Chamberlain, M., Lenton, A., Law, R., Bodman, R., Dix, M., Wang, Y., Dobrohotoff, P., Srbinovsky, J., Stevens, L., Vohralik, P., Mackallah, C., Sullivan, A., O'Farrell, S. and Druken, K.: CSIRO ACCESS-ESM1.5 model output prepared for CMIP6 ScenarioMIP ssp245, Earth System Grid Federation, , doi:<https://doi.org/10.22033/ESGF/CMIP6.4322>, 2019e.
- 1560 Ziehn, T., Chamberlain, M., Lenton, A., Law, R., Bodman, R., Dix, M., Wang, Y., Dobrohotoff, P., Srbinovsky, J., Stevens, L., Vohralik, P., Mackallah, C., Sullivan, A., O'Farrell, S. and Druken, K.: CSIRO ACCESS-ESM1.5 model output prepared for CMIP6 ScenarioMIP ssp370, Earth System Grid Federation, , doi:<https://doi.org/10.22033/ESGF/CMIP6.4324>, 2019f.
- 1560 Ziehn, T., Chamberlain, M., Lenton, A., Law, R., Bodman, R., Dix, M., Wang, Y., Dobrohotoff, P., Srbinovsky, J., Stevens, L., Vohralik, P., Mackallah, C., Sullivan, A., O'Farrell, S. and Druken, K.: CSIRO ACCESS-ESM1.5 model output prepared for CMIP6 ScenarioMIP ssp585, Earth System Grid Federation, , doi:<https://doi.org/10.22033/ESGF/CMIP6.4333>, 2019g.